# Transport Properties of Carbon Nanotubes Using an Atomic Force Microscope

Thesis submitted in partial fulfilment
of the requirements of the degree of
Doctor of Philosophy
of the
University of London

**Elisabetta Brown**

Imperial College London

Experimental work carried out at the
National Physical Laboratory

July 2006

# Declaration

I declare that, unless stated, the work presented in this thesis is my own.

Signed: 
(Elisabetta Brown)

July 2006

# Abstract

Carbon nanotubes (CNTs) are nanoscale tubules made of a graphene sheet rolled into a seamless cylinder. Their small diameter, high aspect ratio and strong carbon-carbon bonds give CNTs unique physical properties.

This work investigated the nanotubes' electrical and thermal conductance and how these were affected by oxygen adsorption.

Multi walled nanotubes (MWNTs – made of more concentric carbon layers) produced by the arc-discharge method were used in this work because of their high quality and crystallinity. The MWNTs outermost diameters were determined by AFM measurements and found to be in the range of 1.8-1.9 nm.

MWNTs fibres were mounted on a Veeco thermal probe in an Atomic Force Microscope (AFM) adapted for operation in air and high vacuum ($10^{-5}$ mbar) and fitted with a variable temperature stage. The electrical and thermal conductance measurements were taken simultaneously on the individual MWNTs that protruded from the tip of the fibre.

The MWNTs electrical conductance and thermal conductance were studied as the nanotubes came into contact with a substrate (both graphite and gold were used).

Flat plateaus in the electrical conductance were observed at room temperature; these occurred at integer values of the electrical conductance quantum. The nanotube's resistance per unit length derived from the plateaus was $< 1000\ \Omega/\mu m$ equivalent to an electronic mean free path $> 6\mu m$. Thus it was concluded that ballistic electron transport was present in these nanotubes at room temperature.

The number of phonon modes transmitted through the nanotubes was estimated from the correlation between the simultaneous thermal and electrical conductance measurements (taken at room temperature in vacuum). It was found that a single nanotube could support more than 250 phonon modes corresponding to a thermal conductivity > 20,000 W/mK. This value is unrealistically high and led to the conclusions that phonon transport in the nanotubes was also ballistic at room temperature.

The effect of oxygen adsorption on the nanotubes was found to cause significant changes in the electron transport: these were fitted with a model indicating that they were due to either an increase from 5 to 10 in the number of parallel ballistic pathways

from the fibre to the substrate or to an increase from 2 to 3 in the electron conductance modes of the nanotube.

The adsorption of oxygen also caused changes in the nanotube's thermal conductance: its value was found to increase by 30% upon exposure to oxygen. These changes were observed in two nanotube fibres and interpreted to be caused by either an increase in the number of phonon modes of the nanotube due to a distortion in the C-C bond induced by the physisorption of oxygen, or to a more efficient intra-shell heat transfer mediated by gas molecules present between the concentric shells of the nanotube.

This work has shown that nanotubes have extremely good thermal properties and are therefore ideal structures for the study of thermal transport at the nanoscale.

# Table of Contents


**Abbreviations and Symbols** 7
**List of Tables** 8
**List of Figures** 9
**Acknowledgements** 14
**Chapter 1 Introduction** 15
**1.1 Motivation for this Work** 15
**1.2 Achievements and Thesis Outline** 16
**Chapter 2 Basic Concepts** 19
**2.1 Carbon Nanotubes – History and the Basics** 19
2.1.1 The Effect of Oxygen and other Gases on Carbon Nanotubes 23
**2.2 Electron Transport and Electrical Conductance Quantisation** 27
2.2.1 Quantised Conductance 27
2.2.2 Quantised Conductance in Carbon Nanotubes 29
**2.3 Phonon Transport and Quantised Thermal Conductance** 39
2.3.1 Quantised Thermal Conductance 39
2.3.2 Thermal Properties of Carbon Nanotubes 41
**Chapter 3 Experimental Techniques** 48
**3.1 The Atomic Force Microscope (AFM)** 48
3.1.1 Introduction to the AFM 48
3.1.2 The Veeco Explorer AFM 55
**3.2 Adapting the AFM for Operation in High Vacuum** 58
**3.3 Experimental Set-up for Electrical Conductance Measurements** 62
**3.4 Structure and Operation of the Veeco Thermal Probe** 66
3.4.1 Study of the Probe-Sample heat Exchange of the Veeco Thermal Probe 69
**3.5 Attaching an MWNT Fibre to the Thermal Probe** 78
**3.6 Building a Variable Temperature Sample Stage for the AFM** 80
**3.7 Experimental Set-up for Simultaneous Thermal and Electrical Conductance Measurements** 86
3.7.1 At Room Temperature 86
3.7.2 At Low Temperatures 92
3.7.3 With the Addition of Oxygen 96
**Chapter 4 Results and Discussion** 98
**4.1 Sample Description and Characterisation** 98
4.1.1 Study of the MWNT Diameter 100
4.1.2 Bending and Buckling of the MWNTs 106
**4.2 Observation of Ballistic Electron Transport in MWNTs at Room Temperature** 111
**4.3 Simultaneous Electrical and Thermal Measurements on MWNTs at Room Temperature** 116
4.3.3 Discussion: Evidence for Ballistic Phonon Transport in MWNTs 122
**4.4 Measurements on MWNTs at Low Temperature** 124
**4.5 Oxygen Doping Effects on Electron Transport in MWNTs** 134

4.6 Comparison of the Oxygen Effects on Electrical and Thermal Transport in MWNTs 142
Chapter 5 Conclusions and Further Work 147
Conclusion 151
References 152
Appendices 160
A - MathCAD programme to model the cooling of the AFM cold stage 160
B - Labview 7.0 programme for simultaneous thermal conductance, electrical conductance and cantilever deflection acquisition 167
C - MathCAD model of the electrical conductance histograms 174
D - Details of the DTI Funded Project 3.5 178

# Abbreviations and Symbols

| | |
|---|---|
| AFM | Atomic Force Microscope |
| CNT | Carbon Nanotube |
| $G_0$ | Quantum of electrical conductance |
| $G_{th}$ | Quantum of thermal conductance |
| HOPG | Highly Oriented Pyrolitic Graphite |
| LT | Low Temperature |
| RT | Room Temperature |
| MWNT | Multi Walled Nanotube |
| SEM | Scanning Electron Microscope |
| STM | Scanning Tunnelling Microscope |
| SWNT | Single Walled Nanotube |

# List of Tables


| | | |
|---|---|---|
| Table 2.1 | Physical properties of carbon nanotubes | Page 22 |
| Table 3.1 | List of other AFM operating modes | Page 52 |
| Table 3.2 | The Veeco thermal probe compared to a standard AFM probe | Page 67 |
| Table 3.3 | Resistivity and thermal conductivity of the main components of the Veeco thermal probe | Page 67 |
| Table 3.4 | List of heat loss sources in the Veeco thermal probe | Page 75 |
| Table 3.5 | Thermal conductivity of some of the materials used in the AFM cold stage | Page 82 |
| Table 4.1 | Calculated number of shells in an MWNT given its outermost and innermost shell diameters | Page 103 |
| Table 4.2 | Derived nanotube resistivity and contact resistance compared with values from the literature | Page 114 |
| Table 4.3 | List of outermost nanotube diameters for given nanotube indices | Page 120 |
| Table 4.4 | Number of phonon modes in nanotubes for given nanotube indices | Page 121 |
| Table 4.5 | Details of Figure 4.18 | Page 126 |
| Table 4.6 | Details of Figure 4.20 | Page 129 |
| Table 4.7 | Details of Figure 4.21 | Page 130 |
| Table 4.8 | Properties of gold and HOPG compared | Page 131 |
| Table 4.9 | Details of Figure 4.22 | Page 133 |

# List of Figures


| | | |
|---|---|---|
| Figure 2.1 | Diagram of three types of SWNTs | Page 20 |
| Figure 2.2 | Diagram of the unrolled honeycomb carbon lattice | Page 20 |
| Figure 2.3 | Details on metallic and semiconducting nanotubes | Page 22 |
| Figure 2.4 | First report on the effect of oxygen doping of carbon nanotubes | Page 24 |
| Figure 2.5 | The effect of oxygen on the CNTs band structure and Fermi level | Page 25 |
| Figure 2.6 | Diagram of a one dimensional wire | Page 27 |
| Figure 2.7 | First experimental observation of electrical conductance quantisation | Page 28 |
| Figure 2.8 | Energy band structure of semiconducting and metallic CNTs | Page 30 |
| Figure 2.9 | Quantised electrical conductance in CNTs | Page 30 |
| Figure 2.10 | Quantised electrical conductance in CNTs: observation of steps of height $2G_0$ | Page 33 |
| Figure 2.11 | Band structure of nanotubes in a rope | Page 34 |
| Figure 2.12 | Simulated STM images of graphite and double wall nanotubes | Page 35 |
| Figure 2.13 | Structure of graphite | Page 36 |
| Figure 2.14 | Electrons encountering an electron scattering centre in a nanowire | Page 38 |
| Figure 2.15 | First experimental observation of thermal conductance quantisation | Page 40 |
| Figure 2.16 | Phonon density of state for a (10,10) SWNT | Page 42 |
| Figure 2.17 | Thermal properties of mats of SWNTs | Page 44 |
| Figure 2.18 | Thermal measurements on an individual MWNT | Page 45 |
| Figure 2.19 | Prediction for thermal conductance quantisation in CNTs | Page 46 |
| Figure 3.1 | Interatomic forces | Page 49 |
| Figure 3.2 | Diagram of AFM operation in contact mode | Page 51 |
| Figure 3.3 | Diagrams of other AFM operating modes | Page 53 |
| Figure 3.4 | AFM force distance curves | Page 54 |
| Figure 3.5 | The Veeco Explorer AFM | Page 56 |

| | | |
|---|---|---|
| Figure 3.6 | Diagram of AFM hardware connections | Page 58 |
| Figure 3.7 | Photograph of the AFM in the vacuum chamber | Page 59 |
| Figure 3.8 | Diagram of the AFM laser adjustment mechanism when the AFM was in the vacuum chamber | Page 61 |
| Figure 3.9 | Diagram of the experimental set-up for electrical conductance measurements on the nanotubes | Page 63 |
| Figure 3.10 | Diagram of the set-up for measurements of the bulk resistance of MWNTs fibres | Page 66 |
| Figure 3.11 | SEM picture of the Veeco thermal probe | Page 66 |
| Figure 3.12 | Details of the operation of the Veeco thermal probe | Page 68 |
| Figure 3.13 | Diagrams of the thermal probe tested on various substrates | Page 70 |
| Figure 3.14 | Diagram of the heat loss sources in the Veeco thermal probe in air and in vacuum | Page 71 |
| Figure 3.15 | Data showing the amount of heat lost by the Veeco thermal probe in air and in vacuum | Page 72 |
| Figure 3.16 | Data of the temperature measured by a Pt100 resistance thermometer as the thermal probe was lowered on it | Page 73 |
| Figure 3.17 | Data of the temperature change in a sample probe as the heated thermal probe was lowered on it | Page 74 |
| Figure 3.18 | Measured heat losses of the thermal probe in air and in vacuum | Page 75 |
| Figure 3.19 | Data showing the amount of heat lost by the thermal probes in different modes | Page 76 |
| Figure 3.20 | Fractional amount of the heat lost by the thermal probe in each mode in air and in vacuum | Page 77 |
| Figure 3.21 | Diagram of the mounting of an MWNT fibre on a Veeco thermal probe | Page 79 |
| Figure 3.22 | Diagram of the cryostat | Page 81 |
| Figure 3.23 | Diagram of the cold stage built for the AFM | Page 82 |
| Figure 3.24 | Experimental data of the cooling of the cold stage compared with a model | Page 85 |
| Figure 3.25 | Diagram of the mechanism to adjust the AFM laser when the AFM was placed in the vacuum chamber on the cold stage | Page 87 |
| Figure 3.26 | Photograph of the AFM on the cold stage | Page 88 |

| | | |
|---|---|---|
| Figure 3.27 | Diagram of the experimental set-up for simultaneous electrical and thermal conductance measurements on the nanotubes | Page 89 |
| Figure 3.28 | Diagram of the break-box for the thermal and electrical conductance measurements on the nanotubes | Page 90 |
| Figure 3.29 | Diagram of the circuit of the experimental set-up shown in Fig. 3.27 | Page 91 |
| Figure 3.30 | Photograph and diagram of the heater attached on the substrate in the AFM cold stage | Page 92 |
| Figure 3.31 | Data showing the effect of the heater on the quality of the electrical conductance measurements at LT | Page 93 |
| Figure 3.32 | Data of the cooling curves for different parts of the cold stage | Page 94 |
| Figure 3.33 | Data of the force curves taken at RT and LT compared | Page 95 |
| Figure 3.34 | Photograph of the experimental set-up for the addition of oxygen to the vacuum chamber | Page 97 |
| Figure 4.1 | Diagram of the arc-evaporation apparatus for the production of CNTs | Page 98 |
| Figure 4.2 | Diagram of the fractal-like organisation of arc-grown MWNT fibres | Page 99 |
| Figure 4.3 | SEM picture of the MWNT fibre | Page 100 |
| Figure 4.4 | AFM images of individual MWNTs dispersed on HOPG | Page 101 |
| Figure 4.5 | Histogram of the MWNT diameter derived from the AFM scans | Page 102 |
| Figure 4.6 | AFM scans of MWNTs dispersed on silicon and mica | Page 104 |
| Figure 4.7 | Raman spectra taken on MWNTs | Page 105 |
| Figure 4.8 | Electrical conductance traces of MWNTs lowered/withdrawn from a substrate compared | Page 107 |
| Figure 4.9 | Diagram of a nanotube bending as it contacts a hard substrate | Page 108 |
| Figure 4.10 | Diagram of nanotubes sliding past each other in a bundle | Page 109 |
| Figure 4.11 | Electrical conductance traces of carbon nanotubes, showing plateaus | Page 111 |
| Figure 4.12 | Analysis of electrical conductance plateaus | Page 113 |
| Figure 4.13 | Electrical conductance curve details | Page 115 |

| | | |
|---|---|---|
| Figure 4.14 | Electrical and thermal conductance and force curve of a nanotube in contact with an HOPG substrate | Page 117 |
| Figure 4.15 | Electrical and thermal and force curve of a nanotube in contact with an HOPG substrate, semiconducting tube | Page 118 |
| Figure 4.16 | Plot of the thermal versus electrical conductance step, evidence of ballistic phonon transport | Page 119 |
| Figure 4.17 | Plot of the thermal versus electrical conductance step, evidence of diffusive phonon transport | Page 123 |
| Figure 4.18 | Thermal versus electrical conductance step at RT and LT on HOPG | Page 125 |
| Figure 4.19 | Electrical conductance signal at LT and low and high voltage bias | Page 127 |
| Figure 4.20 | Thermal versus electrical conductance step at RT and LT on HOPG at high voltage bias | Page 128 |
| Figure 4.21 | Thermal versus electrical conductance step at RT and LT on gold at low voltage bias | Page 130 |
| Figure 4.22 | Evidence of oxygen doping of the nanotubes after LT measurements | Page 132 |
| Figure 4.23 | Example histogram of the (b) conductance curve in Fig 4.11 | Page 135 |
| Figure 4.24 | Histograms of the nanotube electrical conductance taken in air and in vacuum | Page 135 |
| Figure 4.25 | Changes in the bulk resistance of the MWNT fibre as oxygen is desorbed | Page 136 |
| Figure 4.26 | Diagram of the conductance channels in an MWNT bundle coming in contact with HOPG | Page 137 |
| Figure 4.27 | Histograms of the nanotube electrical conductance generated by a MathCAD model | Page 138 |
| Figure 4.28 | MathCAD model of the electrical conductance fitted to the experimental data: change in W | Page 140 |
| Figure 4.29 | MathCAD model of the electrical conductance fitted to the experimental data: change in C | Page 141 |
| Figure 4.30 | Monitoring the electrical and thermal conductance of nanotubes when exposed to oxygen | Page 143 |
| Figure 4.31 | Percentage changes in the electrical and thermal conductance of nanotubes when oxygen is adsorbed | Page 143 |

Figure 4.32 Histograms of the electrical and thermal conductance of the nanotubes as oxygen is desorbed/adsorbed Page 145

Figure 5.1 SEM picture of a prototype nano-bridge for thermal measurements on individual nanotubes Page 149

# Acknowledgements

There are many people I would like to thank, as without them, this work would have not been possible.

I would like to start by thanking the National Physical Laboratory for employing me and also for giving me the possibility to enrol in a part-time PhD at Imperial College.

Great thanks go to my supervisors at NPL: John Gallop and Ling Hao who have been extremely helpful and very encouraging. It has been a real pleasure to work with you!

Many thanks also must go to my supervisor at Imperial College: Lesley Cohen, for her always-helpful advice especially in the final stages of this work.

Then I want to thank Mark Baxendale who helped me to get started with the nanotube work and who provided all the nanotube material.

Many other people in the Time and Quantum Detection group at NPL have offered their help and expertise during the course of this work and I would like to thank all my colleagues for creating such a nice and friendly working environment. I would like to mention in particular John Macfarlane especially for his assistance with anything to do with cryogenics, Patrick Josephs-Franks and Mark Oxborrow for their readiness to help and their wise advice and David Cox for the SEM images.

On a less technical note, I want to thank my husband Chris who willingly took over my share of the household chores while I was busy writing up this report, it was a real treat to have meals cooked, dishes washed and clothes ironed!

Finally, last but not least, I want to thank God not only for keeping me sane throughout this work but also for keeping the little Explorer AFM going. Inherited second hand from another NPL group, it survived, over the course of my time at NPL: three lab moves, one software upgrade, extended time in high vacuum, heating, cooling, frequent rewiring and intense use. I think that, had it broken, I could have figured out something else to do but I'm so glad I never had to face that situation!

# Chapter 1 Introduction

## 1.1 Motivation for this Work

In 1991 Sumio Ijima [Iijima'91] made a momentous discovery, he reported the formation of microtubules made of graphitic carbon: carbon nanotubes. Since then these carbon macromolecules have been at the centre of intense theoretical and experimental studies and their unique properties have fuelled the imagination of many scientists (see for instance Ref. [Yakobson'97]).

Whilst extensive measurements of the electrical and mechanical properties of the nanotubes have been made, the thermal properties of these macromolecules have been, up to now, the subject of only few investigations and these have mainly involved bulk nanotube samples (see Section 2.3.2). Until recently the only thermal measurement on individual nanotubes was that performed by P. Kim et al in 2001 (see Ref. [Kim'01]), however, in the last few months other successful measurements of the thermal properties of *individual* nanotubes have been reported (see Ref. [Choi'05] and [Fujii'05]) showing that this is currently a very much needed and interesting area of research. This is because carbon nanotubes may prove to be ideal materials for thermal management from the macro- to the nano-scale and for the study of low dimensional phonon physics.

It is this context that motivates this work whose aim is to study the electrical and thermal transport properties of individual carbon nanotubes in a variety of conditions. This work in particular aims to focus on the study of evidence of ballistic transport in the nanotubes (first reported in 1998, see Ref. [Frank'98], for electrons in multi-walled nanotubes at room temperature) and on the quantised nature of such transport. This is because evidence of ballistic phonon transport would confirm nanotubes as ideal thermal conductors for nano-scale applications and because the measurement of the quantum of thermal conductance (first observed in 2000 in GaAs nanostructures, see Ref. [Schwab'00]) could form the basis, in the long term, of a more precise determination of the Boltzmann constant ($k_B$) and lead to a redefinition of the Kelvin.

This work is part of the Project 3.5 in the Quantum Metrology Programme of the National Measurement System, funded by the Department of Trade and Industry in the UK (see Appendix D).

## 1.2 Achievements and Thesis Outline

The main achievements of this work are summarised below:

1. A commercially available Atomic Force Microscope was adapted for work in high vacuum and a variable temperature sample stage was designed and built for it.
2. A technique was developed to attach arc-discharge multi-walled nanotube fibres to commercially available thermal probes.
3. A measurement system, based on lowering nanotubes onto fixed solid substrates, was developed allowing simultaneous thermal and electrical conductance and force measurements to be performed on individual carbon nanotubes.
4. A physical model for the distortion that the nanotube undergoes under the force applied by the thermal probe was developed. This was critical to explain the assumption on how the nanotube length changed as the tube was lowered onto a solid substrate.
5. Ballistic phonon and electron transport was observed in the nanotubes at room temperature. The report of the observation of ballistic phonon transport was published in a peer-reviewed journal (see Ref. [Brown'05]) and this is believed to be the first publication of this effect in nanotubes.
6. A comparative study of the ratio of the thermal and electrical conductance of the nanotubes (in their respective quantised units, $G_{th}$ and $G_0$) was carried out at different temperatures and onto different substrates (Au, HOPG). This allowed a calculation of the number of phonon modes available per nanotube assuming each data set to consist of nanotubes of similar structure and diameter.
7. The effect of oxygen on the electrical properties of the nanotubes was measured by writing a statistical analysis MathCAD programme to apply to the experimental data. In the programme the nanotube network was described by W parallel ballistic wires, each with C conducting modes forming a series pathway comprising in total S wires. This was used to study, using a semiclassical approach, how the electron conducting properties of the nanotubes changed with experimental conditions.
8. A preliminary study of the effect of oxygen on the thermal properties of the nanotubes was performed. This is a novel topic, which has not yet received much mention in the scientific literature.

A list of the presentations and publications that have been produced during this work is below.

- Posters:

'*Preliminary Study on the Probe-Sample Heat Exchange Using a Topometrix Thermal Probe in Air and in Vacuum*', Elisabetta Brown, John Gallop, presented at Veeco Users Meeting, Oxford, UK – 9 January 2003.

'*Oxygen Doping of Multiwall Carbon Nanotube Systems: Quantised Conductance Studies*', Elisabetta Brown, Mark Baxendale, John Gallop, presented at NanoteC'03, University of Sussex, Brighton, UK – 27-30 August 2003.

'*Thermal Measurements on Multi Wall Nanotubes*', E Brown, L Hao, J Gallop, J Macfarlane, presented at: IWEPNM 2004, Kirchberg, Austria – 6-13 March 2004; CMMP2004, University of Warwick, UK – April 2004; NT04, San Luis Potosì, Mexico – 19-24 July 2004.

'*Ballistic Thermal and Electrical Conductance Measurements on Individual Multi-wall Carbon Nanotubes*', Elisabetta Brown, Ling Hao, John C. Gallop, Lesley F. Cohen, John C. Macfarlane, presented at IWEPNM 2005, Kirchberg, Austria – 12-19 March 2005 and at Physics 2005, University of Warwick, UK – 10-14 April 2005.

'*AFM and Raman Studies of Carbon Nanotubes*', Ling Hao, Lizzie Brown, John Gallop, Patrick Josephs-Franks and Lesley Cohen, presented at Physics 2005, University of Warwick, UK – 10-14 April 2005

- Oral Presentations (name of speaker underlined)

'*Oxygen Doping of Multiwall Carbon Nanotube Systems: Quantised Conductance Studies*', Elisabetta Brown, Mark Baxendale, John Gallop, presented at NanoteC'03, University of Sussex, Brighton, UK – 27-30 August 2003.

- Publications:

'*Thermal Measurements on Multi-wall Nanotubes*', E. Brown, L. Hao, J. C. Gallop, and J. C. Macfarlane, AIP Conf. Proc. **723**, 91 (2004)

'*Observation of Ballistic Thermal and Electrical Transport in Multi-wall Carbon Nanotubes*', Elisabetta Brown, Ling Hao, John C. Gallop, Lesley F. Cohen, and John C. Macfarlane, AIP Conf. Proc. **786**, 504 (2005)

'*Ballistic thermal and electrical conductance measurements on individual multiwall carbon nanotubes*', Elisabetta Brown, Ling Hao, John C. Gallop, John C. Macfarlane, Appl. Phys. Lett. **87**, 023107 (2005).

**Thesis Outline**

Following the introduction, this Thesis contains four further Chapters:

- Chapter 2 is a literature review that provides the background information needed to understand the scope of this work. It reviews the nanotubes' transport properties, some of the experiments that have been carried out to study them and the evidence of their dependence on environmental conditions. The theoretical origin and experimental evidence for the quantum of electrical and of thermal conductance are also discussed.
- Chapter 3 provides a description of the experimental techniques used and developed in this work. It includes a section on the principles of the operation of the Atomic Force Microscope and the work done to evaluate the sensitivity of the commercially available Veeco thermal probes. The descriptions of the experimental set-ups developed in this work are found in this Chapter.
- Chapter 4 contains the experimental results taken during the course of this work and a discussion of their interpretation. It includes a section on the characterization of the nanotube material used in this work.
- Chapter 5 concludes this report with a discussion of future experiments planned to consolidate and improve the findings made in this work. It also describes the possible future applications of this work.

Finally, Appendixes A, B and C contain copies of mathematical models and data acquisition programmes developed during the course of this work, while Appendix D contains the summary of the DTI funded project of which this work is a part.

# Chapter 2 Basic Concepts

## 2.1 Carbon Nanotubes – History and the Basics

Carbon nanotubes were first mentioned in the scientific literature in the November 1991 issue of the journal Nature [Iijima'91]. The author, Sumio Iijima there reported the discovery of *'helical microtubules of graphitic carbon'* observed whilst performing high-resolution TEM studies on the deposit formed on the graphite cathode in an arc-evaporation apparatus. This arc-evaporation apparatus had been set up to produce fullerenes, nanometre sized 60-atom carbon balls (also known as $C_{60}$), which had been discovered in 1985 by Harry Kroto and Richard Smalley [Kroto'85].

Fullerenes and carbon nanotubes caught the attention of the scientific world because they were a new type of all-carbon crystalline structure alongside the familiar graphite and diamond. Their discoveries have opened a new area in carbon science (See Chapter 1 in [Harris'99]).

Carbon nanotubes are a honeycomb carbon lattice – a graphene sheet – rolled into a cylinder. They are divided into two 'species', single wall nanotubes (SWNTs) made of just one rolled up carbon layer, and multi wall nanotubes (MWNTs) made of concentric carbon sheets rolled inside one another. SWNTs have typical diameter of ~1 nm, while MWNTs have diameters in the range 2-30 nm in both cases their length can be several microns. Carbon nanotubes are closed at both ends by hemispherical caps (see Fig. 2.1) – the caps owe their shape to the presence of pentagons in the hexagonal carbon lattice.

Single wall carbon nanotubes are classified depending on the orientation relative to the tube axis of the six-membered carbon ring in the honeycomb lattice that makes up the tube.

The primary symmetry classification for the tubes is whether they are chiral or achiral. An achiral tube is one whose mirror image is identical in structure to the original one while a chiral tube exhibits a spiral symmetry whose mirror image cannot be superimposed on the original one.

There are only two types of achiral tubes and they are named after the shape of the cross sectional ring structure: armchair and zigzag (see Fig. 2.1).

All the other tubes are chiral. Both chiral and achiral tubes can have different diameters depending on the size of their unit cell.

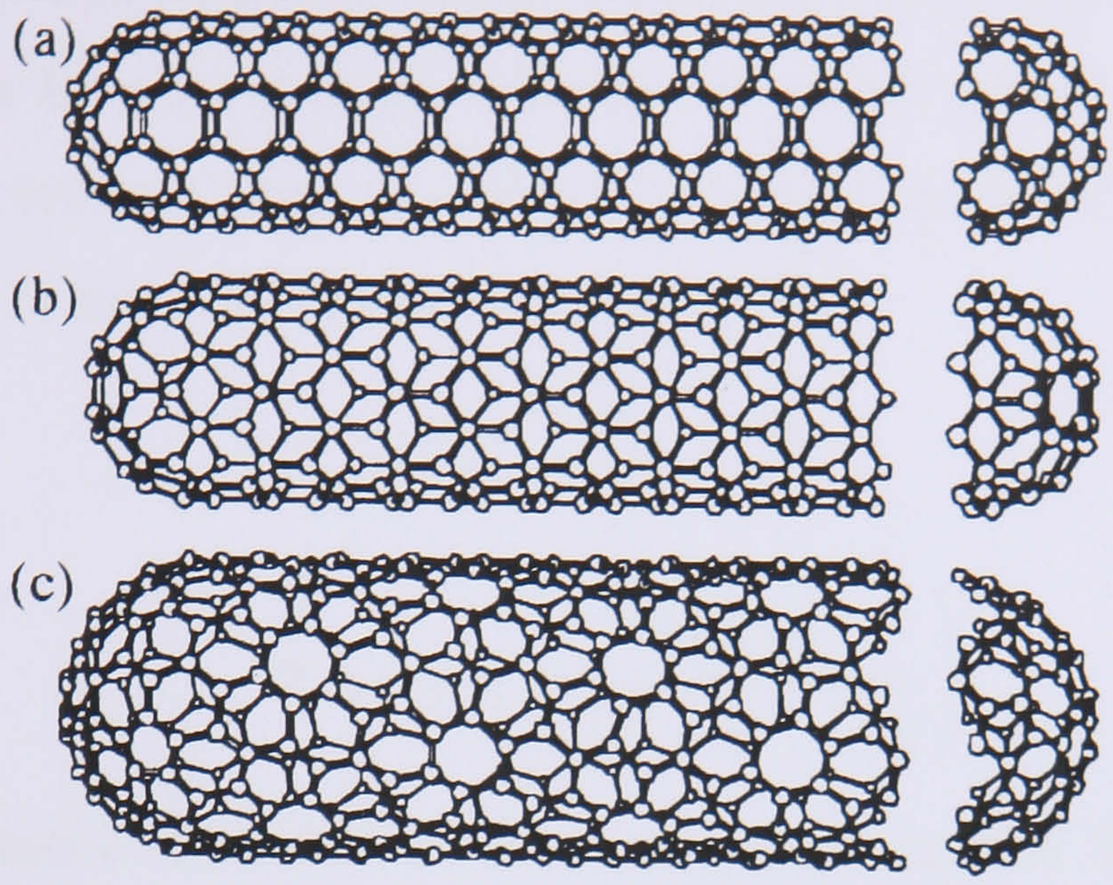



**Figure 2.1**: Three different types of SWNTs: **(a)** armchair, **(b)** zigzag and **(c)** chiral. (Figure taken from Ref. [Saito'98])

In Fig. 2.2 the unrolled honeycomb structure of a nanotube is shown. In it the vector **OA** corresponds to a section perpendicular to the tube axis while vector **OB** lies along the axis of the tube. The area *OABB'* is the unit cell of the nanotube.

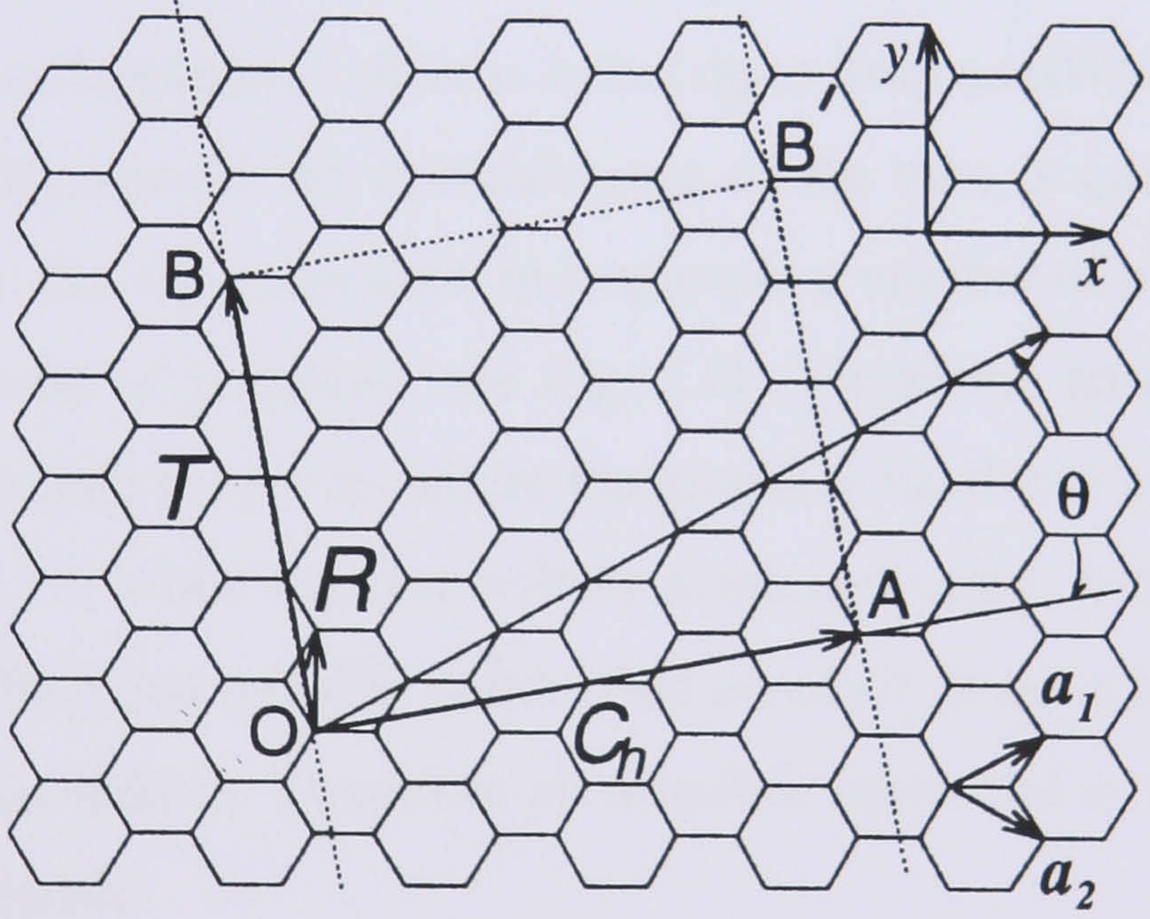



**Figure 2.2**: the unrolled honeycomb lattice of a nanotube. (Figure taken from Ref. [Saito'98])

Vector **OA** is also called the chiral vector of the nanotube ($\mathbf{C}_h$) and vector **OB** the translational vector (**T**).

The honeycomb lattice is built by successive translations of two unit vectors $\mathbf{a}_1$ and $\mathbf{a}_2$. The chiral vector can be expressed in terms of the unit vectors as: $\mathbf{C}_h = n\mathbf{a}_1 + m\mathbf{a}_2 \equiv (n,m)$ where $n$ and $m$ are integers and $0 \le m \le n$*.

---

* This limitation is because, due to the hexagonal symmetry of the honeycomb lattice, the structure of a $(n,m)$ nanotube is the same as that of an $(m,n)$ one and thus new structures are obtained only if $m \le n$.

The armchair nanotubes correspond to cases where $n = m$, while zigzag tubes have $m = 0$, all other *(n,m)* combinations correspond to chiral nanotubes.

Nanotubes are classified with their $n$, $m$ indices (e.g. a (4,2) tube or a (8,8) tube). The $n$ and $m$ indices can be also used to calculate the tube's chiral angle $\theta$ – the angle between the chiral vector $\boldsymbol{C}_h$ and $\boldsymbol{a}_1$ – (see Fig. 2.2) and to derive the tube's diameter $d_t$ using equations (2.1) and (2.2) respectively [Saito'98]:

$$d_t = \frac{a\sqrt{n^2 + m^2 + nm}}{\pi} \qquad (2.1)$$

$$\theta = \cos^{-1}\left(\frac{2n + m}{2\sqrt{n^2 + m^2 + nm}}\right) \qquad (2.2)$$

where $a$ is the lattice constant of the honeycomb carbon lattice: $a$ = 0.249nm. Depending on diameter and chirality a nanotube can be either a metal or semiconductor with an energy gap inversely proportional to the tube diameter. These remarkable electrical properties arise from the electronic structure of graphene from which the nanotubes are derived. Graphene's dispersion relation in momentum (k) space is schematically shown in Fig. 2.3b. Graphene is a zero-gap semiconductor, the band-gap between valence and conduction bands is reduced to zero only at specific points of the Brillouin zone. When a graphene sheet is rolled up to form an SWNT, the momentum of the electrons moving around the circumference of the tube is quantised, reducing the available electron states for a nanotube in k space to a number of parallel slices through the 2D Brillouin zone of graphene, see Fig. 2.3b. Therefore, nanotubes with a set of wavevectors that include the points where the graphene band-gap is zero (Fig. 2.3c) will be metallic (Fig. 2.3d) while the rest will be semiconducting. It has been shown (See chapter 4 in [Saito'98]) that metallic conduction occurs if *(n-m)* is a multiple of 3 where $n$ and $m$ are the tube indices. Therefore all armchair tubes and a third of all chiral and zigzag tubes are metallic.

This has created a lot of interest in the tubes, as no doping is required to change the nanotubes' conducting properties that can be finely tuned by modifications in the tube structure.

In Table 2.1 are shown some of the most significant physical properties of carbon nanotubes that make them truly remarkable nanostructures. Carbon nanotubes have extremely high Young's modulus, thermal conductivity and current density; also, their strength to weight ratio is over 200 times that of steel*.

---

* Grade 301 Stainless steel has tensile strength of 1.8 GPa and density of 8000 kg $m^{-3}$. CNTs have tensile strength of 150 GPa and density of 2600 kg $m^{-3}$.

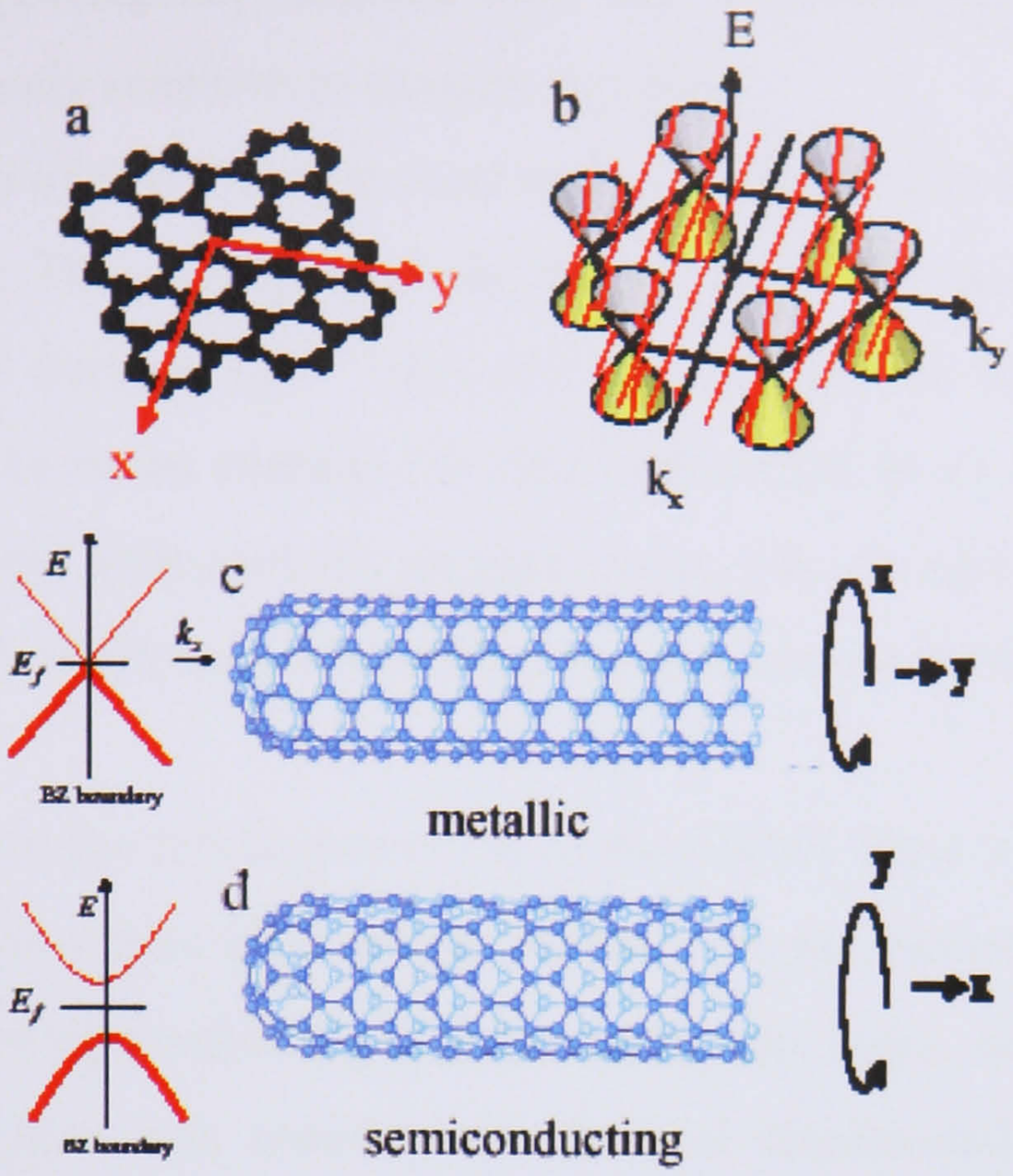



**Figure 2.3**: **a)** the structure of a graphene sheet in real space. **b)** schematic diagram of the graphene dispersion relation in momentum space. The band-gap goes to zero only at specific points in momentum space. The allowed states of a nanotubes are slices through the 2D dispersion relation of graphene. **c)** the band structure of a metallic nanotube. **d)** the band structure of a semiconducting nanotube (diagram taken from [McEuen'02]).

| Physical Property | Experimental Value |
|---|---|
| Thermal Conductivity (at RT) | > 3000 W $m^{-1}$ $K^{-1}$ [a] [Kim'01] |
| Electrical Resistivity (at RT) | ~ $10^{-6}$ Ω cm [b] [Park'04] |
| Maximum Current Density | >$10^{9}$ A $cm^{-2}$ [c] [Yao'00] |
| Young's Modulus | 1.28 TPa [d] [Wong'97] |
| Tensile Strength | 150 GPa [e] [Demczyk'02] |

**Table 2.1**: The highest values of the most significant physical properties of carbon nanotubes.
[a] For an individual MWNT, 14 nm in diameter. Theory predicts a value of ~ 6600 W $m^{-1}$ $K^{-1}$ for a (10,10) SWNT. [Berber'00]
[b] For a SWNT 1.8 nm in diameter (at RT).
[c] For a SWNT ~1 nm in diameter.
[d] Average value for several MWNTs, diameter range 26-76 nm. The Young's modulus was found to be independent of diameter.
[e] For an individual MWNT, 12.5 nm in diameter.

### 2.1.1 The Effect of Oxygen and other Gases on Carbon Nanotubes

The effect of gaseous molecular oxygen ($O_2$) on carbon nanotubes was first reported in the year 2000 when a group at Pennsylvania State University [Sumanasekera'00] and a

group at Berkeley [Collins'00] showed that the electronic properties of carbon nanotubes were extremely sensitive to oxygen exposure.

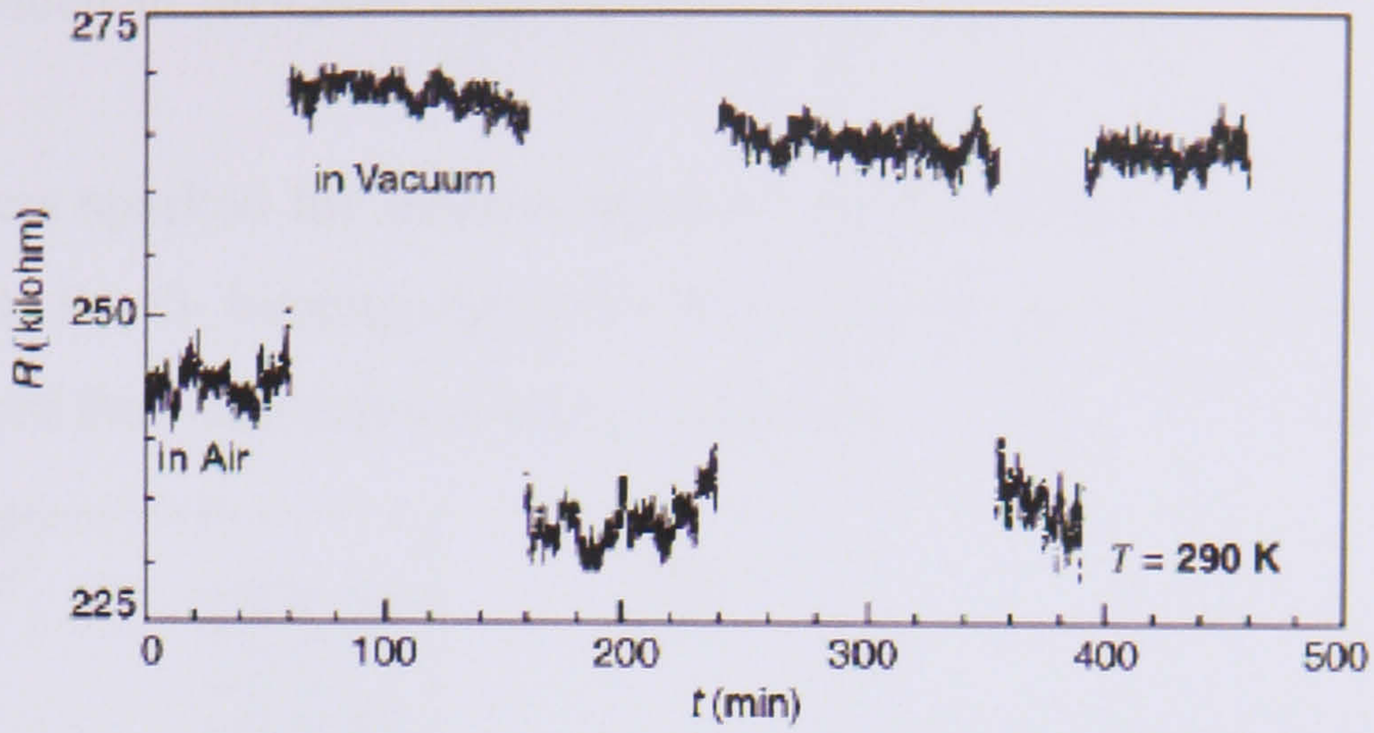
Bundles and thin films of SWNTs were used in the experiments by P. G. Collins et al at Berkeley [Collins'00]. The resistance of the SWNT thin films was measured as they were cycled between vacuum ($10^{-6}$ torr) and air. In vacuum the resistance of the nanotubes was found to be on average 10-15% higher than in air (see Fig. 2.4a). The experiment was repeated with pure dry oxygen rather than air and the same resistance changes were detected, in this way atmospheric oxygen was isolated as the source of the effect.

The effect of oxygen on the thermopower (S) of the SWNT films was also investigated and it was found that in a pure atmospheric pressure oxygen environment S was about +20 μV/K (the positive sign indicating that the carriers are holes, and that the system is p-type) while, as oxygen was removed, S changed continuously from positive to negative with a final value of about –10 μV/K (the negative sign indicating that the carriers are electrons and that the system is n-type – see Fig. 2.4b).

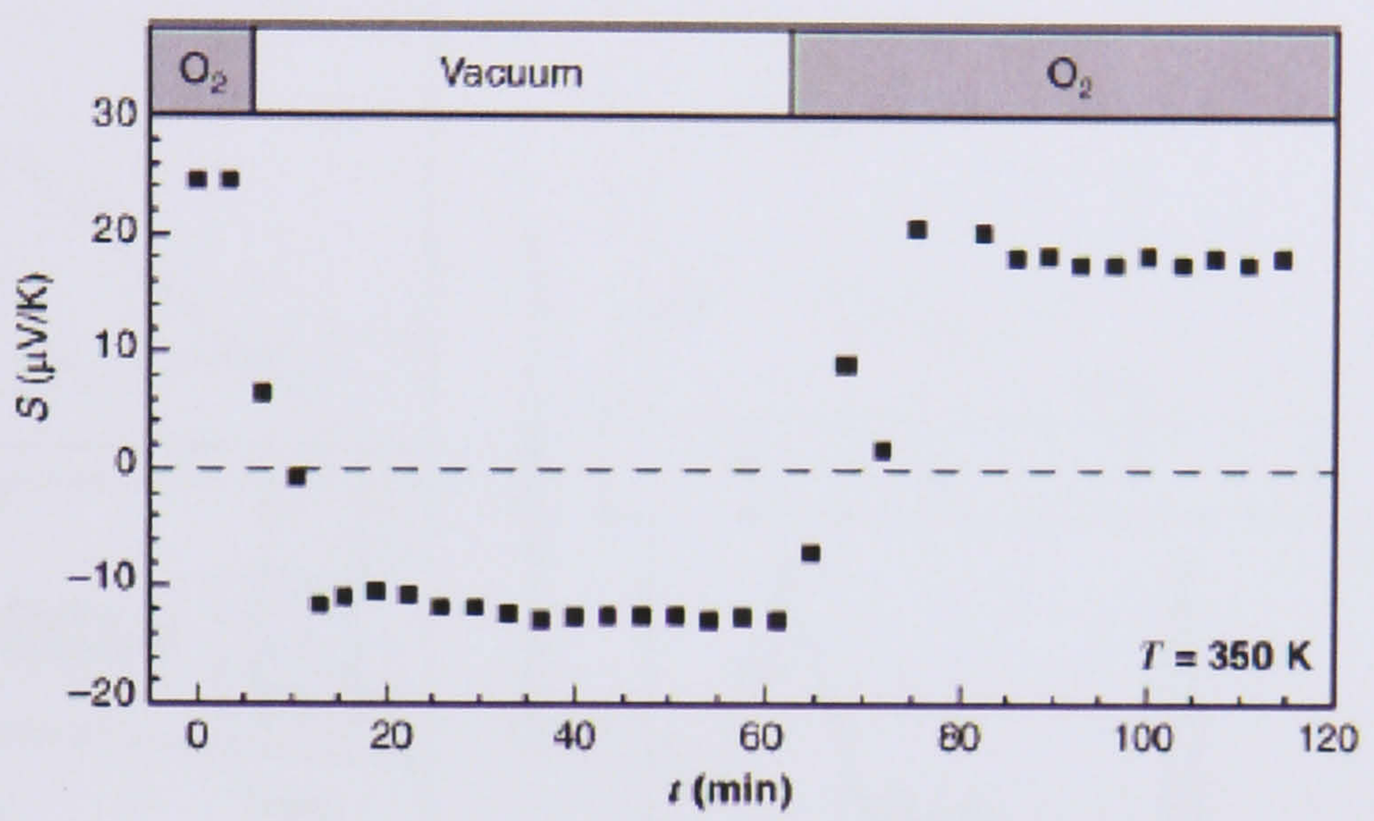
Scanning tunnelling spectroscopy (STS) was then used to study how the local density of states of the nanotubes (isolated or in bundles) was being affected by the presence of oxygen. 17 samples were measured: 7 were metallic in vacuum, 8 were small band gap semiconductors in vacuum (band gap of 175-500 mV) and 2 large gap semiconductors (band gaps >500 mV). It was found that, as oxygen was introduced, the metallic tubes stayed metallic, the small band gap semiconductors became metallic and the semiconducting tubes had their band gap slightly reduced (see Fig. 2.4c).

Similar dramatic changes were reported almost at the same time by G. U. Sumanasekera et al. at Pennsylvania State University [Sumanasekera'00]. Mats of entangled SWNTs were used in this work. The thermopower, S, was again observed going from large and positive values (+48 μV/K) in the presence of oxygen to large negative values (-30 μV/K) when the oxygen was desorbed from the nanotubes. The resistance measurements though showed an effect opposite to the one reported by Collins et al: a decrease in the resistance of the mats was observed as $O_2$ was removed from the sample.

**(a)**




**(b)**




**(c)**

| Sample no. | STS band gaps (mV) | | Neighbors (*n*) |
|---|---|---|---|
| | Baked | $O_2$-exposed | |
| 1 | M | M | 1–3 |
| 2 | M | M | 1–3 |
| 3 | M | M | 1–2 |
| 4 | M | M | 3–5 |
| 5 | M | M | 3–5 |
| 6 | M | M | Multiple |
| 7 | M | M | Multiple |
| 8 | 550 | 500 | 0–2 |
| 9 | 750 | 600 | 0–1 |
| 10 | 175 | M | 0–1 |
| 11 | 175 | M | 1–3 |
| 12 | 190 | M | 1–3 |
| 13 | 250 | M | 1–3 |
| 14 | 300 | M | 0 |
| 15 | 350 | M | 1–3 |
| 16 | 500 | M | 0 |
| 17 | 500 | M | 0–1 |

**Figure 2.4**: Experimental data obtained by Collins et al: **(a)** the resistance of the SWNTs thin films increases when oxygen is removed. **(b)** the changes in the value and sign of the thermopower when oxygen is introduced/removed from the SWNTs thin films **(c)** table showing the change in the band gap (in mV) of semiconducting nanotubes when exposed to oxygen. (pictures from Ref. [Collins'00])

The changes in S were attributed by both groups to a charge transfer occurring from the carbon nanotubes walls to the $O_2$ molecule; this charge transfer injected hole carriers in the nanotubes (hence the change in the sign of S) and also affected the position of the Fermi energy of the tube (hence the change from semiconducting to metallic tubes upon

$O_2$ exposure, which in turn was responsible for the decrease in resistance observed by Collins et al.).

These two papers sparked the interest of many groups and what followed was a large effort to estimate the $O_2$ binding energy to the carbon nanotube walls and the amount of charge transferred from the tubes to the $O_2$ molecule.

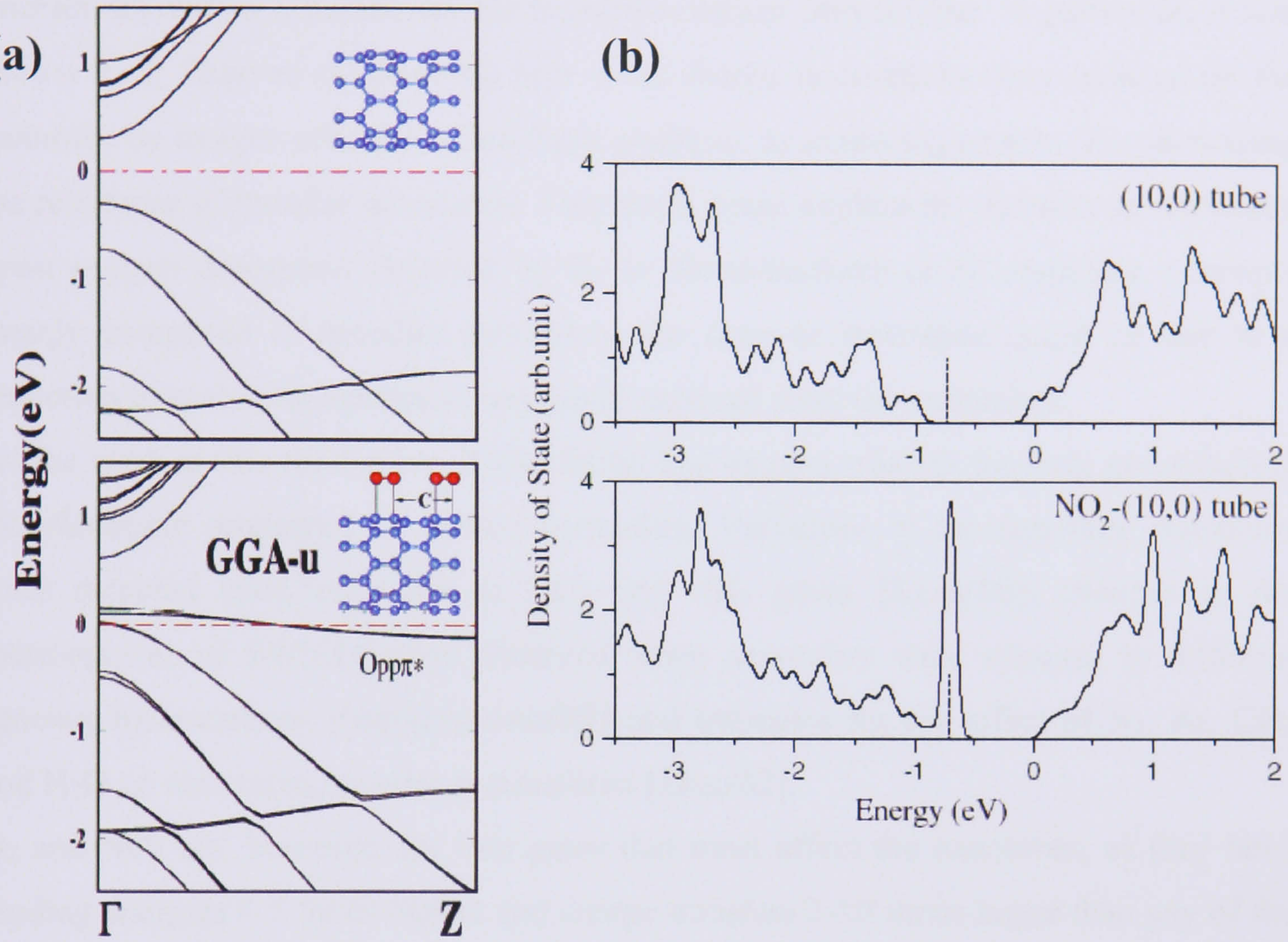



**Figure 2.5**: **(a)** S. Dag et al. [Dag'03] calculated how the adsorption of oxygen modifies the band structure of an (8,0) nanotube. The band structure at the top is for the isolated nanotube, the one at the bottom for the oxygen-nanotube complex. The Fermi level is at E=0. **(b)** Zhao et al. [Zhao'02] calculated the effect of $NO_2$ (very similar to the behaviour of molecular oxygen) on the density of states of a (10,0) nanotube. Notice how the Fermi level (dotted line in the middle of the energy range) is moved into the valence band upon interaction with $NO_2$, making the nanotube a p-type conductor.

Ab initio calculations of $O_2$ interactions with carbon nanotubes were used by S. H. Jhi et al [Jhi'00], it was estimated that the oxygen binding energy to the nanotube was ~0.25 eV (indicating physisorption of the $O_2$ molecule on the nanotube walls) and that the charge transfer was up to 0.1 $e^-$ (electron charge) per molecule. The way in which $O_2$ adsorption modified the electronic structure of nanotubes was also investigated. It was found that the band degeneracies in the SWNTs were broken by the interaction with the oxygen states (see Fig. 2.5a), and this band splitting in turn affected the density of states (DOS) of the tubes (see Fig. 2.5b). The electron transfer also caused the Fermi energy to be shifted towards the valence band and this in turn meant that the DOS of the oxygen–doped carbon nanotubes had a non zero value at the Fermi energy. This thus proved that

oxygen could dope carbon nanotubes giving hole carriers (i.e. accepting electrons) and finite conductance.

Other simulation work on the effect of oxygen adsorption on carbon nanotubes arrived to similar conclusions (see Ref. [Giannozzi'03], [Chan'03], [Zhao'02] and [Ulbricht'02]). with further refinements on the importance of tube chirality, tube defects and tube-tube interactions within a bundle on the nanotube-oxygen interactions. In particular, it was shown by J. Zhao et al [Zhao'02] how local charge fluctuations were induced on the nanotube by oxygen adsorption and these could act as scattering centres thus increasing the resistance of metallic nanotubes. This result could explain the decrease in resistance upon oxygen desorption detected by G. U. Sumanasekera et al: assuming a sample mainly composed of metallic nanotubes, the drop in resistance could be due to a reduction of scattering centres as oxygen is removed from the nanotubes.

As the work in this field grew, it was found that oxygen was not the only gas affecting the electronic properties of carbon nanotubes. Variations in the nanotube resistance were detected upon exposure to $NO_2$ and $NH_3$ gases [Kong'00]; changes in the thermopower of SWNTs were observed when nanotubes were exposed to different gaseous hydrocarbons [Sumanasekera'02] and estimates for the effect of $N_2$, Ar, $CO_2$ and $H_2O$ on nanotubes have been calculated [Zhao'02].

$O_2$ and $NO_2$ are, however, the two gases that most affect the nanotubes, as they have binding energies 4-5 times higher and charge transfers 2-10 times larger than any of the other gases [Zhao'02].

This work on the sensitivity of the carbon nanotubes' properties to their gas exposure history highlighted two issues: i) the study of the *intrinsic* properties of a nanotube is only possible after gaseous/atmospheric contaminants have been desorbed; ii) semiconducting carbon nanotubes could be used as gas sensors. This second issue has sparked a lot of interest because of its potential market: CNTs could be used to develop miniaturised, ultra-sensitive gas detectors. These would be crucial in the detection of, for instance, poisonous gases in a terrorist attack. The CNT-based gas sensors developed so far are promising [Qi'03] [Valentini'03]: they are sensitive to concentrations as low as 1-10 part per billion (ppb), have response times of 1-2 minutes and good gas selectivity.

In conclusion, the sensitivity of the CNTs' electronic properties to gases, which might have initially appeared as a nuisance, could yet prove to be very useful for the commercialisation of CNT-based devices*.

## 2.2 Electron Transport and Electrical Conductance Quantisation

In this section the conditions for electrical conductance quantisation in nanostructures will be described, then the electronic transport properties of the nanotubes will be discussed, focussing on how these are affected by the nanoscale dimensions of the CNTs.

### 2.2.1 Quantised Conductance

When the electronic mean free path $\lambda$ of a wire is larger than the wire's length L, the wire behaves like an electron wave-guide and each wave-guide mode -or conduction channel- contributes exactly an amount $G_0$ to the total conductance of the wire§.

The amount $G_0$ is independent of the material properties and the dimension of the wire and is called the conductance quantum, it is equal to:

$$G_0 = \frac{2e^2}{h} \qquad (2.3)$$

where $e$ is the electron charge and $h$ is Plank's constant. $1G_0$ is ~ $(12.9\ k\Omega)^{-1}$.

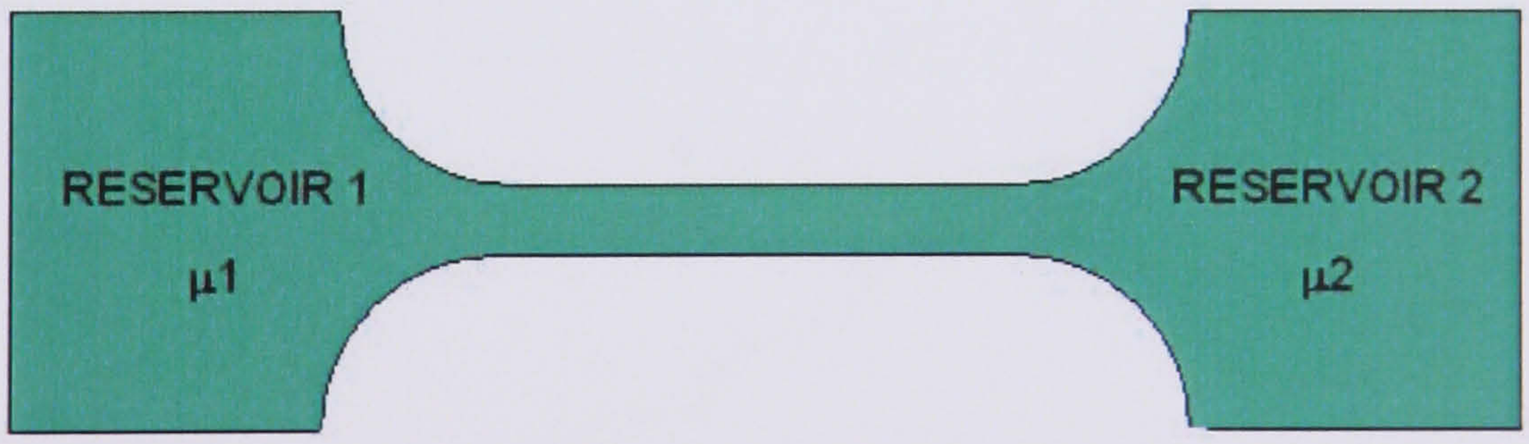



**Figure 2.6**: One dimensional wire connecting adiabatically two reservoirs with chemical potential $\mu_1$ and $\mu_2$.

A simple derivation of the formula for $G_0$ is outlined below (see also [Datta'97] Chapter 2 and [Saito'98] Chapter 8). A one-dimensional (1D) wire (see Fig. 2.6) connects adiabatically two reservoirs with chemical potential $\mu_1$ and $\mu_2$, the connections are

---

* It is worth noting that other CNT based gas sensors have been developed which exploit different features of the CNTs: their sharp tips [Modi'03] and their dielectric properties [Chopra'03].

§ It is assumed that the mode is fully transmitted. The general formula (Landauer formula) for the conductance $G$ is $G=G_0T$ per conduction mode where $T$ is the transmission probability for that mode.

assumed to be non-reflecting, it is also assumed that the wire is sufficiently narrow so that only the lowest transverse mode in the wire is below the Fermi energy ($E_F$).

In 1D the current $I$ is equal to the current density $j$, which is given by: $j = -ev(\mu_1 - \mu_2)dn/d\varepsilon$ where $v$ is the electron velocity and $dn/d\varepsilon$ is the density of states. In 1D: $dn/d\varepsilon = 2/hv$ (including the spin degeneracy). Since $(\mu_1 - \mu_2) = -eV$, where $V$ is the voltage between the two reservoirs, the resulting conductance ($G$) is:

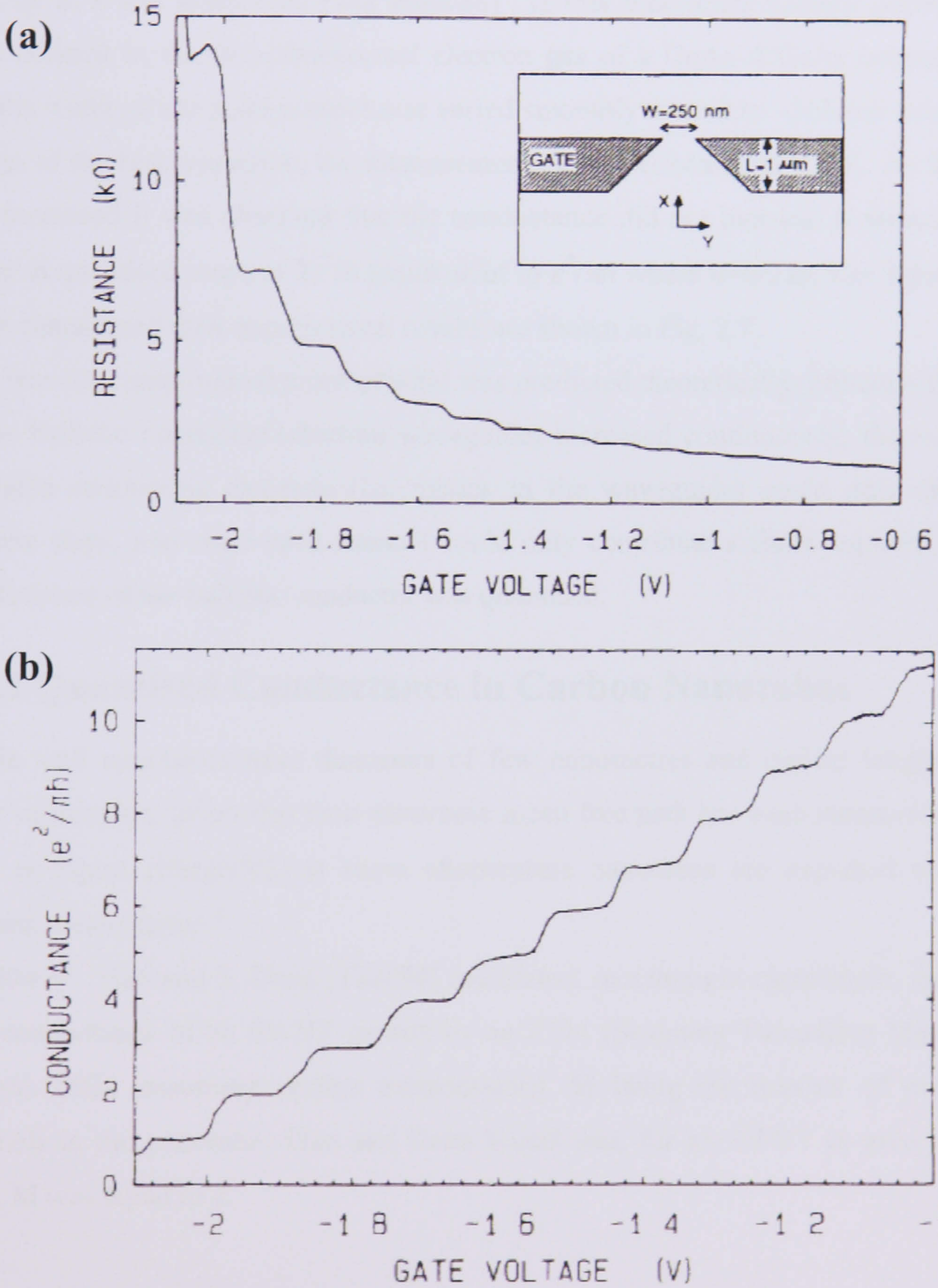



**Figure 2.7**: (**a**) the point contact resistance as a function of the gate voltage (used to vary the width of the point contact shown in the inset) at 0.6 K. (**b**) the point-contact conductance (derived from the resistance readings after subtraction of the lead resistance). The conductance shows plateaus at multiples of $2e^2/h$. (Figure taken from Ref. [van Wees'88])

$G = I/V = 2e^2/h$ which is the quantum of electrical conductance.

It is important to note how in this derivation nothing is mentioned about the material properties of the conductor or its dimensions, therefore $G_0$ is a truly fundamental unit.

Wires in which the inequality $\lambda >> L$ applies are defined ballistic conductors (rather than diffusive conductors) and their conductance can increase (decrease) only in units of $G_0$ (as conduction channels are added or removed), in other words, their conductance is quantised.

Quantised conductance in ballistic conductors was first observed experimentally in 1988 by B. J. van Wees et al. [van Wees'88]*. In this experiment ballistic points contact were defined in the two-dimensional electron gas of a GaAs-AlGaAs heterostructure and the width of the point contact was varied smoothly from 0 to ~360 nm using a gate on top of the heterojunction, the measurements were performed at 0.6 K. As the width was increased it was observed that the conductance did not increase continuously but rather in quantised steps of $2e^2/h$ (equivalent to $e^2/\pi\hbar$ where $\hbar=h/2\pi$). The layout of the point-contact and their experimental results are shown in Fig. 2.7.

This was the experimental proof of what was predicted theoretically: although the width of the ballistic conductor (electron waveguide) increased continuously, the number of available conducting channels (i.e. modes in the waveguide) could only change in discrete steps, and since each channel could only contribute a finite amount, the total conductance of the ballistic conductor was quantised.

## 2.2.2 Quantised Conductance in Carbon Nanotubes

Single wall nanotubes have diameters of few nanometres and typical lengths of the order of microns, given that their electronic mean free path has been measured to be as high as 30μm [Berger'02] at room temperature nanotubes are expected to display ballistic conductance.§

In 1994 W. Tian and S. Datta [Tian'94] calculated, in a thought experiment, that the on axis conductance of an SWNT probed by an STM (Scanning Tunnelling Microscope) tip was $MG_0$ (assuming perfect transmission), M being the number of conducting channels in the nanotube. Tian and Datta found that, for an SWNT in zero magnetic field, M was equal to 2.

---

* Similar results were reported almost simultaneously by D Wharam et al [Wharam'88], also using a 2D electron gas on a GaAs-AlGaAs heterojunction, at 0.1K.

§ This was derived from the nanotube resistance per unit length (measured to be 200Ω μm) using equation (4.6) and setting the number of conduction channels to 2. This topic will be covered in depth in Section 4.2

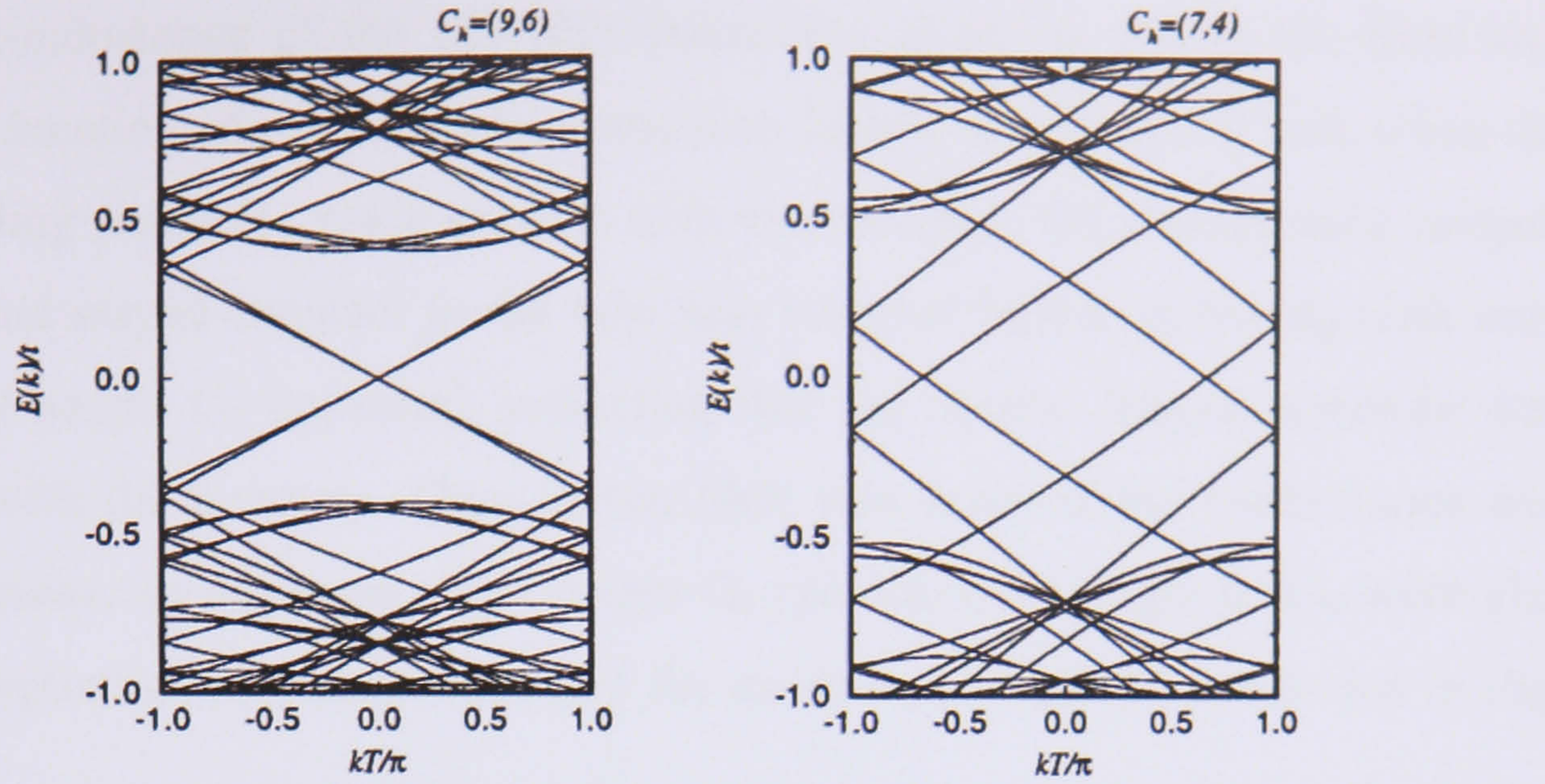



**Figure 2.8**: plots of the energy bands E(k) for the metallic nanotubes (9,6) and (7,4). The Fermi level is at E=0. In both cases two electron bands cross the Fermi level at k≥0, each corresponding to a conducting channel in the nanotube. (Figure taken from Ref. [Saito'98])

This value can be also derived from the band structure of a typical metallic single-wall nanotube by counting the number of energy bands crossing the Fermi energy ($E_F$) at k≥0 [Saito'98]. In Fig. 2.8 the energy dispersion relations of a (9, 6) and a (7, 4) SWNT are shown; two bands cross $E_F$ at k≥0 in both cases, thus these SWNTs have 2 available conducting channels and their conductance in the ballistic limits will be $2G_0$.

In 1998 Stephan Frank et al [Frank'98] reported evidence for ballistic transport in MWNTs, remarkably, ballistic transport was visible in the nanotubes at room temperature. In this work an MWNT fibre was attached to a gold wire and lowered into a mercury (Hg) bath. Applying a voltage difference between the Hg and the gold

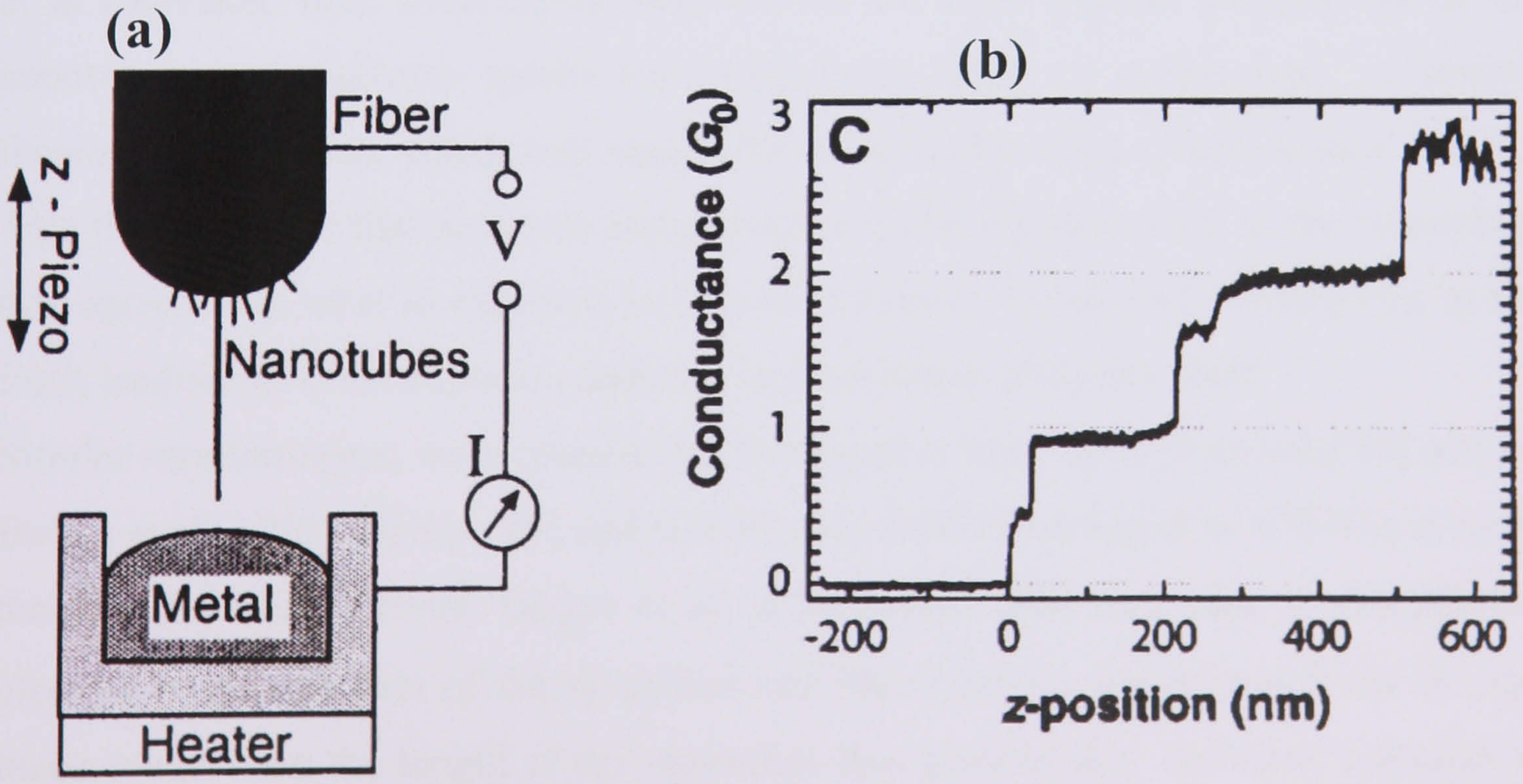



**Figure 2.9**: **(a)** the set-up of the experiment by Frank et al **(b)** one of the conductance traces obtained by Frank et al, steps of $G_0$ (and pre-steps of $0.5G_0$) are visible. The flatness of the steps for immersion lengths of the order of hundreds of nm is an indication of ballistic transport in the MWNTs. (Taken from Ref. [Frank'98])

electrode the conductance of the MWNTs protruding from the end of the fibre was measured as a function of the MWNTs immersion length. It was found that, when the longest protruding nanotube made contact with the mercury, the conductance jumped from 0 to $G_0$ and stayed constant as the tube was lowered further in the Hg bath until another step of height $G_0$ appeared, indicating that the second longest nanotube had made contact with the mercury. Thus, as the fibre was lowered the conductance was observed to increase in flat steps all of height $G_0$ (pre-steps of height $0.5G_0$ were also observed). A typical conductance trace and the experimental layout are shown in Fig. 2.9.

The fact that the conductance steps were all of the same height independent of the nanotubes' diameter and their immersion length brought Frank et al to the conclusion that the nanotubes were ballistic conductors. This because in a classical conductor the conductance G is given by $G = \gamma A/l$, where A is the cross sectional area, $l$ is the length and $\gamma$ the conductivity of the conductor, thus, had the nanotubes been classical conductors, Frank et al would have observed a smooth increase in the conductance as the tube was immersed further into the mercury (i.e. as $l$ decreased) and different contributions to the conductance for nanotubes of different diameters (i.e. different cross section).

A further proof of the ballistic nature of the electronic transport in the nanotubes was given by Frank et al when they observed that nanotubes were not damaged even for large applied voltages (up to 6 V), corresponding to current densities $>10^7$ $Acm^{-2}$. Frank et al calculated that, even taking into account the high thermal conductivity of the nanotubes, such currents would have heated the tubes to temperatures of several thousands of Kelvins, which was impossible as nanotubes start to burn around 700 °C. This thus indicated that heat was being dissipated elsewhere and not in the nanotubes; this agreed with what is expected in ballistic transport where heat is dissipated in the leads leading up to the ballistic conductor and not in the conductor itself.

Similar measurements, were repeated by Poncharal et al in 1999 [Poncharal'99] and by Berger et al in 2002 [Berger'02] and in both cases ballistic transport in MWNTs at room temperature was observed. Berger et al, in particular, used their data to estimate the electron mean free path of the nanotubes and found that its lower bound was 30 μm. much longer than the length of the nanotubes thus proving that electronic transport in the nanotubes was indeed ballistic.

In both cases, however, as in the original experiment by Frank et al, the conductance step height observed were generally only one unit of $G_0$, no steps substantially higher than $1G_0$ were ever observed.

Considering that each carbon layer was predicted to contribute $2G_0$ to the conductance it was expected that a multi-wall nanotube (with typically 10 to 30 concentric carbon layers) would have a conductance equal to $20\text{-}60G_0$. In light of their data Frank et al thus concluded that the current was only flowing in the outermost layer of the MWNT. This conclusion is supported by the work of Bachtold et al [Bachtold'99] studying Aharonov-Bohm oscillations in MWNTs. In this work it was found, that the oscillations were in good agreement with theoretical predictions for the Aharonov-Bohm effect in a hollow conductor with a diameter equal to that of the outermost shell of the multi-wall nanotubes. In both cases however, the MWNTs had only the outermost shell in contact with the electrode*. If all the shells of the MWNT are contacted by the electrodes, then current does flow in all the MWNT shells as shown in the work of Huang et al [Huang'05].

Assuming current flow only in the outermost shell, Frank et al then suggested that intershell interactions in the MWNTs were responsible for the reduction in conductance from $2G_0$ to $G_0$. A further discussion on this issue will follow later in this section.

In 2003 conductance steps of height $2G_0$ were observed experimentally by A. Urbina et al [Urbina'03]. In this experiment an STM (scanning-tunnelling microscope) tip was used to pull one or more multi-wall nanotubes out of a gel–solution of highly concentrated nanotubes deposited on a gold substrate (high concentration was needed to provide a percolative path between the nanotubes in solution and the gold substrate). When the tip was lowered into the gel-solution and contact was made the initial value of the conductance G was measured (applying a bias voltage between the STM tip and the gold substrate), and then, as the tip was withdrawn from the gel-solution, the conductance was observed to decrease in a step-wise fashion, with step height of $2G_0$ as, progressively, the shorter nanotubes attached to the tip lost contact with the gold. A typical conductance trace is shown in Fig. 2.10. No steps higher than $2G_0$ were ever observed thus suggesting that the current flow was limited to the outermost shell of the MWNT, in this case again, however, only the outermost shell of the MWNT was contacted by the electrode.

---

* Multishell conduction in MWNTs with only the outer shell connected to electrodes is however possible, as shown by the work by P G Collins and Ph Avouris [Collins'02]. In this work it was observed that the current flowing in a MWNT hardly changed even when the outermost layer of the MWNT was broken (and the electrode was strictly contacting just the outermost layer of the MWNT). It was concluded that 3 or more concentric shell in the MWNT were conducting at room temperature.

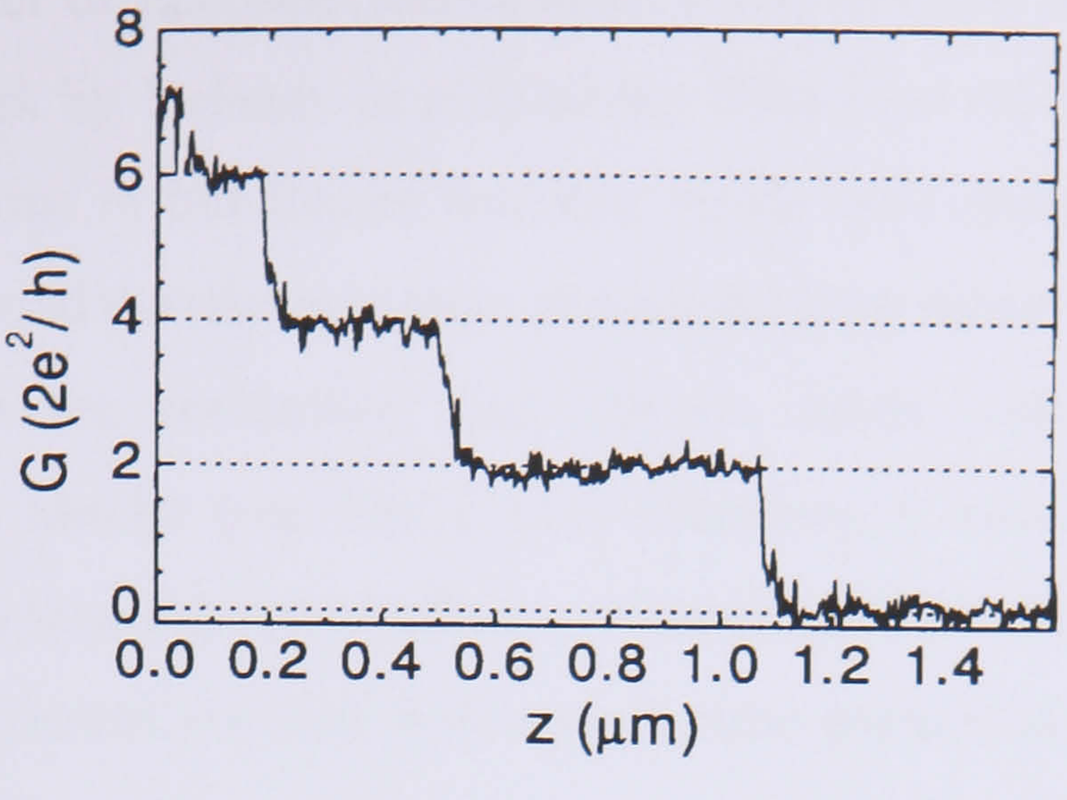



**Figure 2.10**: one of the conductance traces obtained by Urbina et al, steps of $2G_0$ are visible. (Taken from Ref. [Urbina'03])

In conclusion there have been several measurements that provide good evidence of ballistic electron transport both in MWNTs (see for instance, [Berger'02], [Frank'98], [Urbina'03]) and in SWNTs (see for instance, [Park'04], [Kajiura'05]).

The remarkable fact about these experiments is that ballistic conductance in carbon nanotubes was observable even at room temperature* while, when quantised conductance was first observed by B. J. van Wees et al, the experiment had to be performed at 0.6 K for the electron mean free path to be longer that the size of the conductor.

However, there are still some issues about the size of the conductance steps observed in nanotubes experiments: these will be discussed below.

**Conductance steps of $1G_0$ rather than $2G_0$**

The height of the conductance steps recorded by Frank et al was $1G_0$ and not $2G_0$ as expected from energy bands calculations on single wall nanotubes [Saito'98] and as measured in the experiment by Urbina et al.

Most groups suggest that this reduction in the number of conducting channels per carbon layer from two to one is due to intershell interactions within the layers of the multi wall nanotube and/or intertube interactions with other MWNTs in the bundle [Delaney'99a], [Frank'98], [Sanvito'00], [Urbina'03].

---

* It should be stressed that ballistic electron conductance at room temperature is not a universal feature of the nanotubes. In some cases, ballistic conductance in nanotubes is only visible at low temperatures (see for instance [Kong'01]) and there are many reported cases where electron transport in nanotubes is diffusive rather than ballistic (see for instance [Huang'05]). The different behaviours are usually reconciled by looking at differences in two major factors: a) the nanotube purity (affecting the length of the electron mean free path in the tube); b) the quality of the nanotube-electrode interface (which could be highly resistive thus making the observation of ballistic transport impossible).

Evidence for the effect of intertube interaction on the electron transport in nanotubes was shown in the work by Delaney et al [Delaney'99b] who investigated the influence of tube-tube interactions in bundles of metallic single wall nanotubes using *ab initio* calculations. It was found that the presence of neighbouring tubes caused the opening of energy gaps between the conduction and valence bands along some lines of the Brillouin zone of the bundle (see Fig. 2.11). Therefore, it was concluded that, even though all the SWNTs forming the bundle are, if taken individually, metallic, the bundle itself has semimetallic behaviour with hole and electron pockets at the Fermi surface.

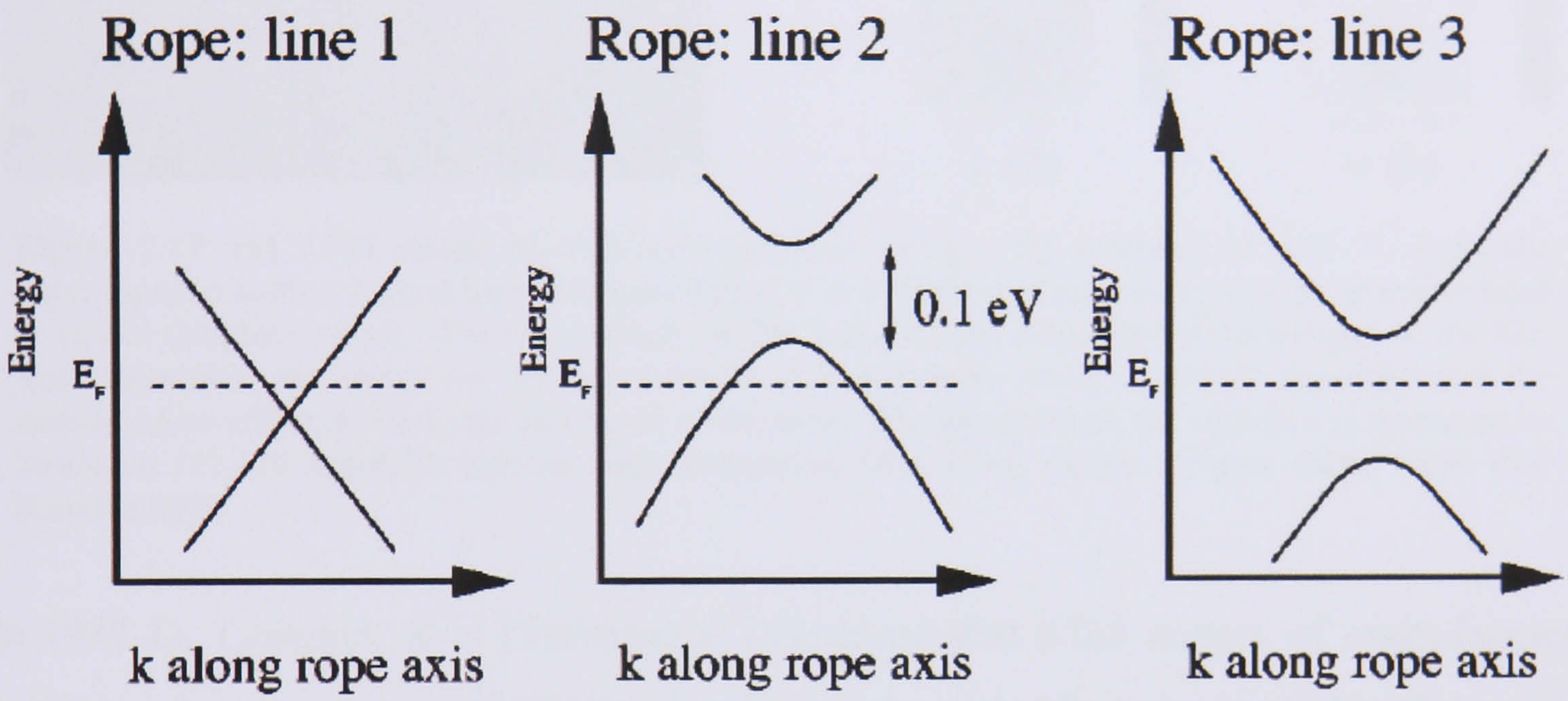



**Figure 2.11**: a schematic display of the band structure of the nanotube rope along various lines in reciprocal space parallel to the tube's axis. Along some lines there is a band gap of about 0.1 eV between the valence and conduction band. The Fermi energy is shown by the dashed line. Pockets of electrons are found along line 1 and pockets of holes are found along line 2. (Taken from Ref. [Delaney'99b])

Tube-tube interactions within a bundle could alter the dispersion relation of the individual nanotube and thus reduce the conductance contribution of the tubes.

A more likely explanation for the halving of the ballistic conductance steps seen in some of the nanotube experiments comes from the study of the effect of carbon layer interactions on electron transport.

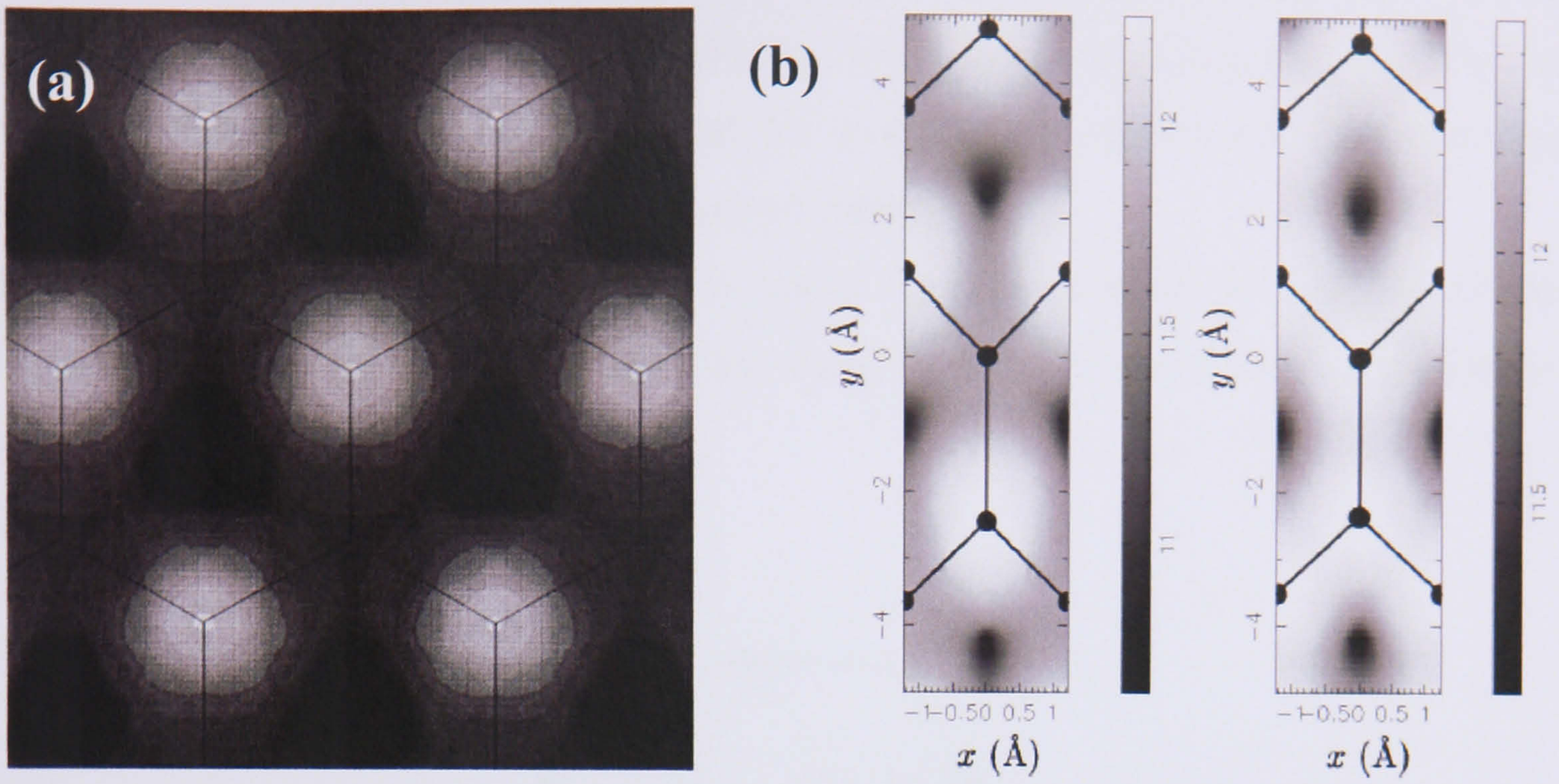



**Figure 2.12**: **(a)** STM image of multilayer graphite, using a tip potential of 0.25 V, from the superimposed carbon honeycomb structure (lines) it is evident that only every second graphite atom is visible (brighter areas). (Picture courtesy of Ph. Lambin) **(b)** calculated STM images of double-wall nanotubes, the image on the left shows a (5,5) nanotube inside a (10,10) nanotube and the missing atom effect is due to the interlayer interactions. The nanotube on the right is a (6,6) nanotube inside an (11,11) nanotube and no such interaction effects are visible. (Figure taken from Ref. [Lambin'00])

In 1987 D. Tománek et al [Tománek'87] observed that STM images of multi-layered graphite taken at constant height and low biases showed only every second surface atom (see Fig. 2.12a). Hexagonal graphite has ABAB stacking and the crystal is composed of an α sublattice (atoms with neighbours directly above) and a β one (no such neighbours) as shown in Fig. 2.13. Tománek et al found that only the β sublattice was visible and this because the α energy bands are pushed away from the Fermi level due to interlayer interactions (see Fig. 2.13). This modification in the band structure therefore leads to a reduction in the local density of states (LDOS) at the Fermi level by a factor of 2 exactly.

This factor of 2 reduction could explain the observation of $1G_0$ rather than $2G_0$ steps in conductance measurements performed on MWNTs, which have several concentric carbon layers. However MWNTs were used in the experiments by Frank et al and Urbina et al, but only in one of those the reduction in conductance contribution per carbon layer was observed.

A possible explanation for this discrepancy can be found in the work of Ph. Lambin et al [Lambin'00]. In this work it was shown that, apart from some special cases, in an MWNT it is impossible to realize the same stacking as in natural graphite. The constant-current STM images of double-wall nanotube systems (MWNTs with only 2 concentric carbon layers) were calculated by Ph. Lambin et al and it was found that only in the case

of monochiral structures (such as a (5,5) tube inside a (10,10) one) the interlayer effects could be seen in the STM topography (see Fig. 2.12b) as in those cases only one atom in two was visible. In other cases however, the image of the double-wall nanotube was indistinguishable from that of just the isolated external layer.

Therefore intershell effects in MWNTs could be the cause of the halving of the conductance contribution per carbon shell observed but this is still only a qualitative explanation for this phenomenon.

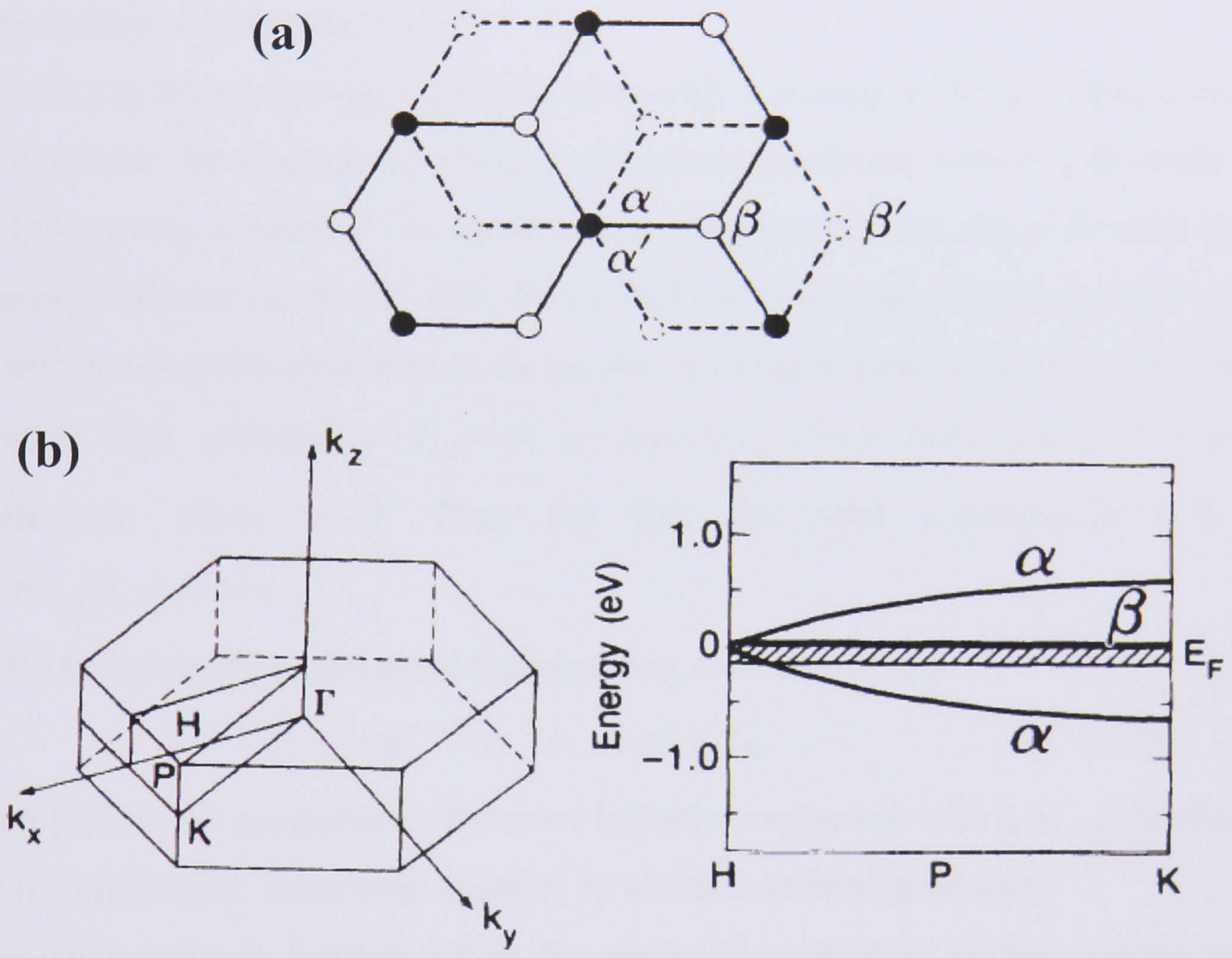



**Figure 2.13**: **(a)** schematic drawing of two successive layers of graphite. **(b)** The Brillouin zone (left) and the band structure of the graphite (right), notice how the α bands are pushed away from the Fermi level. (Figures taken from Ref. [Tománek'87])

**Conductance steps of value < $1G_0$**

Quantised conductance steps of fractional values of $G_0$ have also been observed (e.g. in an experiment by W. A. de Heer on MWNT break junctions [de Heer'97]) and in particular, in the experiment by Frank et al, pre-steps of 0.5 $G_0$ - and no other fraction of $G_0$ - were recorded.

A possible explanation for these fractional values is elastic scattering of the electrons between nanotubes, at defects within the nanotube or at the nanotube-electrode contacts.

In the presence of elastic scattering the conductance is no longer exactly quantised and is given by the Landauer formula:

$$G = G_0 NT \qquad (2.4)$$

where N is the total number of conducting channels in the ballistic conductor and T is the sum of the transmission probabilities from one channel to the other: $T = \sum_{\alpha,\beta}^{N} \left| t_{\alpha\beta} \right|^2$ where $t_{\alpha\beta}$ is the transmission probability from the $\alpha$ to the $\beta$ channel [Delaney'99a], [Urbina'03].

The transmission probability could also be calculated in a semiclassical way. This was done by de Heer et al [de Heer'97].

Semiclassically the scattering process involves only a change in the travelling direction of the electrons. An electron travelling in a ballistic conductor with $n$=2 channels (see Fig. 2.14) arriving at point P (an electron scattering centre), can either forward scatter into the next ballistic conductor with, for example, $m$=4 exiting channels or back-scatter in the $n$=2 entering channels. Hence an electron arriving at point P from the left will be transmitted with probability $T_{nm} = m/(n+m) = 2/3$. Since there are $n$=2 entering channels that arrive at P from the left, the total conductance will be: $G_{nm} = nT_{nm}G_o = 4/3\,G_o$ *.

De Heer et al generalised this for more scattering centres in series:

$$G_{lm\ldots n} = (l^{-1} + m^{-1} + \ldots + n^{-1})^{-1} G_o \qquad (2.5)$$

equation (2.5) is the conductance for more ballistic conductors with $l$, $m$ ...$n$ conducting channels respectively, connected in series by electron scattering centres.

This model is used in Section 4.5 in the statistical evaluation of the changes to the nanotube's electrical conductance due to oxygen doping.

---

*The transmission probability for an electron travelling in the opposite direction (i.e. from right to left) will be: $T_{mn} = n/(m+n)$, however the conductance will be: $G_{mn} = mT_{mn}G_0 = G_{nm}$. Hence although the transmission probability depends on the direction of travel of the electron, the conductance is independent of its direction.

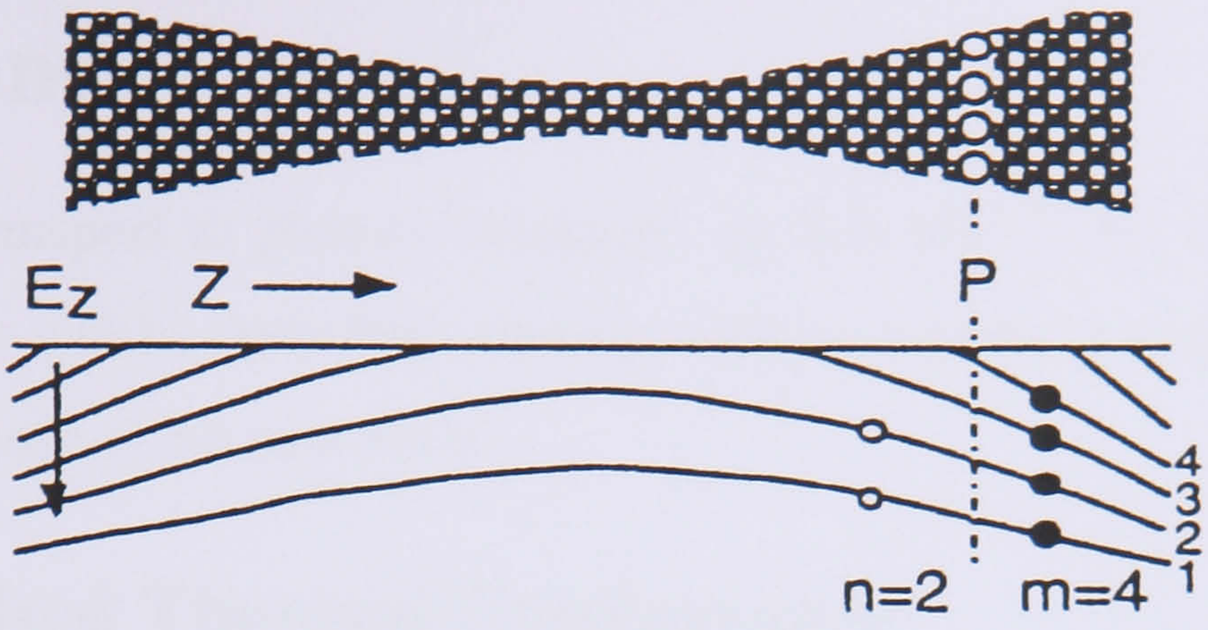



**Figure 2.14**: schematic diagram of an electron encountering an electron scattering centre. (Figures taken from Ref. [de Heer'97])

Both these arguments could account for the origin of fractional conductance values but do not explain fully why Frank et al observed only steps of $0.5G_0$ and no other fraction. Another explanation for the $0.5G_0$ values has been put forward by S. Sanvito et al [Sanvito'00]. They calculated that the inter-wall interactions in an MWNT not only modify the electronic density of states of the tube (as compared to that of an SWNT) but also redistribute the total conduction current non-uniformly across the individual tube walls. They then stated that this change in the conduction current distribution that happens at the interface of two regions with different numbers of walls would cause a backscattering of the current carriers and thus be at the origin of the anomalous conductance reduction observed by Frank et al (such regions could happen at the tip of the MWNT, and then would disappear as the tip is submerged in the mercury). And indeed they found that if the carriers were scattered through three regions with different numbers of concentric walls (i.e. two interfaces) the conductance of the MWNT was reduced to values of $\sim 0.5G_0$, in good agreement with what observed by Frank et al.
Sanvito et al did not state what would happen to the conductance if there were more than three consecutive regions and, given that the structural details of the MWNTs used by Frank et al are not available their predictions cannot be tested.

In conclusion: while the origin of fractional quantised conductance steps in ballistic conductors is well accounted for, a satisfactory explanation for the $0.5G_0$ pre-steps observed by Frank et al is still missing. However, since the steps all appeared when the tips of the MWNTs touched the Hg surface linking these values to the particular structure of the MWNT tips seems to be the right approach.

## 2.3 Phonon Transport and Quantised Thermal Conductance

From electron transport to phonon transport: in this section the thermal properties of carbon nanotubes will be described, starting with an introduction on the quantisation of thermal conductance at the nanoscale.

### 2.3.1 Quantised Thermal Conductance

In 1983 J Pendry published a paper on the quantum limits to the flow of information and entropy [Pendry'83]. In it he showed that there is an inequality that limits the flow of information as a function of the energy flow. He applied this relationship to calculate the limit on the rate of heat flow in a channel and found that this had to be $\leq \frac{1}{3}\pi k_B^2 T^2 \hbar^{-1}$ where $k_B$ is Boltzmann constant and $\hbar$ is Plank's constant over $2\pi$ and $T$ is the temperature of the channel.

In 1998 this topic was re-visited by Luis Rego and George Kirczenow [Rego'98] who demonstrated theoretically that in a low temperature regime dominated by ballistic massless phonon modes the phonon thermal conductance of a 1D quantum wire is quantised, and that the fundamental of quantum thermal conductance ($G_{th}$) is:

$$G_{th} = \frac{\pi^2 k_B^2 T}{3h} \qquad (2.6)$$

where $k_B$ is Boltzmann constant, $h$ is Plank's constant and $T$ is the temperature.

$G_{th}$ is defined as the quantum of thermal conductance and corresponds to the maximum value of energy that can be transported by a single phonon mode; it is equal to: $G_{th} = 9.456 \times 10^{-13}\ W/K^2 \times T$.

The Landauer formulation of transport theory was used by Rego and Kirczenow for their calculations, the argument used was that, just as electron transport in 1D ballistic conductors is possible and shows quantisation in units of the quantum of conductance ($G_0=2e^2/h$ per mode), so should phonon transport in one dimension be possible and similarly quantised.

Experimental evidence for these calculations was provided in 2000 by K. Schwab et al [Schwab'00] who measured the quantum of thermal conductance. In this experiment a suspended silicon-nitride nanostructure with four phonon waveguides was used, its narrowest width was 200 nm and it was shaped so to obtain optimal coupling between the phonons modes of the waveguide and the thermal reservoir (see Fig. 2.15). The cross over temperature ($T_{CO}$) for the depopulation of all the optical phonon modes which marks the onset of the 1D quantization regime was calculated using the following equation: $T_{CO} \approx \pi\hbar v / k_B w$, where $\hbar$ is Plank's constant over $2\pi$, $v$ is the phonon group velocity (i.e. the speed of sound in the material), $w$ is the width of the waveguide and $k_B$ is Boltzmann's constant. In this experiment $T_{CO}$ was 0.8 K ($v$ = 6 km/s, $w$ = 200 nm). Once below $T_{CO}$ DC SQUID-based noise thermometry was used to measure the

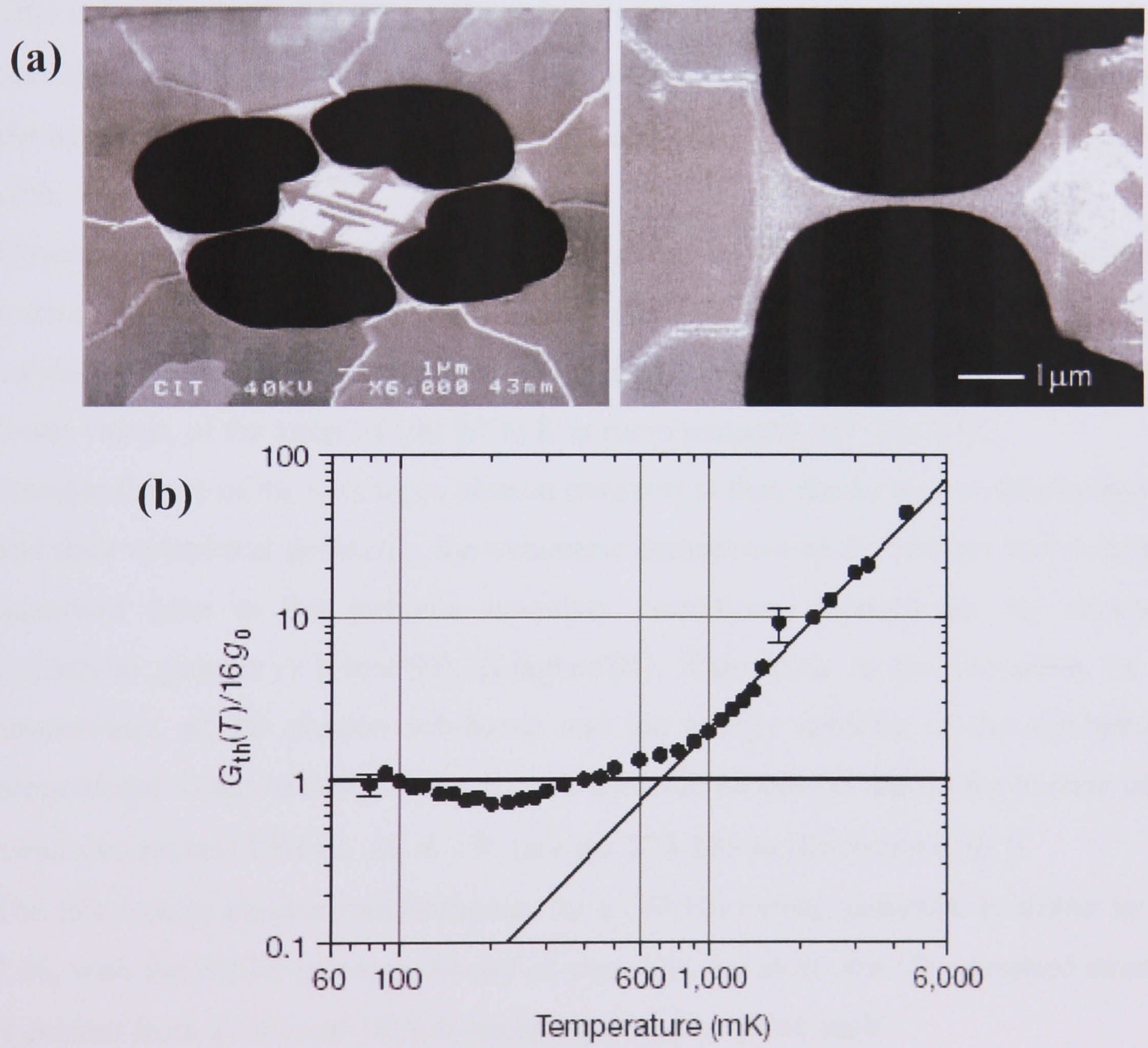



**Figure 2.15**: The thermal conductance data of Schwab et al: **(a)** a view of the suspended device used in the experiment; the device consisted of 4 phonon wave-guides, the narrowest region of the waveguide was 200 nm; **(b)** the conductance of the wave-guides saturates at a value of $16G_{th}$ because at temperatures below $T_{CO}$ all the other phonon modes are depopulated. (Figures taken from Ref. [Schwab'00])

temperature of the system with minimal power dissipation. It was observed that the

thermal conductance of the device saturated at a value of $16G_{th}$ at temperatures below 0.8 K. This was as expected from the theory given that the device had 4 wave-guides each with 4 acoustic modes (see Fig. 2.15), thus 16 modes in total.

To date this is the only experimental measurement of the quantum of thermal conductance.

## 2.3.2 Thermal Properties of Carbon Nanotubes

Calculations have predicted that a (10,10) single-walled carbon nanotubes could have thermal conductivity of about 6600 W/ m K at room temperature* [Berber'00]. This large thermal conductivity value is due to two factors: the high phonon speed in carbon nanotubes (due to very strong $sp^2$ bond in the nanotube's carbon structure) and the large phonon mean free path in the tubes (calculated to be 0.5-1.5 μm at 30 K [Hone'99]). This is because, in solids where the phonon contribution to the conductance dominates (as in nanotubes), the thermal conductivity (κ) is proportional to: $\kappa \propto Cvl$ where C is the heat capacity per unit volume, $v$ is the speed of sound and $l$ is the phonon mean free path.

However the interactions between nanotubes in a bundle or a mat could dramatically reduce these theoretical values and indeed experimental measurements of the thermal conductivity (carried on mats of entangled single-walled nanotubes) have shown much lower values, of the order of 200 W/ m K at room temperature. [Hone'02]

Another feature of the nanotubes phonon transport is that, due to their small dimensions, and their cylindrical geometry, the transverse component of the phonon wave vector is quantised (due to the periodic boundary conditions imposed by the nanotubes cylindrical geometry) [Hone'99], [Llaguno'01]. This leads to the formation, at low temperature, of 1D phonon sub-bands and the energy splitting of the sub-bands is proportional to the velocity of the phonon acoustic modes ($v$) and to the inverse of the nanotubes radius (1/R) i.e. $\Delta E \propto v/R$. (see pp. 273-285 in [Dresselhaus'01])

The low energy phonon band-structure for a (10,10) carbon nanotube is shown in Fig. 2.16, with the PDOS (phonon density of states) in the inset, the 1D quantised structure is evident from a series of 1D sub-bands separated by a few meV.

Fig. 2.16 also shows that nanotubes have four acoustic modes, one longitudinal ($v_{LA}$=24 km/s), two degenerate transverse ($v_{TA}$=9 km/s) and a twist mode ($v_{twist}$=15 km/s) all of which have linear dispersion at low energy ($E \propto k^{\alpha}$, with $\alpha$=1).

---

* This value is extremely high. For comparison: the thermal conductivity of pyrolitic graphite (in plane) is 2130 W/m K at 0°C and the thermal conductivity of diamond is up to 2600 W/m K at 0°C. The thermal conductivity of copper is 403 W/m K at 0°C [data from Kaye&Laby On-line].

At temperatures lower than the Debye temperature ($T < T_D$) the phonon density of states is dominated by acoustic phonons; if the acoustic modes obey a dispersion relation of the type $E \propto k^{\alpha}$ then, for acoustic modes in *d* dimensions the phonon contribution to the specific heat ($C_{ph}$) will obey the following relation: $C_{ph} \propto T^{d/\alpha}$. (see pp. 273-285 in [Dresselhaus'01]) Therefore, in nanotubes, which are 1D structures ($d$=1) and have linear acoustic modes ($\alpha$=1), $C_{ph}$ should be linearly proportional to T. Hence studying the dependence of $C_{ph}$ on T at low temperatures could provide evidence of 1D phonon quantisation in carbon nanotubes.

The specific heat of a conductor has both an electronic contribution ($C_e$) and a phonon contribution ($C_{ph}$), however, in a nanotube, the phonon contribution to the specific heat is always much larger than the electronic contribution ($C_{ph}/C_e \sim 100$) (see pp. 273-285

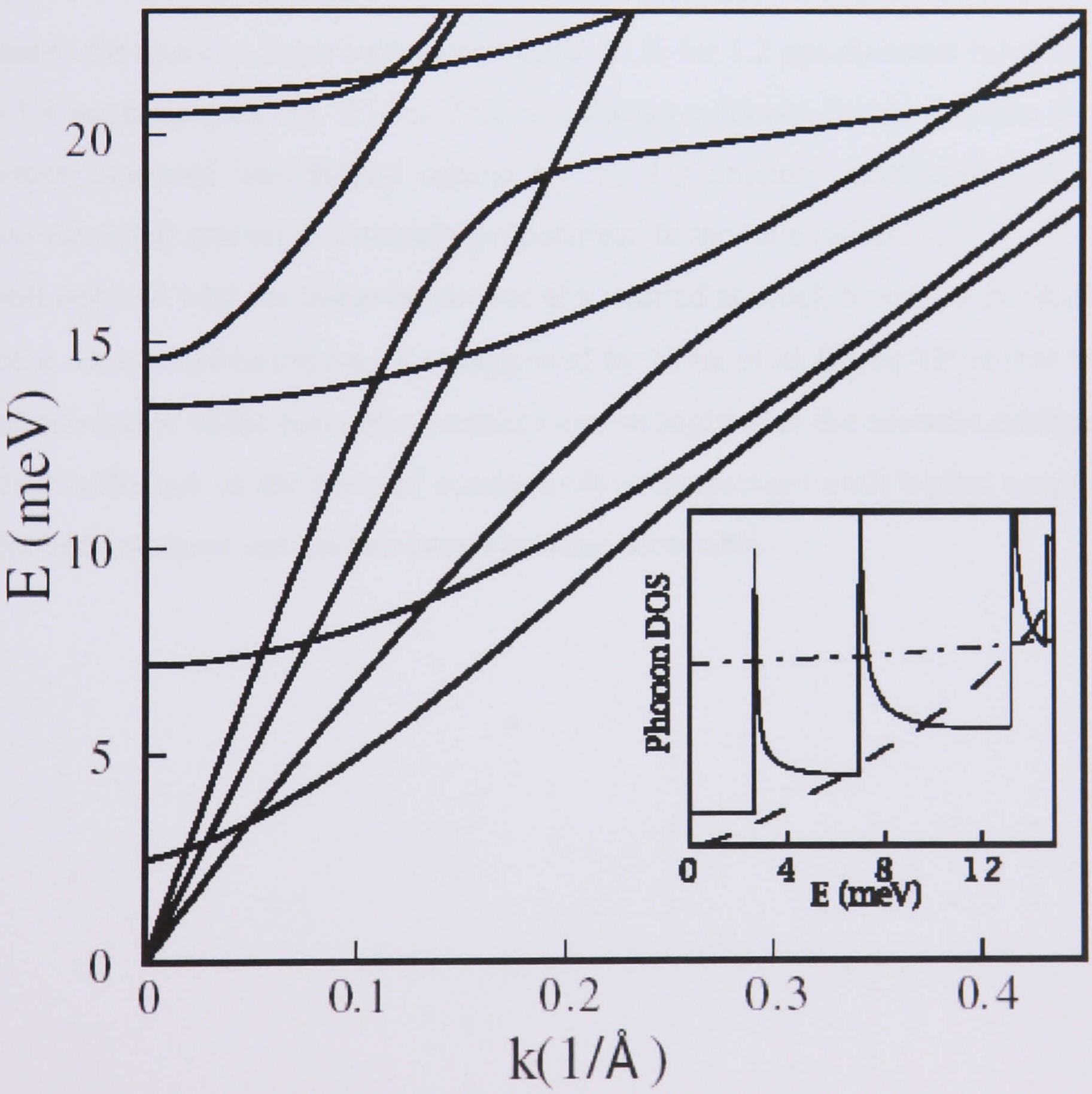



**Figure 2.16**: low energy phonon band structure of a (10,10) nanotube. The inset shows the phonon density of states (PDOS) for an isolated nanotube (solid line) compared to the PDOS of graphene (dot-dashed line) and graphite (dashed line). (Figures taken from Ref. [Hone'02])

in [Dresselhaus'01]) therefore, in nanotubes $C_{tot}$ is approximately equal to $C_{ph}$.

Studies on the temperature dependence of the specific heat of nanotubes have been carried out by J. Hone and co-workers at University of Pennsylvania (Philadelphia)

[Hone'02], [Hone'99], [Llaguno'01], [Hone'00] in mats of entangled single-walled nanotubes and linear T behaviour of $C_{ph}$ was observed experimentally on several occasions (see Fig. 2.17a) thus providing evidence of 1D phonon quantisation in carbon nanotubes. Hone et al also carried out measurements on the temperature dependence of the thermal conductivity (which is expected to show the same linear T dependence for a 1D system) of the mats and found that, at low enough temperatures, it too decreased linearly with T (see Fig. 2.17b).

Hone et al observed that the specific heat of the nanotubes decreased linearly with T at temperatures between 2 and 8 K (see Fig. 2.17a) while the thermal conductivity ($\kappa$) started to show a linear behaviour in T already at temperatures <30-40 K (see Fig. 2.17b). It was also noticed [Hone'02], [Llaguno'01] that the onset of the linear behaviour in $\kappa$ was moved to lower temperatures as the mean diameter of the tubes in the mat was increased: the onset of linear behaviour was at 40 K for 1.2 nm diameter tubes and at 35 K for 1.4 nm tubes (see Fig. 2.17c). This was further evidence for the fact that the linear behaviour observed was indeed caused by the 1D phonon quantisation, as the 1D phonon sub-band spacing is inversely proportional to the tube radius.

It is still debated why the linear behaviour of C started at much lower temperatures than that of $\kappa$. One possible explanation suggested by Hone et al [Hone'02] is that the first optical sub-bands of the nanotubes scatter more strongly than the acoustic sub-bands, so that their influence on the thermal conductivity is suppressed until higher temperatures are reached and more optical sub-bands become accessible.

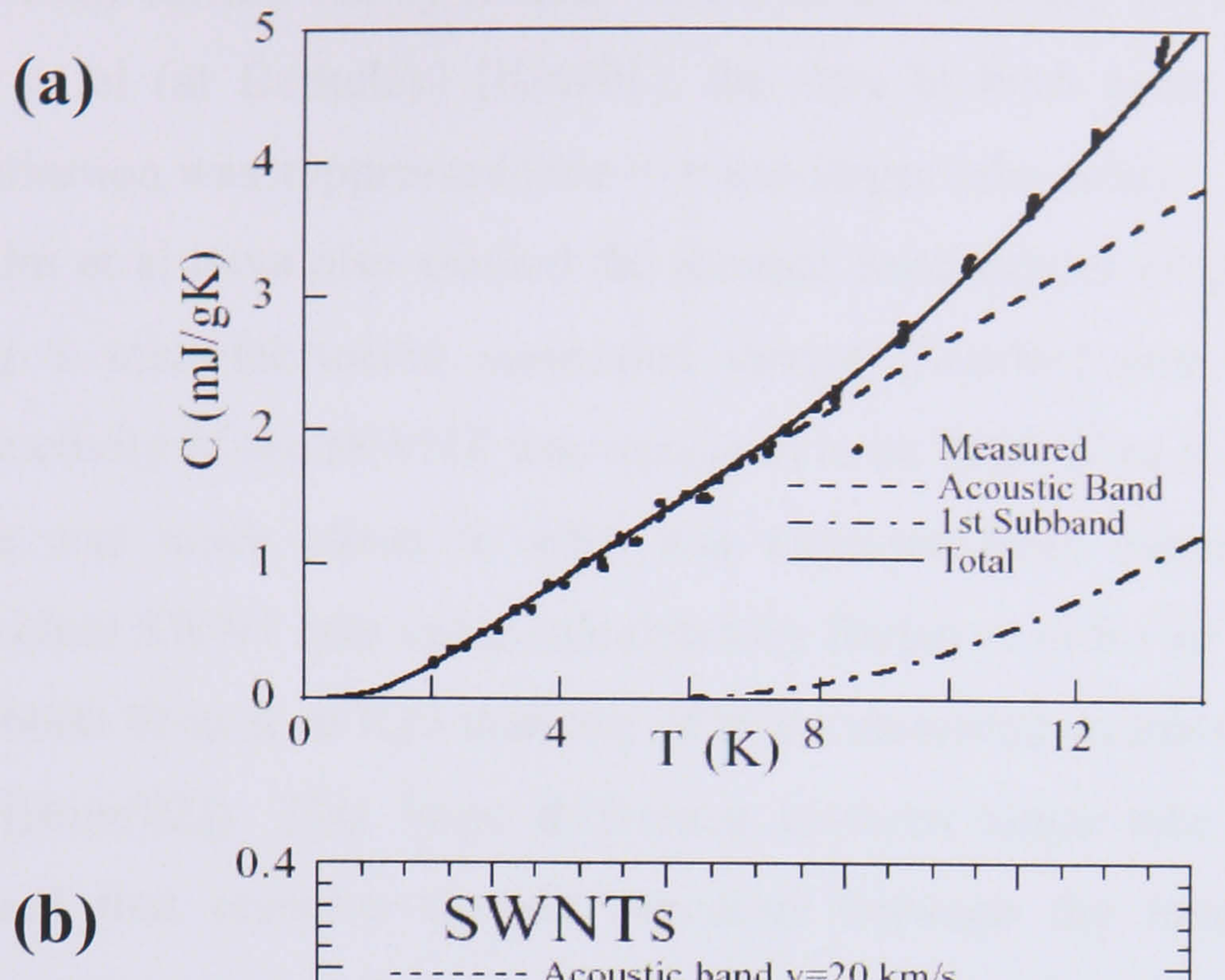



**Figure 2.17**: **(a)** the specific heat of SWNTs decreases linearly with temperature below 8 K. **(b)** the thermal conductivity of SWNTs decreases linearly with temperature below 40 K (Figures taken from pp. 273-285 in [Dresselhaus'01]). **(c)** the onset of linear behaviour in κ is at lower temperatures for SWNTs with larger radii. (Figure taken from Ref. [Hone'02])

Measurements on the temperature dependence of the thermal conductivity in MWNTs have been carried out by J. Hone et al (see pp. 273-285 in [Dresselhaus'01]) and by P. Kim et al (at Berkeley) [Kim'01], the data in both cases showed that 1D phonon quantisation was suppressed (due to much larger tube radii).

P. Kim et al have also studied the thermal conductivity of individual multi-wall tubes using a microfabricated suspended device [Kim'01] (see Fig. 2.18). The thermal conductivity of the MWNT was measured to be 3000 W/m K at room temperature. This value was much closer to what was expected from theoretical calculations for an individual SWNT (the value calculated by Berber et al for an individual (10,10) SWNT was 6600 W/m K at RT) than any of those measured on mats of SWNTs (200 W/m K, see [Hone'02]). This large difference between single-tube and bulk measurements showed that resistive thermal junctions between the tubes dominate the thermal transport in mat samples.

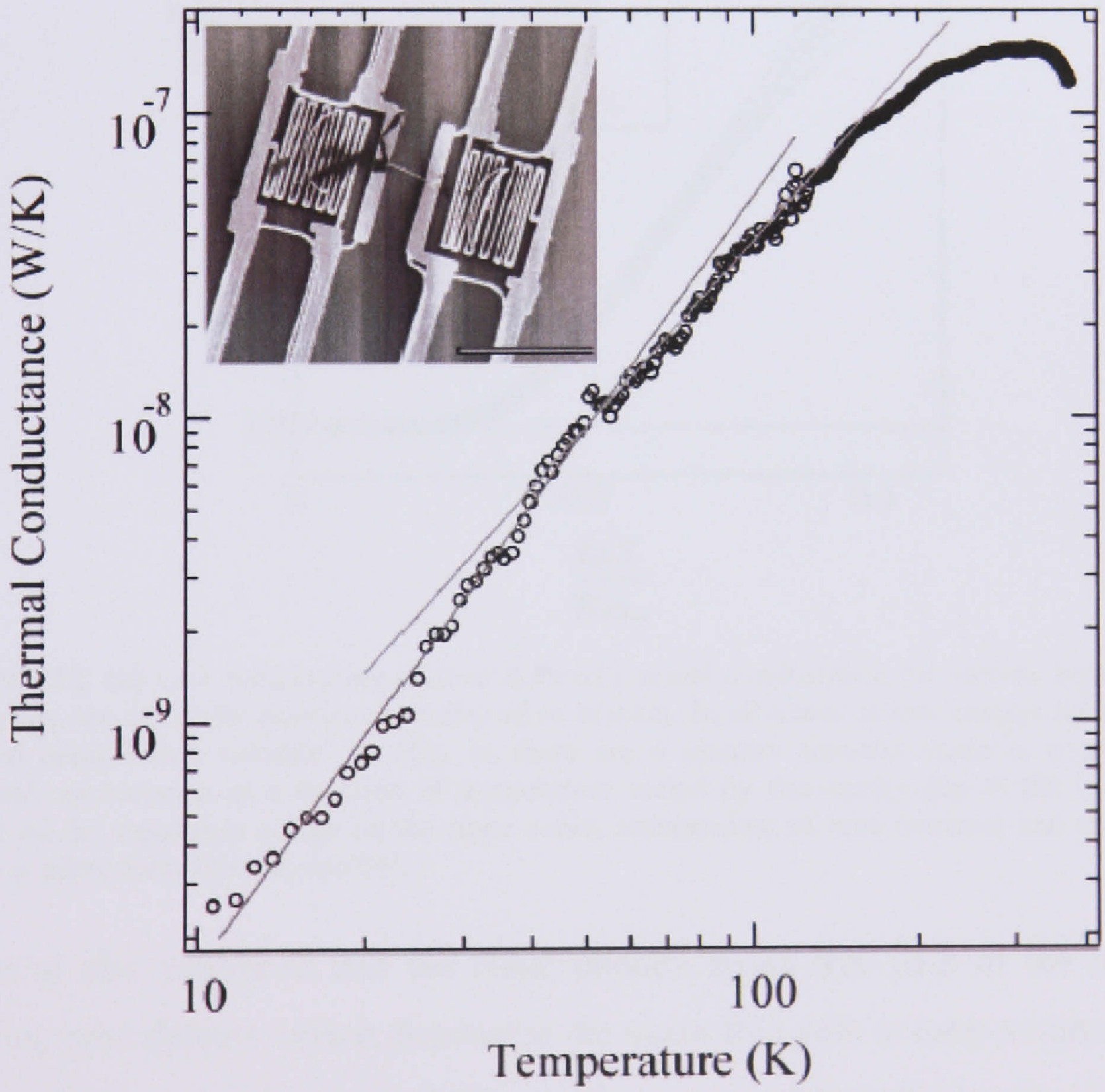



**Figure 2.18**: the thermal conductance of an individual MWNT with diameter of 14 nm. The inset shows the SEM image of the suspended islands with the individual MWNT, the scale bar is 10 μm. (Figure taken from Ref. [Kim'01])

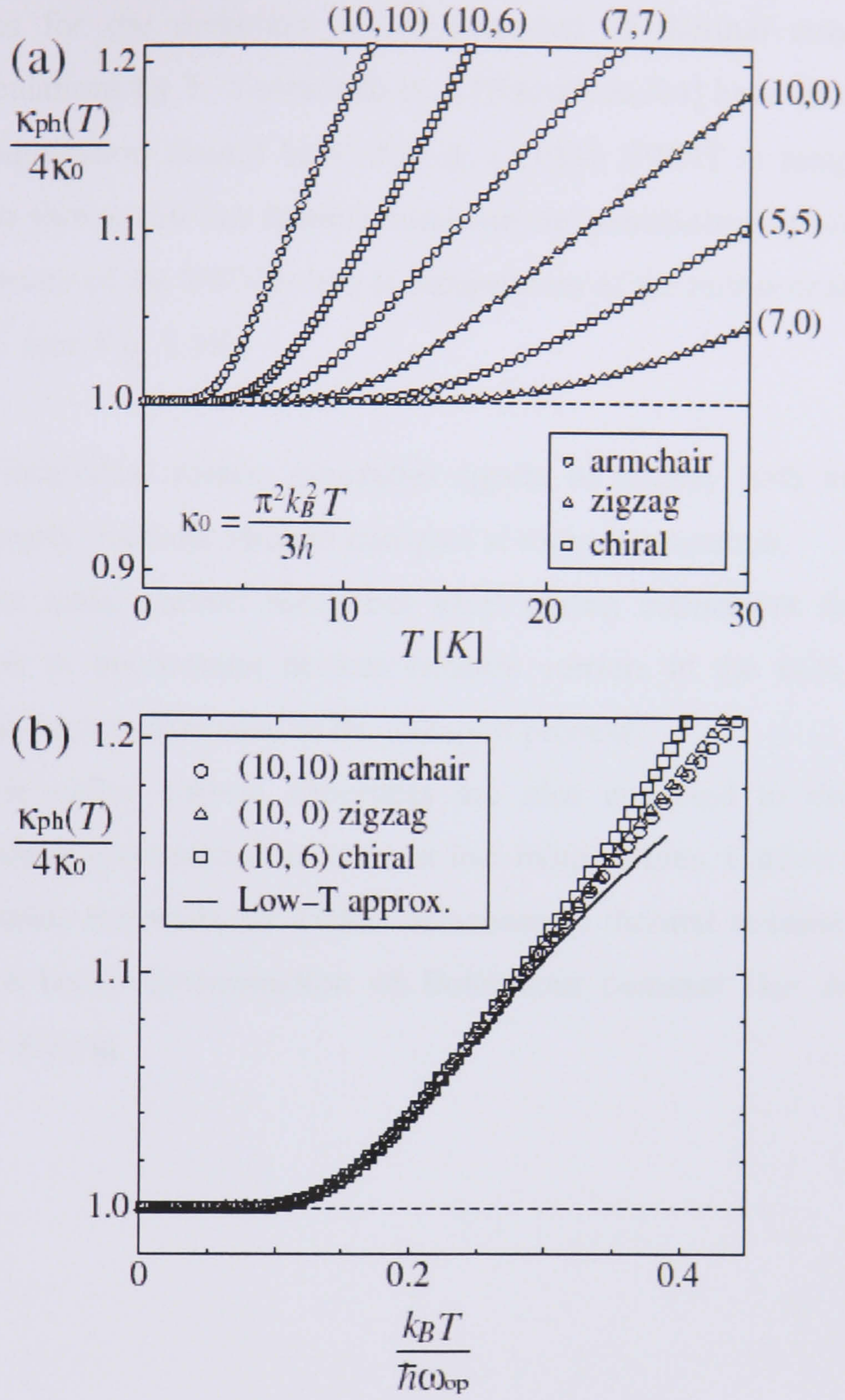



**Figure 2.19**: **(a)** Low-temperature phonon-derived thermal conductance for various types of carbon nanotubes, the nanotube indices are indicated in bracket. In all cases, at low enough temperature the thermal conductance saturates at $4G_{th}$, as there are 4 phonon acoustic mode in a nanotube. **(b)** Thermal conductance as a function of temperature scaled by the energy gap of the lowest optical mode; all the nanotubes merge on the same curve, independent of tube diameter and chirality. This figure is taken from [Yamamoto'04].

Kim et al also estimated that the static phonon mean free path of the tube (due to scattering tube defects, which dominated the mean free path at temperatures below 320 K) was ~500 nm at room temperature, a value comparable to the length of the MWNT used (2.5 μm). It was thus concluded that phonons had only a few scattering events between the thermal reservoirs (for T ≤ room temperature) and that the phonon transport was nearly ballistic.

To date no thermal studies of individual SWNTs have been reported yet. These would be of great interest especially at low temperatures. Nanotubes, because of their high

phonon velocities, long phonon mean free paths and small dimensions could be the ideal candidates for the detection of the quantum of thermal conductance ($G_{th}$). Theoretical calculations by T. Yamamoto et al [Yamamoto'04] have shown that thermal conductance quantisation should be visible in a (10,0) SWNT at temperatures below 10K. It was also shown that the thermal conductance quantisation at low temperatures, is a universal feature of the SWNTs and is independent of the radius or atomic geometry of the nanotube* (see Fig. 2.19).

In conclusion, individual carbon nanotubes appear to display both ballistic electron transport and 'nearly' ballistic phonon transport at room temperature.

These properties make carbon nanotubes ideal wiring connectors for electron and phonon transport in micro-nano devices because carriers in the wire experience no resistance and no heat is dissipated in the transport process.

Individual single-walled carbon nanotubes are also expected to display universal thermal conductance quantisation features at low temperatures. Carbon nanotubes may be the most suitable materials for studies of nanoscale thermal quantum effects which could lead to a better determination of Boltzmann constant ($k_B$) and the unit of temperature, the Kelvin.

---

* This is not unique to carbon nanotubes. A theoretical study on phonon transport in single-walled boron nitride nanotubes [Xiao'04] has come to similar conclusions. Thermal conductance quantisation was found to be a universal feature of the nanotubes at low temperatures (below 10K) independent of the chirality and diameter of the tubes.

# Chapter 3 Experimental Techniques

## 3.1 The Atomic Force Microscope (AFM)

### 3.1.1 Introduction to the AFM

The development of the first Atomic Force Microscope (AFM) was the fruit of a joint collaboration between Stanford University and IBM and was reported in 1986 by G Binnig et al in [Binnig'86]. The AFM was developed to study atomic scale forces (of the order of pico-Newtons, $10^{-18}$ N) and was derived from the Scanning Tunnelling Microscope (STM – whose invention had been reported in 1981 by G Binnig and H Rohrer [Binnig'93]) and the Stylus Profilometer (an instruments used to study the profile of samples by using a sharp stylus to scan their surface).

This first AFM consisted of a sharp diamond tip mounted on a thin Au foil; as the tip was scanned on a sample it followed the surface contour and thus, monitoring the deflection of the Au foil (much softer than the substrate scanned), it was possible to measure the profile of the surface. Binnig et al in [Binnig'86] reported a lateral resolution of 3nm and a vertical resolution of 0.1nm using this technique.

In this first AFM paper Binnig et al wrote: *'The atomic force microscope (AFM) is a new tool [...] We envision a general-purpose device that will measure any type of force; not only the interatomic forces, but electromagnetic forces as well'*. And this proved to be right indeed: nowadays the AFM is a widely available instrument both in industry and academia, able to scan in air, vacuum and liquid and used to study various sample properties using the tip-sample interactions due to interatomic, magnetic and electrostatic forces.

**Working Principle of the AFM and Scanning Modes.**

The AFM probes the surface of a sample with a sharp tip (typical radius of curvature is <50nm) located at the free end of a cantilever (spring constant range is typically 5-0.1N/m), which protrudes from a chip (usually etched from a silicon, silicon nitride or silicon oxide wafer); the whole is often referred to as an 'AFM probe'.

Interatomic forces between the tip apex and the sample surface cause the cantilever motion to change. A detector measures the cantilever motion as the tip is scanned over

the sample. The measured cantilever motion allows a map of surface topography to be generated.

The tip-sample atomic interactions are best exemplified by the van der Waals forces. The dependence of the van der Waals forces on interatomic distance ($r$) can be modelled by the Lennard-Jones 12-6 potential ($V$):

$$F(r) = -\frac{dV}{dr} \qquad (3.1)$$

And V is defined as:

$$V(r) = \frac{A}{r^{12}} - \frac{B}{r^{6}} \qquad (3.2)$$

where $A$ and $B$ are constants. The value and the sign of the slope of the potential give, respectively, the magnitude and direction of the van der Waals forces: positive slopes correspond to attractive forces and negative slopes to repulsive forces. The term in $r^{-6}$ dominates at larger $r$ values and gives rise to the attractive forces, the term in $r^{-12}$ dominates at short $r$ values and gives rise to repulsive forces. A schematic diagram of the dependence of the potential on the interatomic distance is shown in Fig. 3.1.

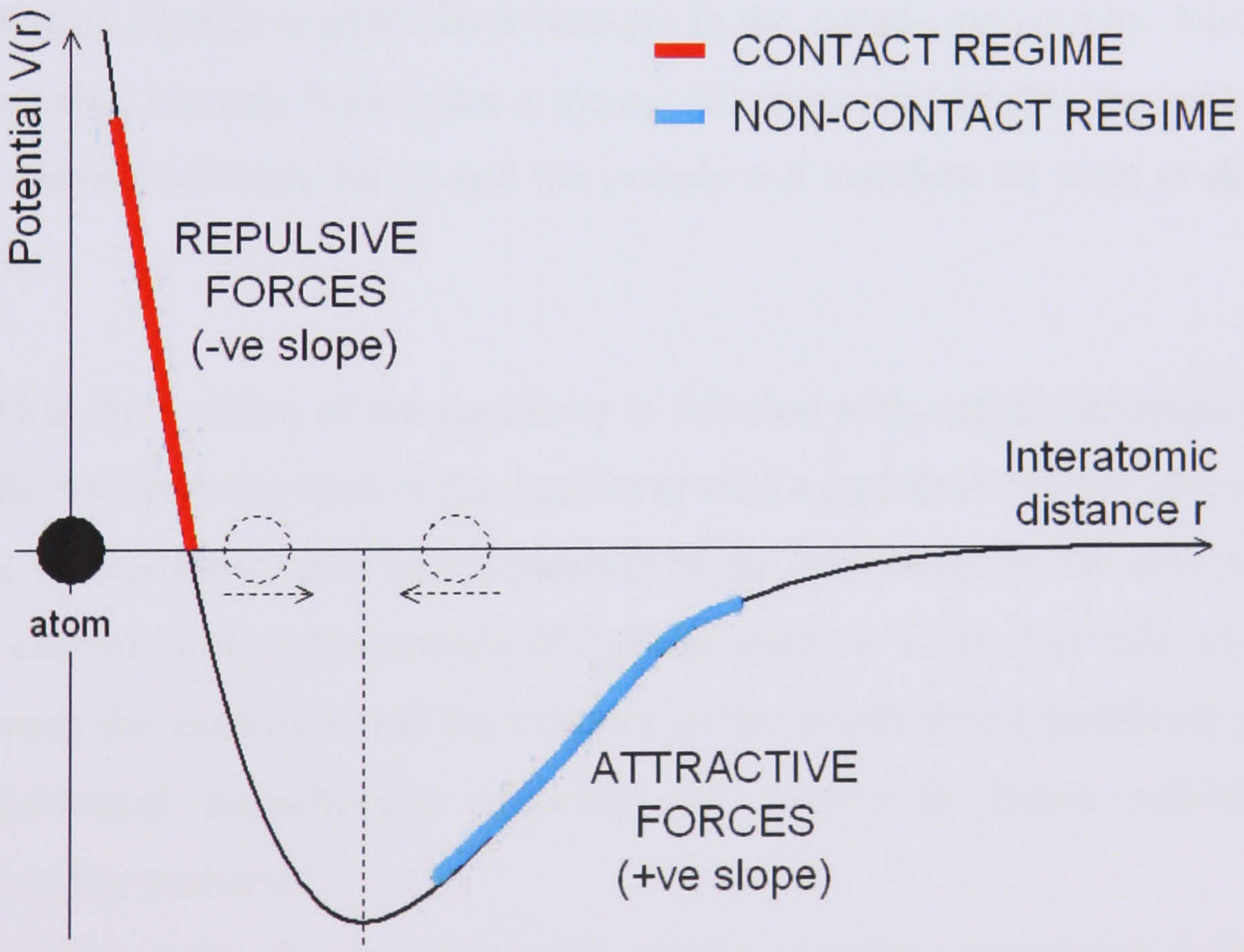



**Figure 3.1**: Schematic diagram showing how the tip-sample interatomic force varies with distance. A repulsive force dominates at small interatomic distances, while an attractive force dominates at larger separations with the equilibrium interatomic spacing at the lowest point of the curve. The working distance for contact and non-contact modes of operation of the AFM are indicated.

The AFM can operate in two distance regimes: a) the contact regime and b) the non-contact regime (see Fig. 3.1). In the contact regime the cantilever is held less than 0.1 nanometres from the sample surface, and the interatomic force between the cantilever and the sample is repulsive. In the non-contact regime the cantilever is held several tens



BIBL. LONDON UNIV.

of nanometres from the sample surface and the interatomic force between the cantilever and the sample is attractive.

-Contact Mode.

In contact mode, as the tip approaches the sample surface the interatomic forces will become very strongly repulsive and, since the cantilever to which the tip is attached has a low spring constant (lower that the effective spring constant holding the atoms of the sample together), the force will cause the cantilever to bend, following the topography of the sample. Therefore, detecting the deflection of the cantilever will lead to a topographic map of the sample surface.

-Non-Contact Mode.

In non-contact mode the cantilever is vibrated near the surface of the sample. The spacing between the tip and the sample is of the order of tens of nanometres (see spacing indicated in Fig. 3.1). The cantilever is set into vibration near its resonant frequency. The resonant frequency (or the phase) of the cantilever oscillation varies as the force gradient experienced by the cantilever changes, this in turns depends on the tip-sample separation. Thus changes in the amplitude resonant frequency (or the phase) of the oscillating cantilever will reflect changes in the sample topography. Non-contact AFM is desirable because it provides a means for measuring sample topography with little or no contact between the tip and the sample and therefore no wear or damage to sample or tip.

In most AFMs the position of the cantilever is detected with optical techniques: a laser beam is reflected from the back of the cantilever onto a position-sensitive photodetector (PSPD). As the cantilever moves, the position of the laser beam on the detector shifts. The PSPD can measure displacements of light as small as 1 nm. The ratio of the path length between the cantilever and the detector to the length of the cantilever produces further mechanical amplification allowing the system to detect sub-nanometre movements of the cantilever.

In both scanning modes the changes in the cantilever motion (cantilever deflection in contact mode and cantilever resonant frequency or phase in non-contact mode). as detected by the photodiode, are the input of a feedback system that moves the z-position of the AFM tip with respect to the sample surface in order maintain a constant deflection in contact mode and a constant phase/resonance frequency shift in non-contact mode. This has the effect of keeping the tip-surface distance approximately constant.

The fine x-y and z-direction control of the AFM tip over the sample surface is achieved using piezoelectric ceramics. The physical dimensions of these materials undergo nanometre to micrometre size changes depending on the electrical potential applied across them. The piezoelectric ceramic element is called the 'AFM scanner' and is either positioned under the sample (the sample is scanned under a fixed tip) or over the cantilever (the tip is scanned over a static sample).

The topography of the sample surface is thus given by recording the change in height of the piezoelectric element (which has to be calibrated) necessary to keep the AFM tip-sample distance constant during the scan.

A schematic diagram of the feedback loop in a contact mode image acquisition (with a scanning tip configuration) is shown in Fig. 3.2.

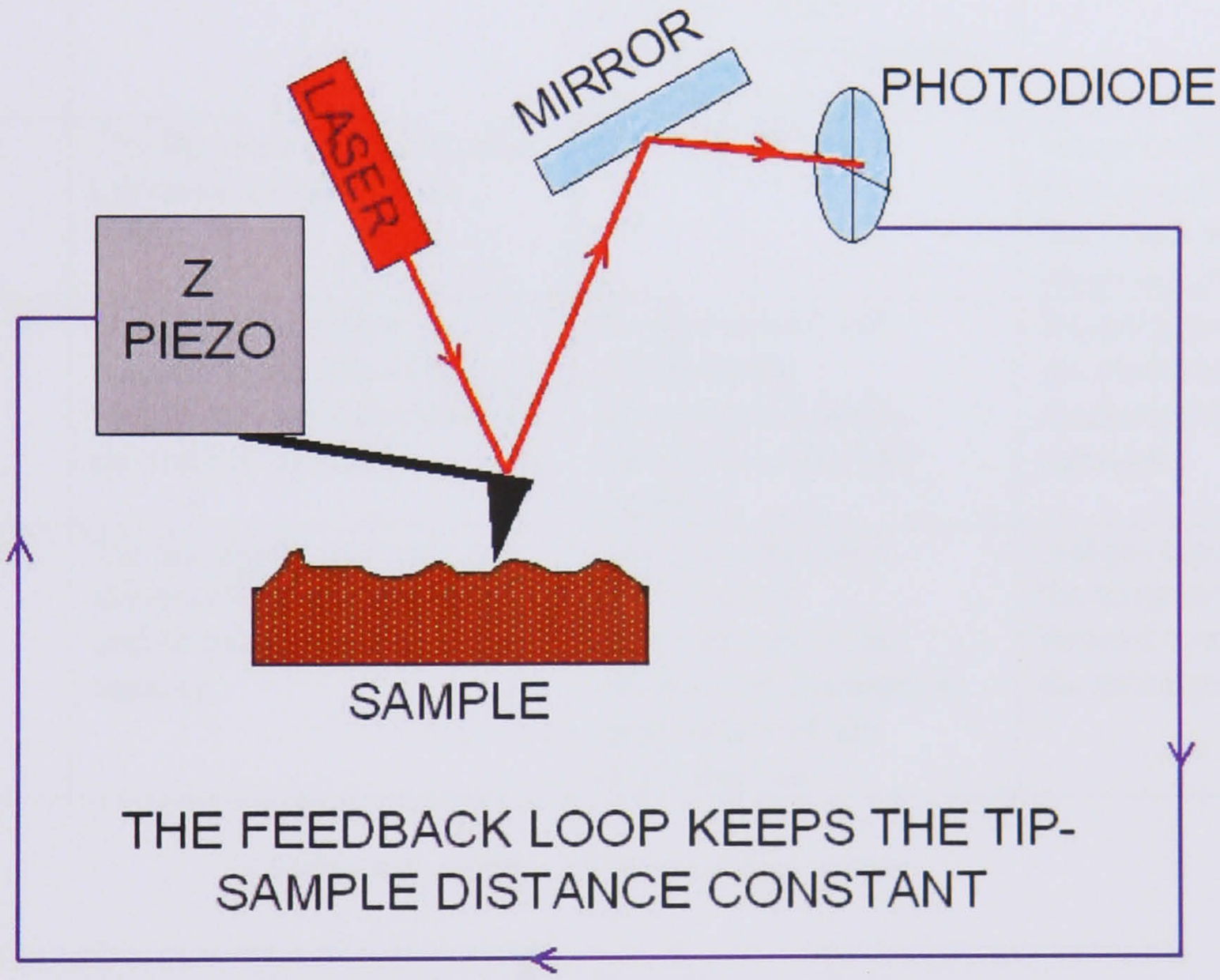



**Figure 3.2**: Schematic diagram of the AFM operation in contact-mode. The sharp tip on the AFM cantilever is scanned over the sample surface (using the x and y piezos, not shown). The deflection of the cantilever is monitored using the reflection of a laser from the back of the cantilever onto a photodiode. The photodiode difference signal is input into a feedback system that adjusts the height of the z-piezo element in order to keep the photodiode signal constant. In this way the cantilever deflection is kept constant. The record of the z-piezo movements as the tip is scanned over the surface will produce the sample topography.

## AFM Scanning Techniques and Applications

The AFM is a versatile instrument. It can be applied to image the topography of conducting and insulating samples, it can operate in air, liquid, vacuum environments and at cryogenic temperatures. It can also be used to probe different properties of the sample (other than its topography) simply by changing the scanning probe and/or the

scanning mode. Some of the operating modes of the AFM and the sample properties they probe are shown in Table 3.1 and illustrated in Fig. 3.3.

| Operating Mode | Tip Type | Scanning Mode | Sample Property |
|---|---|---|---|
| Magnetic Force Microscopy (MFM) | Tip is coated with a ferromagnetic thin film (e.g. cobalt) | Non-contact mode at different heights above the sample surface. | Images topography and magnetic field gradient of substrate. |
| Electrostatic Force Microscopy (EFM) | Tip is coated with a metallic layer (e.g. platinum/iridium alloy); a voltage bias is applied across the gap between the tip and the sample to create a charged region on the tip. | Non-contact mode at different heights above the sample surface. | Images topography and charge carrier density of the substrate. |
| Lateral Force Microscopy (LFM) | Standard tip, with cantilever of known lateral stiffness. | Contact mode with a quadrant position-sensitive detector (PSD) able to measure the vertical and lateral deflection of the cantilever independently yet simultaneously. | Images topography and frictional forces between the substrate and the tip |
| Chemical Force Microscopy (CFM) | The tip has a known organic molecule attached at its apex. | Contact mode | Images adhesion and frictional forces between known chemical groups |
| Conducting Atomic Force Microscopy (c-AFM) | Tip is coated with a conducting layer; a voltage bias is applied between the tip and the substrate. | Contact mode with simultaneous measurement of the current flow into the substrate. | Images topography and the electrical conductivity of the substrate. |
| Scanning Thermal Microscopy (SThM) | Tip incorporates a resistive element that can be heated and/or used for temperature sensing. | Contact mode with simultaneous measurement of the temperature, change in temperature of the thermal probe. | Images topography and the temperature or the thermal conductivity of the substrate. |

**Table 3.1** – Other AFM operating modes

The AFM versatility has been the reason for the rapid spread of its usage in many different scientific fields; some of its applications are listed below.

-Bioscience:

The AFM capability to scan in liquids whilst applying virtually no damage to the substrate has made it an important tool in biology where the AFM can provide nanometre-scale imaging of samples in their natural biological environment. The AFM can also be used to measure the force required to pull and unravel biological molecules (e.g. proteins) thus providing information on their structural arrangement.

-Tribology of micro- nano-structures:

The AFM is of great importance is the study of friction forces at the micro and nanoscale (the science and technology of friction, lubrication and wear is knows as

tribology). As devices are downscaled in size the surface to volume ratio increases dramatically and with it the importance of surface interactions. AFM and LFM can provide quantitative information on the surface properties of the samples: for instance, on its roughness, friction, scratching and wear.

-Nano-manipulations:

The AFM tip can be used as a tool to move and shape structures at the nanoscale. It can be used to pick-up and move molecules, deform, pick-up and move carbon

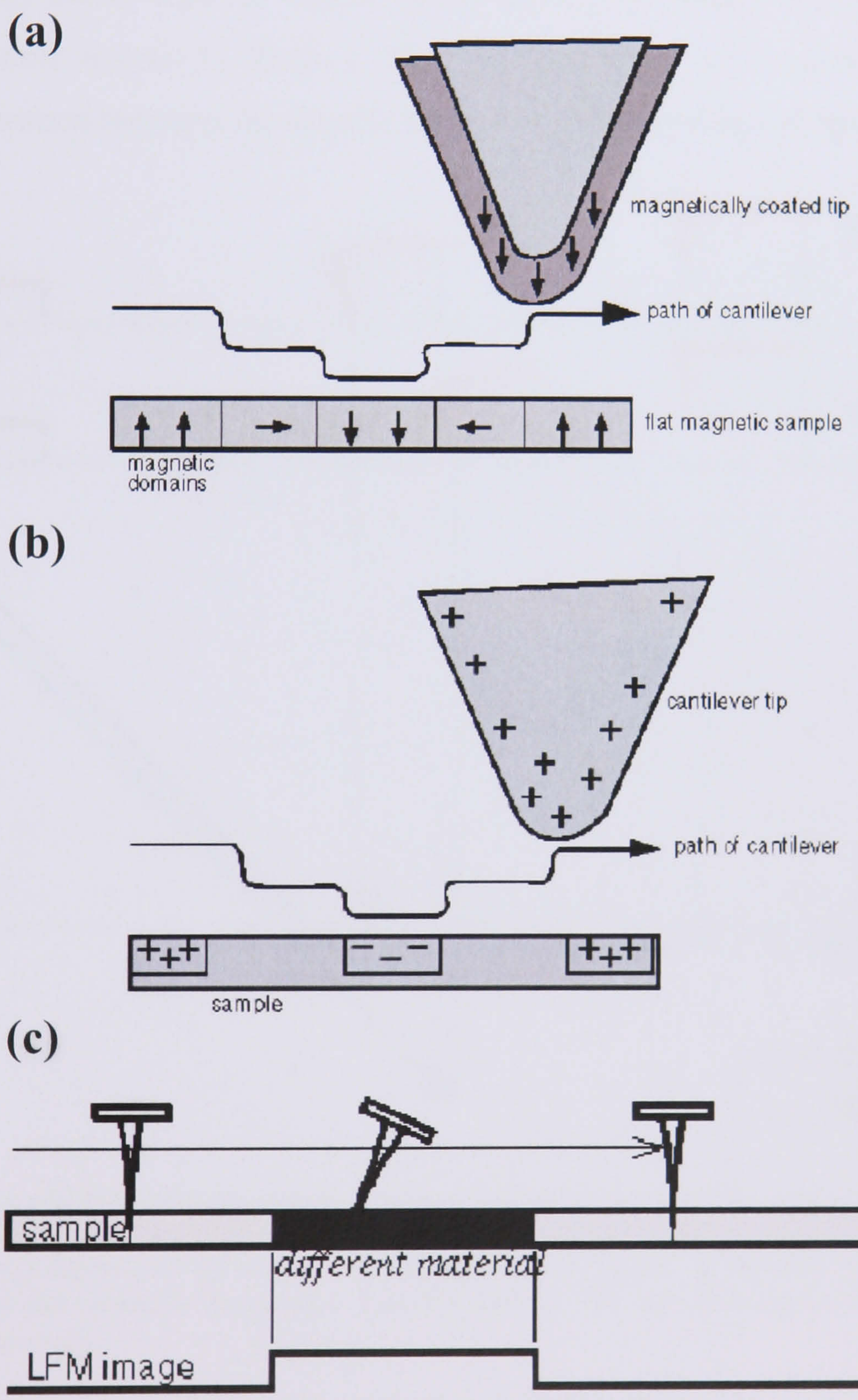



**Figure 3.3**: **a)** Schematic diagram of MFM imaging. The orientation of the magnetic domain in the substrate can be derived from the path of the scanning magnetized tip. **b)** Schematic diagram of EFM imaging. In this case the scanning tip's path depends on the charge distribution on the substrate. **c)** Schematic diagram of LFM imaging. Areas of higher/lower friction will cause a larger/smaller lateral deflection on the cantilever attached to the scanning tip. (Pictures taken from 'A Practical Guide to SPM', CD-rom produced by ThermoMicroscopes – now Veeco)

nanotubes, create nano indentations, and induce local oxidation of the sample surface.

**Force Measurements with the AFM**

If the spring constant of the cantilever to which the AFM tip is mounted is known, it is possible to calculate the force exerted by the tip onto the sample surface from the measured cantilever deflection using Hooke's law equation: $F = -kx$ where $F$ is the force, $k$ is the spring constant of the cantilever and $x$ the deflection of the cantilever. The force applied by the tip onto the sample can be plotted as a function of the extension of the z-piezoelectric scanner to obtain a 'force-distance curve' (F-D curve) - the distance being the separation between the sample surface and the fixed end of the cantilever (see

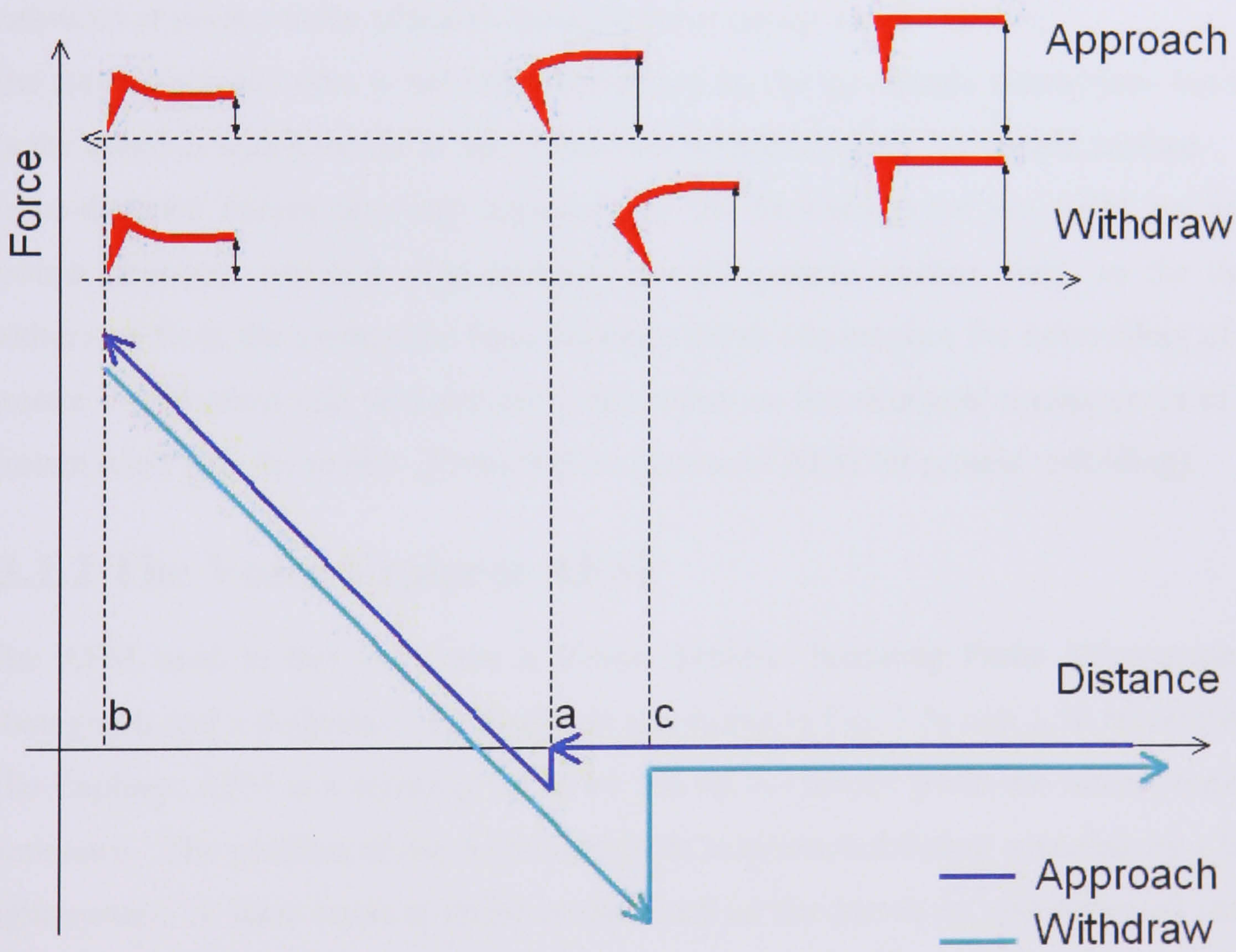



**Figure 3.4**: A typical force-distance curve. The force applied by the AFM tip on the sample surface is on the y-axis, the x-axis shows the distance between the sample surface and the fixed end of the cantilever. The deflection of the cantilever (exaggerated) is shown at different points along the approach (blue) and withdraw (turquoise) from the surface. The withdraw curve is offset to lower Force values for clarity.

Fig. 3.4). These curves can be used to study sample hardness, the tip-sample adhesion, and other tip-sample interactions.

In Fig. 3.4 a typical F-D curve on a hard sample (harder than the cantilever spring constant) is shown. Initially the tip is not in contact with the sample so the cantilever deflection is independent of distance and is constant and equal to zero. At point *a* the tip

of the AFM is close enough to the sample surface to feel the interatomic attractive pull. if the cantilever is soft enough it will register a 'jump-to-contact'. If the sample surface is covered by a moisture liquid layer then this 'jump-to-contact' effect will be enhanced by capillary forces. From position *a* to *b* the tip is in contact with the sample surface and as the distance decreases, the cantilever deflection increases (assuming that the cantilever is softer than the sample surface). When point *b* is reached the movement of the AFM tip is reversed and the deflection of the cantilever decreases – approach and withdraw curves may not exactly resemble each other due to hysteresis of the elastic properties of the cantilever. At point *c* the tip loses contact with the sample surface, position *c* is often at larger distances than *a* due to interactions between the sample and the tip (these could be due again to capillary forces of the moisture layer) the force measured at point *c* is the adhesive force between the tip and the sample.

The force-distance curve is not only determined by the tip-sample interactions but also by the speed at which the AFM tip approaches/withdraws from the sample surface.

Force-distance curves are very important in the biosciences: if the AFM tip has a protein attached, which is also anchored on the sample surface, then, as the tip is withdrawn from the surface the force-distance curve can monitor the unravelling of the protein components and thus provide information on the structural arrangement of the protein itself (see the review [Fisher'99] on the use of AFM for protein unfolding).

## 3.1.2 The Veeco Explorer AFM

The AFM used in this work was a Veeco Explorer Scanning Probe Microscope. A photograph and a diagram of the Explorer are shown in Fig. 3.5a and 3.5b respectively. The Explorer AFM is a scanning tip AFM: the tip is scanned while the sample remains stationary. The position of the AFM cantilever is monitored during scanning by a laser light system. A laser beam is shone on the back of the cantilever and reflected onto a mirror that can be adjusted so that the beam reaches a quadrant photodiode. The laser used is a Class IIIa, red diode laser (wavelength 670nm) of 3mW power. The laser spot is approximately 25μm in diameter. Two screws are used to adjust the position of the laser beam on the cantilever. The photodiode signal is then input into the signal feedback system connected to the z-piezo. The Explorer has an integrated black-white CCD video camera for viewing the tip and the sample (at an angle of 45°, the field of view is 1.5×1.5 mm and the resolution is 10 μm) and this can be used also to locate the laser spot and move it onto the cantilever.

The piezoelectric scanner used was a tripod scanner. Tripod scanners are made of separate x, y and z-direction piezoelectric components. The x and y piezos are mounted horizontally and move the laser tower and detector assembly laterally. The z piezo is mounted at the bottom of the laser-detector assembly and the AFM probe is mounted directly on the under-side of the z scanner. The tripod scanner ranges were 100μm in x and y and 10μm in z. The non-linearity, hysteresis and creep of the piezoelectric

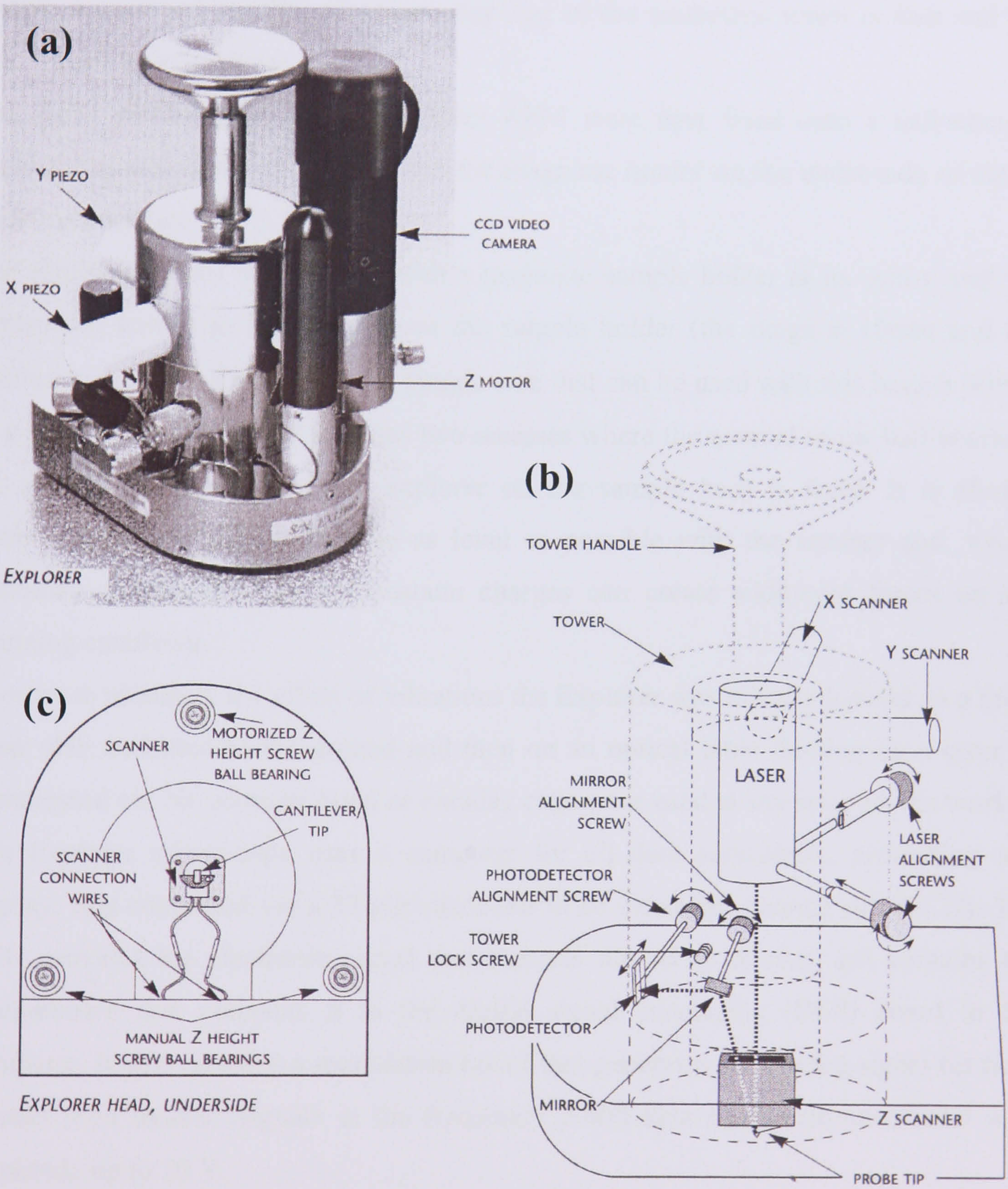



**Figure 3.5**: **a)** photograph of the Veeco Explorer AFM head. The x and y piezoelectric ceramics, the CCD video camera and the motorized screw ball-bearing are visible. **b)** Diagram showing the structure inside the AFM head. The position of the three piezos is indicated, together with a diagram of the laser light path. The laser light is used to monitor the deflection of the AFM cantilever. **c)** Diagram showing the under-side of the AFM head. The position of the three screw ball-bearings is indicated and the magnetic holder for the AFM probes is visible. The AFM probes, attached on a magnetic half-circular mount, are positioned on the under-side of the z-piezo (see also diagram in **b**). Figures taken from the Veeco Explorer AFM Operations Manual.

elements were corrected by a TrueMetrix™ close-loop scanner linearization technique (integral to the AFM hardware).

On the under-side of the Explorer (see Fig. 3.5c) are three screw ball-bearings. Two are adjusted manually and one is motorized. These were used to adjust to the z-height of the AFM head over the sample surface; once the tip is in close proximity with the sample surface, the motorized z-screw ball bearing is used to slowly approach the surface until the cantilever motion starts to be affected by the tip-sample interaction and the feedback system is switched on. The minimum step size of the motorized screw is 4nm and the total travel range is 10mm.

The AFM probes used on the Explorer AFM were first fixed onto a half-circular magnetic mount, and then attached on the magnetic holder on the under-side of the z-piezo scanner (see Fig. 3.5c).

The Explorer comes with a base with a magnetic sample holder at its centre and x-y adjustment screws to manually move the sample holder (the range is 10mm and the resolution is 5μm). The maximum sample size that can be used with this base is 60mm in x-y and 10mm in z. The base has two recesses where the manual screw ball-bearings fit, so that the position of the Explorer on the sample base is fixed. It is always important to maintain the sample as level as possible with the scanner and, when, necessary to ground it as electrostatic charges can create additional forces on the scanning cantilever.

In order to minimize the effect of vibrations the Explorer was initially located on a thick stone slab anchored to the ground and then on an optical table floating on a layer of compressed air. No acoustic hood or Faraday cage were used at any stage in this work.

The Explorer microscope uses a computer for all data acquisition, processing and display. It is connected via a 37-pin connector to an electronic control unit (ECU). The ECU provides the electronic signal that controls the AFM scanner and contains the motherboard that connects it to the digital signal processing (DSP) board in the computer. It also contains a modulation board that generates the driving signal for non-contact scan modes. Signals in the frequency 2-600 kHz can be produced and with amplitude up to 10 V.

A diagram of the connections from the Explorer AFM to the other components is shown in Fig. 3.6.

Two external signals can be input into the ECU via BNC connectors labelled IN 1 and IN 2 (see Fig. 3.6); they can be thus monitored simultaneously as the voltage signal from the z-piezo during scanning or F-D curve acquisition.

The vertical laser position on the photodiode (which is used to monitor the deflection of the cantilever) can be output from the ECU using the OUT 2 BNC connector. The signal is a DC voltage with range ±10V.

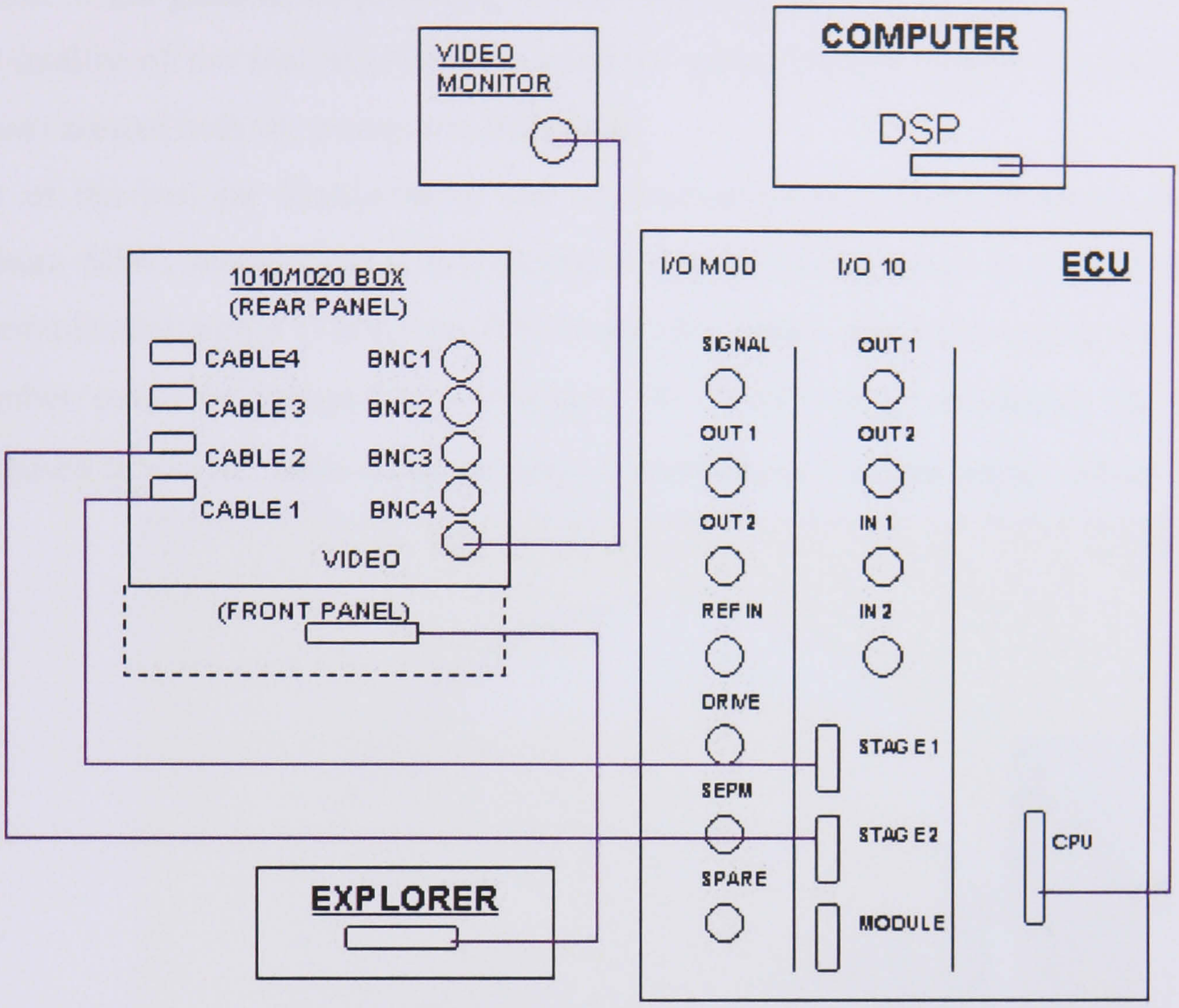



**Figure 3.6**: Diagram showing the connection of the various components. The Explorer is connected to the ECU via a 1010/1020 box which houses the diode laser controls. The video connection displays on a monitor the image from the CCD camera in the Explorer AFM. The connection from the computer to the ECU allows the computer software to perform data acquisition, analysis and display. Two external inputs (IN1 and IN2) can be fed in the ECU to monitor other quantities while scanning.

## 3.2 Adapting the AFM for Operation in High Vacuum

In order to reduce the environmental influence on thermal measurements performed in the AFM, the Explorer AFM was repositioned inside a vacuum chamber (see Fig. 3.7). This has not previously been reported for this AFM model.

The vacuum chamber was based on components from the Kurt J. Lesker Company. The vacuum chamber had three components: i) a stainless steel disc-shaped base, 2 cm thick and 35 cm in diameter; ii) a cylindrical, stainless steel feedthrough collar 33 cm in diameter and ~15 cm high with 8 feedthroughs with KF40 type flange; iii) a glass dome, ~1 cm thick, ~30 cm high and ~31 cm in diameter. The cylindrical stainless steel collar

was placed on the stainless steel base and the vacuum seal between the two was provided by a rubber O-ring fitted in a groove at the bottom of the cylindrical unit. The glass dome was then placed on top of the cylindrical unit; a rubber gasket fitted on the bottom of the glass dome provided the vacuum seal between the dome and the collar. The quality of the seal was further enhanced using vacuum grease (Apiezon, L-type grease) around both the o-ring and the gasket.

One of the bell jar feedthroughs was connected via a flexible stainless steel hose (Caburn-MDC, model DN40) to a Leybold rotary (Trivac) pump incorporating also a turbomolecular pump (Turbovac 50). Using the rotary and turbo pump the vacuum chamber could be pumped to a pressure of $\sim 5\times10^{-5}$ mbar overnight, the pressure decreased to $\sim 5\times10^{-6}$ mbar if the pumping continued over several days, without baking.




**Figure 3.7**: Photograph of the Explorer AFM inside the vacuum chamber. Some of the feedthroughs in the bell jar cylindrical collar (8 in total) are in use: 1) Penning cold-cathode gauge; 2) motion feed-through to adjust laser position on the AFM; 3) inline valve and stainless steel hose; 4) Pirani gauge; 5) 37-pin connector electrical feed-through.

An inline manual operation valve (Caburn-MDC model KIV-150) was inserted between the collar feedthrough and the flexible stainless steel hose, this allowed high vacuum to be maintained within the chamber even if the vacuum pump had to be switched off.

The pressure inside the chamber was measured by a Pirani gauge (Balzers, model TPR) for pressures down to ~$5\times10^{-4}$ mbar and by a Penning cold-cathode gauge (Balzers, model IKR 020) for lower pressures. These gauges were fitted in two of the 8 feedthroughs of the collar. The pressures measured by the gauges were displayed in a 'Pirani and cold cathode gauge control' unit (Balzers, model PKG 100).

The Explorer AFM was placed in the chamber on top of the stainless steel disc-base. The 37-wires from the AFM were connected to the ECU via a 37-pin electrical feed-through using one of the feedthroughs in the collar.

When operating in vacuum the Explorer AFM was observed to heat up, this effect was absent at ambient pressure as the heat was probably lost by air convection and/or conduction, both these mechanism were suppressed in vacuum. When operating in vacuum, the CCD camera mounted on the Explorer was removed and the light bulb used to illuminate the AFM tip for the CCD camera was switched off. These precautions reduced the heating but did not make it disappear. The source of the heating was initially thought to be only the diode laser, but it was found that even when the laser was switched off there was still a residual heating source. This was connected to the switching on of the AFM ECU, which energizes the various components in the AFM thus causing them to heat up. The temperature of the AFM was measured to increase by about 1 °C every 4-5 minutes during continuous operation. Distortions in the AFM image started to appear after 30-40 minutes of operation in vacuum due to heating-caused expansion of the AFM components.

When operating in vacuum the deflection of the cantilevers of the AFM probe was sometimes subject to changes: the air pressure induced a slight deflection on the softest AFM cantilevers and, in vacuum, this air-induced deflection disappeared. This meant that, as the pressure decreased, the vertical laser position on the photodiode was observed shifting upwards (as the cantilever deflection decreased). Sometime the effect was such that the laser spot was no longer positioned on the photodiode. No significant shift in the horizontal laser position on the photodiode was ever observed.

It was thus necessary to control the mirror regulating the vertical laser position on the photodiode, from outside the bell jar. This was implemented using a motion feed-through rod: a combination rotary and push-pull linear drive (Caburn-MDC, flange DN40 KF, model K-CRPP-1), see Fig. 3.8. The rod of the motion feed-through had a

linear travel of ~20 cm and could be rotated clockwise/anticlockwise. At the end of the rod was inserted a T-shape structure made of PTFE. On the knob of the mirror controlling the vertical laser position on the photodiode was fixed a U-shape PTFE structure. These PTFE 'cogs' allowed the knob to be rotated in either direction. Once the mirror was adjusted using the rod, this was disengaged and pulled away from the

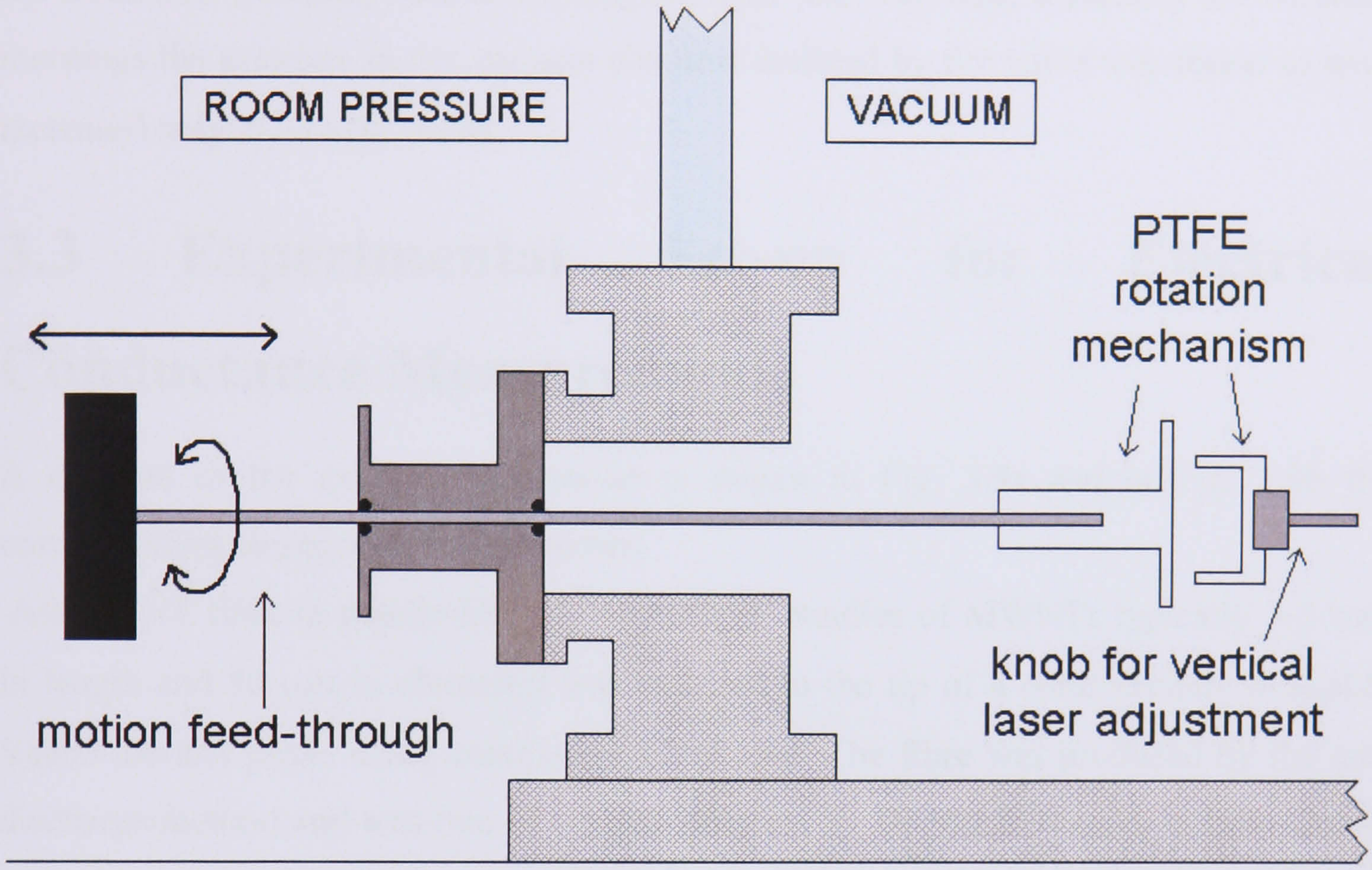



**Figure 3.8**: Diagram of the mechanism to adjust the vertical laser position on the photodiode when the AFM was inside the bell jar. The motion feed-through rod could be rotated clock/anticlock-wise and be pushed in and out of the bell jar. A dual o-ring shaft ensured that high vacuum inside the bell jar was not compromised during such movements. A PTFE T-shaped and U-shaped mechanism was used to rotate the knob for vertical laser alignment using the rod. The rod was retracted when the adjustment was complete to avoid coupling unwanted noise to the AFM.

knob. In this way there was no physical contact between the motion feed-through and the AFM during scanning, and no vibrations were coupled into the AFM via the motion feed-through rod. A schematic diagram of the laser adjustment mechanism is shown in Fig. 3.8.

Noise increase was an issue when operating in vacuum as the rotary pump induced vibrations were coupled to the vacuum chamber via the stainless steel hose (which is flexible but rigid). Since the AFM was placed on top of the chamber base it thus registered an increased level of vibration during operation in vacuum. Scanning was still feasible but imaging structures at the nanometre scale was compromised (tests were made using samples of DNA deposited on mica, the DNA diameter was 1-3 nm). The effect on the force distance curves was less pronounced.

This problem was provisionally solved with the inclusion of the inline manual operation valve (Caburn-MDC model KIV-150) between the vacuum chamber feedthrough and the stainless steel hose. During scanning or data acquisition the valve was closed and the pumping switched off. The pressure was always observed to rise slightly when the pumping ceased but high vacuum was preserved in the vacuum chamber.

On occasions pumping had to be stopped over the weekend; invariably on Monday mornings the pressure in the vacuum chamber isolated by the valve was found to have increased only to $\sim 1\times10^{-3}$ mbar.

## 3.3 Experimental Set-up for Electrical Conductance Measurements

A diagram of the experimental set-up is shown in Fig. 3.9a and in Fig. 3.9b the corresponding electrical circuit is shown.

An MWNT fibre (a needle-like agglomerate of bundles of MWNTs typically 3-5 mm in length and 50 μm in diameter) was attached to the tip of a commercially available Veeco thermal probe using conductive silver glue. The fibre was produced by the arc-discharge method and was one of a batch supplied by Dr Mark Baxendale from Queen Mary University of London. The fibre is made up of millions of MWNTs, and at its ends, several long individual MWNTs protrude from the bulk. The fibre is large and robust enough to be handled with sharp tweezers and is thus the ideal medium to couple individual nanotubes to macroscopic measuring devices. Arc-grown MWNT fibres were used to study ballistic electron transport in individual MWNTs by S. Frank et al as reported in Ref. [Frank'98]. A detailed description of the MWNT fibre is to be found in Section 4.1.

The Veeco thermal probe is larger and stiffer than other AFM probes and it is formed by two 75 μm diameter, silver coated, conductive arms. In this experiment, it was used just as a conductive support for the MWNT fibre; a description of the probe's design and thermal properties is to be found in Section 3.4.

The Veeco thermal probe is specifically designed to operate in an Explorer AFM and thus comes already fixed on a semi-circular magnetic disc. It also comes with its two silver arms already wired up to copper contact pads on the semi-circular disc. Copper wires were soldered onto the pads for the electrical conductance measurements.

The thermal probe with attached MWNT fibre was mounted on the magnetic probe holder inside the Veeco Explorer AFM and a freshly cleaved highly-oriented-pyrolitic-

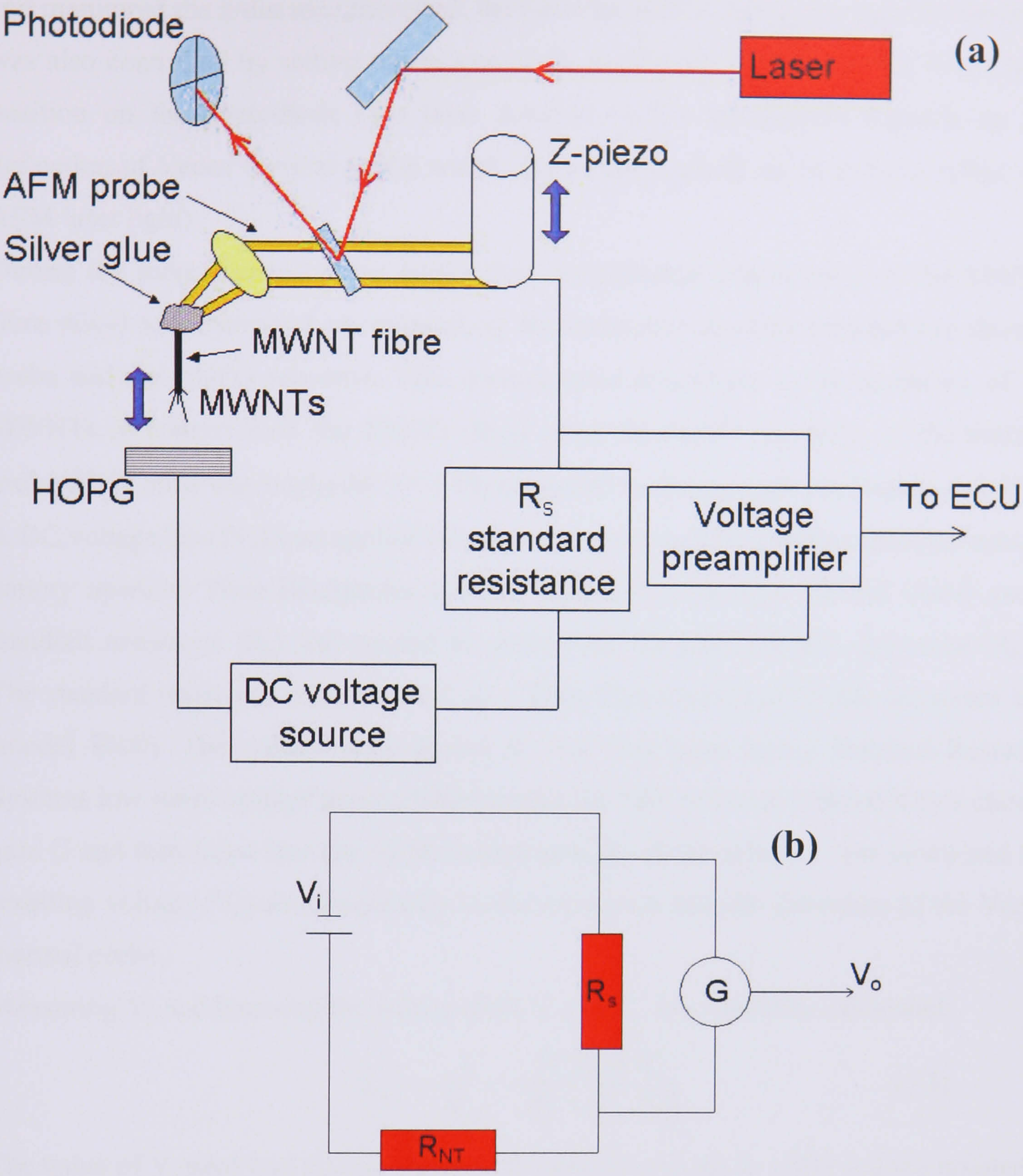



**Figure 3.9**: **(a)** Diagram of the experimental set-up used to study the electrical conductance properties of the nanotubes in air and in vacuum. The laser light reflected from the mirror on the thermal probe is used to measure the cantilever deflection from its position on the photodiode. The MWNT fibre is glued on the thermal probe with conductive silver glue and the AFM z-piezo is used to lower the fibre onto the HOPG. The longest protruding individual MWNTs from the fibre make contact with the HOPG and their resistance is measured. **(b)** Diagram of the corresponding electrical circuit used. $V_i$ is the DC bias voltage, $R_{NT}$ is the nanotubes resistance, $R_s$ is the standard resistance, G is the voltage gain set on the voltage preamplifier. The resulting voltage $V_o$ is input into the AFM control unit.

graphite (HOPG) substrate was placed in the AFM sample holder. A copper wire was attached using conductive silver glue to the top layer of the HOPG for the electrical conductance measurements.

The piezo drive of the AFM was used to perform a force-distance curve measurement during which the MWNT fibre was moved in and out of contact with the graphite surface. The AFM control unit allowed the approach/withdraw speed to be controlled

and monitored the z-distance travelled; the force applied by the probe onto the substrate was also controlled by setting the values of the maximum change allowed in the laser position on the photodiode (the laser position on the photodiode depends on the deflection of Veeco thermal probe which has a mirror glued on its arms to reflect the AFM laser light).

During the force-distance curve acquisition the electrical conductance of the MWNT fibre ($G_{NT}$) was measured by monitoring the resistance changes between the thermal probe and the HOPG substrate. This corresponded effectively to the resistance of the MWNTs in contact with the HOPG ($R_{NT}$) since the series resistance of the thermal probe silver arms was negligible (< 1 Ω) compared to the nanotube resistance (> 1 kΩ). A DC voltage bias ($V_i$) was applied between the probe and the graphite substrate using a battery operated Time Electronics Ltd DC Millivolt pot-source (Model 404N) and a standard resistance ($R_s$) was placed in series with the probe-HOPG resistance ($R_{NT}$). The standard resistance was provided by a Time Electronics Ltd decade resistance box (model 8000). The voltage drop across $R_s$ was first input into a Stanford Research Systems low-noise voltage preamplifier (model SR 560) which multiplied it by a chosen gain G and then input into the AFM control unit, the AFM software thus monitored the resulting voltage ($V_o$) simultaneously as the z-position and the deflection of the Veeco thermal probe.

Measuring $V_o$ and knowing the values of G, $V_i$ and $R_s$, $G_{NT}$ could be calculated:

$$G_{NT} = \frac{1}{R_{NT}} = \frac{(V_o/G)/R_s}{[V_i - (V_o/G)]} \qquad (3.3)$$

The value of $V_i$ used was always 9.0 mV, the gain G was set to 1,000 and the resistance $R_s$ was 1.2 kΩ in most measurements, though in some values of 1.0 and 0.7 kΩ were also used.

The force-distance curves were performed at a speeds ranging from 130 to 10 nm/s (the most common value used was 50 nm/s) and data points were acquired every 10 nm of travel in the z-direction. The 'zero' value in the z-travel was an arbitrary position and it corresponded to the position where the probe's deflection reached the maximum allowed value input (by the user) in the system. Negative z values corresponded to the amount in nm by which the z-piezo had shrunk from the 0-value position: thus –1000 nm corresponded to a piezo extension 1000 nm shorter than that required for maximum deflection to be achieved. Positive values corresponded to further piezo extension from the 0-value position. The allowed z-value range was +500 to –9500 nm.

The probe deflection and the value of $V_o$ at a given z-point were recorded simultaneously by the AFM built in software. They both appeared in units of nA (default unit in the system). The corresponding value for $V_o$ in volts was obtained by first calibrating the AFM system using a 1 V input, the calibration factor was found to be: 0.1546 ± 0.0042 V/nA. The probe deflection was expressed in nA because the position of the laser reflected from the back of the probe's cantilever onto the photodiode was expressed in such units. 0 nA corresponded to the laser spot being at the centre of the photodiode, and ±64.52 nA corresponded to the laser spot being at the very top/bottom of the photodiode respectively. In order to convert the deflection in nA to the force in N applied by the probe onto the substrate, the spring constant (k) of the thermal probe had to be known. The nominal value of k = 5 N/m supplied by the Veeco probe manufacturer was used.

43 force-distance curve measurements were recorded in air (at room temperature and pressure).

The AFM was then placed in the vacuum chamber in order to repeat the conductance measurements in high vacuum ($10^{-5}$-$10^{-6}$ mbar). The same set-up was used but the connections from the HOPG and the thermal probe had to be wired through a 9-pin electrical feedthrough connector across the chamber's feedthrough collar. The DC voltage supply, the standard resistance and the voltage preamplifier all remained outside the vacuum chamber. 44 force-distance curve measurements were recorded in vacuum at room temperature over a period of a week. The first measurement was taken after the MWNT fibre mounted on the thermal probe had spent 2½ days in high vacuum.

**Bulk Resistance Measurements in Air and Vacuum**

In order to measure the changes of the bulk resistance of the MWNT fibre during progressive oxygen desorption and adsorption from the MWNTs, one MWNT fibre was placed on a microscope cover slip and fixed to it with two conductive silver glue tracks at each end. Copper wires were then attached to the 4 conductive glue tracks in order to measure the resistance of the MWNT fibre. The fibre and cover slip were placed in the vacuum chamber and the four wires were connected through the 9-pin electrical feedthrough connector across the chamber's feedthrough collar. A fixed current of 5 mA was passed through the MWNT fibre and the voltage drop across it ($V_o$) was monitored. The resistance of the fibre was measured at room temperature and pressure and then the fibre was placed in the vacuum chamber. The changes in resistance were monitored as the MWNT spent a total of ~290 hours (over 12 days) in high vacuum.

After the prolonged time in high vacuum the vacuum chamber was opened and the MWNT fibre resistance was monitored at room temperature and pressure for a further period of ~80 hours (~4 days). A diagram of the set-up used to study the bulk resistance changes of the MWNT fibre at room pressure and in vacuum is shown in Fig. 3.10.

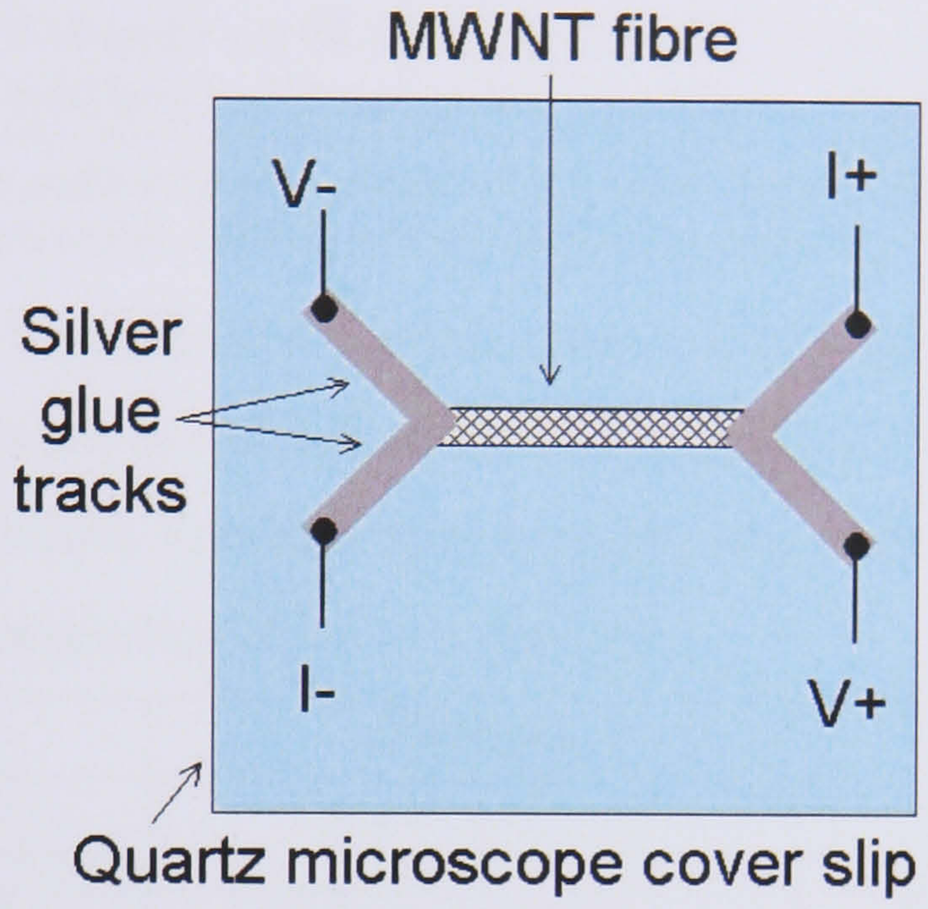



**Figure 3.10**: Diagram of the set-up used for bulk resistance measurement of the MWNT fibre. The fibre was fixed on a microscope cover slip using conductive silver glue; the glue was also used to shape 4 tracks for the resistance measurements of the MWNT fibre.

## 3.4 Structure and Operation of the Veeco Thermal Probe

In Fig. 3.11 is shown an SEM picture of the Veeco thermal probe. This probe is used for SThM (Scanning Thermal Microscopy) studies and is much larger than the standard silicon or silicon-nitride probes conventionally used by the AFM – see Table 3.2.

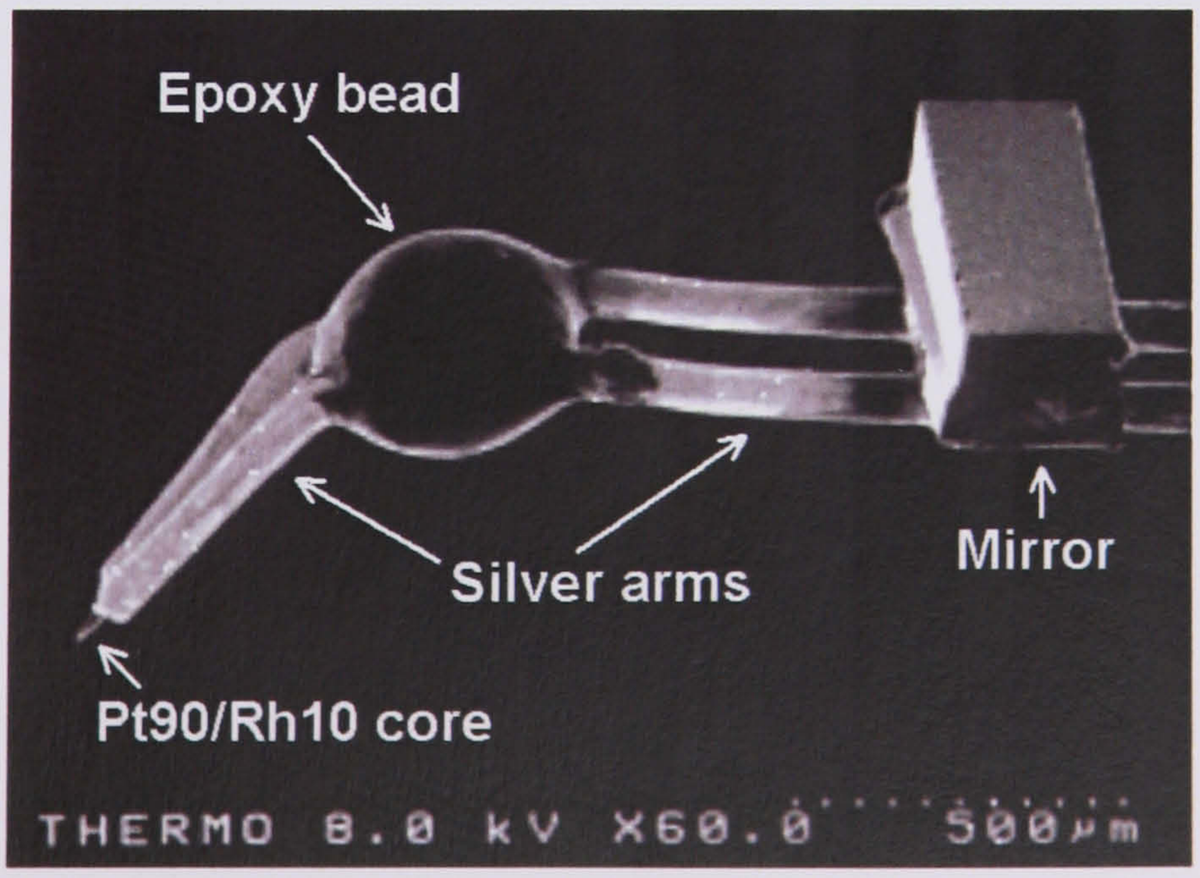



**Figure 3.11**: the Veeco thermal probe. In the SEM image are visible the silver arms of the cantilever, the Platinum/Rhodium alloy thermal element, the epoxy bead and the mirror (figure taken from the Veeco website – www.veeco.com).

| | Veeco Thermal Probe | Veeco Silicon Nitride Probe |
|---|---|---|
| Cantilever Length | > 600 μm (from epoxy bead) | ~200 μm |
| Cantilever Thickness | ~75 μm | ~ 0.6 μm |
| Cantilever Width | 170-300 μm | ~20 μm |
| Cantilever Stiffness | ~5 N/m | ~0.02 N/m |
| Tip Details | V-shaped 5 μm thick Pt90/Rh10 wire; total length ~156 μm, height ~60 μm | Pyramidal Silicon Nitride tip; 3.5 μm high, ~10 μm wide at the base |

**Table 3.2**: The average size, stiffness and tip details of the Veeco thermal probe compared to that of a standard, diving board silicon nitride AFM cantilever for contact mode scanning.

The probe's backbone consists of two silver-coated 'arms'; the silver coating is etched at the probe's tip to expose the V-shaped thermal element of the probe: a core filament made of 90% Platinum-10% Rhodium thermocouple alloy – in Table 3.3 are shown the electrical and thermal properties of the two elements.

| | Pt90/Rh10 | Ag |
|---|---|---|
| Electrical Resistivity | 18.4-19.2 μΩ cm | 1.63 μΩ cm @ 20 °C |
| Thermal Conductivity | 38 W $m^{-1}$ $K^{-1}$ @ 23 °C | 429 W $m^{-1}$ $K^{-1}$ @ 0-100 °C |

**Table 3.3**: The electrical resistivity and the thermal conductivity of the two components of the Veeco thermal probe compared. Data taken from Goodfellow – www.goodfellow.com.

The thickness of the silver-coated arms is 75 μm, while the thickness of the core filament is 5 μm. In Fig. 3.11 is also visible a mirror, mounted on the back of the silver arms; this mirror is used to reflect the laser that, in the AFM, is used to locate the position (and deflection) of the probe (see also Fig. 3.9a). The other visible feature is an epoxy bead fixed on the bent part of the silver-coated arms, this bead is added to increase the mechanical strength of the cantilever; the nominal spring constant of the cantilever (as provided by the manufacturers) is 5 N/m.

The thermal probe can operate in two modes: temperature and conductivity contrast mode.

In the temperature contrast mode the thermal probe is used as a resistance thermometer: changes in the probe temperature cause the probe's resistance to change.

The probe is one of the legs of a Wheatstone bridge (see Fig. 3.12a), and a small constant current (to avoid self heating of the probe) is passed through the bridge. As the probe scans over a given sample with hot and cold parts, the temperature of the probe changes; the corresponding change in its resistance will alter the voltage balance of the bridge, changing the voltage output $V_{out}$. Measuring $V_{out}$ the temperature of the probe (and hence of the sample) is derived using the equation:

$$V_{out} = (R_o \alpha Ci)(T - T_o) + V_o \qquad (3.4)$$

where $R_o$ is the resistance of the thermal probe measured at the reference temperature $T_o$ (usually room temperature), $\alpha$ is the temperature coefficient of resistance of the probe material, C is the calibration gain (set by the user), $i$ is the current applied to the probe (set by the user) and $V_o$ is the bridge voltage at the reference temperature (measured by user).

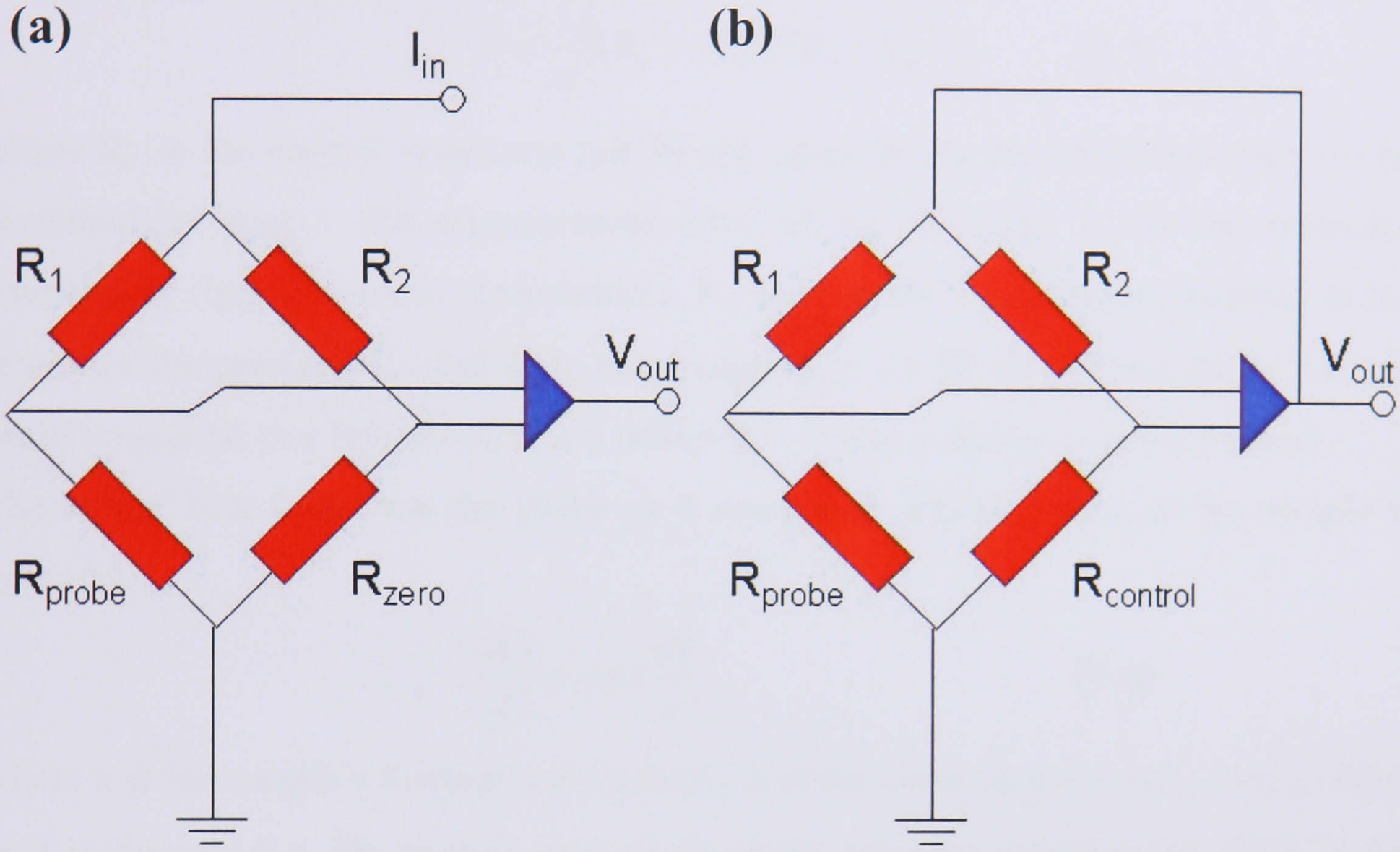



**Figure 3.12**: **(a)** the Wheatstone bridge configuration for the temperature contrast mode. **(b)** the Wheatstone bridge configuration for the conductivity contrast mode. $R_1$ and $R_2$ are high quality resistances of 20 Ω and 100 Ω respectively.

This mode of use has two potential problems: first, if the current through the probe is too large it will induce self heating in the probe and this will in turn cause errors in the temperature measurements. The second problem is the scanning speed: the response of the system is limited by the response time of the thermal probe, i.e. the time necessary to establish a new thermal equilibrium in the probe.

In this work the thermal probe was always used in conductivity contrast mode. In this mode the resistive element of the thermal probe is used as a resistive heater. As in the temperature contrast mode, the thermal probe is one of the legs of a Wheatstone bridge (see Fig. 3.12b) but in this case self-heating of the probe is desired. Furthermore, there is a feedback loop that adjusts the voltage applied to the bridge in order to keep the probe at a constant temperature (by keeping it at a constant resistance). The total amount of heat lost by the self heating thermal probe (Q) is measured by monitoring the voltage needed to balance the bridge ($V_{out}$) using the equation:

$$Q = \frac{R_P}{(R_1 - R_P)^2} V_{out}^2 \qquad (3.5)$$

where $R_1$ is equal to 20 Ω (value built in the system) and $R_P$ is the probe's resistance at its operating temperature T (i.e. the temperature to which the probe is being self heated), and it is given by:

$$R_P = R_o[(T - T_o)\alpha + 1] \qquad (3.6)$$

Finally, the operating temperature of the probe (T) is given by:

$$T = \frac{1}{\alpha}[(R_C - R_L)/5R_o - 1] + T_o \qquad (3.7)$$

where $R_C$ is the control resistance (set by the user), $R_L$ is the leads resistance (to be measured by user – the measurement error of $R_L$ is <2%), $T_o$ is the reference temperature (typically room temperature), $R_o$ is the probe's resistance measured at the reference temperature $T_o$ and $\alpha$ is the temperature coefficient of resistance for the probe's material (for Pt90/Rh10 it is 0.00165 $K^{-1}$ – value supplied with the probes).

The rate of heat flow from the probe as it scans over different areas of the sample is given by:

$$\frac{dQ}{dt} = -\kappa A \frac{dT}{dx} \qquad (3.8)$$

where κ is the sample's thermal conductivity, A is the cross sectional area across which heat is flowing (i.e. the contact area of the probe onto the sample) and *dT/dx* is the temperature gradient between the probe and the sample. Therefore, given that the contact area A is kept constant by the feedback loop that controls the force applied by the AFM tip onto the sample (see Section 3.1.1) and given that the thermal gradient *dT/dx* is kept constant by the feedback loop on the thermal probe, the rate of heat flow from the probe is proportional to the thermal conductivity of the sample. Using this method the thermal conductivity of an unknown sample can thus be determined by comparing the heat flow rate of the sample to that on a flat sample of known thermal conductivity.

### 3.4.1 Study of the Probe-Sample heat Exchange of the Veeco Thermal Probe

The heat lost by the Veeco thermal probe (with the resistive element heated at different temperatures) was monitored as the probe was lowered onto three samples: i) a freshly cleaved HOPG substrate (Fig. 3.13a); ii) a Pt100 resistance thermometer (Fig. 3.13b); iii) the tip (resistive element) of a second Veeco thermal probe (Fig. 3.13c).

The probe was operated in conductivity contrast mode. In cases ii) and iii) the temperature of the Pt100 thermometer and of the resistive element of the Veeco thermal

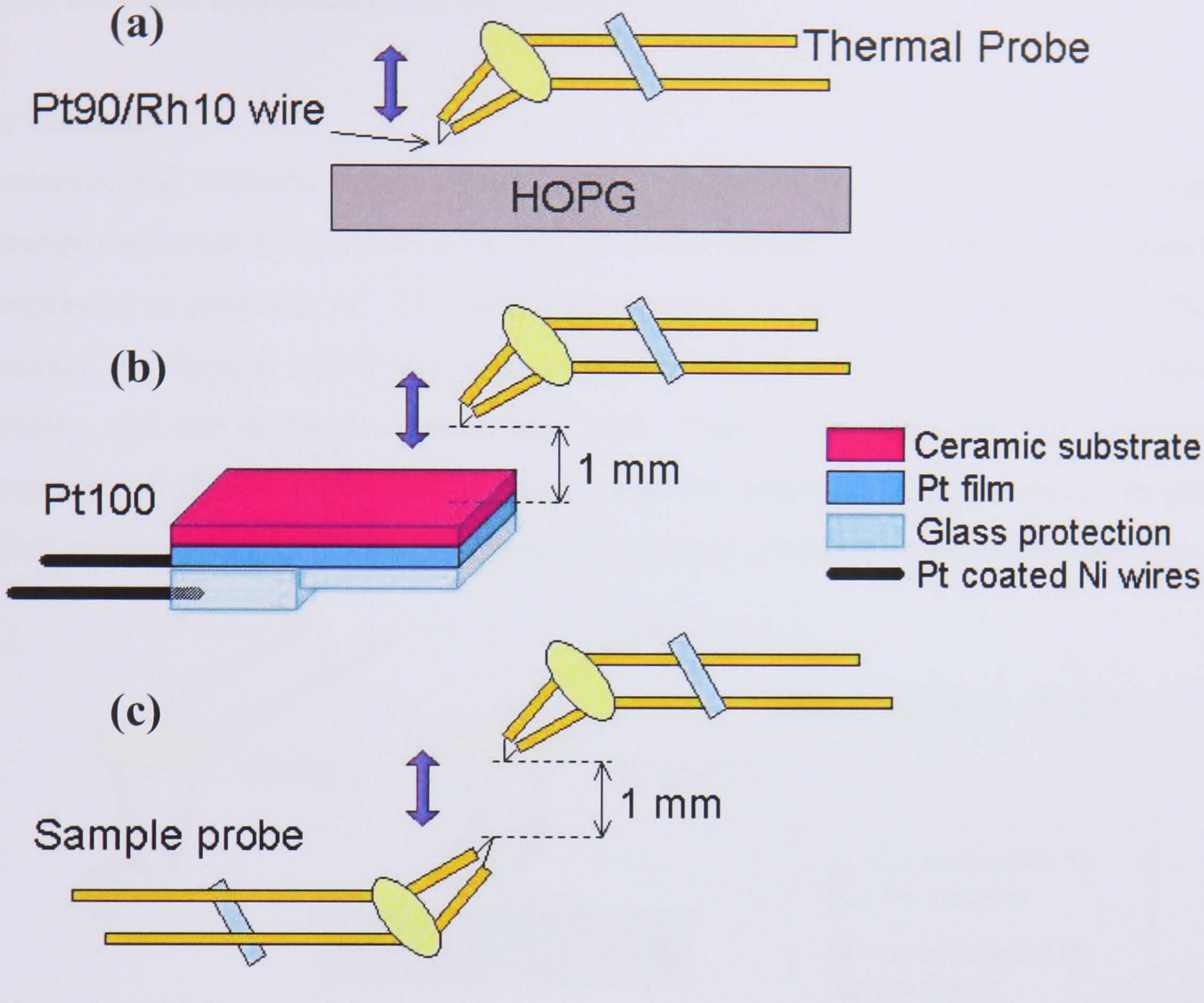



**Figure 3.13**: **(a)** diagram of the thermal probe lowered on graphite. **(b)** diagram of the thermal probe lowered on the Pt100 platinum resistance thermometer. The Pt100 was made of a ceramic substrate deposited on a platinum (Pt) film with lead wires of Pt coated Nickel. Under the Pt film was a glass layer to protect the film and the lead wires. The thermometer had a nominal resistance of 100 Ω at 0 °C and a temperature coefficient of 0.00385 $K^{-1}$. **(c)** diagram of the thermal probe lowered on another probe.

probe, respectively, were monitored simultaneously as the heat loss by the approaching probe. Measurements on samples i) and ii) were repeated in air (room pressure) and in high vacuum (pressure ~ $5\times10^{-5}$ mbar), measurements on sample iii) were taken in air only.

Before analysing the data acquired, all the possible sources of heat loss in the Veeco thermal probe both at room pressure (in air) and in vacuum are discussed (Fig. 3.14).

**In air.**

Radiative and convective heat losses can be assumed as negligible [Lefèvre'02]. Heat can be lost by: i) conduction through the air [Gomès'99], [Majumdar'99]; ii) conduction

into the capillary water layer due to moisture which is present on most substrates*; iii) conduction into the probe's supporting leads; iv) conduction into the sample – only when the probe is in contact with the sample.

**In vacuum.**

Radiative and convective heat losses are still negligible of course. Conductive losses through the air can be assumed as negligible as the thermal conductivity of air is greatly suppressed at pressures of ~$10^{-5}$ mbar (see Section 5.4 in Ref. [de Podesta'96]). This because the thermal conductivity of air is proportional to the air molecules number density and the molecules mean free path. These two parameters are inversely proportional: if the number density of air molecules decreases then the mean free path of air molecules increases; and this keeps the thermal conductivity of air constant over a

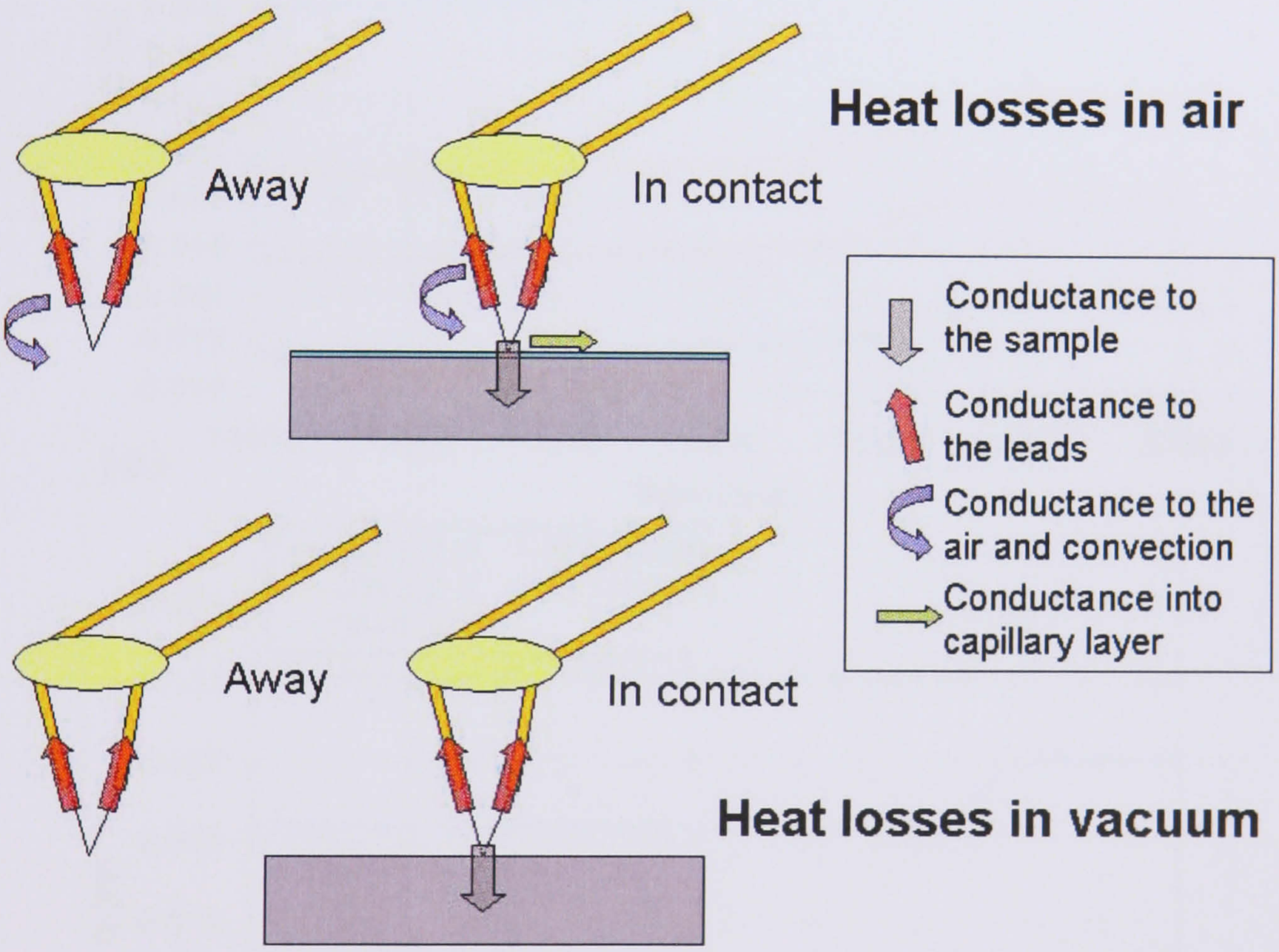



**Figure 3.14**: diagram of the sources of heat loss in the thermal probe in air and in vacuum.

large pressure range. However, when the pressure is so low that the mean free path of the air molecules is larger than the distance between the thermal probe and the sample, the air molecules will travel from one to the other without colliding with each other. In this regime, the thermal conductivity of the air will therefore be proportional to the probe-sample separation (a constant) and the air molecules number density

---

* Studies done by S. Gomes et al. [Gomès'99] however have shown that the effect of this capillary water layer is greatly reduced when the probe's temperature is above 100 °C as the layer evaporates when the probe contacts the substrate's surface.

(proportional to the pressure). Therefore for pressures lower than this 'threshold pressure' (of the order of $10^{-2}$ mbar for a separation of around one centimetre) the thermal conductivity of air will decrease linearly with pressure. Therefore, at the operating pressures of $10^{-5}$ mbar the thermal conductivity of air will be reduced by three orders of magnitude and this is why heat conduction through the air can be neglected. Conductive losses into the moisture-capillary water layer covering the substrate's surface can also be assumed as negligible because most of the layer evaporates in

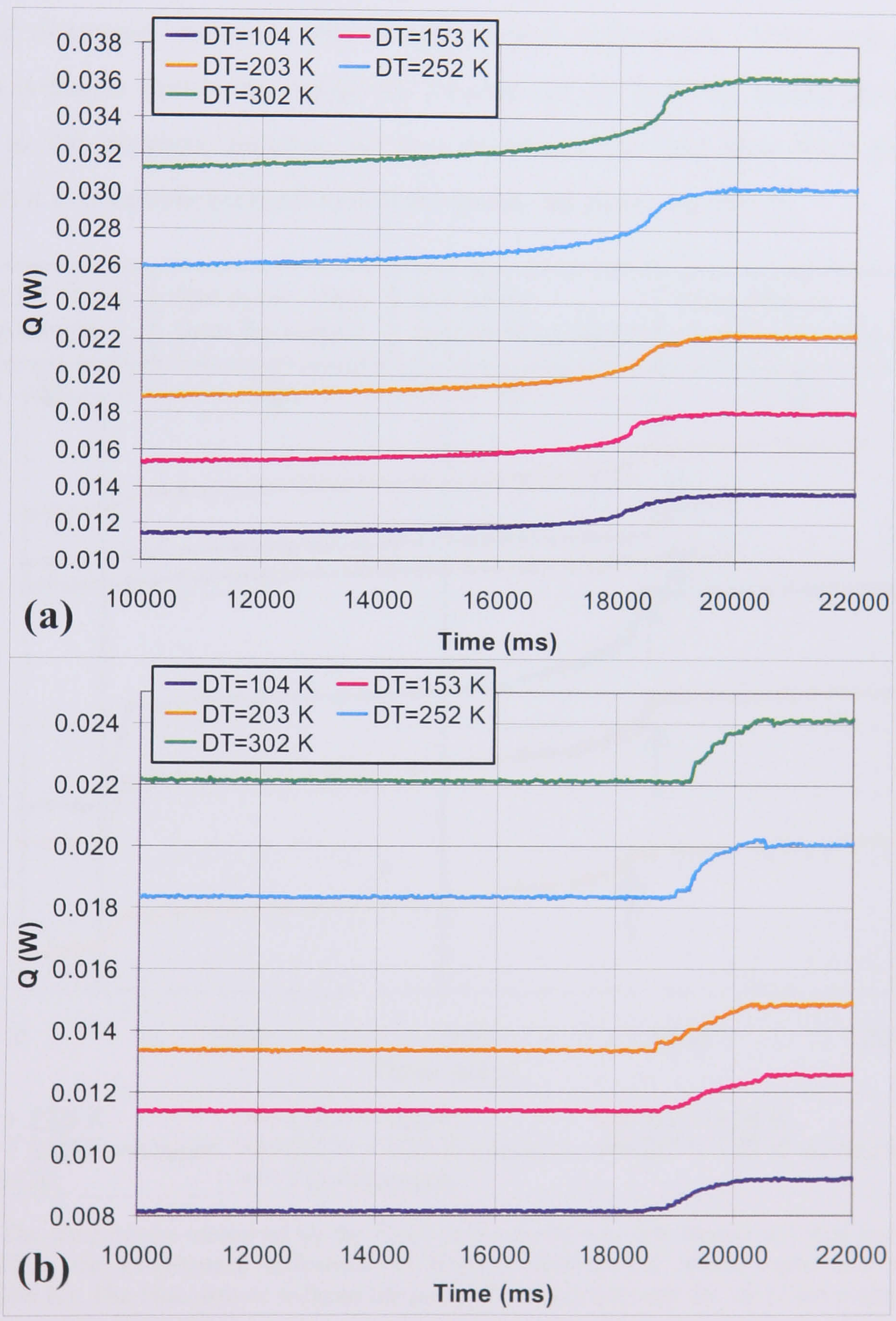



**Figure 3.15**: Heat lost by the Veeco thermal probe (in W) as it was lowered onto the HOPG sample, in air **(a)** and in vacuum **(b)**. The measurements were repeated at 6 different probe temperatures (see legends). DT indicates the temperature difference between the heated probe and room temperature (296 K) and is expressed in K.

vacuum. Heat can be lost only by: iii) conduction into the probe's supporting leads; iv) conduction into the sample.

**Data Analysis and Discussion**

Figures 3.15a and 3.16 show that, in air, there is probe-sample heat exchange *before* the probe comes in physical contact with the substrate. In Fig. 3.15a, the heat lost by the probe increases while the probe approaches the HOPG substrate, and in Fig. 3.16 the temperature of the Pt100 increases when the probe, placed 1 mm above the sample, is heated and increases more as the heated probe approaches. This probe-sample interaction is due to heat being conducted through the air from the heated probe to the substrate: as the distance between the two decreases the heat flow from the probe increases as it is inversely proportional to the probe-substrate separation.

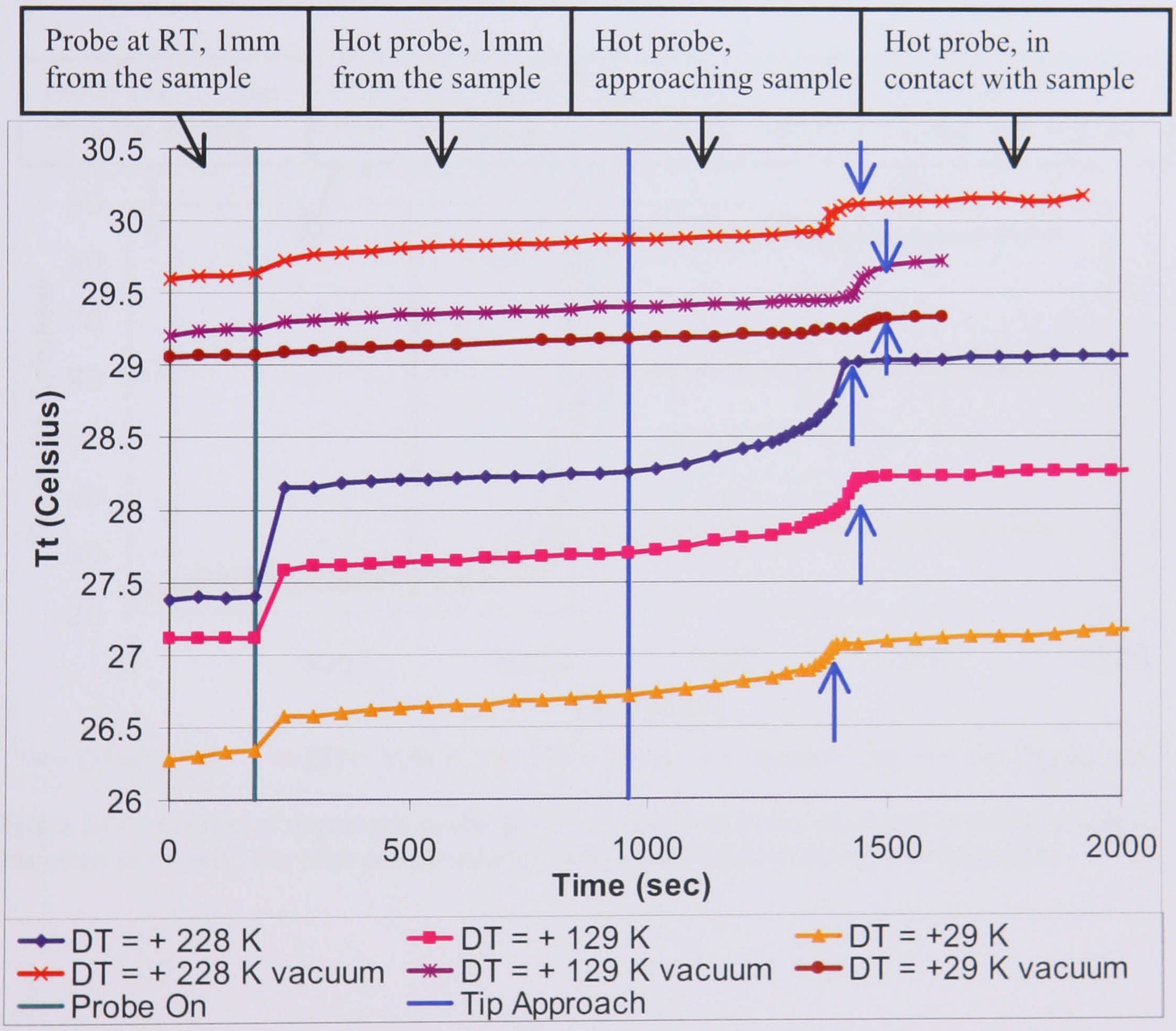



**Figure 3.16**: The temperature measured by the Pt100 as the probe was first heated and then lowered towards it. DT is the temperature difference (in Kelvin) between the heated probe and room temperature (296 K). The blue arrows indicate the point of contact between the tip of the probe and the sample.

The data in Fig. 3.17 show, however, that the effect of air conduction on the probe-sample heat exchange can be reduced, in air, by reducing the sample surface area (when the sample was the tip of another thermal probe, the surface area was only a few $\mu m^2$).

Therefore, for extremely small samples, heat conduction through the air can be neglected even at atmospheric pressure, but for larger samples this is not the case.
In vacuum however, there is no probe-sample heat exchange until contact is made between the probe and the sample (Figures 3.15b and 3.16). After contact the heat exchanged is proportional to the probe-sample contact area.

In order to quantify the amount of heat lost in the different modes the total heat lost by the probe heated at different temperatures, in contact and away from a graphite substrate was measured. The measurements were repeated in air and in vacuum (Fig. 3.18).
It was found that, at all temperatures, the amount of heat lost at atmospheric pressure was larger than the amount of heat lost in vacuum, both when the probe was in contact and when it was away from the graphite surface.

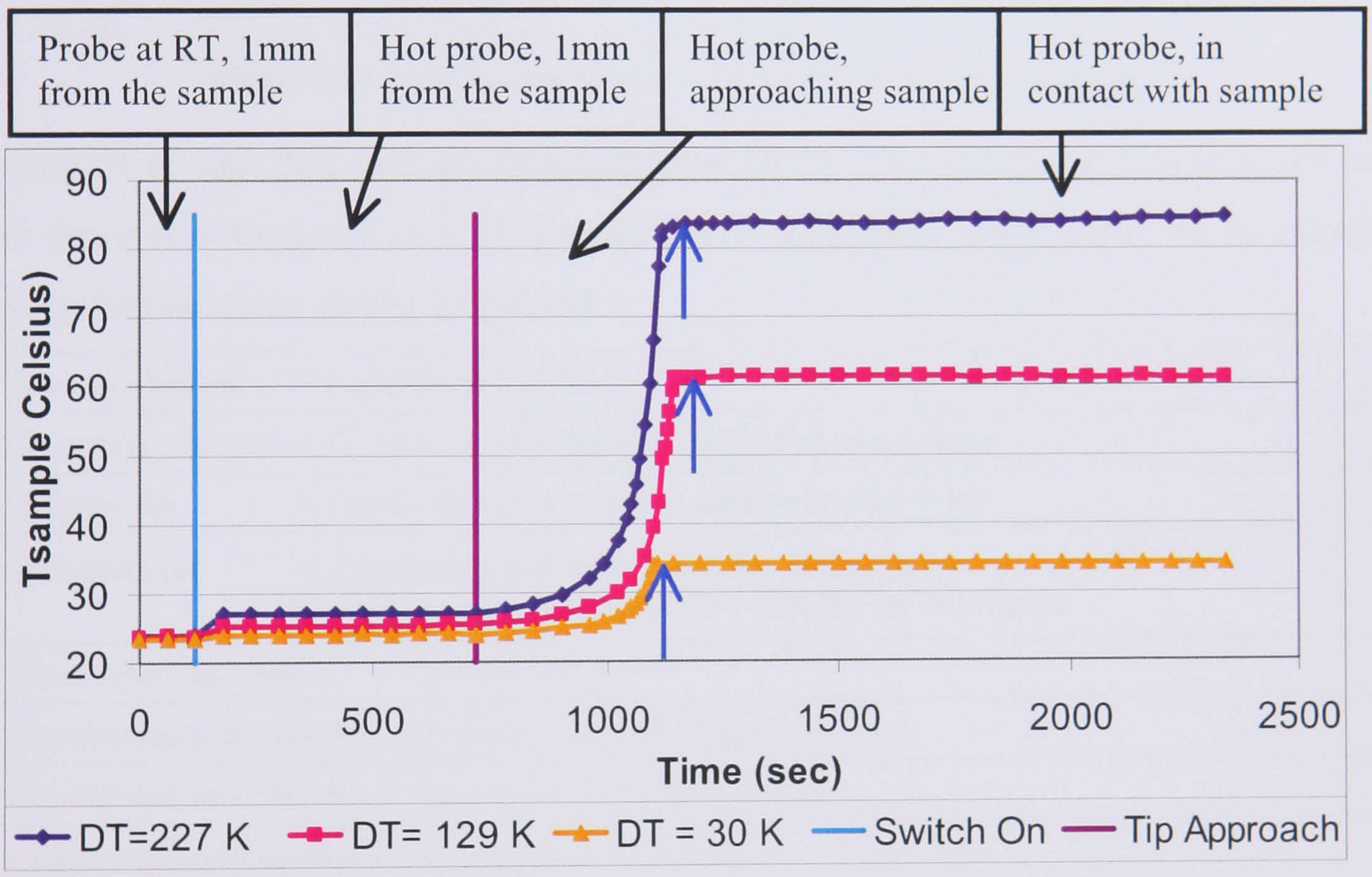



**Figure 3.17**: Heating of the sample probe as the hot probe was switched on and lowered towards it; data taken in air only. The blue arrows indicate the point of contact between the two probes.

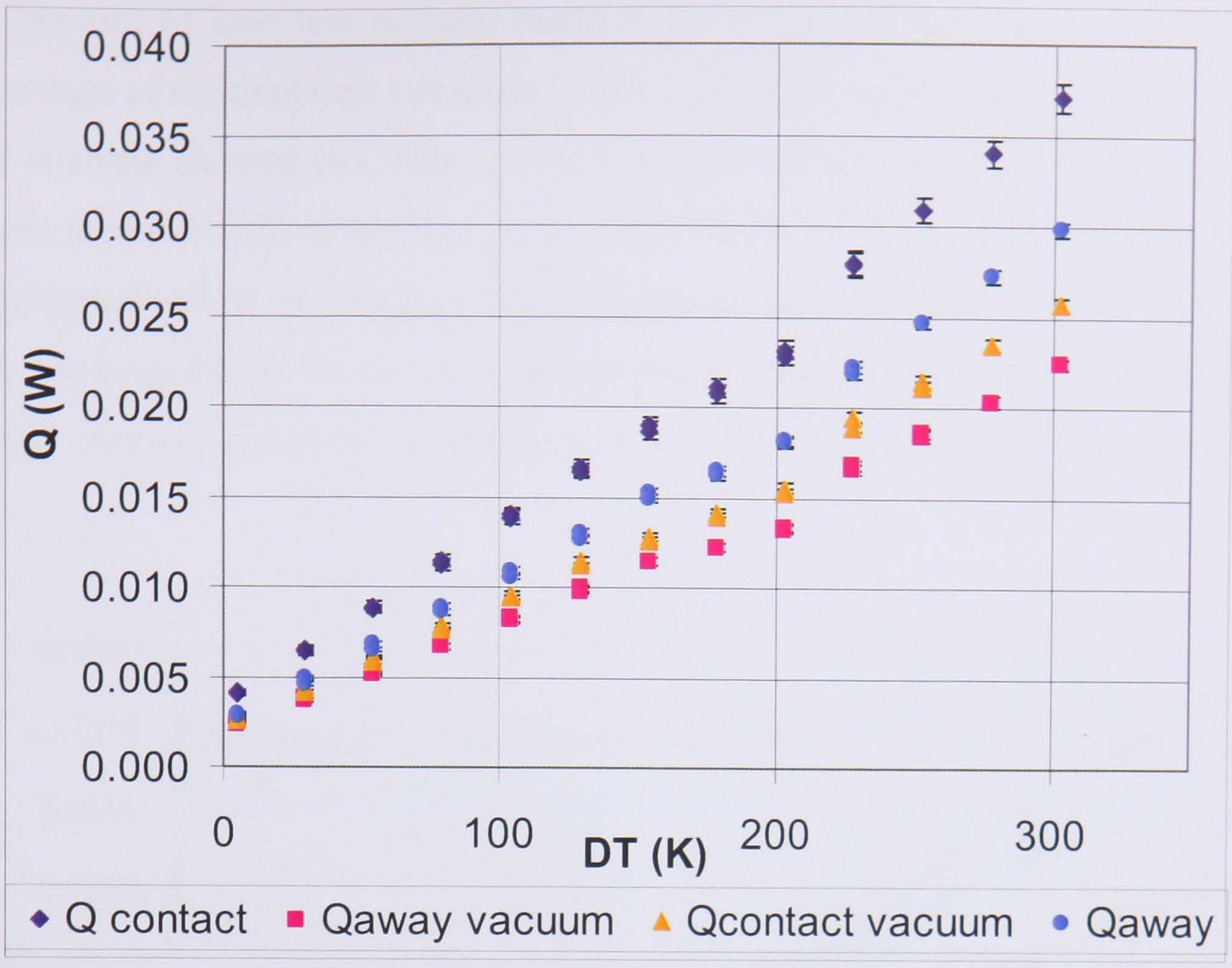



**Figure 3.18**: Measured heat losses on graphite in air and in vacuum.

Using these four data sets and assuming that all the sources of heat loss from the probe are those described in Fig. 3.14 the amount of heat lost in each mode can be calculated using the equations shown in Table 3.4.

| | |
|---|---|
| **Q away vacuum** | = Conduction into leads |
| **Q contact vacuum** | = Conduction into leads + Conduction into sample |
| **Q away air** | = Conduction into leads + Conduction into the air |
| **Q contact air** | = Conduction into leads + Conduction into air + Conduction into capillary layer + Conduction into the air |
| **Conduction into leads** | = Q away vacuum |
| **Conduction into sample** | = Q contact vacuum – Q away vacuum |
| **Conduction into the air** | = Q away air – Q away vacuum |
| **Conduction into capillary water layer** | = Q contact air – Q away air – (Q contact vacuum – Q away vacuum) |

**Table 3.4** The first 4 rows show the heat loss sources in each measurement condition. The Last 4 rows use the equations derived in the first 4 to calculate how much heat is lost by each of the mechanisms described in Fig. 3.14 using the data displayed in Fig. 3.18.

The amount of heat lost in each mode is shown in Fig. 3.19 and in Fig. 3.20 as a percentage of the total heat lost in air (3.20a) and in vacuum (3.20b).

This analysis showed that only a small fraction of the total heat loss was due to the sample (about 9-10% of the total in air, and 12-13% of the total in vacuum) while most of the heat was lost into the probe's leads (about 60% in air and up to 90% in vacuum). This was because the leads of the thermal probe were 15 times thicker than the probe's thermal element and made of silver (a very good thermal conductor – see also Table 3.3).

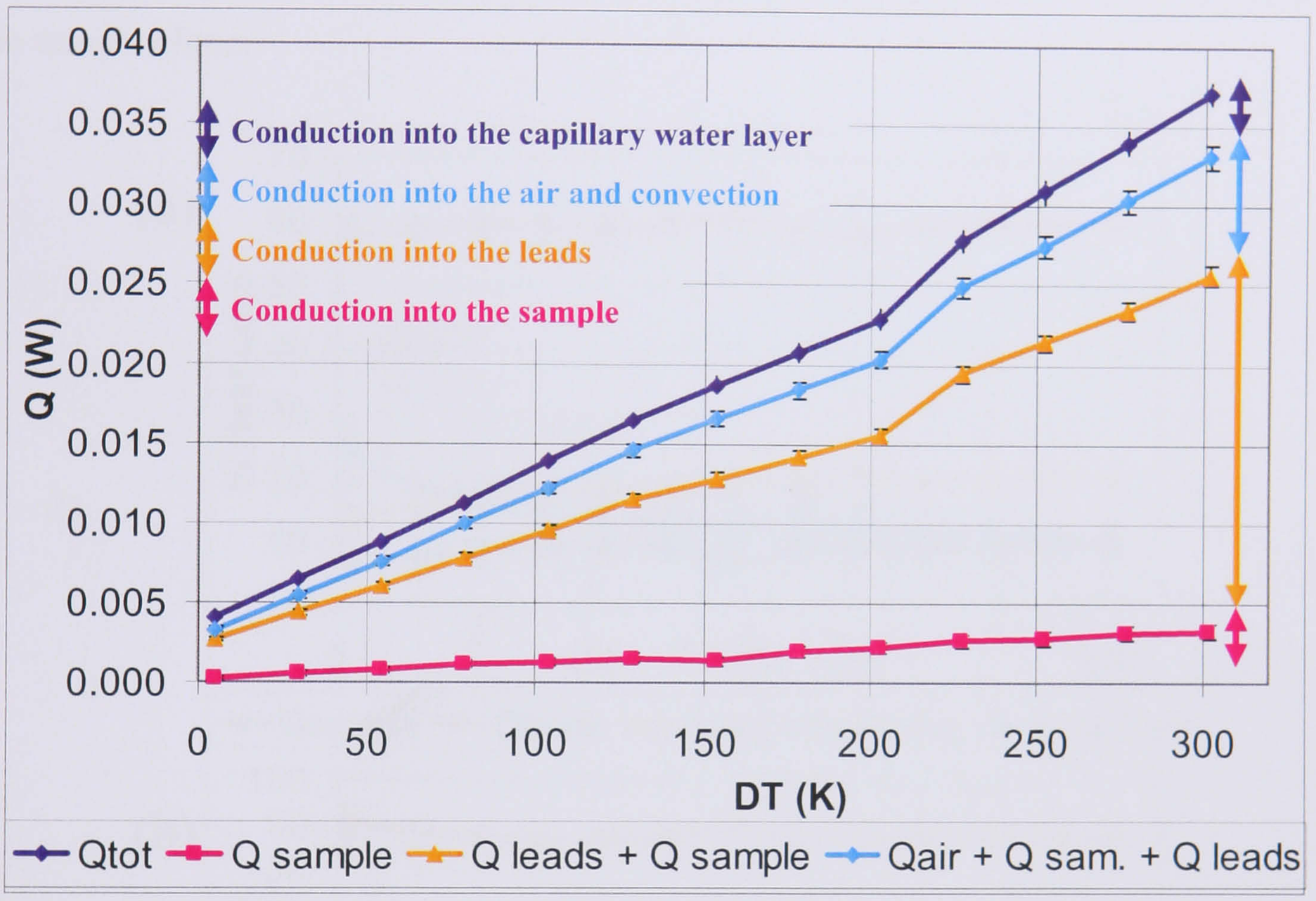



**Figure 3.19**: The data in Fig. 3.18 is used to calculate the amount of heat lost in each mode using the equations derived in Table 3.4.

Heat lost by conduction through the air amounted to up to 20% of the total and heat lost by conduction into the capillary water layer was over 20% of the total for low probe heating but quickly decreased as the probe temperature increased. This is in agreement with what was observed by S. Gomes et al [Gomès'99] and due to the fact that at high probe temperatures most of the moisture capillary water layer evaporates upon contact with the thermal probe.

This study of the probe-sample heat exchange showed that a large fraction of the thermal probe's heat loss is due to factors other than the sample itself (these are three: heat loss through the air, heat loss through the capillary water layer and heat loss through the probe's leads). This implies that in order to acquire thermal information of the sample these heat loss sources need to be either eliminated or measured and subtracted out. The solution proposed in this study is to work in vacuum; this eliminates two of the three heat loss sources (heat loss through the air and through the capillary water layer) and allows a measurement to be done of the third (heat loss through the probe's leads) which is subtracted from the total to obtain the amount of heat loss due to the sample alone.

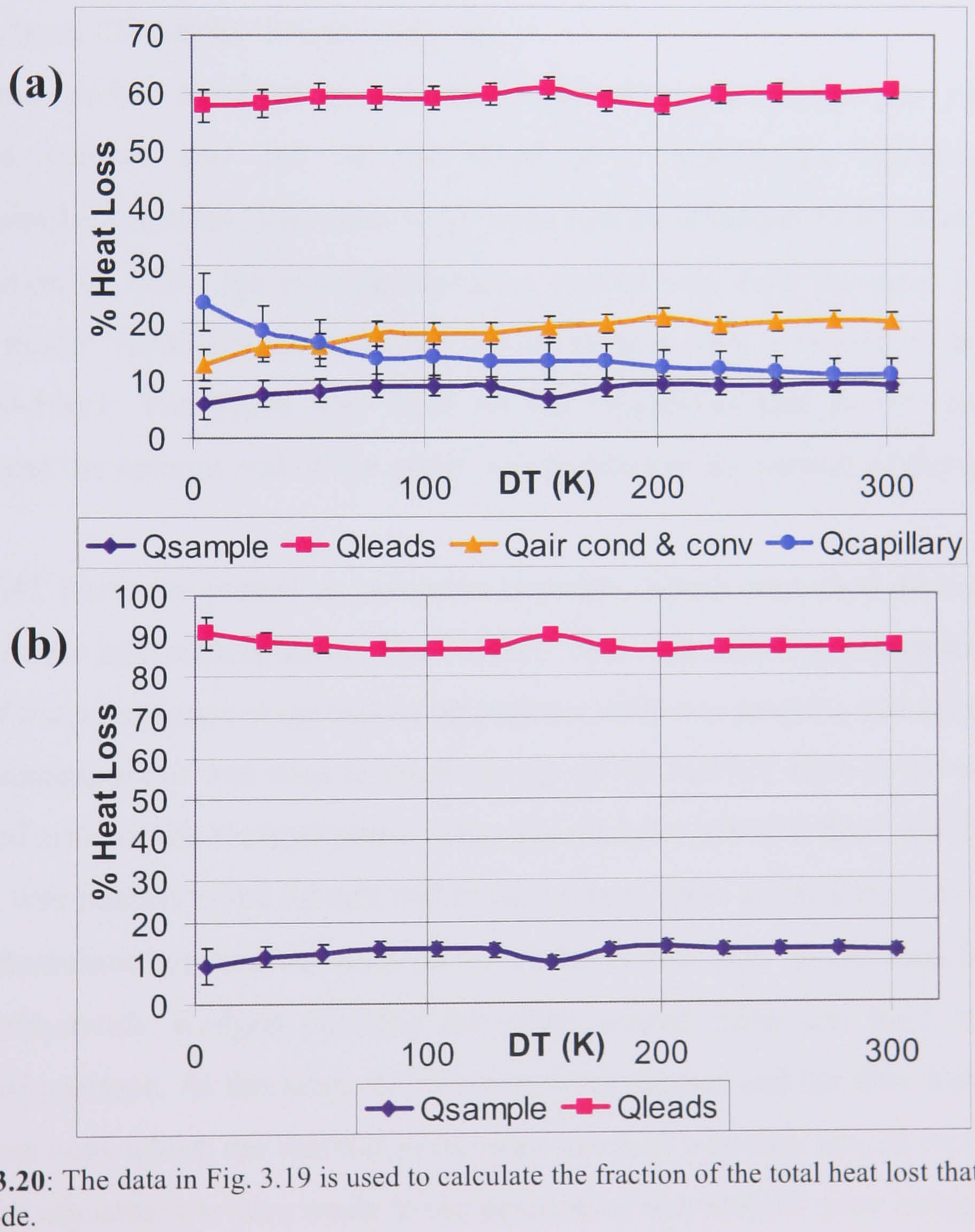



**Figure 3.20**: The data in Fig. 3.19 is used to calculate the fraction of the total heat lost that is lost in each mode.

## 3.5 Attaching an MWNT Fibre to the Thermal Probe

In order to acquire simultaneous data on the thermal and electrical conductance of MWNTs, an MWNT fibre had to be mounted on the Veeco thermal probe. This had to be done without damaging the thermal element of the probe.

MWNT fibres are needle-like agglomerates of bundles of MWNTs typically 3-5 mm in length and 50 μm in diameter, and can be handled using a pointed pair of tweezers*. The thermal probe is also quite large (see Fig. 3.11 and Table 3.2); the two silver-coated arms that form the backbone of the probe taper at the tip: the arms separation smoothly decreases from 120 μm to <20 μm at the tip.

The thermal probe, mounted on a semi-circular magnetic holder, was placed on a permanent magnet and put on the stage of a microscope equipped with a micromanipulator system. The microscope used was an Olympus SZ40, with maximum magnification of 240×; the micromanipulator system was from Research Instruments Limited, model TLO5000, and allowed 3D movement with a reduction factor in the range 100-500:1. The probe was fixed on the magnet so that its tip was pointing upwards and the tapered end of the probe was parallel to the surface of the microscope stage.

The MWNT fibre was picked up using the tweezers, which were then placed in one of the arms of the micromanipulator. The MWNT fibre was standing perpendicular to the surface of the microscope stage and its tip (thinner end) was pointing upwards.

The micromanipulator was used to insert the tip of the MWNT fibre at the wide end of the tapered arms of the thermal probe. Once inserted the MWNT fibre, still held by the tweezers, was pushed to the thinner end of the tapered arms of the probe. At the thinner end the separation between the arms of the probe is less than 20 μm thus the MWNT fibre is effectively wedged between the silver coated arms and held in place by mechanical pressure. At this stage the tweezers were opened and the fibre was released. The magnet onto which the thermal probe was attached was then placed on its side and further fine adjustments were made to the position of the MWNT fibre using the tips of the tweezers. This was to ensure that the MWNT fibre was firmly held between the arms of the thermal probe and that it was going to be as perpendicular as possible to the sample surface once the thermal probe was mounted on the AFM.

---

* The best tweezers for handling the MWNT fibres were found to be the Dumostar ® high-precision, non-magnetic tweezers, Dumont style 5.

A schematic diagram of the initial position of the thermal probe and the MWNT fibre, the insertion process of the fibre in between the arms of the thermal probe and a photo of the final product are shown in Fig. 3.21.

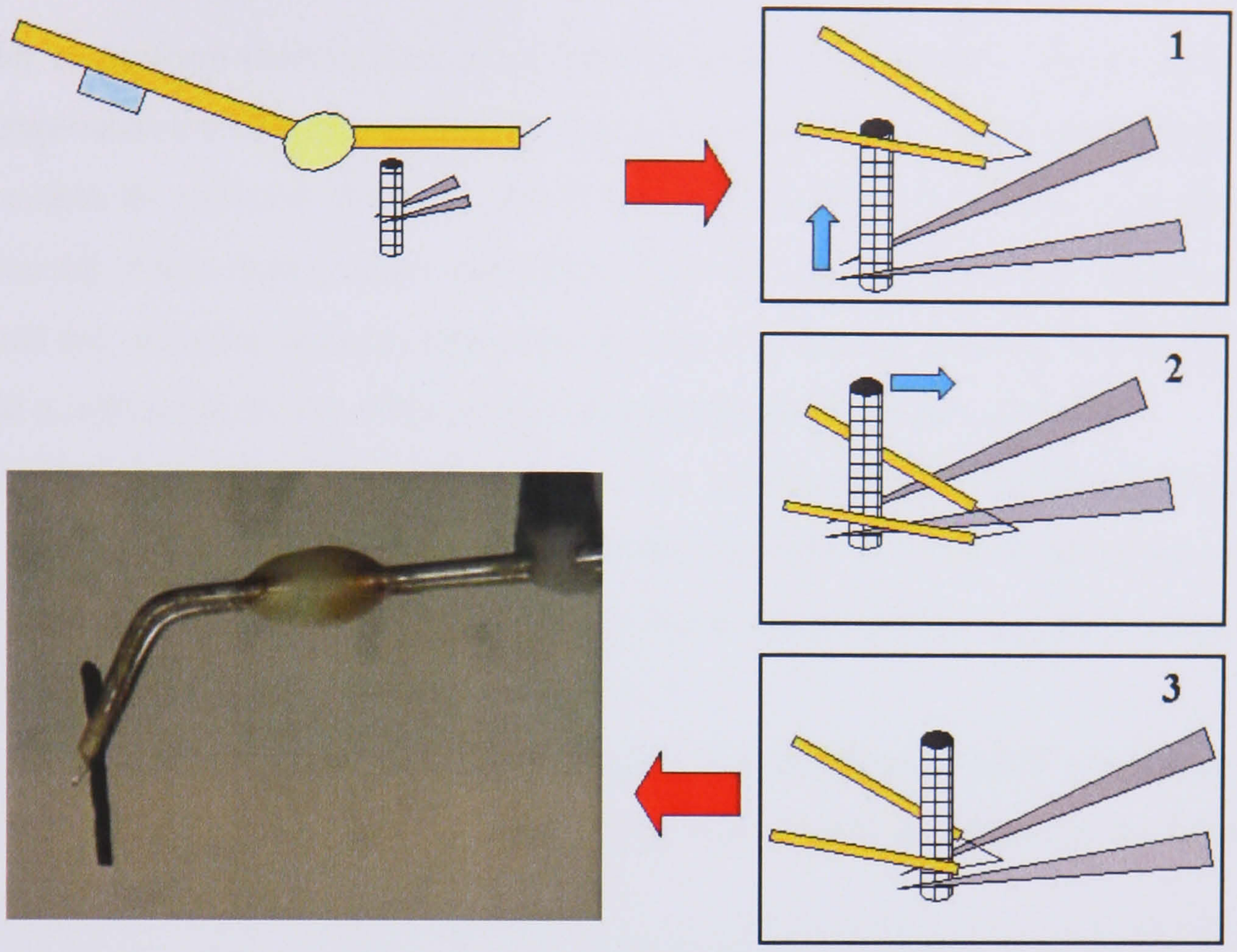



**Figure 3.21**: Top-left: diagram showing the initial positions of the thermal probe and the MWNT fibre held in the tweezers. In rectangles numbered 1-3 are three diagrams showing how the MWNT fibre was inserted in between the arms of the thermal probe and pushed to the thinner end of the probe. Bottom-left, a photo of the final product (Tip I2b, on thermal probe N17).

It was important to place the fibre as close as possible to the very end of the silver-coated arms but this had to be done without pushing the MWNT fibre all the way to the thin Pt90/Rh10 V-shaped tip of the thermal probe. This would damage the tip itself (i.e. the resistive element of the thermal probe) thus compromising the operation of the probe; also, it was found that the tip was not solid enough to hold the MWNT fibre firmly causing the fibre to move during the measurement acquisition.

The MWNT fibre, using this method, could be placed in close proximity to the thermal element of the probe; this technique also ensured good thermal contact between the silver coated arms of the probe and the fibre itself. Adding to this the fact that Ag is a good thermal conductor, it was thus assumed that the temperature at the probe-fibre interface would be the same as that of the thermal element of the probe when this was heated.

## 3.6 Building a Variable Temperature Sample Stage for the AFM

In order to perform thermal and electrical transport measurements on the MWNTs at low temperatures a variable temperature sample stage for the Explorer AFM was built to fit within the vacuum chamber. Since the AFM would not operate at temperatures significantly lower than room temperature (because the piezos in the AFM were not designed for operation at cryogenic temperatures and risked cracking) it was necessary to build a cold stage for the AFM samples thermally isolated from the AFM.

The key design parameters for such a stage were: a) ability for the AFM sample to reach liquid nitrogen temperatures (i.e. ~77 K) whilst ensuring that the AFM stayed at room temperature; b) low stage vibration during the cooling process; c) good temperature stability while at cold temperatures.

The cooling element chosen for the cold stage was an Ultrastat UHV continuous flow cryostat from Oxford Instruments given that it was already available in the laboratory (see Fig. 3.22).

A diagram of the stage is shown in Fig. 3.23 and in Table 3.5 are shown the thermal properties of some of the materials used in the cold stage. At the core of the cold stage is a copper cylinder with a square base, this is cooled by the cryostat via flexible copper braids and is insulated thermally from the rest of the stage by its supporting stainless steel rods. In vacuum, this enables the copper to be cooled while the rest of the stage stays at room temperature. The sample is placed on the top of the copper cylinder and can thus be cooled, while the AFM is placed on the bulk of the stage and remains at room temperature. The use of flexible copper braids to connect the cryostat to the copper structure limits the transfer of vibration from the cryostat to the sample. Once cooled, the copper structure, due to its mass, remains at a constant temperature even if there are temporary changes in the temperature of the cryostat due to fluctuations in the flow of nitrogen, this thus ensures that the temperature of the sample remains stable.

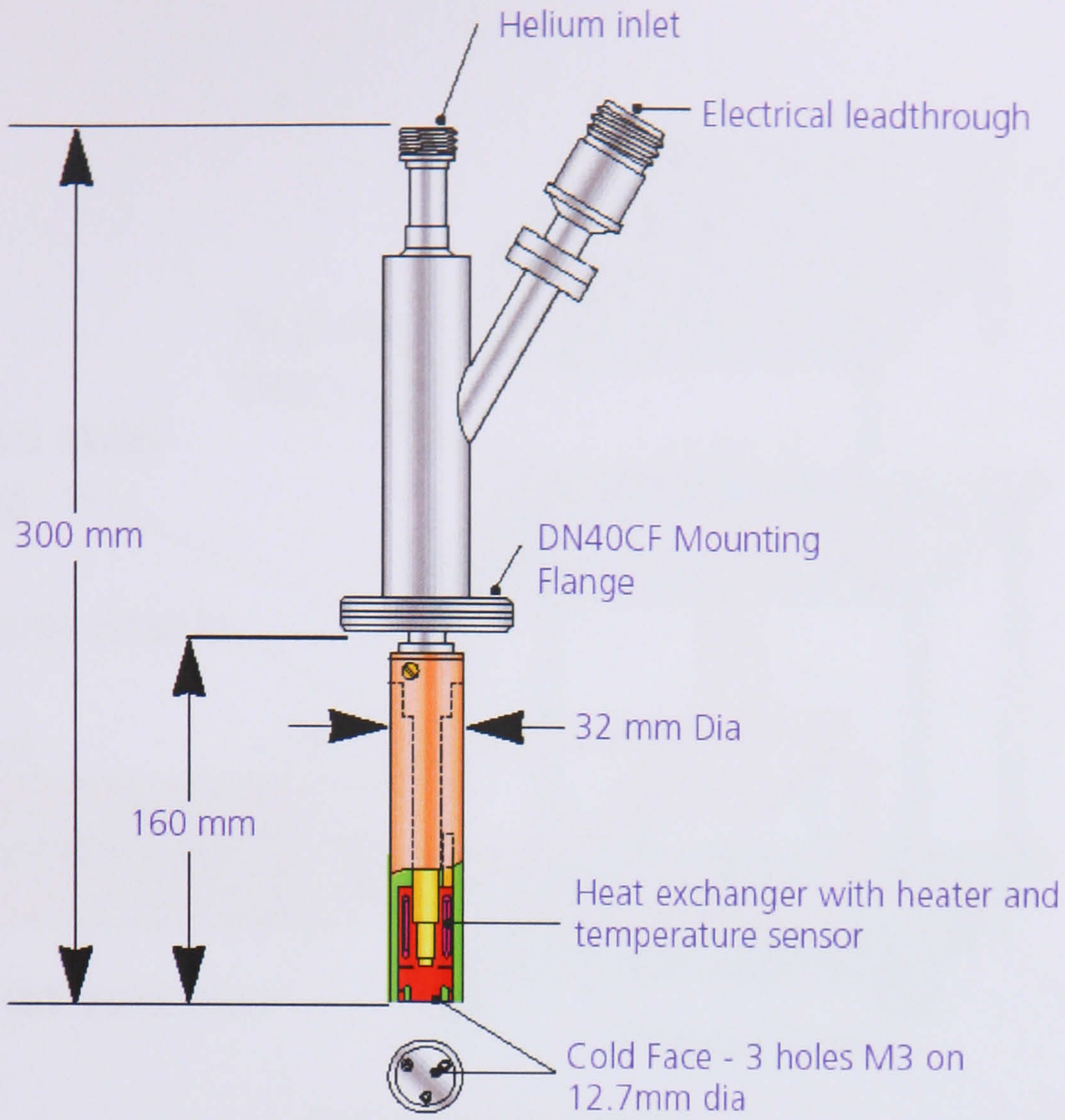



**Figure 3.22**: Diagram of the Ultrastat Continuous flow Cryostat from Oxford Instruments (taken from the Oxford Instruments product guide – see www.oxford-instruments.com. The cryostat could be operated with liquid Helium or liquid Nitrogen. In this work, liquid Nitrogen was used. The cold face of the cryostat was connected to the copper base of the cold stage by copper braids (see Fig. 3.23). A Pt100 resistance thermometer was glued to the cold face of the cryostat to monitor its temperature while cooling.

The stage was built using two solid Aluminium plates (from NewPort, SA Series, model: M-SA-08×08), 200×200 mm in size and 13 mm thick. The plates had 8 rows of 8 holes, all with M6 thread. The lower plate was fitted with 4 anti-vibration levelling feet (made of natural rubber, bought from RS, model: 257-8640), 18 mm in height; the feet were fitted with a zinc plated steel M6 screw to fix them on the Al plate. This was done to prevent the vibrations from the base of the vacuum chamber being transmitted to the cold stage.

The two Al plates were held together by 4 A4 stainless steel studding (with stainless steel washers and bolts), 160 mm long, with M6 thread (from RS). The top plate had a 35 mm diameter hole drilled in the centre for the insertion of the copper stage.

The copper stage was formed of two parts: i) a square copper base, 67 mm in size and 10 mm thick with a threaded hole in the centre ~12 mm in diameter; ii) a cylindrical copper rod, 12 mm in diameter and 120 mm long. The lower end of the rod had a thread that fitted in the threaded hole in the middle of the copper base. The top surface of the rod fitted through the hole on the top Al plate and on it was placed the sample to be cooled. These copper elements were designed and built specifically for this work.

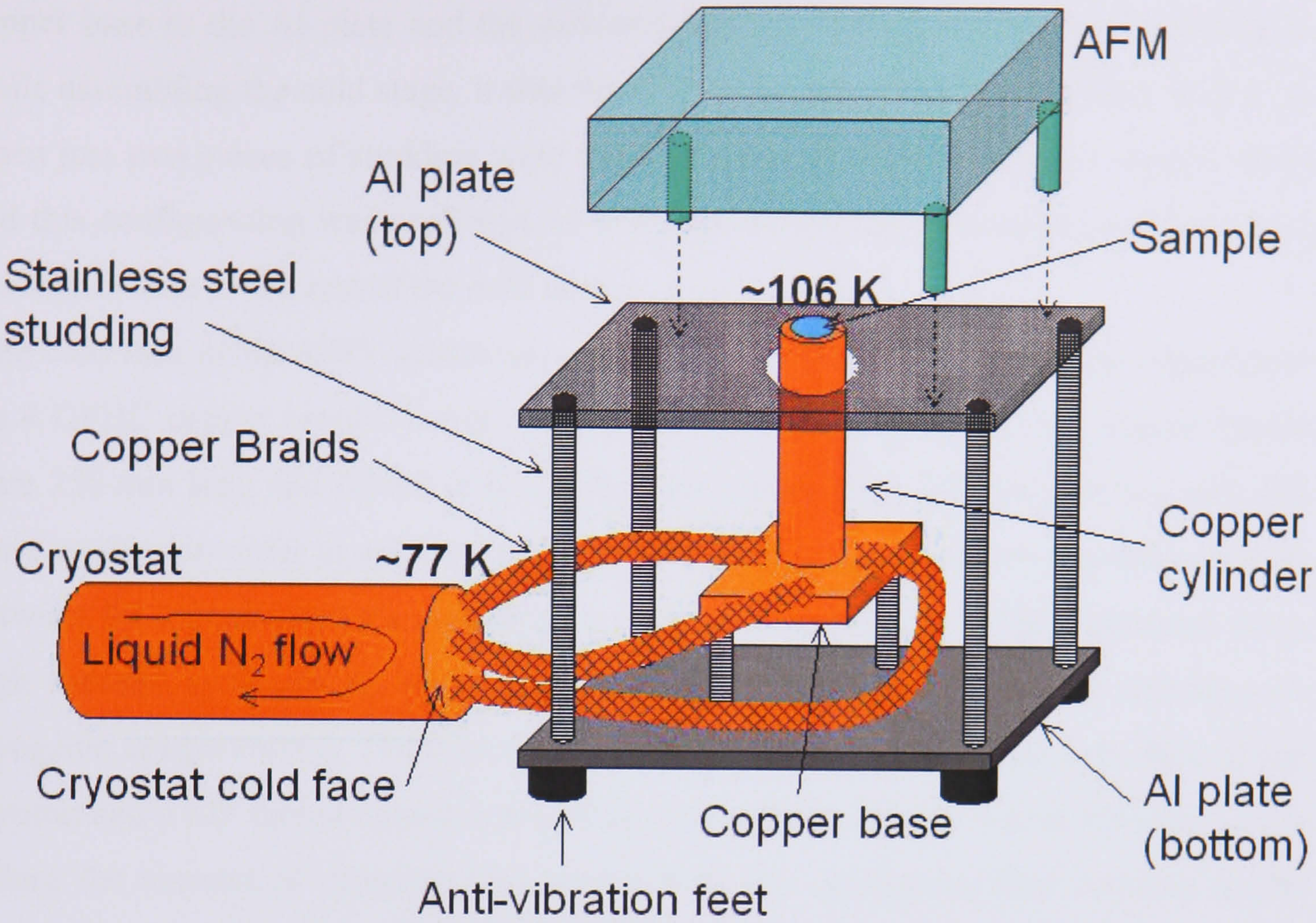



**Figure 3.23**: Diagram of the cold stage. The backbone of the stage are two Al plates held in place by stainless steel studding, the core of the cold stage is a copper cylinder with a square base. This is connected to the cryostat via flexible copper braids and is supported onto the stage by stainless steel studding. The sample is placed on the top of the copper cylinder, while the AFM is placed on the top Al plate – isolated from the copper cylinder. The flexible braids limit the transport of vibration from the cryostat to the sample. The anti-vibration feet also provide some vibration isolation of the whole cold stage. The stainless steel studding, chosen because of its poor thermal conductivity, insulates thermally the copper core from the Al plates (and thus the AFM).
With liquid nitrogen in the cryostat the top of the cylindrical copper rod (where the sample was placed) could be cooled to just above 100 K.

| | **$\kappa$ (W $m^{-1}$ $K^{-1}$) at 273.2 K** | **$\kappa$ (W $m^{-1}$ $K^{-1}$) at 100 K** |
|---|---|---|
| **Copper (Cu)** | 400 | 480 |
| **Aluminium (Al)** | 228 | 295 |
| **Stainless Steel** | 14.5 | 11.5 |
| **Brass** | 106 | 70 |
| **Phosphor Bronze wire*** | 50-75 (at 298 K) | -- |

**Table 3.5**: The thermal conductivity $\kappa$ for some of the materials used in the cold stage at 0°C and at 100 K. All the data is from Kaye and Laby Online – www.kayelaby.npl.co.uk apart from the data for Phosphor Bronze wire which is from Goodfellows – www.goodfellows.com. The resistivity of the phosphor bronze wire is 11-16 μΩ cm at room temperature, while that of copper is 1.69 μΩ cm (data from Goodfellows).

The copper base also had 4 M6 thread holes at each corner; these were used to fix the copper base above the lower Al plate using the stainless steel studding (and stainless steel washers and bolts). Stainless steel was chosen because of its poor thermal

conductivity, in order to limit the amount of heat lost by conduction from the cold copper base to the Al plate and the surroundings (at room temperature). Furthermore, while assembling the cold stage, it was found that the copper base was firmly held even when just two pieces of studding were used (diagonally opposite, on the copper base), and this configuration was preferred, as it would reduce the amount of heat flow from the copper base to the rest of the cold stage.

The cold face of the UHV continuous flow cryostat was connected to the copper base via 4 OFHC copper braids (Caburn MDC, reference OFHC6-1000). The copper braids were 250 mm long and folded in half, they were fixed using M3 brass screws with M3 brass washers in order to achieve good contact and hence improve the thermal transport between the cryostat and the copper base. The contact area was further enhanced using high thermal conductivity vacuum grease (Apiezon N grease - which solidifies at cryogenic temperatures). There were 3 M3 thread tapped holes on the cold face of the cryostat and 4 M3 thread tapped holes on the copper base. Copper braids were chosen to reduce the amount of vibration transmitted from the continuous flow cryostat to the copper base (the vibration was caused by the liquid gas flow in the cryostat).

The UHV continuous flow cryostat was equipped with a CF flange for mounting to an UHV chamber, thus it was connected to one of the KF flanges in the feedthrough collar of the vacuum chamber using a CF to KF adaptor (Caburn MDC, reference ST40-K40). The adaptor was 51 mm long and thus the top of the heat exchanger protruded approximately 80 mm inside the vacuum chamber.

The assembly of the cold stage within the vacuum chamber was as follows:

i) the lower Al plate with the 4 anti-vibration feet was placed on the base of the vacuum chamber;

ii) the cryostat was mounted on one of the feedthroughs of the feedthrough collar of the vacuum chamber, placed on top of the chamber base;

iii) the copper stage, with the base and rod assembled, was fixed above the lower Al plate using two stainless steel studding;

iv) the cold face of the cryostat was connected to the copper base using 4 copper braids;

v) the second Al plate was fixed above the other using 4 stainless steel studding, the copper rod protruded through the second plate's central hole;

During the assembly 3 Pt100 resistance thermometers (from RS, model 362-9834) were fixed on: i) the cold face of the cryostat; ii) the copper base; iii) the top of the copper rod. They were glued to the surfaces using G-Varnish and wired using phosphor bronze

wire in a 4-lead configuration (two twisted pairs). The phosphor bronze wire was from LakeShore (Quad Twist™, 36 AWG), and was used to minimize the heat leak into the sensor (phosphor bronze wires have much lower thermal conductivity than copper wires, but also higher resistivity – see Table 3.5 and caption – hence the need to make a 4-wire resistance measurement on the Pt100 thermometers). These thermometers were used to monitor the change in temperature of the different parts of the cold stage during the cooling process. A fourth Pt100 thermometer was glued on the side of the AFM tip holder and wired up in the same way; this was used to monitor the temperature of the AFM during cooling to ensure that the AFM stayed at room temperature.

In order to estimate the cooling curve for the copper stage, a simple lump capacitance model was used assuming that no heat was lost due to convection (given that the system was in vacuum) and that the temperature of the cryostat cold face was constant.

In this model the rate of change of the internal energy of the copper stage ($\Delta Q_{st}$) was given by the rate of heat entering the system ($Q_{in}$ – due to radiation and conduction through the stainless steel studding) minus the rate of heat leaving the system ($Q_{out}$ – due to conduction through the copper braids):

$$Q_{in} - Q_{out} = \Delta Q_{st} \qquad (3.9)$$

in detail (3.9) becomes:

$$A_{tot}\varepsilon\sigma\left(T_{sur}^4 - T^4\right) + \frac{k_s(T)A_s}{L_s}\left(T_{sur} - T\right) - \frac{k(T)A}{L}\left(T - T_c\right) = \rho V C_p(T)\frac{dT}{dt} \qquad (3.10)$$

where:

$A_{tot}$ = total surface area of Cu stage

$\varepsilon$ = emissivity of copper

$\sigma$ = Stefan Boltzmann constant

$T_{sur}$ = room temperature

$T$ = temperature (variable)

$k_s(T)$ = thermal conductivity of stainless steel (temperature dependent)

$A_s$ = contact area between steel studding and Cu stage

$L_s$ = length of steel studding

$k(T)$ = thermal conductivity of Cu braids (temperature dependent)

$A$ = contact area between Cu braids and Cu stage

$L$ = length of Cu braid

$T_c$ = temperature of the cryostat cold face

$\rho$ = density of Cu

$V$ = total volume of Cu stage

$C_p(T)$ = specific heat capacity of Cu (temperature dependent)

$t$ = time (variable)

The first term on the left side of equation (3.9) is the heat flow *into* the copper stage due to radiation from the surroundings (at room temperature); the second term is the heat flow *into* the stage due to conduction from the stainless steel studding (whose ends are at room temperature) and the third term is the heat flow *out* of the stage due to

conduction through the copper braids (whose ends are at the temperature of the cryostat cold face). The term on the right represents the rate of temperature change in the copper stage.

The equation was solved numerically using MathCAD and the results were compared to experimental data. One example is shown in Fig. 3.24. In this case both the temperature of the Cu base and that of the cold face of the cryostat were monitored. The temperature of the cold face was measured to plateau at ~90 K and the comparison between the model and the data is limited to the portion of the curve acquired when the temperature

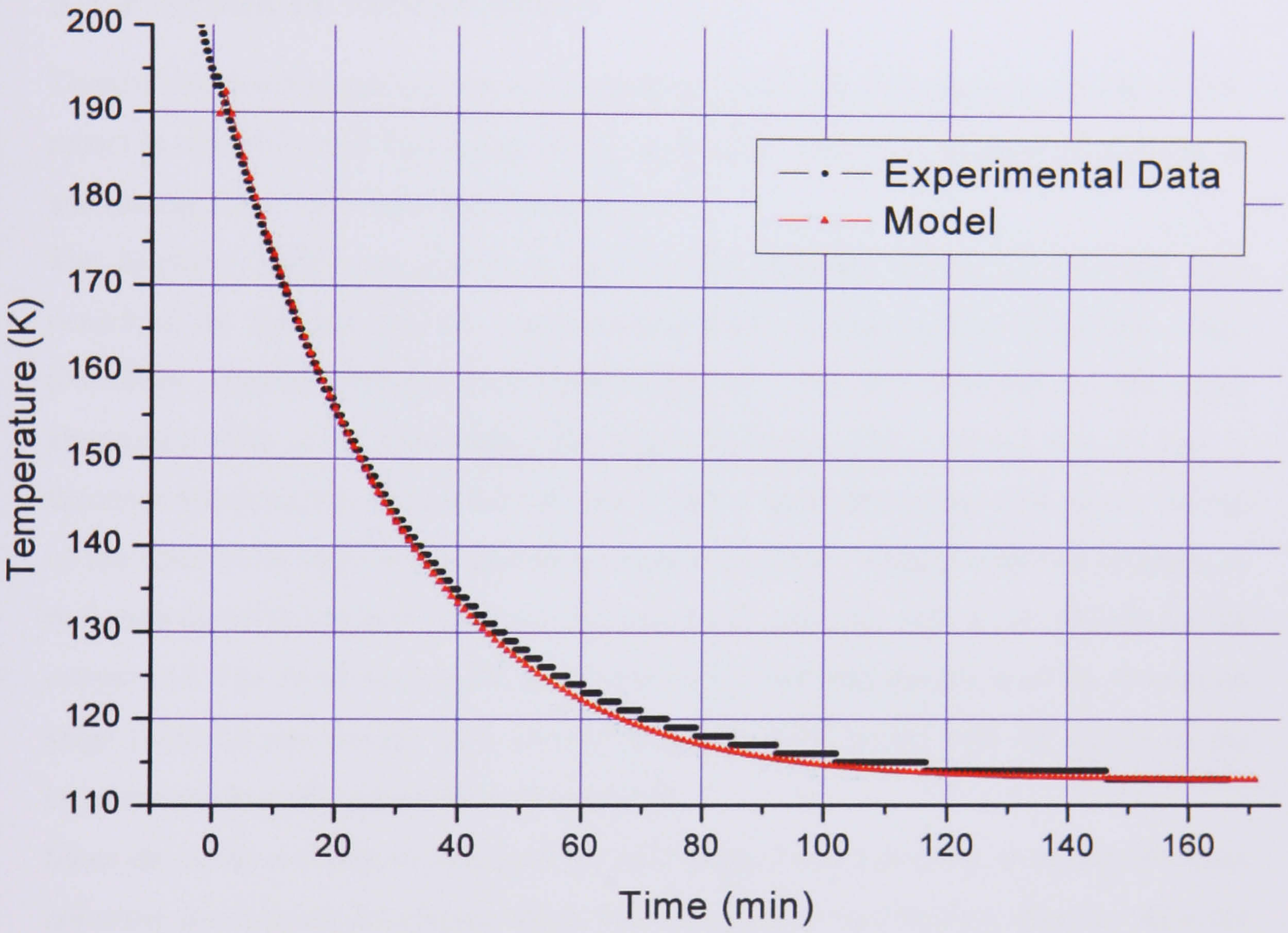



**Figure 3.24**: Graph comparing the experimental cooling data measured on the Cu base with a Pt100 resistance thermometer (black circles) with the data from the lumped resistance model (red triangles). The best fitting values for some of the parameters are used. The good agreement proves that the assumptions made in the model are realistic.

of the cold face had reached its minimum value (time = 0). The agreement is remarkable* indicating that the model correctly assumes the sources of heat gain and heat loss affecting the Cu stage.

---

* Two of the parameters in equation (3.9) had to be estimated. The emissivity of Cu varies from 0.023 for polished Cu to 0.78 for oxidised copper. In Fig. 24 the value of 0.75 was chosen given that the Cu used for the stage is rather tarnished. The contact area between the Cu stage and the Cu braids is also an estimate. The value chosen in Fig. 3.24 (for a best fit) is 2.5 $cm^2$, which is within the expected range.

Details on the MathCAD programme used to solve equation (3.9) can be found in Appendix A.

## 3.7 Experimental Set-up for Simultaneous Thermal and Electrical Conductance Measurements

### 3.7.1 At Room Temperature

Thermal conductance measurements were performed in high vacuum (pressures $\leq 5\times10^{-5}$ mbar) in order to avoid heat being lost by convection and/or conduction through the air and the capillary water layer (see Section 3.4.1).

The Explorer AFM was placed in the vacuum chamber on top of the cold stage described in Section 3.6. A vacuum-compatible manual linear translation stage (NewPort, UMR8A Series, model M-UMR8.51A V6) was screwed on the upper aluminium plate of the cold stage. The translation stage had a central hole 25 mm in diameter allowing it to fit around the copper rod at the centre of the cold stage. On top of the translation stage was screwed an aluminium plate, shaped with two recesses as the original AFM-Explorer base (see Section 3.1.2) and also with a central hole for the copper rod. The AFM was placed on top of this Al plate and the screw of the translation stage (with 10 μm thread) was used to align the AFM probe with the centre of the copper rod where the sample was to be placed.

Since the AFM was placed on top of the cold stage it was necessary to modify the laser adjusting mechanism developed when first operating in the vacuum chamber with the AFM placed on the chamber base. The feedthrough-rod system described in Section 3.2 was modified using two L-shaped right angle drive boxes (RS, stock number: 748-437). These drives had two perpendicular gearboxes, with ratio 1:1, to change circular motion along one axis to circular motion along another axis at a 90° angle to the original one. One drive box was attached to the feedthrough rod using a hollow cylinder of PTFE which was shaped to fit tightly both to the end of the rod and to the gearbox of the drive – the horizontal circular motion on the rod was thus changed to vertical circular motion. The drive was then connected to a second drive (fixed to a metal support on the top aluminium plate of the cold stage) using another PTFE hollow cylinder to recover the initial horizontal circular motion of the rod. On the other gear of this second drive was

then fixed the T-shaped PTFE structure that together with the U-shaped PTFE structure on the laser-mirror knob allowed the laser position of the AFM to be adjusted from outside the vacuum chamber. A diagram of this mechanism is shown in Fig. 3.25. This modification of the laser-adjusting mechanism made it impossible though to move the feedthrough rod in and out of the vacuum chamber, only the rotational motion was possible. Also, in this arrangement the rod was in contact with the stage where the AFM was positioned thus allowing for vibrations in the rod to be transferred to the AFM.

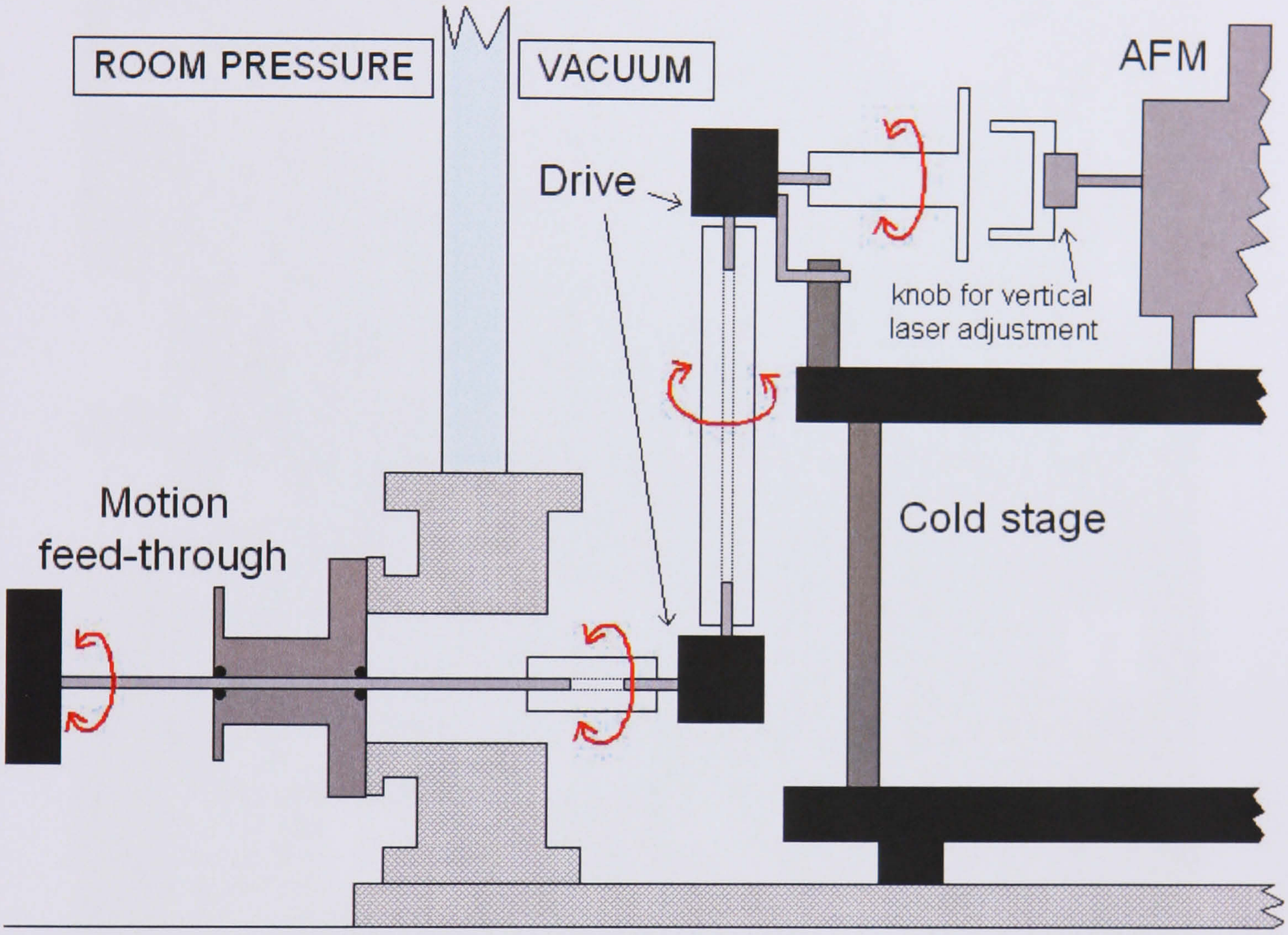



**Figure 3.25**: Diagram of the mechanism to adjust the vertical laser position on the AFM after this was placed on the cold stage inside the vacuum chamber. Two L-shaped right angle drives were used to first change the rotational motion of the feed-through rod from horizontal to vertical and then back to horizontal rotation. The second drive was screwed to an L-shaped Al plate that was fixed to the top plate of the cold stage using stainless steel studding. This mechanism proved efficient but made it impossible for the feedthrough rod to be moved in and out of the vacuum chamber and also coupled it to the cold stage thus allowing some vibration to be transmitted to the AFM.

A photograph of the AFM inside the vacuum chamber on top of the cold stage is shown in Fig. 3.26.

In order to measure both the thermal and electrical conductance of the MWNTs it was necessary to mount an MWNT fibre on a working Veeco Thermal Probe. To do this the technique described in Section 3.5 was used: an MWNT fibre (of the same batch used in the set-up described in Section 3.3) was inserted between the arms of the thermal probe; the probe was then placed on the magnetic holder within the AFM.

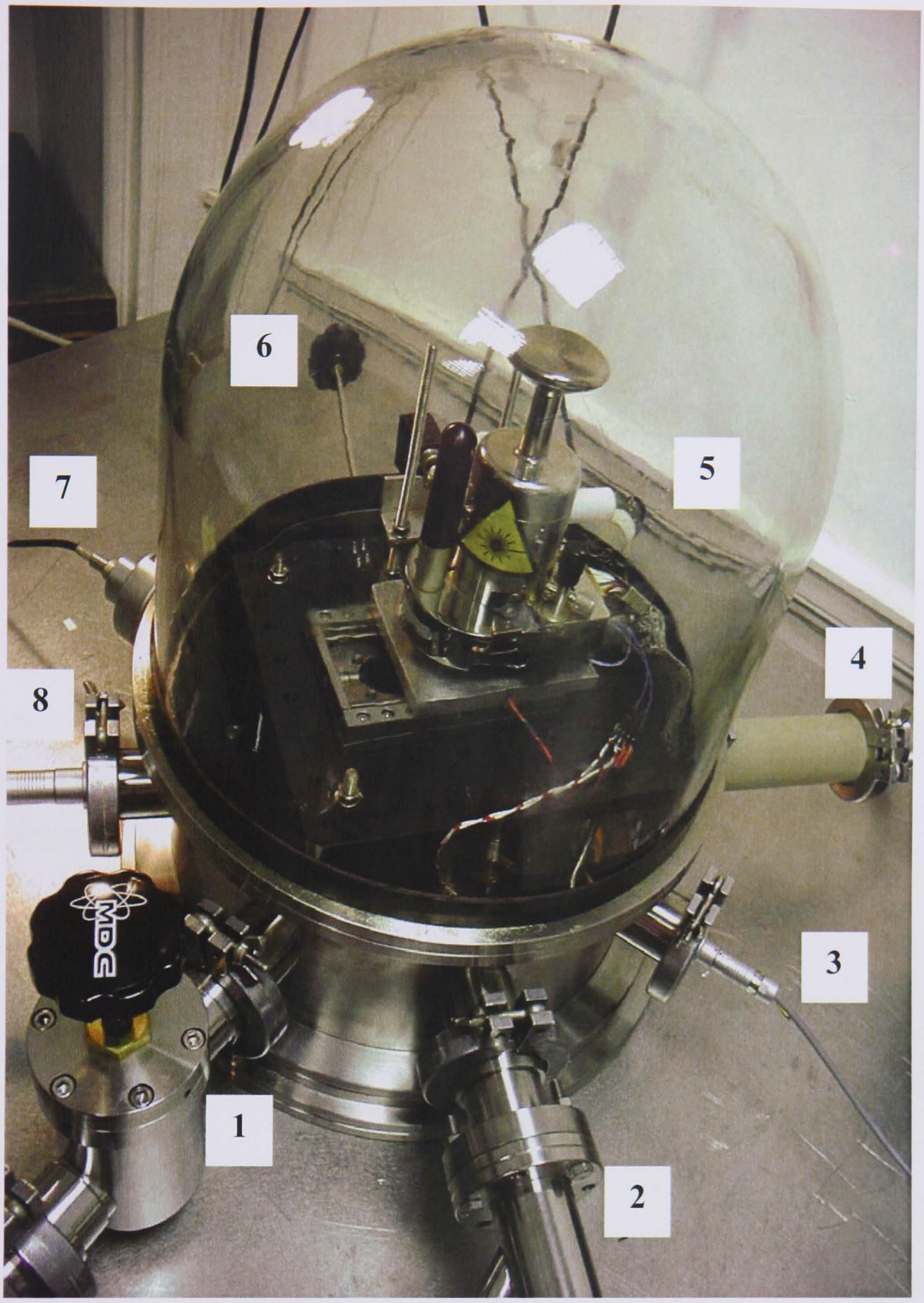



**Figure 3.26**: Photograph of the Explorer AFM inside the vacuum chamber, on top of the cold stage. The vacuum chamber was placed on a compressed air optical table to reduce the transfer of vibration from the floor to the AFM. All the feedthroughs in the bell jar cylindrical collar are in use: 1) inline valve and stainless steel hose; 2) cold finger; 3) 12-pin connector for electrical and thermal conductance measurements; 4) 37-pin connector for AFM control wires; 5) Pirani gauge; 6) motion feed-through to adjust laser position on the AFM; 7) Penning cold-cathode gauge; 8) 24-pin connector for Pt100 thermometers wires.

Two additional plastic-coated copper wires were soldered onto one of the copper pads of the thermal probe, these were to be used for the electrical conductance measurements while the two other copper wires (one on each of the two copper pads) were used for the thermal measurements.

A freshly cleaved HOPG sample was glued (using G-Varnish) on a thin (<500 μm) mica sheet fixed (with G-varnish) to the top of the copper rod of the cold-stage. The

mica was used to provide electrical insulation of the HOPG from the copper rod (to avoid earthing problems) whilst ensuring good thermal contact between the HOPG and the copper rod (this was important for the measurements at low temperatures). A plastic-coated copper wire (of the same type as those used on the Veeco Thermal Probe) was glued to the top layer of the HOPG using conducting silver glue, for the electrical conductance measurements. A diagram of the experimental set-up is shown in Fig. 3.27.

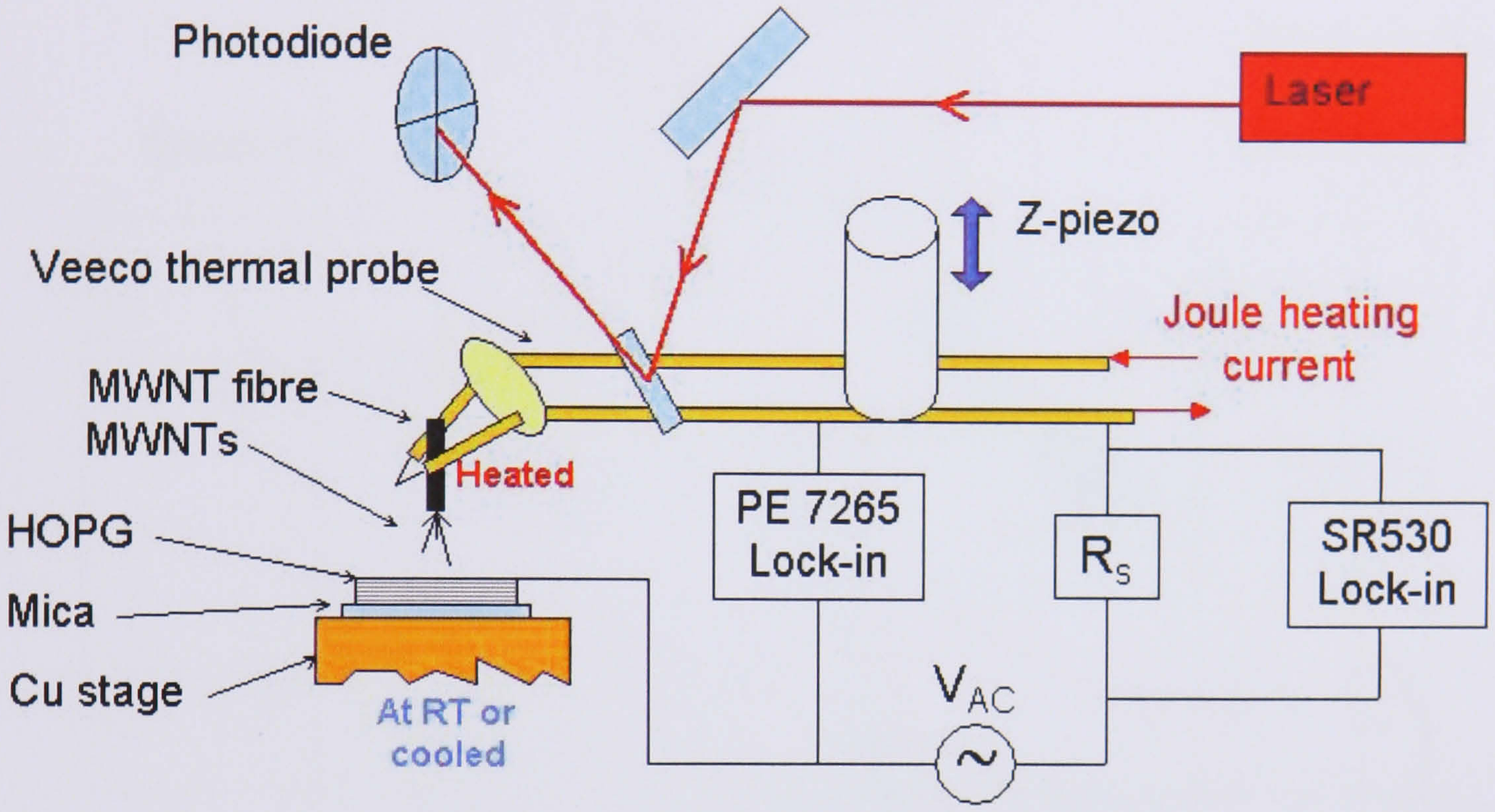



**Figure 3.27**: Diagram of the experimental set-up used to study the electrical and thermal conductance of the nanotubes simultaneously (all measurements were done in vacuum). The MWNT fibre was mounted on a Veeco thermal probe using the technique described in Section 3.5. The thermal probe was heated by a DC current. The heat lost by the probe as the MWNTs came in contact with the HOPG substrate was monitored simultaneously as the MWNTs electrical conductance and the probe deflection. The electrical conductance circuit used an AC voltage to avoid cross talk between the two measurements.

The wires to perform the electrical and thermal conductance measurements (6 in total) were connected to a 12-pin vacuum compatible electrical feedthrough connector (from Fischer Connectors). Outside the vacuum chamber these wires were connected to a 'breakout' box (via a 12 core insulated lead and a second 12-pin connector). The break box was made of die cast aluminium (RS, model: IP54 Enclosures) and provided electrical shielding to the connections inside it.

A diagram of the wiring inside the break box (including a sketch of the wiring from the HOPG and the Veeco thermal probe) is shown in Fig. 3.28 and a diagram of the corresponding electrical circuit (including a simplified circuit of the control unit of the Veeco thermal probe) is shown in Fig. 3.29.

In order to minimise cross talk between the electrical and the thermal conductance circuits the electrical conductance measurements were performed using an AC voltage source (with synchronous detection) since the thermal probe operated with a DC current

(previously a DC source was used for the electrical measurements – see section 3.3). The source was a Perkin-Elmer 7265 DSP Lock-in Amplifier and was input into the break-box at the I+, I- connections.

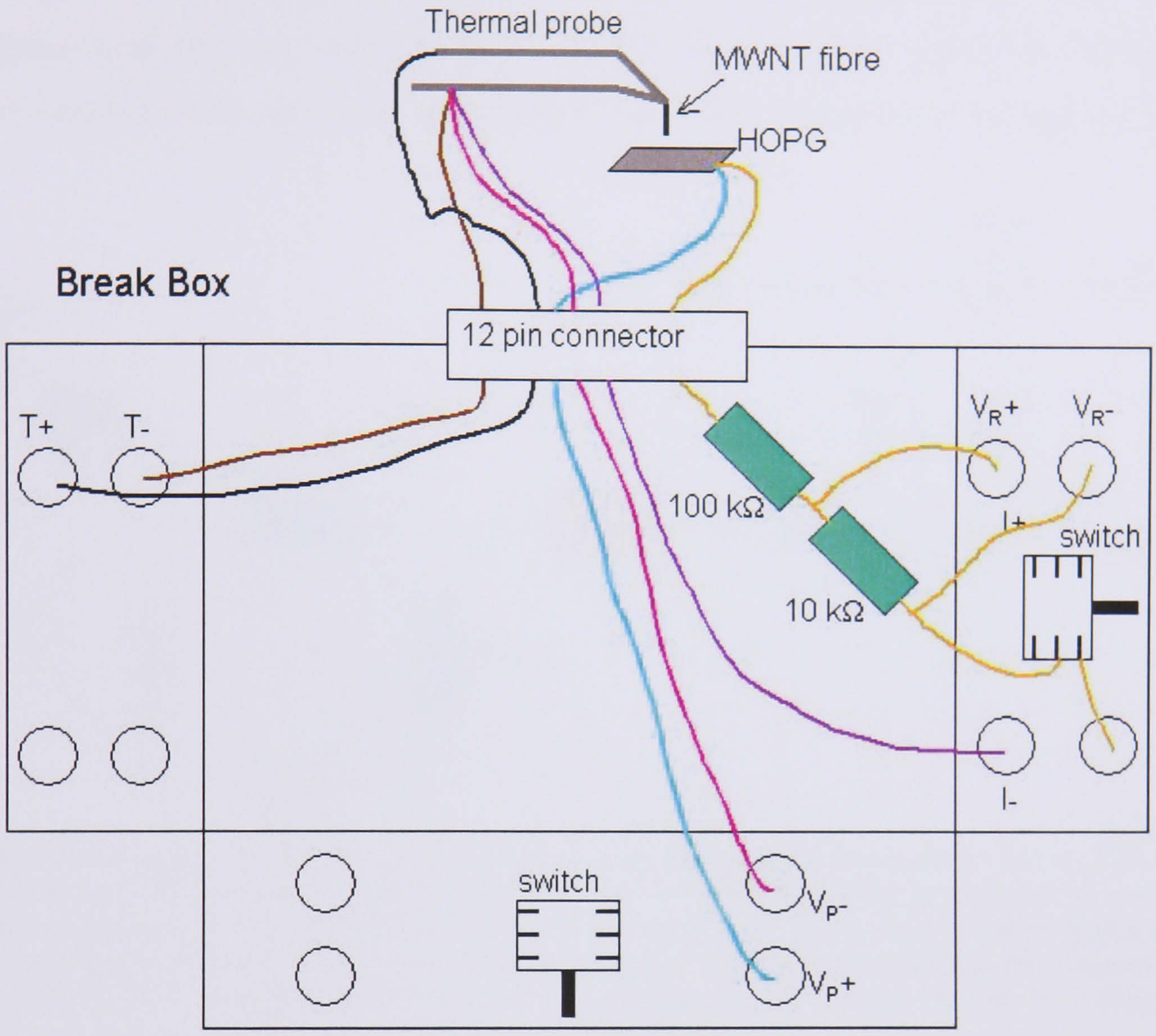



**Figure 3.28**: Diagram of the wiring inside the break box (drawn as if it was opened up flat) and on the HOPG and the Veeco thermal probe. The switch in the box allowed any current across the MWNTs to be interrupted.

The voltage drop across the MWNTs ($V_P$- and $V_P$+) was measured with the Perkin-Elmer 7265 DSP Lock-in Amplifier, while the voltage drop across the known resistance $R_S$, chosen to be 10 kΩ, ($V_R$- and $V_R$+) was measured with an SR530 Lock-in Amplifier (Stanford Research Systems). In both cases the + signal was connected to the A input of the lock-in and the – signal to the B input (via coaxial cables), that is in differential input mode. The lock-ins were set to work in differential mode in order to avoid earthing and common mode problems. Knowing $V_P$, $V_R$ and $R_S$ it was possible to calculate $R_{NT}$, the nanotube resistance, and then the nanotube electrical conductance: $G_{NT}$ (= $1/R_{NT}$) using the following equation:

$$G_{NT} = \frac{V_R}{V_P R_S} \qquad (3.11)$$

$G_{NT}$ was measured in units of the quantum of electrical conductance ($G_0$) which corresponds to ~ $(12.9\ k\Omega)^{-1}$, see Equation 2.3 in Chapter 2.

The wires across the thermal probe (connections T+ and T- in the break box) were connected to the Thermal Control Unit of the Veeco thermal probe. The control resistance used ($R_{control}$), was not that provided by a built-in system in the thermal control unit but was supplied by a resistance box (Time Electronics Limited, Resistance

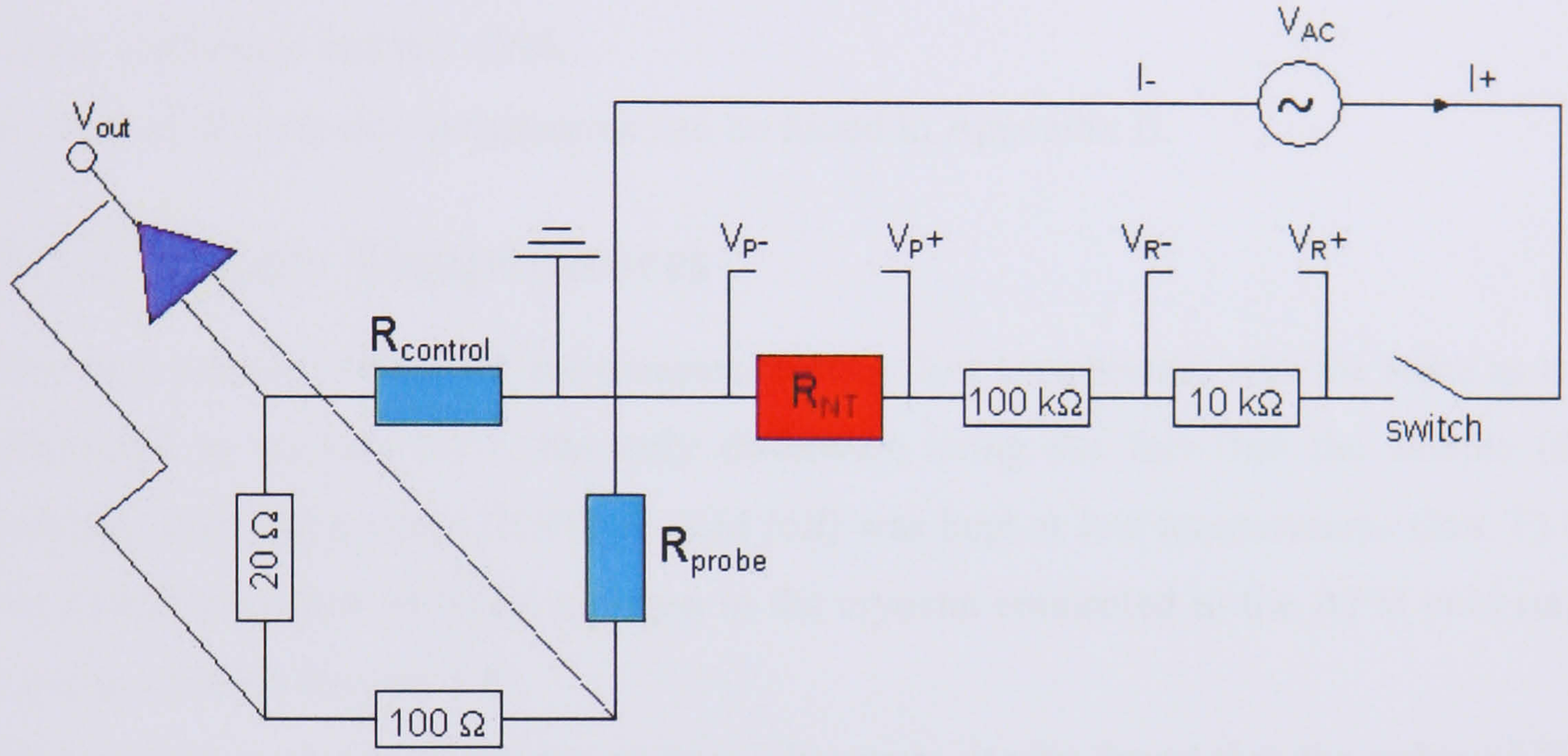



**Figure 3.29**: Diagram of the circuit corresponding to the experimental set-up shown in Fig. 3.27. The circuit on the left hand-side is that of the Veeco thermal probe operating in conductivity contrast mode (see Section 3.4). The amount of Joule heating induced in the probe was controlled by changing the control resistance $R_{control}$. The circuit on the right-hand side is used to measure the resistance of the MWNTs (and hence the MWNTs electrical conductance). This circuit used an AC voltage to avoid cross talk with the thermal circuit that used a DC current.

Box 1051), as this was calibrated and more precise. The output from the thermal control unit (a DC voltage: $V_{out}$) was measured by a multimeter (Fluke 8842A Multimeter).

The wires to measure the 4-wire resistance of the four Pt100 thermometers (16 in total) were connected to a 24-pin vacuum compatible electrical feedthrough connector (from Fischer Connectors). From the outside of the vacuum chamber the 4-wire resistances of Pt100 thermometers were measured by an Agilent Data Acquisition/Switch Unit (Model 34970A).

In order to measure the thermal probe cantilever deflection simultaneously as the thermal and electrical conductance of the MWNTs, the signal measured by the AFM software was sent to an output socket in the AFM ECU, this was connected to a multimeter (Fluke 8842A multimeter) which displayed a DC voltage output proportional to the thermal probe cantilever deflection ($V_F$).

The multimeters, lock-ins and the Agilent data acquisition unit were connected to a data acquisition card (National Instruments, PCI-GPIB, IEEE488.2) in a computer via

IEEE488 cables; a programme was written in Labview 7.0 in order to record simultaneously the data measured from these instruments.

The Labview 7.0 programme recorded simultaneously: $V_{out}$ and $V_F$ from the multimeters and $V_P$ and $V_R$ from the lock-ins. From these values it calculated Q (the rate of heat loss by the thermal probe) in units of μW using equations 3.4 to 3.6 and $G_{NT}$ in units of $G_0$ using equation 3.10. The same programme could in addition also be set to record the 4-wire resistance measurements of the Pt100 resistance thermometers placed on the cold stage and the AFM.

A copy of the Labview programme can be found in Appendix B.

### 3.7.2 At Low Temperatures

The experimental set-up for the measurements at low temperature was the same as that described in Section 3.7.1, the only difference being the fact that the sample (the samples used were either HOPG or gold foil) was kept at low temperatures (low T) by the continuous flow of liquid nitrogen in the cryostat connected to the AFM cold stage (as described in Section 3.6).

During the initial measurements at low T however, it was found that the value of $G_{NT}$ was always close to 0. This was explained as due to the formation of a thin ice-layer on the sample surface. If the capillary water layer due to moisture had not entirely evaporated in vacuum it would then have solidified into ice as the sample temperature dropped else, if the layer had evaporated, the residual water vapour in the vacuum chamber could have re-condensed onto the cold parts of the system during the cryo-pumping. This ice layer had to be removed in order to perform reliable electrical

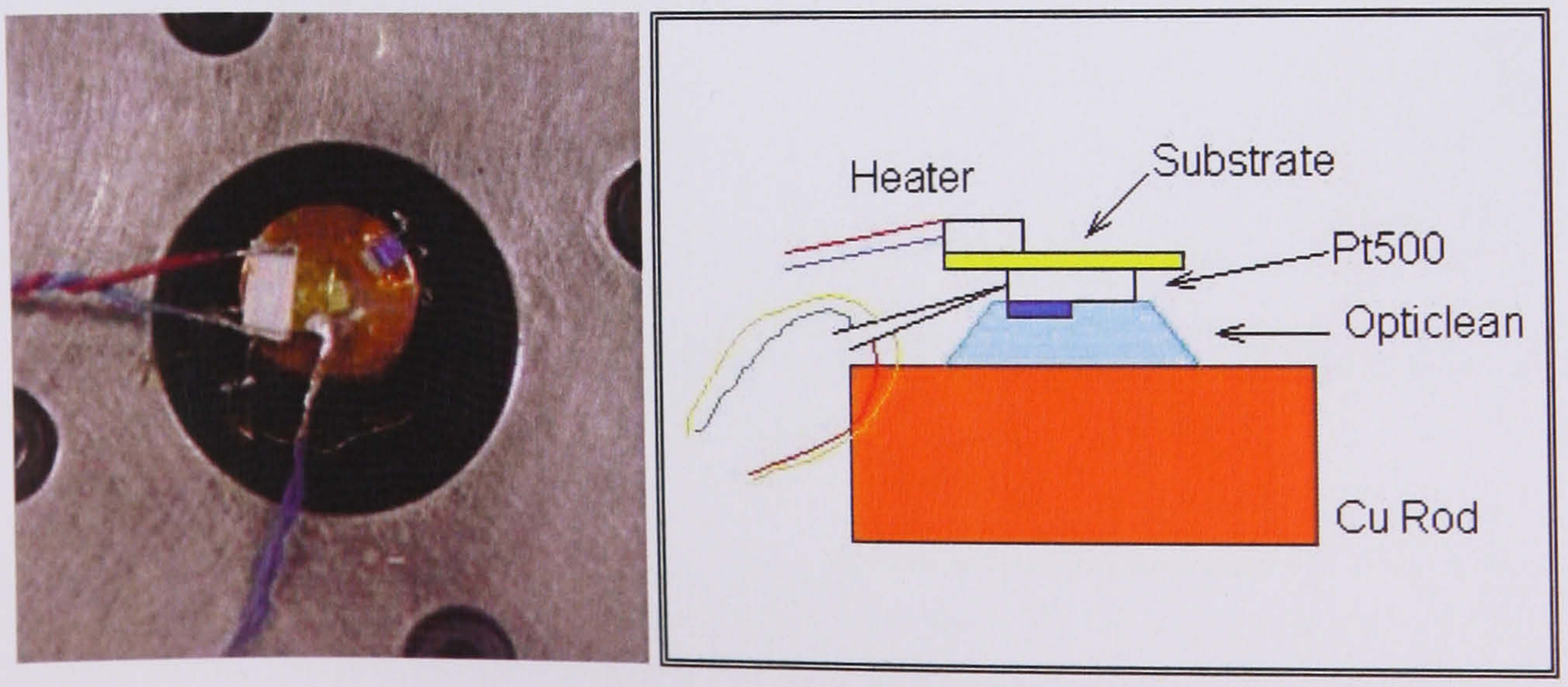



**Figure 3.30**: On the left a photo of the top of the copper rod with the heater glued on top of the substrate (in this case it was gold) with G-varnish. On the right a diagram of the set-up. The substrate had to be partially thermally insulated from the copper rod, as the heating power of the heater was much lower than the cooling power of the cold stage. The insulation was provided by a thick layer of Opticlean, a polymer solution with low thermal conductivity. A Pt500 resistance thermometer was glued on the substrate (with G-varnish) to monitor the temperature of the substrate and thus regulate the power input in the heater. Both the heater and the thermometer were controlled by a Lakeshore 340 temperature controller.

conductance measurements on the nanotubes at low T and this was done by adding a heater on the surface of the sample near the area of contact of the MWNTs. The heater was a thick film chip resistor (from RS, Ref. number: 224-0222) with resistance of 47 Ω at room temperature and maximum power handling at 70 °C of 1 W. It was used during the cooling process to keep the temperature of the sample above freezing. This ensured that all the moisture on the sample surface evaporated and condensed instead on the colder parts of the stage (the copper rod, copper base and cold finger) during the cooling process. For the heater to have an effect, the sample had to be partially insulated thermally from the copper rod of the cold stage, since the cooling power of the cold stage was higher than the heating power of the heater. This was done by gluing the sample on the copper rod with Opticlean (from www.caliope.co.uk), a polymer solution with low thermal conductivity.

The heater was switched off just before the electrical conductance measurements were taken so that the sample surface was at low T when the electrical and thermal conductance data was acquired. The heater worked together with a Pt500 resistance thermometer in contact with the sample (to monitor the sample temperature and regulate the heating); the layout is shown in Fig. 3.30.

Both heater and thermometer were wired to the 24-pin connector and then, outside the vacuum chamber, connected to a temperature controller (Lakeshore, model 340).

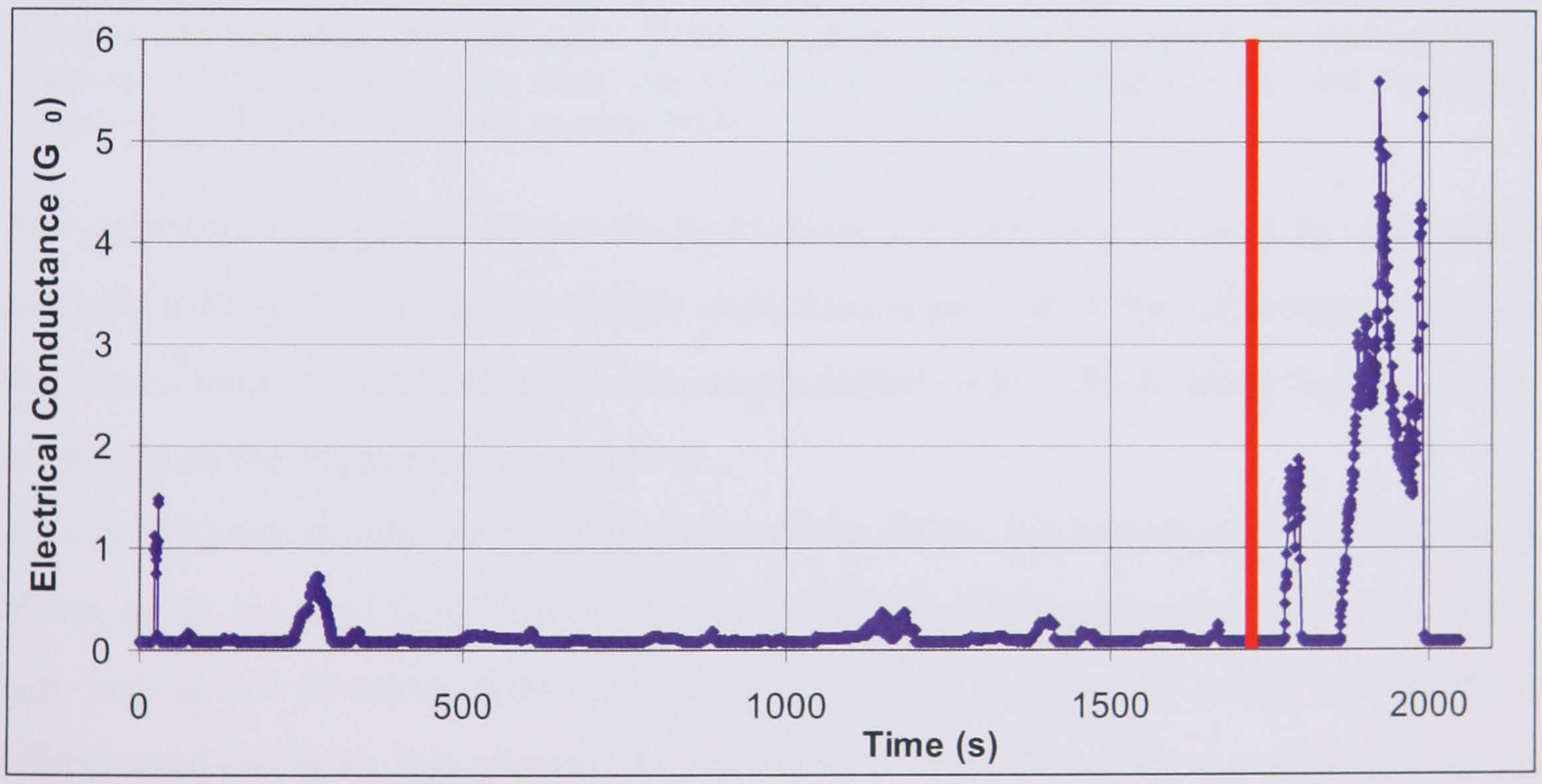



**Figure 3.31**: The electrical conductance data acquired at low temperature on an HOPG sample. The signal was very low in spite of the MWNTs coming repeatedly in and out of contact with the HOPG. The red line marks the point when the heater was switched on to bring the HOPG to above freezing temperature for a few seconds and then switched off again. The effect of the heating on the quality of the contact between the MWNTs and the HOPG was dramatic confirming the assumption that it was an ice-layer which caused the high contact resistance at low temperatures (data taken with probe N16, tip H2b, on 27.05.05).

In Fig. 3.31 are shown electrical conductance measurements taken at low temperature before and after the heating of the sample surface (in this case HOPG), the dramatic increase in conductance after the heating confirmed the fact that the initial small conductance measurements were due to a water ice-layer formation.

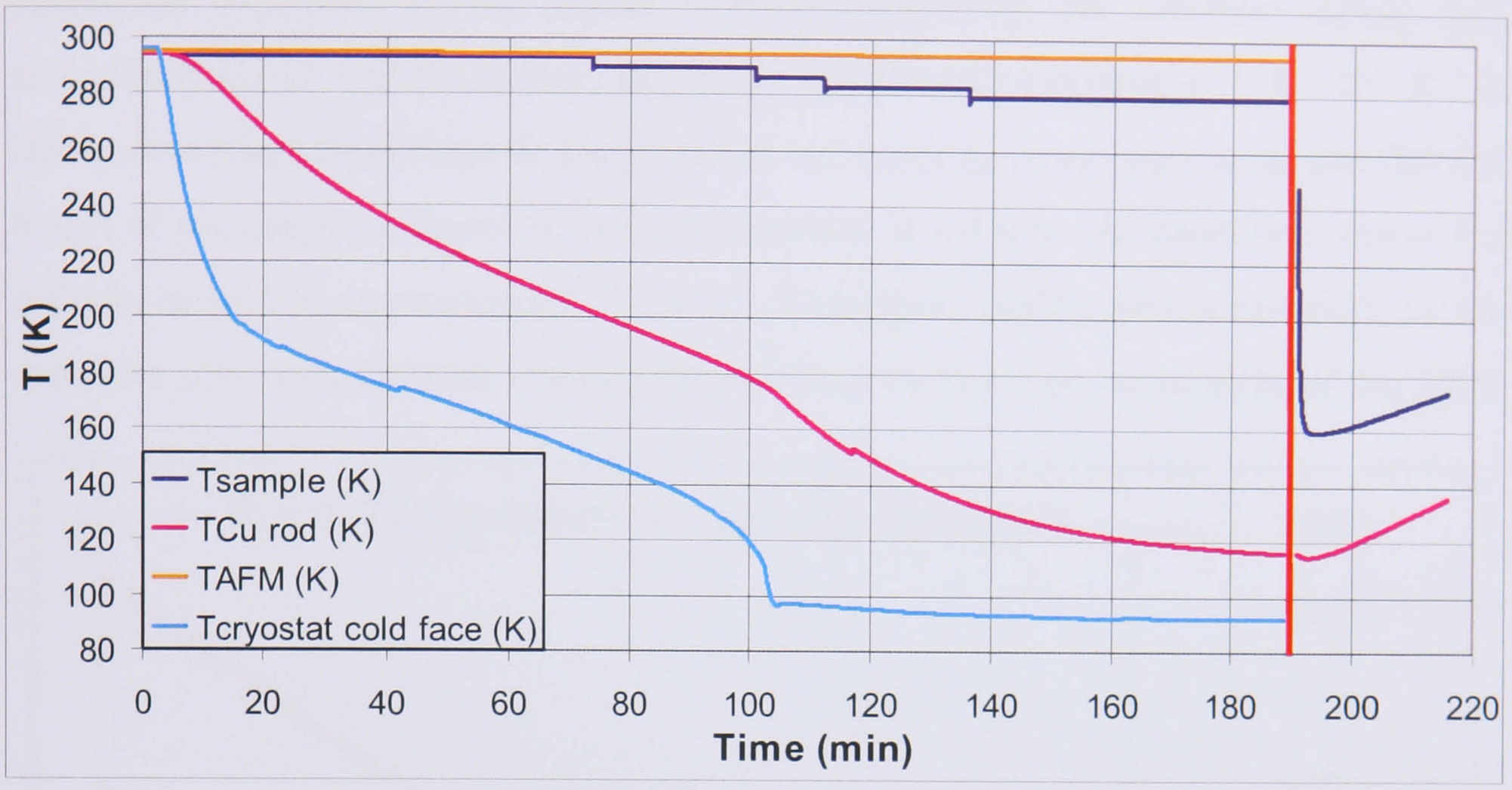



**Figure 3.32**: The cooling curves of: the cryostat cold face, the top of the copper rod in the cold stage, the sample (gold) and the AFM. While the flow of liquid nitrogen in the cryostat cooled the cold face and the copper rod of the cold stage, the sample was kept above freezing by the heater (the small temperature steps were necessary as the heater was reaching its maximum power limit). After about 3 hours of cooling, when the copper rod had reached a plateau temperature around 115 K, the heater was switched off (red line). After the sample had cooled down (lowest temperature of ~160 K) the measurements could start. During the measurements the flow of nitrogen in the cryostat had to be stopped and this cause the temperature of the cold stage (and hence the sample) to increase. This increase was limited due to the large thermal mass of the copper element in the cold stage (file acquired on 11.01.05 with tip A2 on probe N13).

The addition of the heater solved the problem of the insulating ice layer but the need to partially insulate thermally the sample from the copper rod of the cold stage meant that the lowest temperature reached by the sample surface was ~160 K when the temperature of the top of the copper rod was ~115 K.

In Fig. 3.32 are shown the cooling curves of the AFM, the sample surface (in this case it was gold), the cold face of the cryostat and the top of the copper rod while the sample was kept above freezing. After about 190 minutes of cooling the heater was switched off (vertical red line), this allowed the sample to cool down before the acquisition of the electrical and thermal conductance data.

The subsequent heating of both copper rod and HOPG was due to the fact that the flow of liquid nitrogen in the cryostat had to be stopped during data acquisition. The precaution taken to limit the transfer of vibration from the cryostat (due to the flow of nitrogen) to the cold stage using copper braids (see Section 3.6) was not enough and

data acquisition was possible only if the flow of nitrogen in the cryostat was temporarily suspended. The large thermal mass of the copper rod and copper base of the cold stage though ensured that the temperature change during the data acquisition was limited to only a few degrees (< 10 K). This temperature change however, caused a small but significant expansion in the copper cylinder supporting the substrate during data acquisition. Given that the thermal expansion coefficient of copper is $15.2 \times 10^{-6}$ $K^{-1}$ at 200K (data taken from Kaye & Laby Online, see www.kayelaby.npl.co.uk) and that the length of the copper cylinder at room temperature is 120mm, the expansion rate of the cylinder would be approximately $2\mu m/K^{-1}$. Therefore, during data acquisition, as the nanotube fibre was lowered towards the substrate by the z-piezo element of the AFM

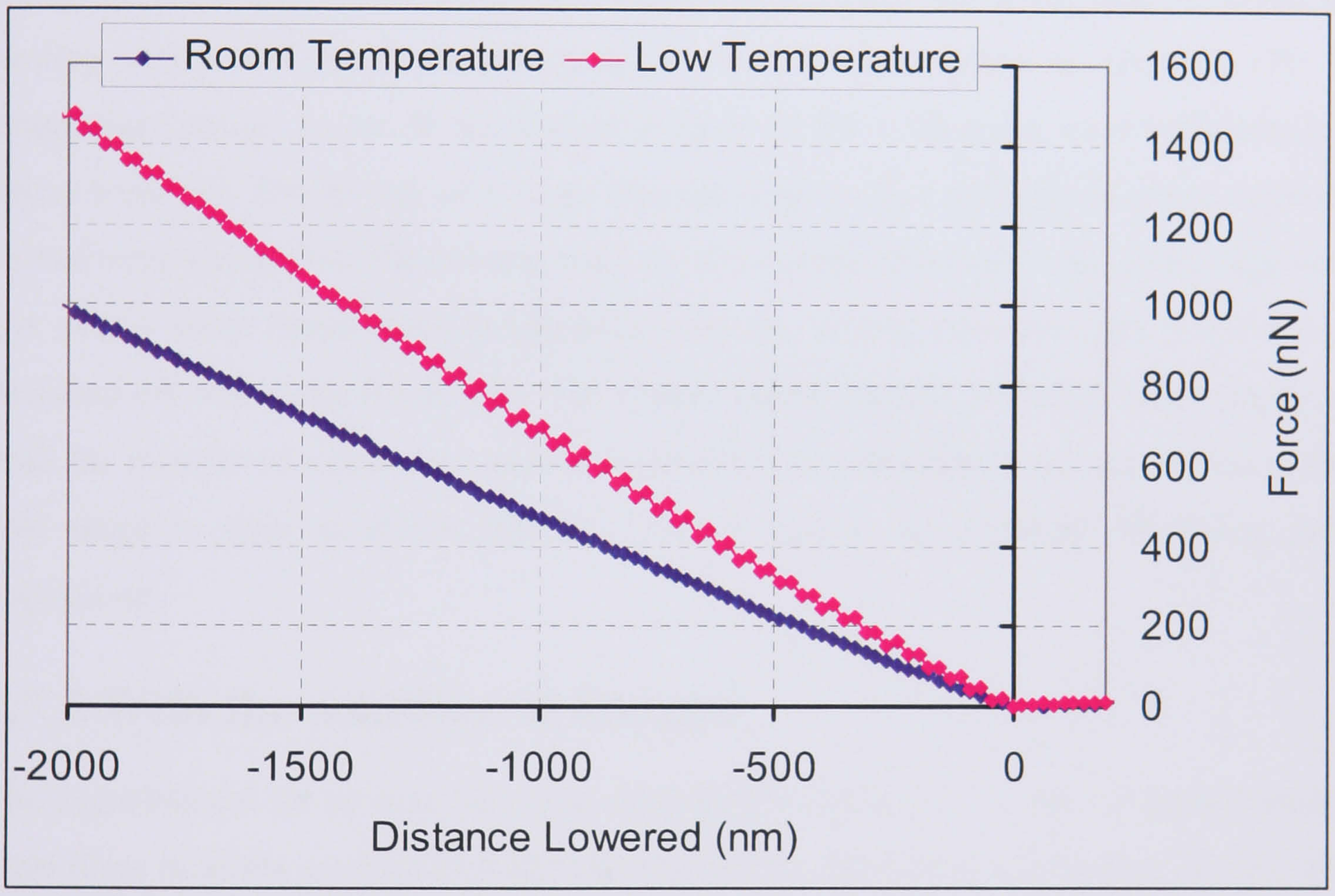



**Figure 3.33**: The deflection curves taken at room temperature (blue) and at low temperatures (pink). The deflection at low temperatures has an apparent higher slope because, while the piezo moves the fibre towards the substrate (the distance moved is indicated on the x-axis of the graph), the warming of the cold stage support moves the substrate upwards towards the fibre.

the substrate also moved towards the fibre! This movement could be detected by noticing an increase in the total deflection of the force curves acquired at low temperatures (see Fig. 3.33). Thus extreme care had to be taken, at low temperatures, not to crush the nanotube fibre on the substrate.

The 4-wire resistance measurements of 3 Pt100 thermometers (one on the AFM, one of the cold face of the cryostat and one on the copper base of the cold stage – not shown in Fig. 3.32) were measured with an Agilent Data Acquisition and Switch unit (Model 35970A) and recorded on the PC with a programme written in Labview 7.0 (see Section

3.7.1 and Appendix B). The 4-wire resistance of the Pt500 thermometer on the sample and that of the Pt100 thermometer on the top of the copper rod were measured with a Lakeshore temperature controller (model 340) that also regulated the power input on the heater. The data was recorded on the PC with the same Labview 7.0 programme. During the thermal and electrical conductance data acquisition process the Labview programme was set not to record the data from the Agilent unit as that slowed its operation down by about 0.3-0.5 s for each measurement loop (this is why the $T_{AFM}$ and $T_{cryostat}$ data is missing in Fig. 3.32 in the latter part of the graph).

In conclusion, even though the cold stage was designed so that the AFM sample could reach liquid nitrogen temperatures (see Section 3.6), in practice other factors limited its cooling effect and most measurements at low T were taken in the 160-170 K temperature range. Some of the design features of the cold stage were effective, but others were not. The design of a large thermal mass to give good temperature stability proved very successful: the cooling time for the copper elements in the cold stage was just over 3 hours (from room temperature) and the heating rate when the cryostat was switched off was about 0.5 K/min. The copper braids though, included in the design to limit the transfer of vibrations, proved ineffective, as vibrations were transferred to the cold stage to such an extent that the cryostat had to be switched off during data acquisition.

### 3.7.3 With the Addition of Oxygen

The experimental set-up was the same described in Section 3.7.1. Minor modifications were done to allow a controlled amount of pure oxygen (from a cylinder) to enter the vacuum chamber. A photo of the set-up is shown in Fig. 3.34.

A valve (Model 96-83406, from MDC) to control gas flow into the vacuum chamber was added using a T-piece on one of the chamber feedthroughs (the one used for the Pirani gauge). This was connected to another T-piece, on one end was a vacuum pump (rotary pup and turbo pump) and on the other a variable leak valve (Model 283-41, from Leybold) to control the amount of oxygen input. The vacuum pump was used to degas all the connectors before opening the valve to the vacuum chamber so as not to compromise the vacuum there and also to ensure that only oxygen from the cylinder was added to the chamber. When the connectors were all degassed (the vacuum pump was equipped with a Pirani and a Penning gauge to monitor the pressure in the connectors) the valve to the pump was closed and the pump switched off then the valve

to the vacuum chamber was opened. Usually there was always a small pressure change and the system was allowed to settle for sometime (typically 10-20 minutes). The pressure in the bell jar was recorded and then the oxygen was added by slowly turning the needle valve to the desired value. After another 10-20 minutes, the pressure in the chamber was recorded, and the pressure difference gave the amount of oxygen added to the vacuum chamber.

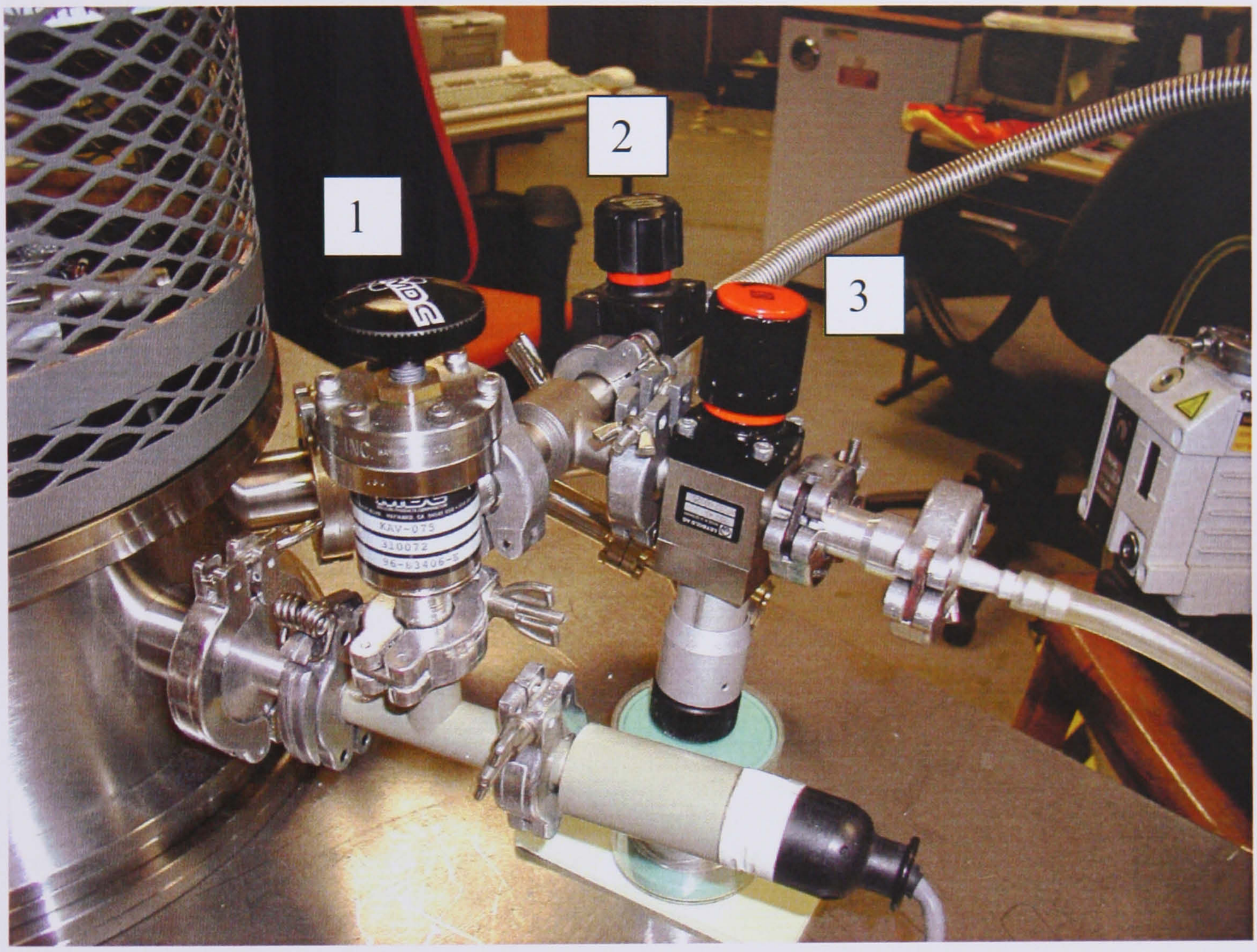



**Figure 3.34**: The additional set-up for the introduction of small quantities of pure oxygen to the vacuum chamber. 1) the valve added to control gas input to the chamber; 2) valve connecting the extra tubing to a vacuum pump, so that the connectors could be all degassed before opening up the valve to the vacuum chamber; 3) the needle valve to control the oxygen input. The oxygen was supplied from a gas cylinder.

# Chapter 4 Results and Discussion

## 4.1 Sample Description and Characterisation

The MWNTs used in this work were supplied by Dr Mark Baxendale at Queen Mary University of London. The MWNTs were produced by the carbon arc synthesis method also know as arc-discharge (for more details see Section 2.1.1 in [Harris'99] and Section 5.3 in [Saito'98a]).

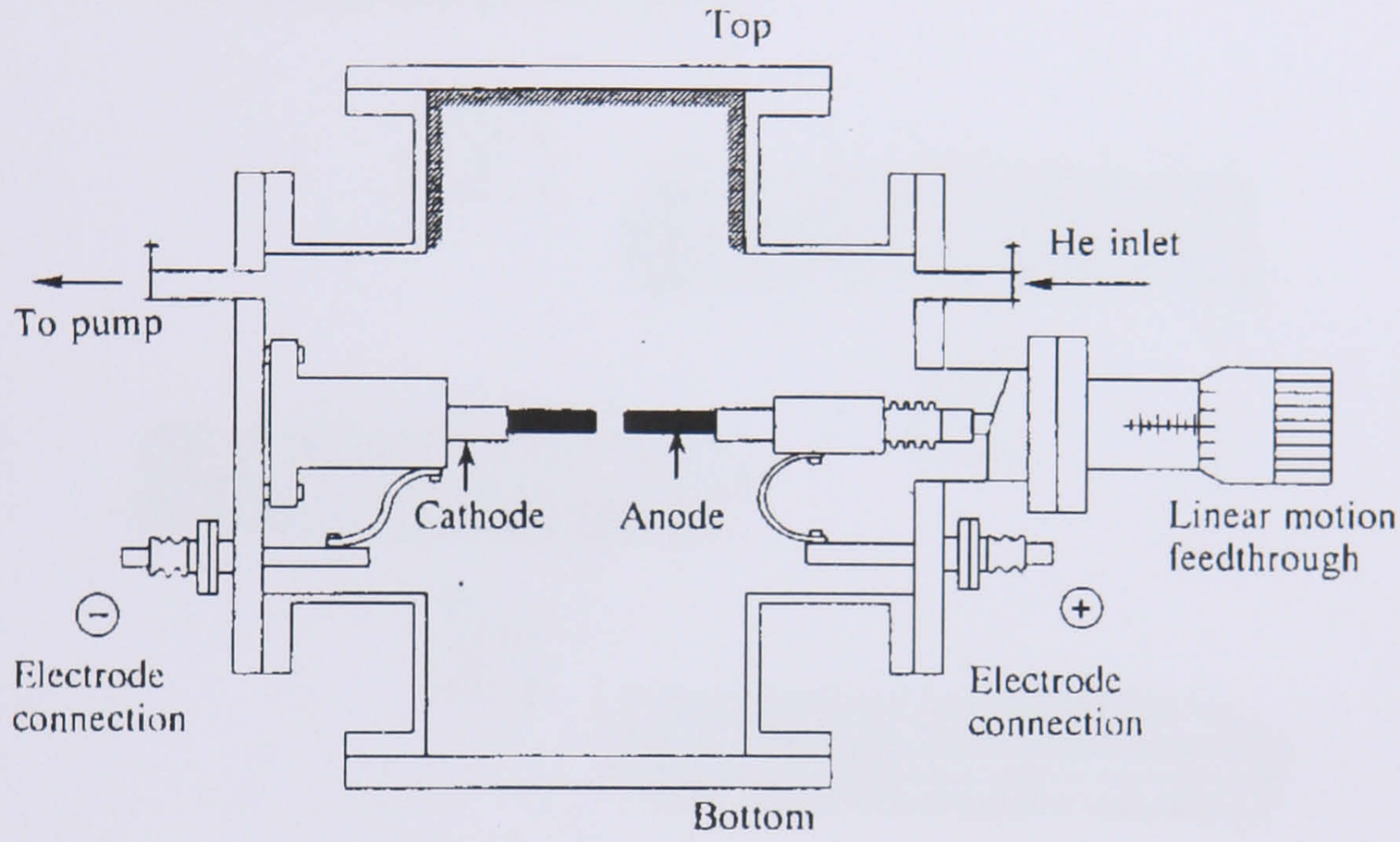



**Figure 4.1**: A diagram of the arc-evaporation apparatus used for the production of nanotubes. A high current and voltage across the two carbon rod electrodes produces an arc. Water-cooling of the cathode and a helium atmosphere in the chamber optimise nanotube growth. The nanotubes are found in the core of the deposit formed on the cathode (figure taken from Section 2.1.1 in [Harris'99]).

In this synthesis method a large voltage (typically 20-25 V) is applied across carbon rod electrodes (5-20 mm in diameter) separated by ~1 mm; the current flowing between the electrodes is typically 50-120 A. These conditions produce an arc between the electrodes, the carbon atoms in the electrodes experience temperatures >3000 °C and are vaporized into a plasma. The arc is typically operated in a vacuum chamber with a continuous flow of Helium at pressures ~670 mbar (a schematic diagram of the apparatus is shown in Fig. 4.1). Once the arc is in operation a carbon deposit forms on the negative electrode (cathode) while the length of the positive electrode (anode) decreases. The cathode is usually water cooled as this has been shown to produce better quality nanotubes. In the multi-walled nanotube synthesis no catalyst is used and the nanotubes are found in the core of the cathode deposit where the temperature is maximum. Because they form at such high temperatures, arc-discharge nanotubes tend to have higher crystallinity and fewer defects than nanotubes produced by other

methods (see section 2.11 in [Harris'99]). Surrounding the core is a hard grey shell consisting of nanoparticles, fullerenes and amorphous carbon fused together. The core of the deposit is soft and fibrous and contains typically about 66% nanotubes (the rest consisting of carbon nanoparticles). The fibrous material has a fractal like structure: the fibres are bundles of smaller fibres that are themselves composed of smaller bundles and so on, eventually reaching the individual nanotube as shown in Fig. 4.2 [Ebbesen'94].

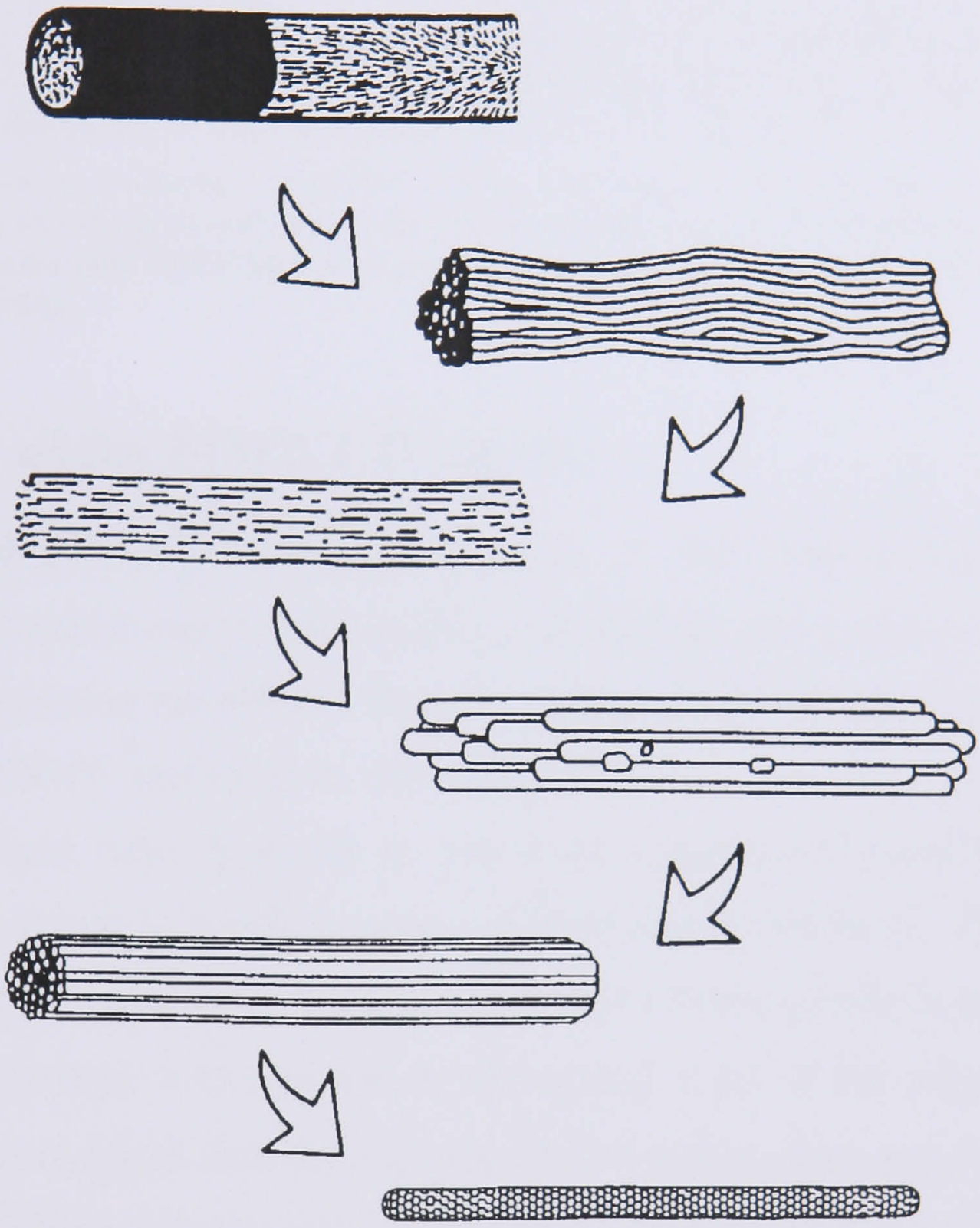


**Figure 4.2**: Diagram of the fractal-like organisation of the nanotube rich, fibrous material found in the core of the deposit on the cathode in the arc-discharge synthesis (figure from Ref. [Ebbesen'94]).

The MWNT fibres used in this work were fine and compact and usually about 50 μm in diameter and 1 to 3 mm long. SEM images of the fibres revealed that several particularly long bundles made up of few nanotubes protruded from the tip of the fibre (see Fig. 4.3). The bundles tapered away from the bulk of the fibre and most would have an individual nanotube at their extreme end.

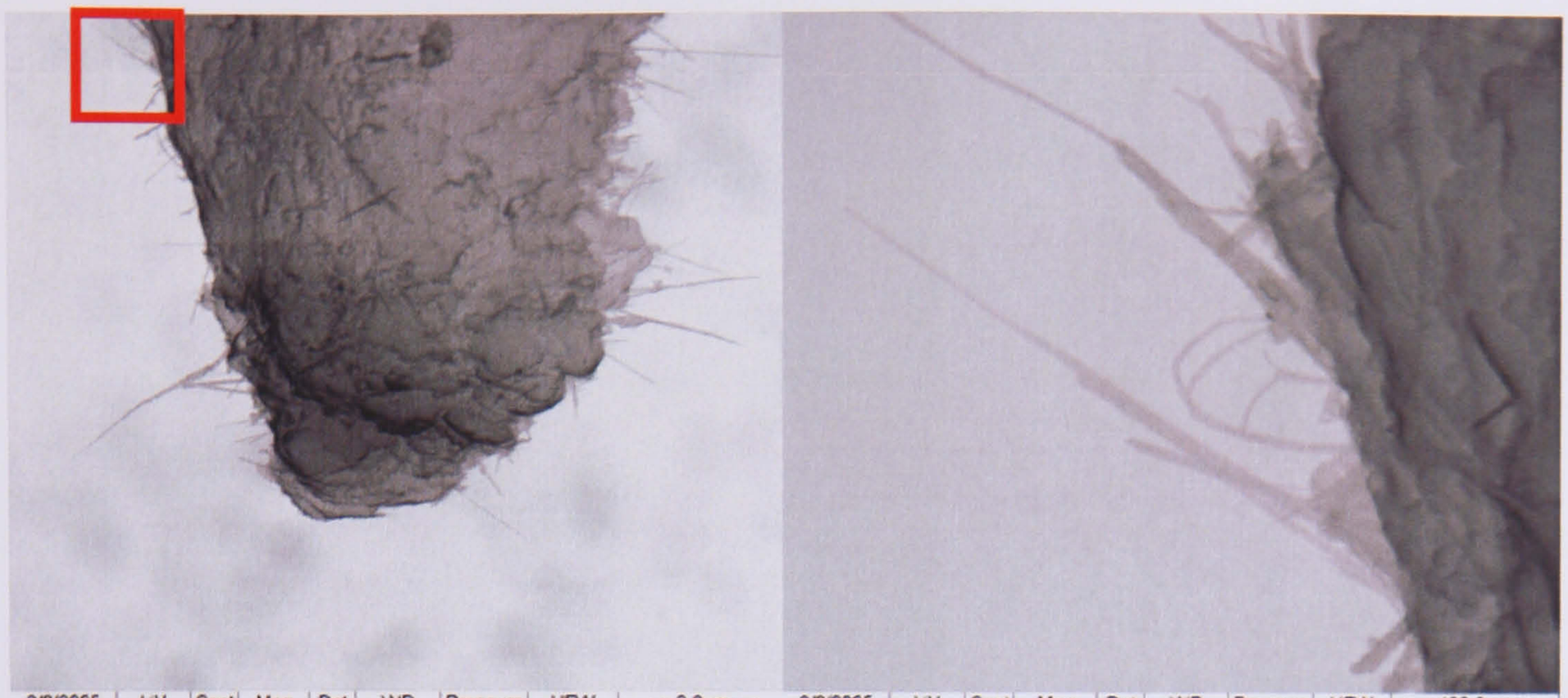



**Figure 4.3**: SEM images of the tip of an MWNT fibre. The image on the right is a zoom in the red-square of the image shown on the left. Small bundles of nanotubes protrude from the bulk of the fibre and taper away to individual MWNTs at their ends. These images were taken by Dr David Cox from the University of Surrey.

## 4.1.1 Study of the MWNT Diameter

In order to calculate the thermal conductivity of the MWNTs from the thermal conductance measurements it was necessary to estimate the nanotube diameter. This was done by dispersing the MWNT fibres in methanol and depositing the solution on a freshly cleaved HOPG surface to be imaged by AFM.

The MWNT fibres were dispersed in low residue methanol (dystol) by repeatedly sonicating the solution in a bath sonicator (Fisherbrand® FB11002). The solution was also progressively diluted until the desired nanotube concentration was achieved. The nanotube concentration was checked by dispersing 5 µl of the solution on freshly cleaved HOPG (purchased from Agar Scientific, 5×5 mm in size), which was blown dry with an air gun after a few seconds. The dilution series varied depending on the fibres used. Because of their small size the fibres could not be weighed so the starting solution was made of a certain number of fibres (N) dispersed in N×10.5 µl of methanol (typically $N \geq 10$). Each dilution step doubled the amount of methanol used (halved the nanotube concentration); the number of steps varied from 6 (64× diluted) to 11 (2048× diluted). In between dilution steps the solution was sonicated for up to 1 hour in the bath sonicator at maximum power.

In Fig. 4.4 are shown AFM images of two different nanotube solutions on HOPG. The images were acquired in tapping mode with a Veeco Multimode AFM (with Nanoscope III controller) at room temperature and pressure. The nanotubes appeared as needle-like structures in the scans, smaller dot-like features were also visible and these were

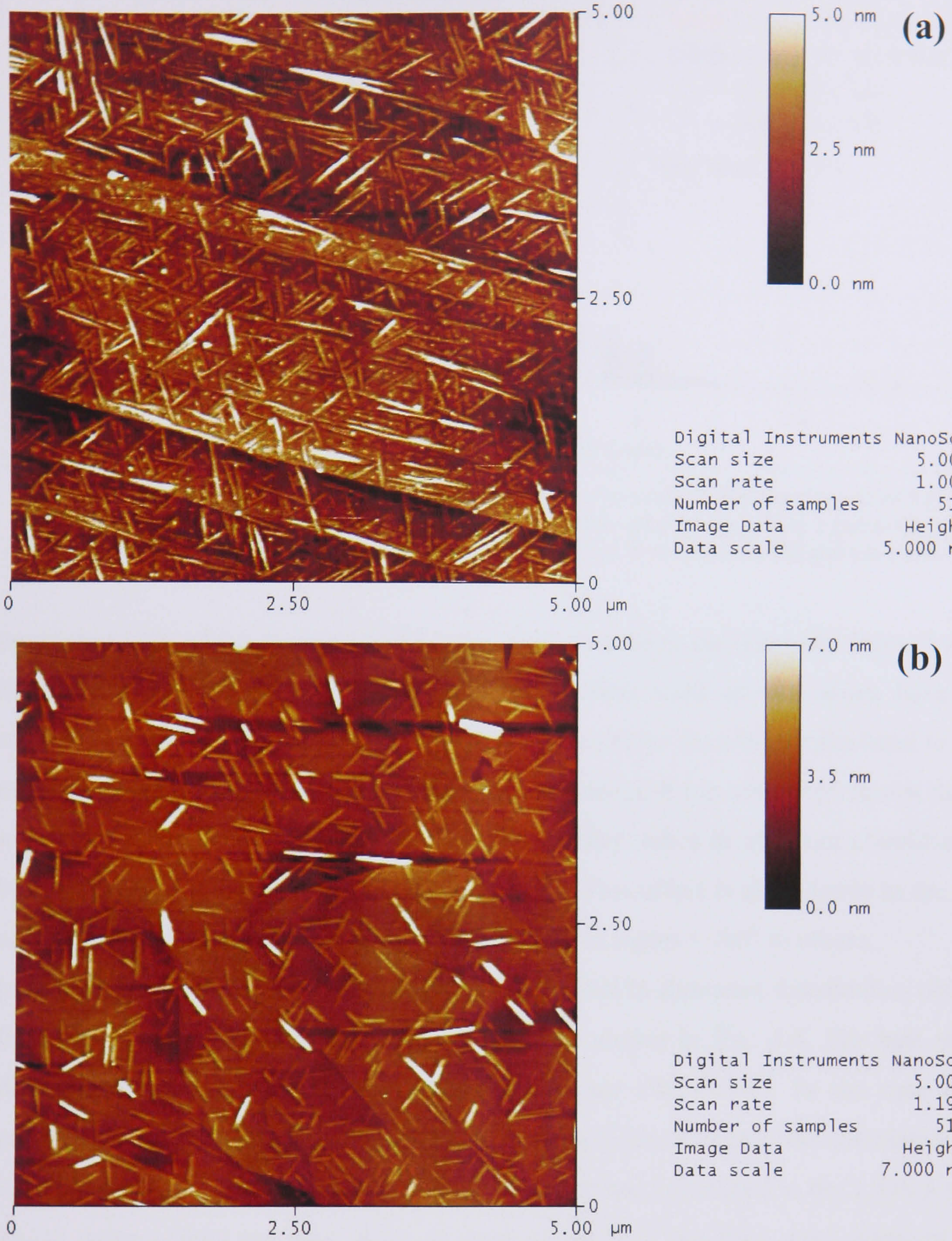



**Figure 4.4**: **(a)** AFM image of 5 µl of nanotube solution M6 (diluted 64×) dispersed on freshly cleaved HOPG, the initial solution M1 contained 40 MWNT fibres. **(b)** AFM image of 5 µl of nanotube solution M11 (diluted 2048×) dispersed on freshly cleaved HOPG, the initial solution M1 contained 10 MWNT fibres.

interpreted to be carbon nanoparticles, the surface coverage was uniform in all the areas of the sample imaged with the AFM. In both images most nanotubes seemed to lie along three axes all at 60° to each other. This is a genuine alignment; it has been reported in the literature [Liu'98] that nanotubes deposited on HOPG tend to align along specific directions so that the carbon lattice on the CNT is commensurate (or in registry) with that of the HOPG. This alignment has only been observed with high quality

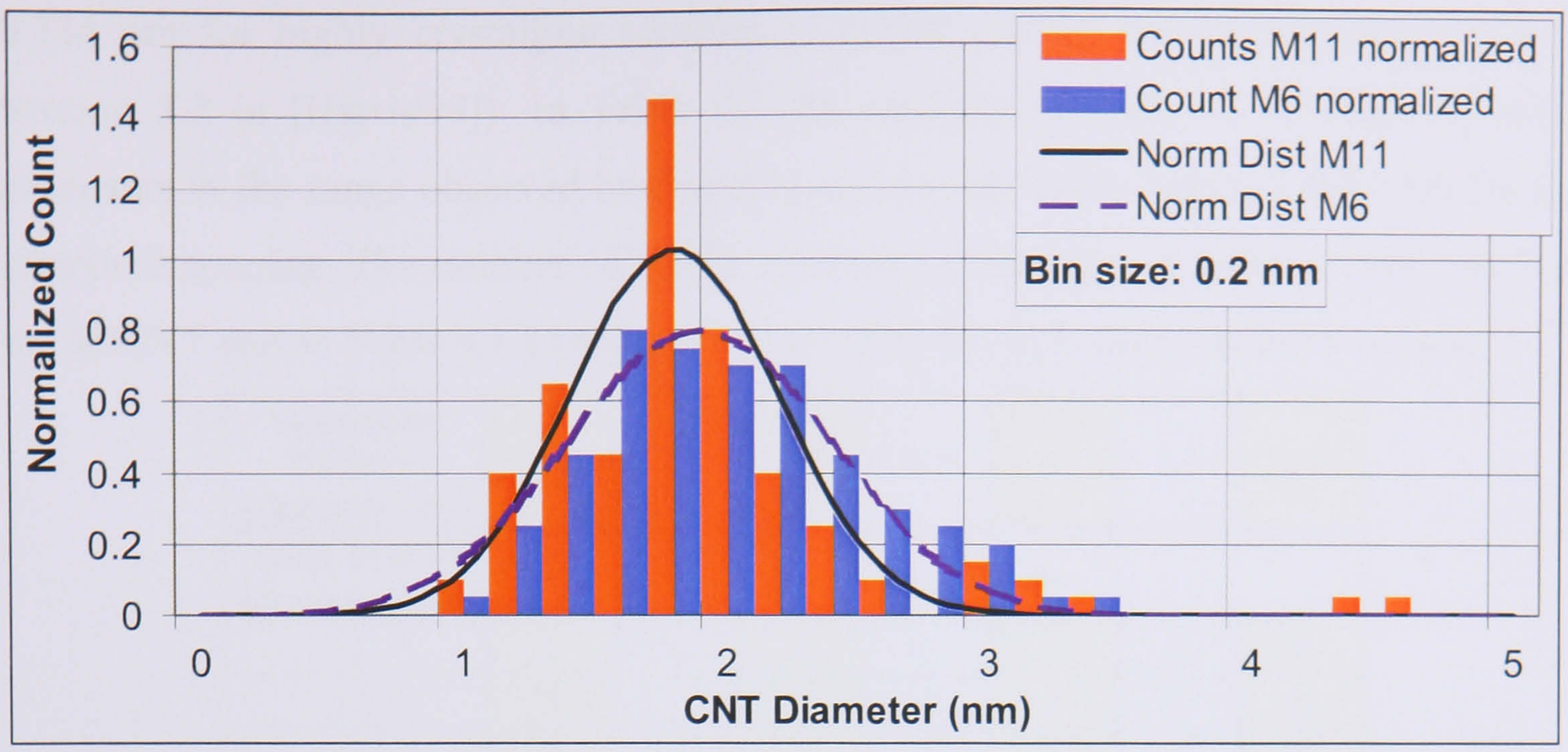



**Figure 4.5**: Histogram of the distribution of the MWNTs diameters as measured by AFM topography sections in both solutions: M6 and M11 (see also Fig. 4). The solid line is a fit to a normal distribution with mean 1.8±0.4 nm for solution M11; the dashed line is the fit for solution M6 and has mean 1.9±0.5 nm.

nanotubes with a high degree of molecular cleanness along the nanotube sides, thus this confirms that the nanotubes in the MWNTs fibres used in this work have high crystallinity and few defects. These 'on registry' positions have been calculated to occur at 60° intervals [Falvo'00], which is what was observed. It has also been shown that the alignment direction is dependent on the tube chirality: tubes of different chiralities will be 'on registry' at different angles on the HOPG. This effect is also visible in the AFM scans shown in Fig. 4.4 where some CNTs appear at angles <<60° to others.

In Fig. 4.5 are shown two histograms of the MWNTs diameter distribution obtained from 100 topography sections of the AFM scans shown in Fig. 4.4. The best normal distribution fits for the two sets of histograms are also shown. In the case of the nanotube dispersion obtained from solution M6 the mean diameter was calculated to be: 1.9±0.5 nm while for the solution M11 the diameter was calculated to be: 1.8±0.4 nm. These mean values are very close in spite of the fact that they were obtained from different solutions made of different MWNT fibres of the batch.

The measured mean diameters indicate that these MWNTs have only a few concentric carbon shells: the number of shells is calculated to be between 2 to 4 shells depending on the inner-most tube diameter (see Table 4.1).

The thinnest nanotube measured inside an MWNT synthesised by the arc-discharge method had a diameter of 0.4 nm (see Ref. [Qin'00]). In the same paper, inner nanotubes of diameters 0.5 and 0.7 nm were also observed. The interlayer spacing in MWNTs is similar to the distance between graphene layers in 3D graphite. This distance depends on the graphite purity, and increases for less crystalline samples. The reported range is:

0.334 nm for highly crystalline samples to 0.344 nm for less perfect samples (see Section 3.2 in [Harris'99]). In Table 4.1 the number of shells in MWNTs of outer diameters in the range observed has been calculated using the value of 0.34 nm for the intershell spacing. The number of shells depends on the size of the innermost shell in the MWNT and in Table 4.1 a range of values from 0.4 to 1.4 nm has been chosen.

| **Innermost MWNT Diameter (nm)** | 0.4 | 0.5 | 0.7 | 0.8 | 1 | 1.2 | 1.4 |
|---|---|---|---|---|---|---|---|
| **Outer MWNT Diameter (nm)** | **Number of Shells** | | | | | | |
| 1 | 1 | 1 | 1 | 1 | 1 | 0 | 0 |
| 1.1 | 2 | 1 | 1 | 1 | 1 | 0 | 0 |
| 1.2 | 2 | 2 | 1 | 1 | 1 | 1 | 0 |
| 1.3 | 2 | 2 | 1 | 1 | 1 | 1 | 0 |
| 1.4 | 2 | 2 | 2 | 1 | 1 | 1 | 1 |
| 1.5 | 2 | 2 | 2 | 2 | 1 | 1 | 1 |
| 1.6 | 2 | 2 | 2 | 2 | 1 | 1 | 1 |
| 1.7 | 2 | 2 | 2 | 2 | 2 | 1 | 1 |
| **1.8** | 3 | 2 | 2 | 2 | 2 | 1 | 1 |
| **1.9** | 3 | 3 | 2 | 2 | 2 | 2 | 1 |
| 2 | 3 | 3 | 2 | 2 | 2 | 2 | 1 |
| 2.1 | 3 | 3 | 3 | 2 | 2 | 2 | 2 |
| 2.2 | 3 | 3 | 3 | 3 | 2 | 2 | 2 |
| 2.3 | 3 | 3 | 3 | 3 | 2 | 2 | 2 |
| 2.4 | 3 | 3 | 3 | 3 | 3 | 2 | 2 |
| 2.5 | 4 | 3 | 3 | 3 | 3 | 2 | 2 |
| 2.6 | 4 | 4 | 3 | 3 | 3 | 3 | 2 |
| 2.7 | 4 | 4 | 3 | 3 | 3 | 3 | 2 |
| 2.8 | 4 | 4 | 4 | 3 | 3 | 3 | 3 |
| 2.9 | 4 | 4 | 4 | 4 | 3 | 3 | 3 |
| 3 | 4 | 4 | 4 | 4 | 3 | 3 | 3 |

**Table 4.1**: Calculated number of shells in an MWNT with given outer and inner-most shell diameter.

Attempts were made to obtain nanotube dispersions on mica and on silicon but these did not produce a uniform coverage of the substrate and were not very reproducible. The solvent used for silicon was dichloroethane (DCE) while for mica was ethyl alcohol (ethanol). These choices were made after a literature search: see Ref. [Falvo'97] for the mica dispersion and Ref. [Bourlon'04] for the silicon dispersion. The procedures used for the most successful dispersions on mica and on silicon are described below:

Mica: 10 MWNT fibres were dispersed in 600 μl ethanol and the solution was sonicated in the bath sonicator for over one hour, 10 μl of the solution was deposited on freshly cleaved mica (10×10 mm in size) and allowed to dry on it.

Silicon: 30 MWNT fibres were dispersed in 300 μl DCE and the solution was sonicated in the bath sonicator for over one hour, the solution was diluted 32 times and sonicated for further 15 minutes. 10 μl of the solution was deposited on polished silicon substrate (~10×10 mm in size), which was then rinsed with isopropanol and dried with an air gun. In Fig. 4.6 are shown AFM scans (obtained in tapping mode with the Veeco Multimode AFM) of the best dispersions obtained on Si and on mica.




**Figure 4.6**: **(a)** Arc-grown MWNTs dispersed on Silicon from a solution of DCE. The nanotube coverage was not uniform and most MWNTs were in bundles of 2-3 individual MWNTs. **(b)** MWNTs dispersed on freshly cleaved Mica from a solution made with ethanol. Only large bundles were visible and the nanotube coverage was not uniform over the mica surface.

A polished silicon substrate with a very concentrated MWNT solution dispersed on it (concentrated enough to see 'clumps' of nanotube material on the Si surface with an optical microscope) was used for Raman measurements (these were performed by Dr John Gallop, using a Renishaw Raman Microscope) in order to provide a further estimate of the MWNTs diameter.

In MWNTs with small diameters the observation of peaks in the radial breathing mode part of the Raman spectrum (frequencies in the range 200-500 $cm^{-1}$ – see page 240 in Ref. [Dresselhaus'01]) is possible. These peaks are usually assigned to the innermost tube of the MWNTs (see Ref. [Zhang'03] and page 242 in Ref. [Dresselhaus'01]). This is because interlayer interactions between the carbon shells of an MWNT cause a decrease in the resonant Raman intensity of all but the innermost and outermost shells of an MWNT which have only one neighbouring carbon layer, while the others have two; the outermost layer though, on account of its larger diameter, is too low in Raman frequency to be measured, thus leaving only the innermost layer to be available for Raman detection.

The measurements were taken at the laser frequency of 633 nm: the spectra was first taken on a bare portion of the silicon surface and then on an area covered with nanotube material. The two spectra were then subtracted to highlight the peaks due to the nanotube resonances.

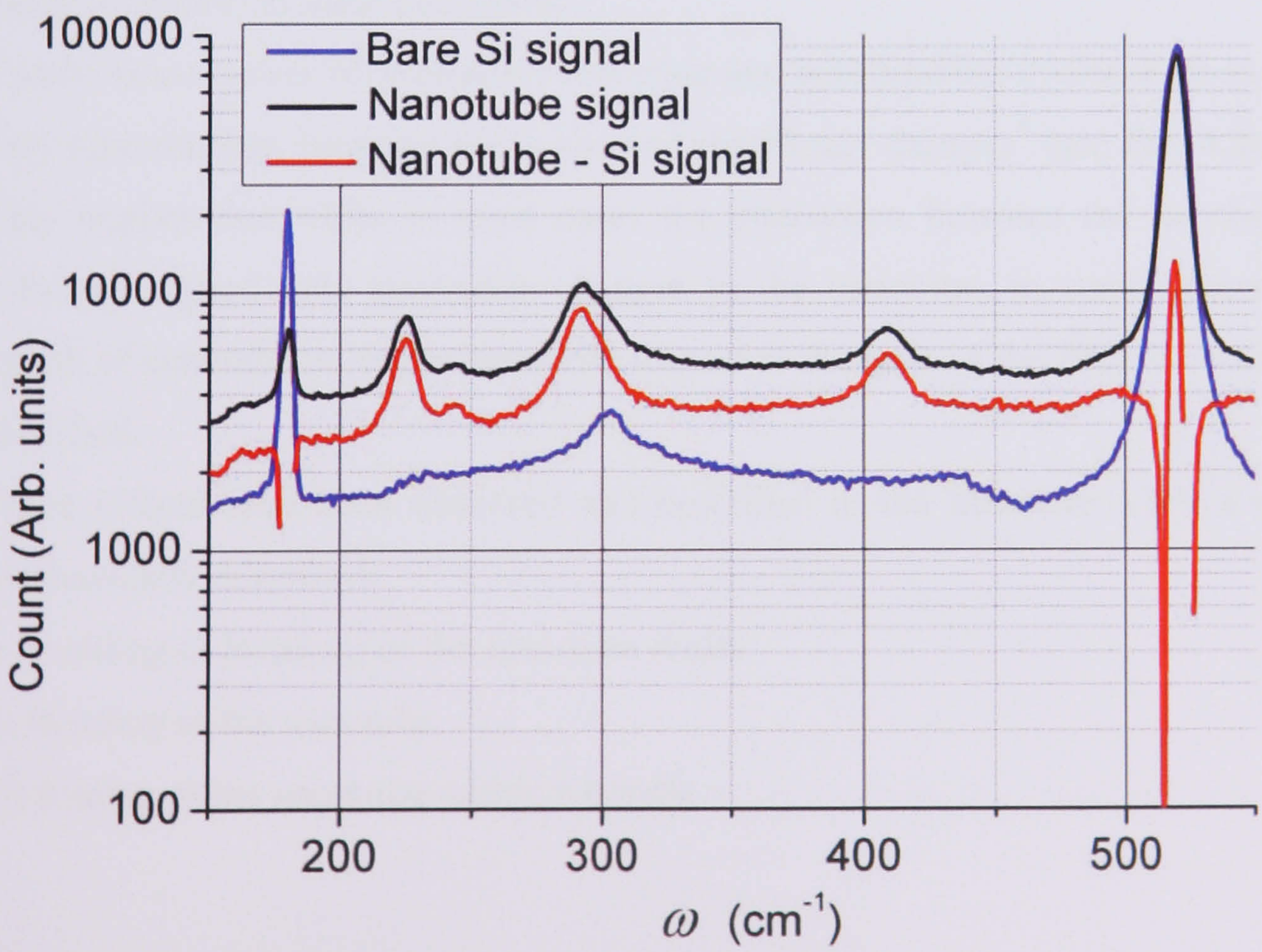



**Figure 4.7**: The Raman spectra of the MWNTs deposited on Si. Radial breathing mode peaks are seen at 225, 293 and 408 $cm^{-1}$, corresponding to MWNTs with inner diameters of 1.01, 0.78 and 0.56 nm respectively (data courtesy of Dr John Gallop).

Nanotube peaks in the range for radial breathing modes (RBM) were seen at 225, 293 and 408 $cm^{-1}$ (see Fig. 4.7). The predicted innermost shell diameters from these peaks are: 1.01, 0.78, 0.56 nm respectively, corresponding to nanotubes with indices: (11,3), (8,3) and (5,3). These were calculated using equation (see Ref. [Saito'98b] and [Zhang'03]):

$$\omega_{(n,m)} = \frac{223.75}{d_{(n,m)}} = \frac{223.75 \cdot \pi}{a\sqrt{n^2 + m^2 + nm}} \qquad (4.1)$$

where $\omega$ is the radial breathing mode frequency (in $cm^{-1}$) and $d$ is the nanotube diameter (in nm); $n$ and $m$ are the tube indices and $a$ is the lattice constant of the honeycomb carbon lattice: $a = 0.249$ nm (see also equation 2.1).

These values of the MNWT innermost diameters are in agreement with those reported in Ref. [Qin'00] and provide some albeit limited support to the assumption that the MWNTs used in this work had an outer diameter < 2 nm and were made of between 2 and 3 concentric shells.

## 4.1.2 Bending and Buckling of the MWNTs

In this work nanotubes were repeatedly brought in and out of contact with a hard substrate (HOPG or Au), in this section it will be discussed how the nanotubes were likely to deform in these processes.

Conductance curves of successive lowering and withdrawing cycles were in most cases very reproducible, however some showed significant changes* (see Fig. 4.8a and 4.8b). This implies that while in most cases the interaction between the nanotube and the substrate caused only reversible changes to the nanotube, in some others either the length of nanotube or its position with respect to the bulk of the fibre (or both) had been modified.

Three effects have been observed and described in the literature when a nanotube is mechanically deformed:

i) Buckling or breaking of the nanotube shells

ii) Bending of the nanotube

iii) Sliding of the nanotube within a bundle

---

* Small differences in the distance between making contact on approach and breaking contact on withdrawal were attributed to drift in the separation between cantilever and substrate during the course of the measurements, believed to be due to laser warming of the cantilever.

i) **Buckling or breaking of the nanotube shells**. Under high tensile or compressive stresses along the MWNTs axis, the MWNTs' shells have been observed to break or buckle irreversibly thus changing the overall nanotube length.

In [Yu'00] Yu et al reported that the outermost shell of an arc-grown MWNT was broken under high tensile stresses (the forces applied at fracture ranged from 390 to 1340 nN) and that the length of the fragments far exceeded that of the original nanotube. This was explained by a "sword-in-sheath" fracture mechanism in which the inner shells were pulled out during the fracture. In [Waters'05] Waters et al observed that at high compressive stresses the shells of MWNTs buckle in an irreversible way, thus shortening the overall length of the nanotube. They measured the critical buckling load

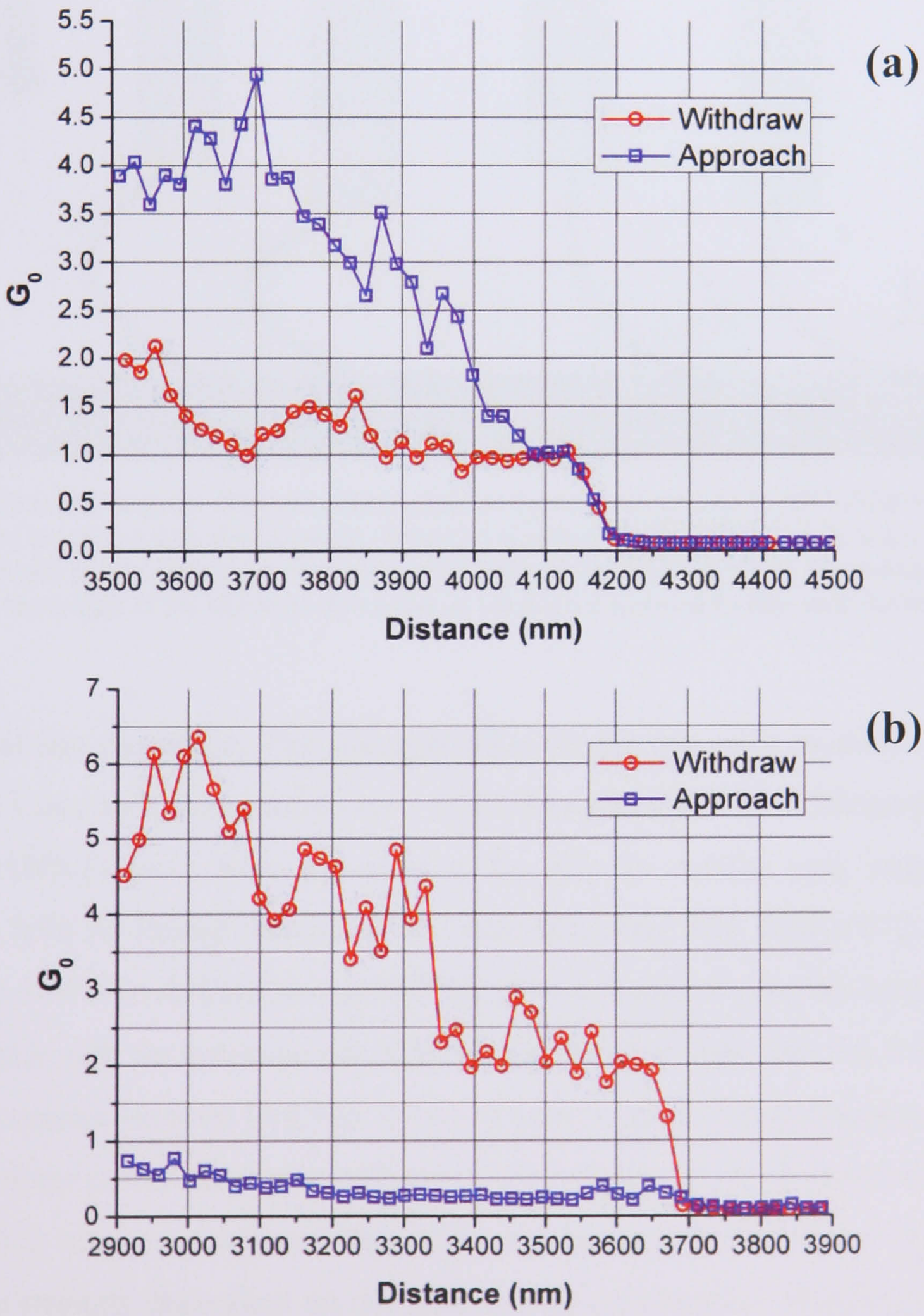



**Figure 4.8**: Electrical conductance traces of successive withdraw/approach curves. The curves shown in **(a)** show good reproducibility while those in **(b)** didn't. These curves were taken in vacuum with the same probe and tip and have been corrected for the slight drift attributed to the heating of the AFM piezo during operation in high vacuum.

to be between 2 and 2.5 μN.

In both these experiments the nanotubes were firmly anchored during the extension-compression measurements, and the forces were applied to individual nanotubes.

In this work the typical forces applied to the most protruding nanotubes from the MWNT fibre were <200 nN[§] and the nanotubes were not anchored in any way to the substrate. It is thus highly unlikely that the changes in nanotube length/position observed are due to the breaking or buckling of nanotube shells.

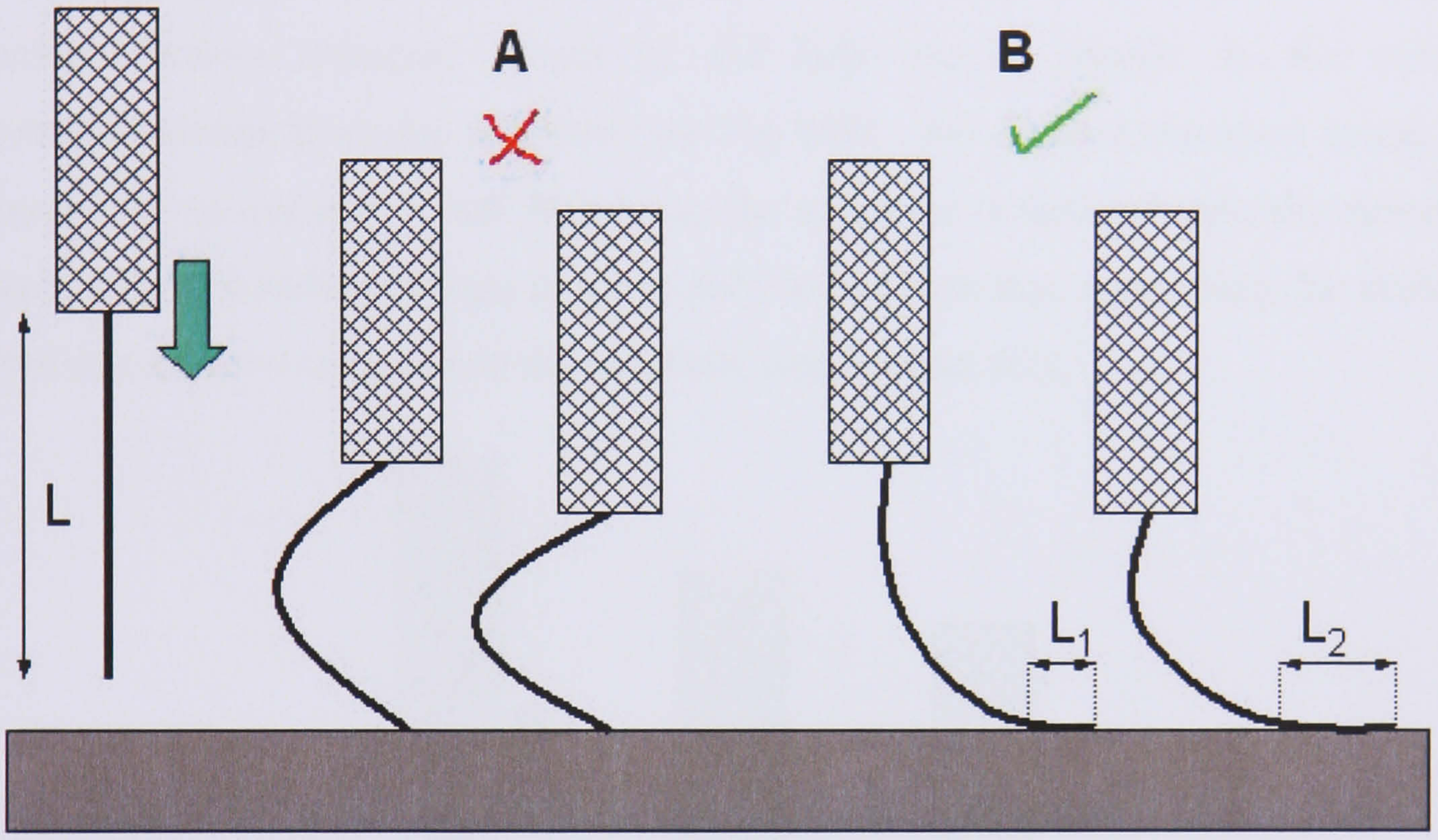



**Figure 4.9**: Schematic diagram of what could happen as the most protruding MWNT from the bulk of the fibre comes in contact with the substrate. From the electrical conductance curves it is most likely that the tube bends gently sliding on the surface (B) rather than stays pinned to the contact location (A). In case B the length of the nanotube decreases as the fibre is lowered further onto the substrate.

ii) **Bending of the nanotube**. The average value for the Young's modulus of an arc-grown MWNT has been measured to be ~ 810 GPa (see page 379 in [Dresselhaus'01]). Arc-grown MWNTs have been observed to be able to sustain very large bending deformations with no lasting damage to the nanotubes (see Ref. [Falvo'97]). It is very likely that the MWNTs do bend as the MWNT fibre is lowered onto the hard substrate. When in contact with the substrate the MWNT could either slide (see Fig 4.9B) or stay pinned to the contact location (see Fig. 4.9A), however, the fact that plateaus of lengths of hundreds of nm in the electrical conductance curves have been observed in this work (see Section 4.2) rules out the latter. This is because the electrical transport properties of nanotubes are strongly dependent on the type of tube deformation. Bending a nanotube

---

[§] These forces were estimated from the F-D curves acquired with the AFM using the nominal spring constant of the Veeco thermal probes (~ 5 N/m) and are thus subject to considerable uncertainty. There are plans to perform an accurate calibration of the thermal probes spring constant in the near future.

by an angle >10° has been observed to cause a reduction in its electrical conductance by up to two orders of magnitude (see Ref. [Tombler'00]); however small elastic strains have been observed not to cause any changes in the electronic properties of the tubes (see Ref. [Tekleab'01]).

This gentle bending of the nanotube as they slide on the substrate is thus in agreement with what is observed in the electrical conductance measurements and with those conductance traces that show remarkable reproducibility after successive lowering and withdrawing cycles. Furthermore, if the MWNTs do slide on the substrate, then the effective electron transport length of the tube would change as the tube is lowered/withdrawn from the substrate (see Fig 4.9B – the electron transport length L is decreased by an amount $L_1$ and then $L_2$ as the nanotube is lowered onto the substrate) without a corresponding change in electrical conductance thus supporting the evidence for ballistic electron transport in the nanotube (see Section 4.2).

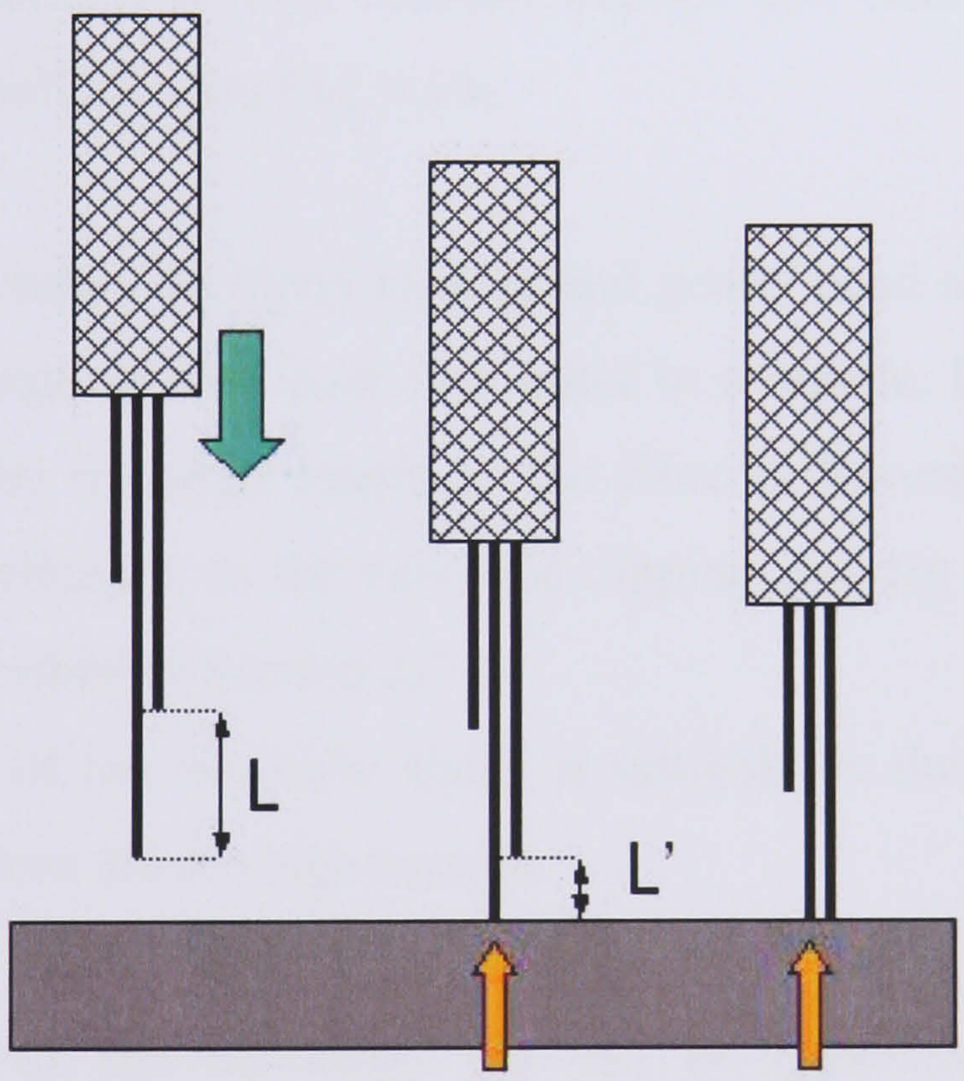



**Figure 4.10**: Diagram showing the sliding of MWNTs in a bundle past each other as the most protruding nanotube (indicated with an orange arrow) comes in contact with the substrate. Given that the shear modulus is lower than the Young's modulus of the nanotube by about two orders of magnitude, tubes are likely to slide rather than bend (unless something stops the sliding motion). The electron transport length of the tube, L, decreases as the nanotube fibre is lowered onto the substrate.

iii) **Sliding of the nanotube within a bundle**. The shear modulus of single-walled nanotubes sliding past each other within a bundle was measured by Salvetat et al (see Ref. [Salvetat'99]) to be ~1 GPa. Assuming that the shear modulus between MWNTs in a bundle is of the same order of magnitude, it is likely that the MWNTs could slide past each other as the MWNT fibre is lowered towards the substrate. When the fibre is withdrawn, capillary forces or van der Waals forces between the substrate and the

MWNT in contact with it could also cause the MWNTs to slide. Given that the Young's modulus of the MWNTs is typically two orders of magnitude larger than the shear modulus of the MWNTs in a bundle, nanotubes would be expected to slide past each other rather than bend unless something causes the sliding to stop. This could be due to imperfections in the bundle and/or crosslinking between the outermost shells of the MWNTs (as suggested by Salvetat et al).

Sliding of the nanotubes within a bundle could explain why, in this work, on some occasions, conductance curves of successive lowering and withdrawing cycles have been observed to show significant differences. This scenario would also be in agreement with the electrical conductance plateaus observed in this work and support the claim of ballistic electron transport in the tubes (see Section 4.2): as the most protruding nanotube in a bundle comes into contact with the substrate, it starts sliding more into the bulk of the bundle, thus causing the length of the free tube to decrease, however the fact that the electrical conductance stays constant implies that electron transport is length independent and thus ballistic (see Fig. 4.10).

In conclusion the nanotubes are likely to slide and gently bend as they are brought into contact with the substrate or slide past each other in a bundle. Both scenarios imply a change in the nanotube transport length as the fibre is lowered/withdrawn from the substrate similar, in principle, to the nanotube-dipping-into-Hg experiment performed by Frank et al and described in Section 2.2.2.

Breaking or buckling of the nanotube shells is unlikely as the forces applied by the thermal probe to the tubes are not high enough.

The spring constant of the nanotubes (k) can be estimated from the nanotube dimensions and its Young's modulus:

$$k = \frac{AY}{l} \qquad (4.2)$$

A is the nanotube cross sectional area, Y the nanotube Young's modulus and l the length of the nanotube.

Using Y = 810 GPa, l = 1 μm, and deriving A from the average inner and outer shell diameter values calculated in Table 4.1, the value of k is ~ 1 N/m. This is of the same order of magnitude as the nominal spring constant of the Veeco thermal probe (5 N/m). Thus the amount of deflection of the probe and that of the nanotubes are expected to be in the same order of magnitude.

## 4.2 Observation of Ballistic Electron Transport in MWNTs at Room Temperature

In Fig. 4.11 are shown three electrical conductance traces. These were taken at room temperature and pressure with the same MWNT fibre mounted on the Veeco thermal probe, using the set-up described in Section 3.3. The data shown was taken while the fibre was lowered onto the HOPG substrate, in all three curves the approach speed was 50 nm/s; in curve (a) the readings were taken every 5.5 nm of travel while in curves (b) and (c) the readings were taken every 4 nm. The bias voltage applied between the graphite substrate and the MWNT fibre ($V_i$) was 9 mV, the gain (G) set on the Stanford Preamplifier was 1000 and the standard resistance in series with the nanotube-graphite resistance ($R_s$) was 1 kΩ.

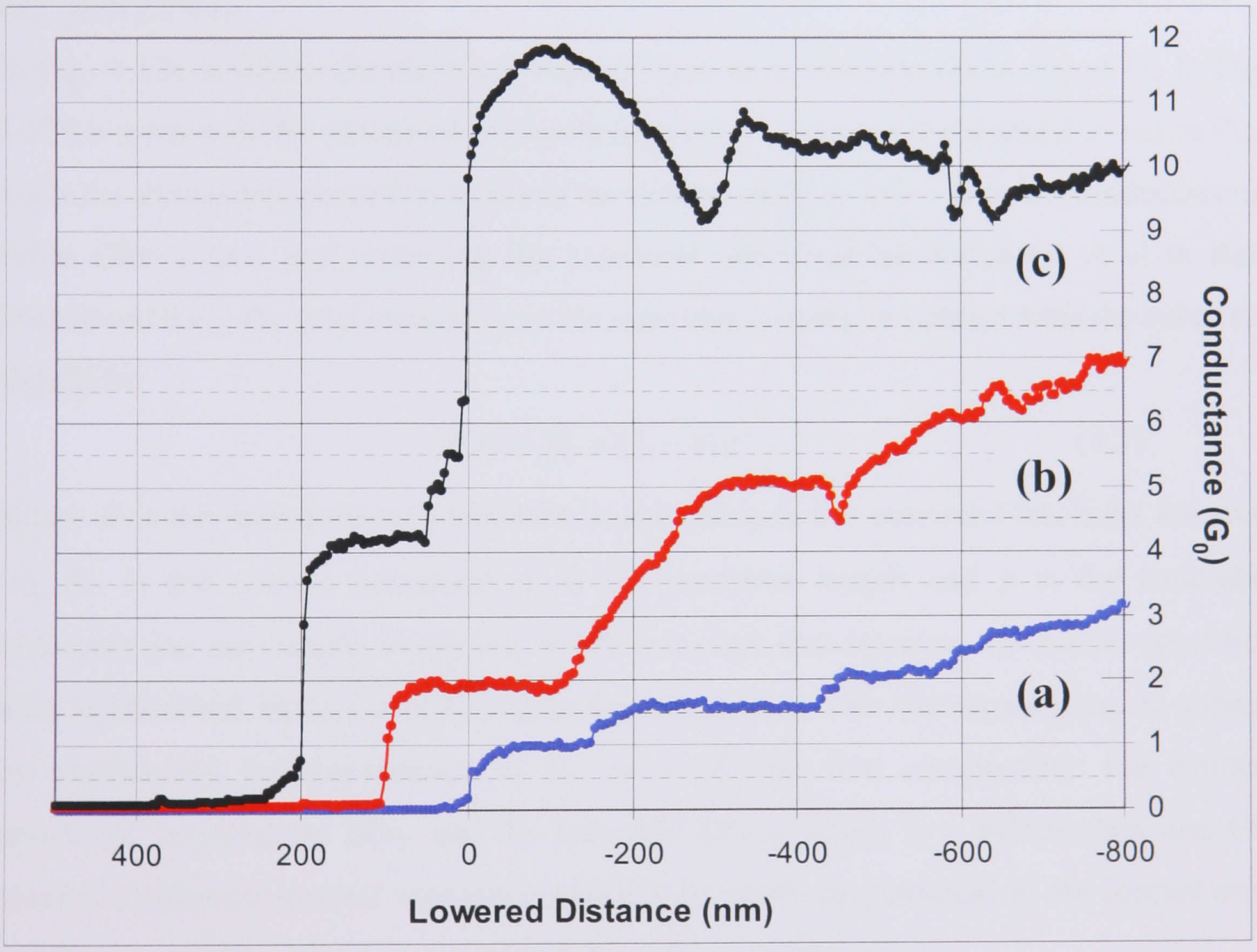



**Figure 4.11**: **(a)** Conductance trace showing three steps, the step heights are $1G_0$ and $0.5G_0$. **(b)** Conductance trace with step of height $2G_0$. **(c)** Conductance trace with step of $\sim 4G_0$.
The 0 nm position on the x-axis indicates the point of contact between the nanotube and the substrate; positive values indicate the region where the nanotube is away from the substrate, negative values that where the nanotube is in contact with the substrate. Curves **(b)** and **(c)** have been offset for clarity by +100 and +200 nm respectively.

Plateaus and step-like increases in the electrical conductance traces shown in Fig. 4.11 are visible. The step-increases in the conductance are due to successive individual

MWNTs protruding from the bulk of the MWNT fibre coming in contact with the HOPG substrate.

Evidence for ballistic transport is given by the long plateaus where the electrical conductance of the MWNTs does not change while the MWNT fibre is moved towards the substrate a distance of several tens of nanometres. As discussed in Section 4.1, moving the MWNT fibre towards the substrate causes the electron transport length in individual nanotubes to decrease, thus the electrical conductance plateaus show that electron transport in the MWNTs is independent of the tube length and hence ballistic (in classical conductors the conductance is proportional to the inverse of the length of the conducting element). Most plateaus are between 50 to 250 nm in length, values that closely resemble those reported by Frank et al in Ref. [Frank'98].

It is possible to estimate the electronic mean free path from a detailed analysis of the plateaus using the formulas derived by Poncharal et al in Ref. [Poncharal'02] (see also Ref. [Berger'02]).

In Fig. 4.12a is shown the electrical conductance trace of curve (b) in Fig. 4.11, in Fig. 4.12b a portion of the same plateau (corresponding to the area highlighted in red in Fig. 4.12a) is shown represented in terms of the resistance ($R = 1/G$ – G is the conductance). From Ohm's law, and following the argument described by Poncharal et al in Ref. [Poncharal'02][*], the total resistance of the nanotube coming in contact with the substrate should be:

$$R(x) = R_C + (L - x)\rho \qquad (4.3)$$

where $R$ is the resistance as a function of the distance the nanotube has been lowered ($x$), $R_C$ is the contact resistance, $L$ is the nanotube length and $\rho$ is the nanotube resistance per unit length. From Fig. 4.12b is it clear that equation 4.3 poorly describes what is observed, since $R$ is not linearly dependent on $x$. This discrepancy can be solved by considering the dependence of $R_C$ on $x$. $R_C$ has two components: the contact resistance between the fibre and the nanotube ($R_{N\text{-}F}$) which is $x$ independent and the nanotube-substrate contact resistance which is inversely proportional to the contact area and hence to $x$ ($R_{N\text{-}S}/x$). Thus equation 4.3 can be re-written as:

$$R(x) = R_{N\text{-}F} + (L - x)\rho + R_{N\text{-}S}/x \qquad (4.4)$$

---

[*] Poncharal et al used these formulas to describe the conductance curves obtained when dipping an MWNT fibre in liquid mercury; as the submerged portion of the nanotube did not contribute to the conduction the dipping had the effect of shortening the nanotube length. In this work, the nanotubes were not submerged but, following the arguments developed in section 4.1.2, their conduction length was also shortened as they were lowered onto the graphite substrate. This was either due to the nanotube sliding on the graphite substrate or being pushed further into the bulk of the bundle it was protruding from.

From equation 4.4 an upper bound for $\rho$ can be estimated by measuring the slope of

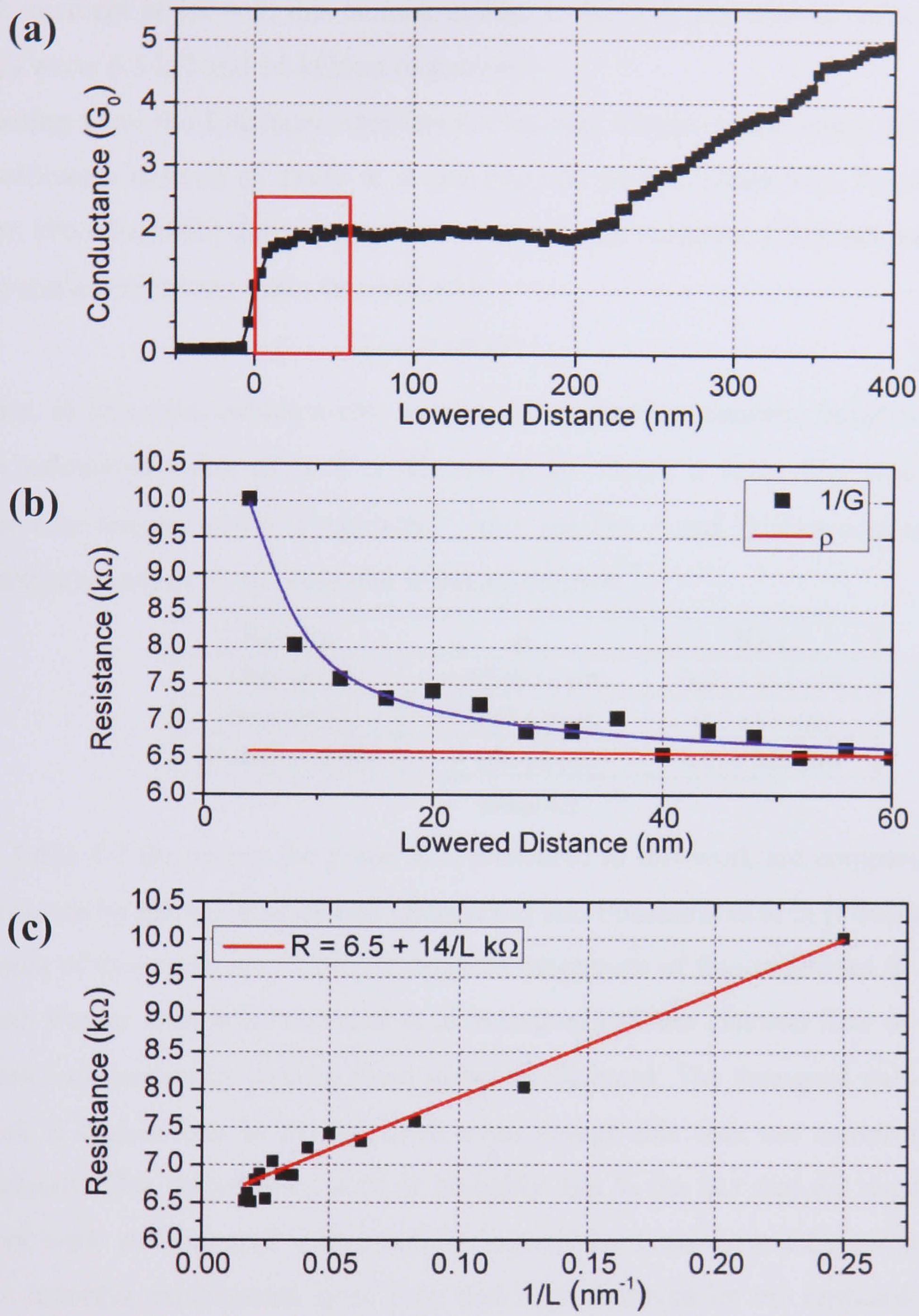



**Figure 12**: **(a)** The electrical conductance trace of curve b in Fig. 11. **(b)** The portion of the curve in the red rectangle in (a) is plotted as resistance (R=1/G). The slope of the curve at large distance values is an upper bound on the value of $\rho$: the nanotube resistance per unit length. **(c)** The resistance is plotted as a function of 1/L where L is the lowered distance in nanometres. The curve is fitted with a straight line; the slope of the line is determined by the nanotube-substrate contact resistance while the intercept of the line at 0 is determined by the nanotube-fibre contact resistance.

$R(x)$ at large $x$ values (where the term in $1/x$ will be negligible). From Fig. 4.12b, the upper bound for $\rho$ was found to be 1Ω/nm (equivalent to 1kΩ/μm). Given the low value of $\rho$, equation 4.4 can be approximated to:

$$R(x) \approx R_{N-F} + R_{N-S}/x \qquad (4.5)$$

Equation 4.5 allows the values of $R_{N\text{-}F}$ and $R_{N\text{-}S}$ to be derived by plotting $R(x)$ versus $1/x$ and fitting the curve with a straight line: $R_{N\text{-}S}$ will be the slope of the linear fit and $R_{N\text{-}F}$ the intercept at $1/x = 0$; this is done in Fig. 4.12c. The thus derived values of $R_{N\text{-}F}$ and $R_{N\text{-}S}$ were: 6.5 kΩ and 14 kΩ/nm respectively.

Starting from the Landauer equation for ballistic transport, and using the transmission coefficients derived by Datta et al (see page 62 of Ref. [Datta'97]), Poncharal et al in Ref. [Poncharal'02] derive the relation between the nanotube resistance per unit length ($\rho$) and its electronic mean free path ($\lambda$):

$$\lambda = 1/(nG_0\rho) \qquad (4.6)$$

Thus, in this case, setting $n$ (the number of conducting channels) equal to 2 and using the calculated value of $\rho$, $\lambda$ is derived to be >6μm; a value that well exceeds the nanotube length (which is typically < 1μm, see Fig. 4 and 5), thus confirming that the electron transport in the nanotube is indeed ballistic.*

| Source | ρ | $R_{N\text{-}S}$ |
|---|---|---|
| This work | < 1000 Ω/μm | 0.014 kΩ μm |
| [Berger'02] | < 200 Ω/μm | 0.2 kΩ μm |
| [Poncharal'02] | < 100 Ω/μm | 0.1-1 kΩ μm |

**Table 4.2**

In Table 4.2 the values for $\rho$ and $R_{N\text{-}S}$ measured in this work are compared with those measured by Berger et al in Ref. [Berger'02] and Poncharal et al in [Poncharal'02]. The values of this work are within an order of magnitude of those reported in the literature (both Berger et al and Poncharal et al measured ballistic electron flow in nanotubes at room temperature by dipping them in liquid mercury). The measured value of $\rho$ in this work is higher than in the literature, even though this does not compromise ballistic transport. This discrepancy is most probably due to the fact that the nanotubes in this work were still covered with graphitic impurities, these were not present in the other two reported experiments since they had been removed by the repeated dipping into mercury (as reported by Poncharal et al in [Poncharal'02]). The value or $R_{N\text{-}S}$ though is lower than that of the nanotube-mercury contact. This is not unexpected as the substrate used was HOPG, which is made of carbon like the MWNTs, and has a similar workfunction .

The step heights observed in the electrical conductance traces varied from small fractions of $G_0$ (about 0.2-0.4$G_0$) to several units of $G_0$.

---

* If the value of $\rho$ obtained by Berger et al (200Ω μm) is used in equation (4.6), setting $n$ equal to 2, the value of $\lambda$ is >30μm as reported in Section 2.2.2.

The origin of the fractional conductance values has been discussed in Section 2.2.2. However sometimes the fractional steps appear as short pre-steps before the 'major' conductance steps (see Fig. 4.13 which corresponds to curve a in Fig. 4.11). The height of these pre-steps is usually half the height of the major steps (see Fig. 4.13), their length varies from about 6 to 20 nm; Frank et al. observed in Ref. [Frank'98] pre-steps of width in the range of 10-50 nm and, given their length, they attributed them to the tip structure of the MWNTs. It is thus possible, given the similarities between the two experiments, that the pre-steps observed are due to the tip first coming in contact with

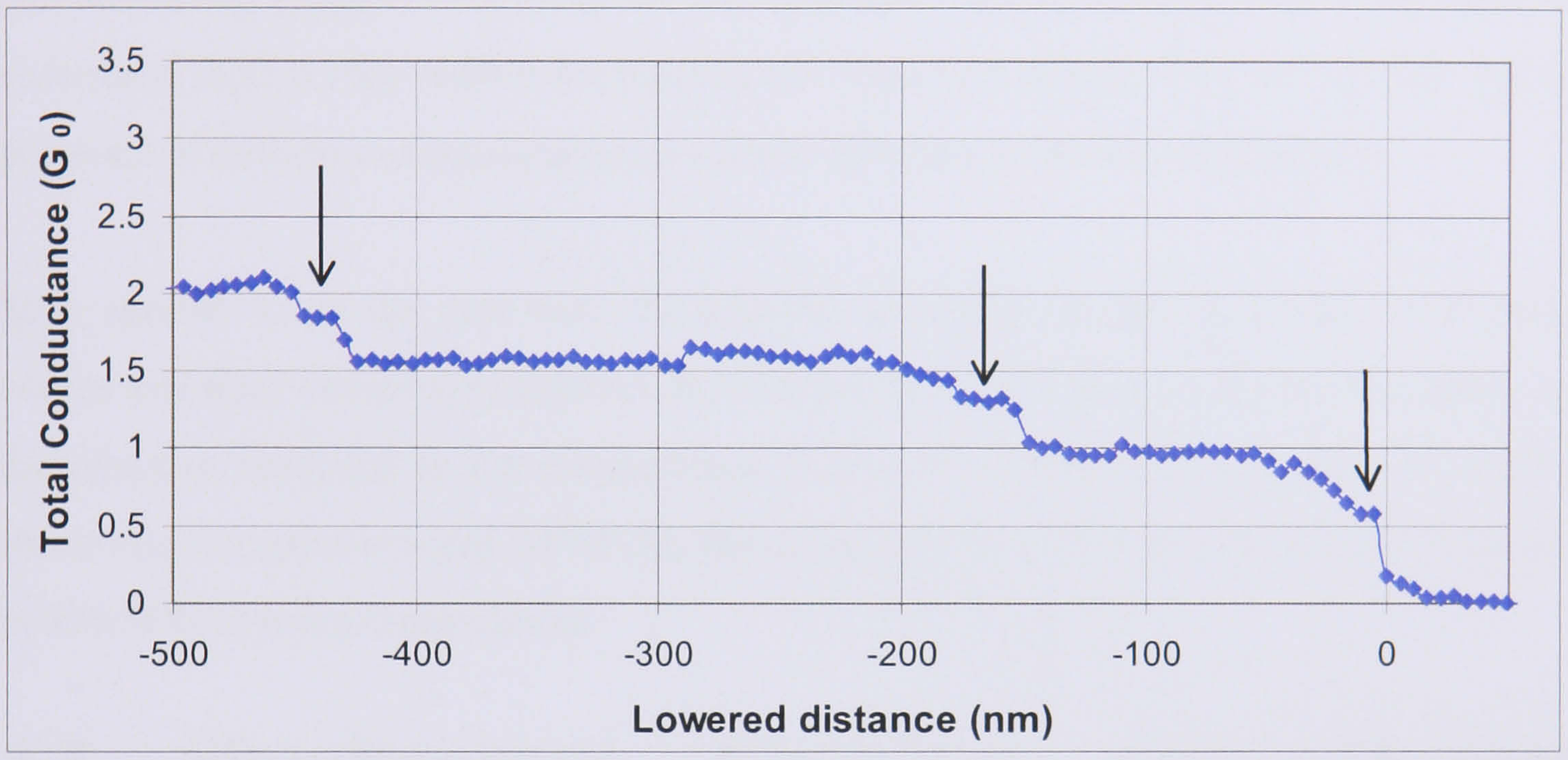



**Figure 4.13**: The conductance curve a in Fig. 4.11 is shown with the pre-steps indicated by arrows. The pre-step height is about half the height of the major step (about 0.5 $G_o$ for the first step of $G_o$, then about 0.3 $G_o$ for the subsequent smaller steps of 0.6 $G_o$) and their length is in the range 6-20 nm.

the HOPG, then, as the tube is further pushed towards the graphite substrate, the tip slides away and the side of the MWNT contacts the HOPG. The reduced conductance can be explained in terms of the tip-to-shaft interface which can scatter the electrons thus reducing the transmission coefficient (semiclasically this could be interpreted as an extra series resistance in equation 4.4: $R_{N\text{-}T}$, the nanotube-tip resistance, which is $x$ independent. The extra series resistance reduces the height of conductance step when the tip of the nanotube first contacts the substrate).

Frank et al [Frank'98], Berger et al [Berger'02] and Poncharal et al [Poncharal'02] all reported to have never observed steps higher than $1G_0$ but in this work steps of 2, $\sim 3G_0$ have been observed (see curves b and c in Fig. 4.11). These values imply that, in some occasions at least, there was more than one carbon shell contributing to the electron transport (see Section 2.2.2 and Ref. [Collins'02])

Diffusive behaviour is also observed in the electrical conductance traces: in curve b in Fig. 4.11 and in Fig. 4.12a the plateau at $2G_0$ is followed by a region where the conductance increases linearly with distance – as expected for a diffusive conductor. In this region the resistance dependence on the lowered distance ($x$) is well described by equation 4.3. Plotting $R$ versus $x$, and measuring the slope of the curve, the value of $\rho$ was found to be 18 kΩ/μm; this corresponds to a mean free path of ~ 300nm (calculated using equation 4.6), which is shorter than the average nanotube length of 500-1000 nm. The diffusive nature of some nanotubes can be explained as due to defects or contaminating graphitic particles on the nanotube outermost shell; this is because the outermost shell is responsible for most of the electronic transport in the MWNT and the presence of defects and nanoparticles creates electron scattering centres on it.

So it appears to be the case that, the presence of diffusive regions in the conductance curves and their obviously different dependence on $x$, acts as a further confirmation that the plateaus observed in the conductance curves are indeed due to a different type of electronic transport in some MWNTs, thus strengthening the claim for ballistic transport in MWNTs at room temperature.

## 4.3 Simultaneous Electrical and Thermal Measurements on MWNTs at Room Temperature

The simultaneous measurements of the nanotube electrical and thermal conductance were taken using the set-up described in Section 3.7.1. The aim of this work was to measure the thermal properties of the nanotubes and to see their correlation (or lack of) to the electrical properties. Furthermore, the electrical conductance signal was used to estimate the number of nanotubes in contact with the substrate, using the assumption that each (metallic) nanotube in contact with the substrate would contribute an amount $G_0$ to the electrical conductance (as described in [Frank'98] and in Section 4.2).

In Fig. 4.14 and 4.15 are shown graphs with the three simultaneous measurements as MWNTs were withdrawn from a substrate (HOPG). The thermal and the electrical conductance are shown in units of $G_{th}$ and $G_0$ respectively, while the force applied by the probe on the nanotubes is indicated in nN.

In Fig. 4.14 the thermal and electrical conductance curves closely follow each other, and to each electrical conductance step corresponds a thermal conductance step. Curves where the two conductances are not related were also observed, as shown in Fig. 4.15 where the thermal conductance drops to 0 well after the electrical conductance.

There are two reasons for any discrepancies between the two conductances: a) metallic tubes only would cause a change in the electrical conductance trace while both metallic

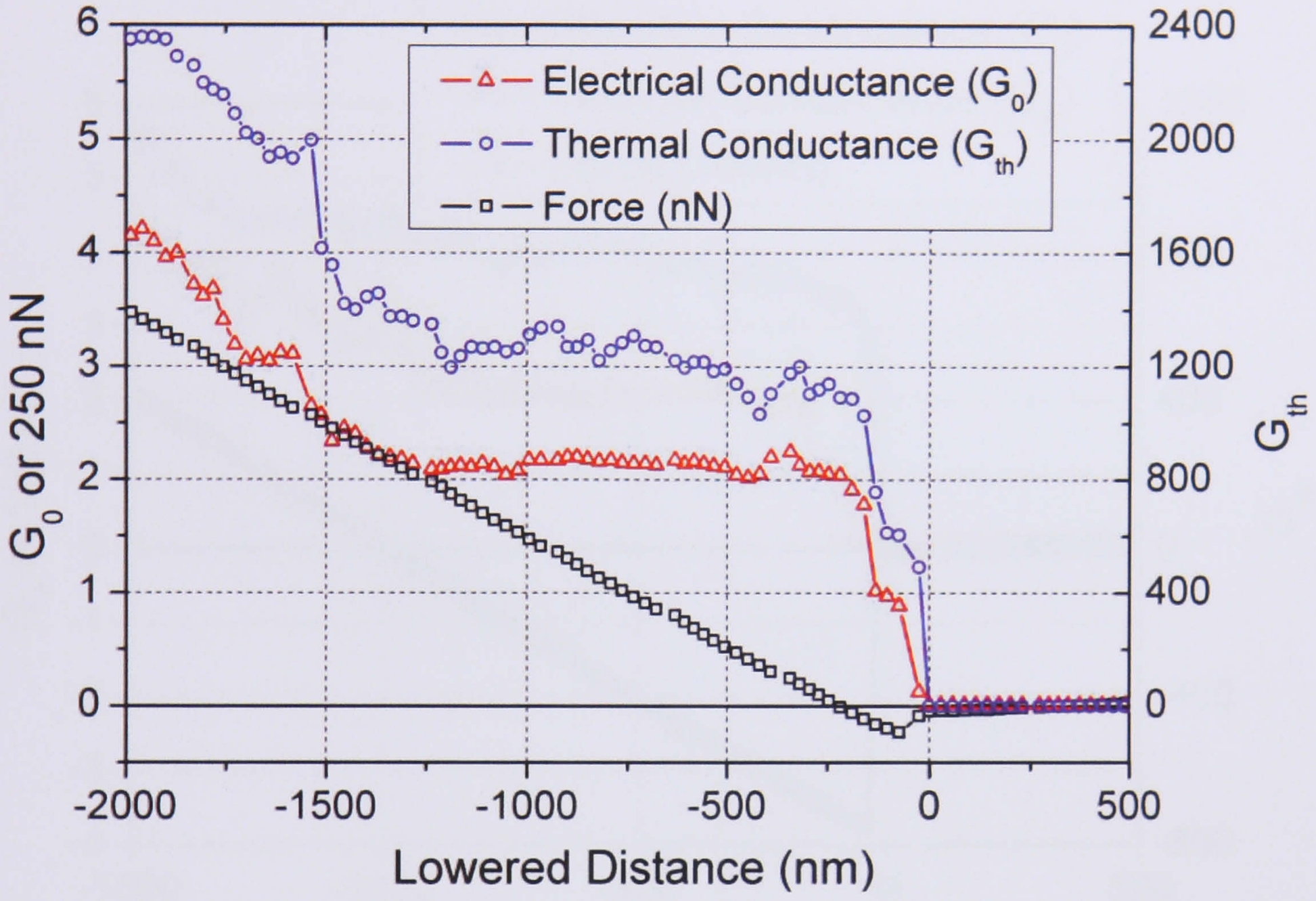



**Figure 4.14**: The three simultaneous measurements on the MWNTs as they were withdrawn from the substrate (HOPG in this case): electrical and thermal conductance and the force applied on the nanotubes by the AFM cantilever. The measurement was taken at room temperature and pressure with the set-up described in Section 3.7.1, using a bias $V_i$ of 500mV, a series resistance $R_S$ of 100kΩ. The data points were acquired every ~30nm of travel and the withdraw speed was 60nm/s. The temperature gradient across the MWNT fibre was ~100K.

and semiconducting nanotubes are expected to conduct heat and thus contribute to the thermal conductance; b) the electronic contribution to the heat flow is negligible at room temperature for all nanotubes, semiconducting and metallic (see page 284 in Ref. [Dresselhaus'01]). Explanation (a) seems to fit the situation in Fig. 4.15, given that both the force curve and the thermal conductance curve go to 0 at the same time and both at larger distances than the electrical conductance trace, it can be concluded that the last nanotube to lose contact with the substrate was a semiconducting tube, which made no contribution to the electrical conductance.

The correlation between the electrical and thermal conductance steps was studied by plotting the thermal step size (measured in units of $G_{th}$) versus the corresponding electrical step size (in units of $G_0$), this study was thus limited to metallic nanotubes in

the MWNT fibre since only traces with simultaneous electrical and thermal conductance steps were selected; the data is shown in Fig. 4.16. The data of Fig. 4.16 was taken using the set-up described in Section 3.7.1; all the data was taken with the same MWNT fibre, at pressures ranging between 4.5-4.0 $\times$ $10^{-5}$ mbar to avoid the thermal measurement being affected by conduction and/or convection through the air. The temperature difference across the MWNT fibre as measured with the Veeco thermal

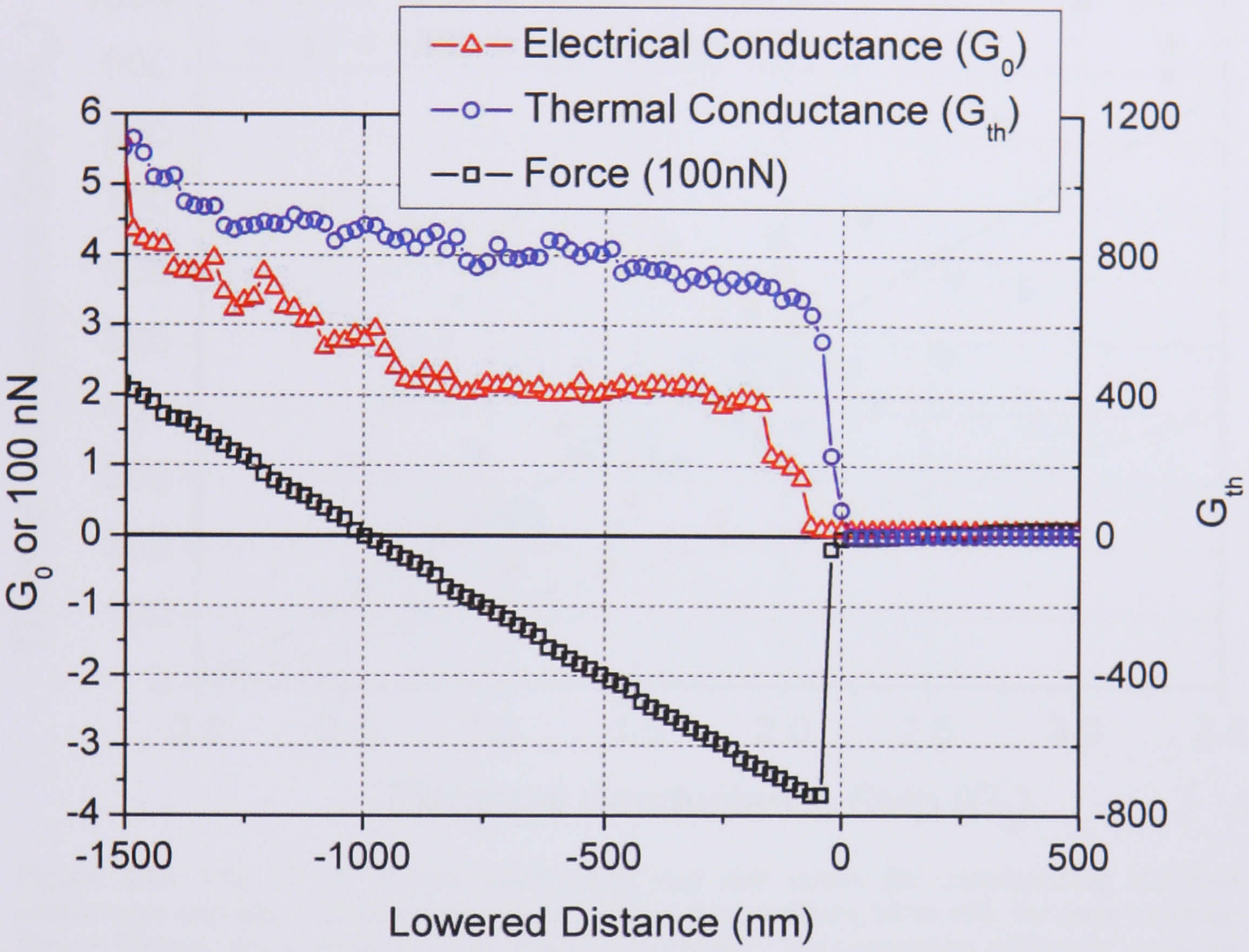



**Figure 4.15**: The three simultaneous measurements on the MWNTs as they were withdrawn from the substrate (HOPG). The measurement was taken at room temperature and at pressure of 2.0 $\times 10^{-5}$ mbar with the set-up described in Section 3.7.1, using a bias $V_i$ of 10mV, a series resistance $R_S$ of 10k$\Omega$. The data points were acquired every ~20nm of travel and the withdraw speed was 40nm/s. The temperature gradient across the MWNT fibre was 55K.

probe ranged from 192K to 299K, the substrate used was HOPG and it was at room temperature (296K); the voltage bias applied between the nanotube and the HOPG substrate ($V_i$) was 0.5V and the series resistance $R_S$ was 100k$\Omega$.

The data in Fig. 4.16 lies preferentially along a line passing through the origin*, a linear fit of the data has been superimposed and is indicated by a solid line: its slope is $250G_{th}/G_0$. Assuming that each individual nanotube contributed $1G_0$ to the electrical

* The fact that the fit passes through the origin is important as it shows that the nanotubes in this set of data all contributed to both electrical and thermal conductance. If some nanotubes had not contributed to the electrical conductance the fit would have crossed the y-axis at a positive value. Such an example is shown in Fig. 4.16 and 4.18 and is discussed in Section 4.4.

conductance trace, the conclusion is that, on average, each metallic nanotube contributed $250G_{th}$ to the thermal conductance: this is independent of the temperature difference across the nanotube.

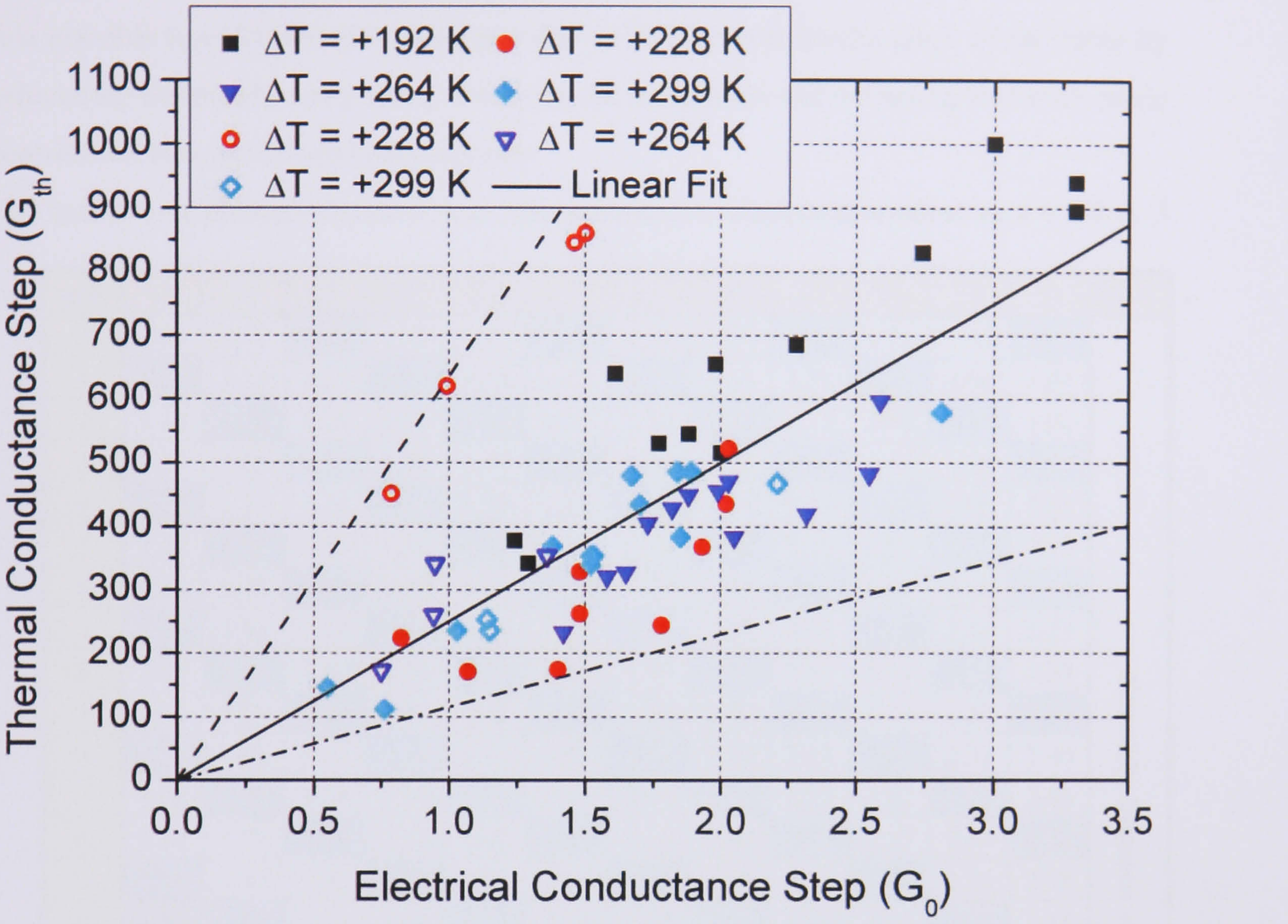



**Figure 4.16**: Plot of the thermal conductance step size versus the corresponding electrical conductance step size. The data comes from 6 sets of measurements, taken with the same nanotube fibre in vacuum (pressures in the range: 4.0-4.5×10-6 mbar). The temperature difference across the nanotube fibre (ΔT) is shown in the legend, in all cases the cold end of the nanotube fibre was at RT (296 K). The solid line is a linear fit to the data that passes through the origin.

The ratio of $G_{th}/G_0$ can be used to estimate the Lorentz number for the metallic nanotubes in the MWNT fibre.

The Lorentz number (L) is defined as:

$$L = \frac{\kappa}{\sigma T} = \frac{\pi^2 k_B^2}{3e^2} = 2.44 \times 10^{-8}\ \mathrm{W\Omega/K^2} \qquad (4.7)$$

where $\kappa$ is the thermal conductivity, $\sigma$ is the electrical conductivity and $T$ is the temperature of the conductor, $k_B$ is Boltzmann constant and $e$ is the electron charge (for a derivation of the Lorentz number see Chapter 2 and Chapter 13 in [Ashcroft'76]); this equation comes from the Wiedemann-Franz law which states that the ratio of the thermal conductivity ($\kappa$) to the electrical conductivity ($\sigma$) of a metal is proportional to the temperature ($T$). Using the average value of $G_{th}$: $4.0\times10^{-4}$ μW/K and the highest temperature in the data set: 595K, knowing that $G_0$ is $(12.9k\Omega)^{-1}$ and that the $G_{th}/G_0$

ratio is 250, the calculated value of the nanotube Lorentz number ($L_{NT}$ – using the conductances rather than the conductivities) is $21.7\times10^{-7}$ $W\Omega/K^2$, i.e. $L_{NT} \sim 100L$. This confirms that the electronic contribution to the thermal conductance of the nanotubes is negligible, as widely accepted in the literature (see page 284 in Ref. [Dresselhaus'01]).

It is possible to calculate the expected value of the thermal conductance of the tubes by calculating the number of phonon modes in the nanotubes and assuming that each mode contributed $1G_{th}$ to the total conductance.

The number of phonon channels (i.e. the number of vibrational modes) in a CNT is 3

| m↓ | 13 | 14 | 15 | 16 | 17 | 18 | 19 | 20 | 21 | 22 | 23 | 24 | ←n |
|---|---|---|---|---|---|---|---|---|---|---|---|---|---|
| 0 | 1.03 | 1.11 | 1.19 | 1.27 | 1.35 | 1.43 | 1.51 | 1.59 | 1.67 | 1.74 | 1.82 | **1.90** | |
| 1 | 1.07 | 1.15 | 1.23 | 1.31 | 1.39 | 1.47 | 1.55 | 1.63 | 1.71 | **1.79** | 1.86 | 1.94 | |
| 2 | 1.12 | 1.20 | 1.28 | 1.36 | 1.43 | 1.51 | 1.59 | 1.67 | 1.75 | 1.83 | **1.91** | 1.99 | |
| 3 | 1.17 | 1.25 | 1.32 | 1.40 | 1.48 | 1.56 | 1.64 | 1.72 | **1.80** | 1.87 | 1.95 | 2.03 | |
| 4 | 1.22 | 1.30 | 1.38 | 1.45 | 1.53 | 1.61 | 1.69 | 1.77 | 1.84 | **1.92** | 2.00 | 2.08 | |
| 5 | 1.28 | 1.35 | 1.43 | 1.51 | 1.58 | 1.66 | 1.74 | **1.82** | 1.89 | 1.97 | 2.05 | 2.13 | |
| 6 | 1.33 | 1.41 | 1.49 | 1.56 | 1.64 | 1.72 | 1.79 | 1.87 | 1.95 | 2.02 | 2.10 | 2.18 | |
| 7 | 1.39 | 1.47 | 1.54 | 1.62 | 1.70 | 1.77 | **1.85** | 1.92 | 2.00 | 2.08 | 2.16 | 2.23 | |
| 8 | 1.46 | 1.53 | 1.60 | 1.68 | **1.75** | 1.83 | 1.90 | 1.98 | 2.06 | 2.13 | 2.21 | 2.29 | |
| 9 | 1.52 | 1.59 | 1.67 | 1.74 | 1.81 | **1.89** | 1.96 | 2.04 | 2.11 | 2.19 | 2.27 | 2.34 | |
| 10 | 1.58 | 1.66 | 1.73 | **1.80** | 1.87 | 1.95 | 2.02 | 2.10 | 2.17 | 2.25 | 2.32 | 2.40 | |
| 11 | 1.65 | 1.72 | 1.79 | 1.86 | **1.94** | 2.01 | 2.08 | 2.16 | 2.23 | 2.31 | 2.38 | 2.46 | |
| 12 | 1.72 | 1.79 | **1.86** | 1.93 | 2.00 | 2.07 | 2.15 | 2.22 | 2.29 | 2.37 | 2.44 | 2.52 | |
| 13 | **1.79** | 1.85 | 1.92 | 2.00 | 2.07 | 2.14 | 2.21 | 2.28 | 2.36 | 2.43 | 2.50 | 2.58 | |
| 14 | | **1.92** | 1.99 | 2.06 | 2.13 | 2.20 | 2.27 | 2.35 | 2.42 | 2.49 | 2.57 | 2.64 | |
| 15 | | | 2.06 | 2.13 | 2.20 | 2.27 | 2.34 | 2.41 | 2.48 | 2.56 | 2.63 | 2.70 | |
| 16 | | | | 2.20 | 2.27 | 2.34 | 2.41 | 2.48 | 2.55 | 2.62 | 2.69 | 2.77 | |
| 17 | | | | | 2.33 | 2.40 | 2.47 | 2.54 | 2.61 | 2.69 | 2.76 | 2.83 | |
| 18 | | | | | | 2.47 | 2.54 | 2.61 | 2.68 | 2.75 | 2.82 | 2.89 | |
| 19 | | | | | | | 2.61 | 2.68 | 2.75 | 2.82 | 2.89 | 2.96 | |
| 20 | | | | | | | | 2.75 | 2.82 | 2.89 | 2.96 | 3.03 | |
| 21 | | | | | | | | | 2.88 | 2.95 | 3.02 | 3.09 | |
| 22 | | | | | | | | | | 3.02 | 3.09 | 3.16 | |
| 23 | | | | | | | | | | | 3.16 | 3.23 | |
| 24 | | | | | | | | | | | | 3.30 | |

Nanotube Diameter ($d_T$) nm

times the number of carbon atoms in the unit cell of the carbon nanotube (for a

**Table 4.3**: The value of the *n* index is indicated in the orange shaded cells. The value of the *m* index is indicated in the yellow shaded cells. The nanotube diameters corresponding to given indices are shown, those corresponding to metallic nanotubes are shaded in turquoise. Amongst those, the ones with the diameter in the range derived from the AFM measurements described in section 4.1.1 are highlighted in bold and shaded in blue.

definition of the CNT unit cell see Section 2.1), where the number 3 is for vibrations along the x, y and z axis for each carbon atom of the tube (see Chapter 9 in Ref. [Saito'98a]).

The number of carbon atoms in the unit cell of a CNT is 2N where N is defined as:

$$N = \frac{2(m^2 + n^2 + nm)}{d_R} \qquad (4.8)$$

In equation 4.8 $n$, $m$ are the nanotube indices and $d_R$ is the greatest common divisor between $(2n+m)$ and $(2m+n)$. Thus, for any given $(n, m)$ nanotube there are 6N phonon modes.

The diameter of a CNT, $d_T$, can also be calculated from its $n$ and $m$ indices using equation 2.1 (see Section 2.1). Thus, for instance, a (10,10) nanotube would have, $d_T$ = 1.4 nm, N = 20 and 120 phonon modes*.

Given the nanotube diameter measured in Section 4.1.1 and the fact that the nanotubes were metallic (since they all contributed to the electrical conductance), there is a range of possible $(n, m)$ indices as shown in Table 4.3.

| (*n*,*m*) | $d_T$ (nm) | N | 6N |
|---|---|---|---|
| 13,13 | 1.79 | 26 | 156 |
| 14,14 | 1.92 | 28 | 168 |
| 15,12 | 1.86 | 366 | 2196 |
| 16,10 | 1.80 | 172 | 1032 |
| 17,8 | 1.75 | 326 | 1956 |
| 17,11 | 1.94 | 398 | 2388 |
| 18,9 | 1.89 | 126 | 756 |
| 19,7 | 1.85 | 362 | 2172 |
| 20,5 | 1.82 | 70 | 420 |
| 21,3 | 1.80 | 114 | 684 |
| 22,1 | 1.79 | 338 | 2028 |
| 22,4 | 1.92 | 196 | 1176 |
| 23,2 | 1.91 | 386 | 2316 |
| 24,0 | 1.90 | 48 | 288 |

**Table 4.4**: The value of N and 6N (the number of phonon modes) have been calculated based on the (n,m) indices of the nanotubes highlighted in Table 4.3. The cells highlighted in yellow correspond to armchair nanotubes, those highlighted in blue to zig-zag nanotubes (see also Section 2.1) and the rest to chiral tubes.

The value of N and the number of phonon modes (6N) for the nanotubes with indices corresponding to the cells highlighted in Table 4.3 have been calculated and are shown in Table 4.4.

It is clear from Table 4.4 that, depending on the nanotube type, tubes with similar diameters can have very different numbers of phonon modes. Zig-zag and armchair nanotubes, because of their higher symmetry, have a lower number of phonon modes than chiral nanotubes.

---

* These values have been derived for single-walled nanotubes. And are thus just first approximations for calculating the number of phonon modes in a multi-walled nanotube.

The highest and lowest $G_{th}/G_0$ ratios, derived from Fig. 4.16 (indicated, respectively, by the dashed and dot-dashed lines on the graph) are: 635 and 115. This scatter, given the uncertainty in nanotube diameter and the fact that, depending on the nanotube indices the number of phonon modes even for tubes of similar diameters can be subject to drastic changes, is limited. It is thus likely that the data acquired was all due to the same nanotube (or possibly a small number of different nanotubes): the one that was protruding the furthest from the MWNT fibre (all the data was indeed taken with the same MWNT fibre).

The value derived from Fig. 4.16 of 250 phonon modes per nanotube is remarkably close to the number of modes in a metallic zig-zag nanotube with indices (24,0) and diameter 1.9 nm (which would be in the range of diameters measured in Section 4.1.1). If this nanotube were indeed the one measured, the fact that the observed number of phonon modes is very close to the calculated one would imply perfect phonon transport along the nanotube, i.e. *ballistic* (scatter free) phonon transport: this is the topic of the next Section.

### 4.3.3 Discussion: Evidence for Ballistic Phonon Transport in MWNTs

Kim et al (see Ref. [Kim'01]) measured the thermal conductivity of an individual MWNT, of diameter 14nm: it was >3,000 W/mK at RT. From their measurements they also estimated the phonon scattering length of the nanotube (due to impurities) to be ~500 nm, which was comparable to the length of the nanotube itself (2.5μm). They thus concluded '*the phonon transport is "nearly" ballistic*'.

Therefore, in sufficiently defect-free nanotubes, well coupled to thermal reservoirs, ballistic phonon transport should be possible even at room temperature.

In this work, there are two pieces of evidence to support the claim that the phonon transport in the nanotubes is ballistic:

1. Both electrical and thermal conductance measurements show little change as the tube is withdrawn from the HOPG surface even though the length of the tube is expected to change by tube sliding or bending in this process (see Fig. 4.14 and 4.15, and Ref. [Brown'05]); this is strong evidence that electron and phonon transport is length independent and thus ballistic.
2. If diffusive transport was assumed, the lower bound on the estimated room temperature *diffusive* thermal conductivity from the data in Fig. 4.16 (assuming the nanotube to be a solid rod of diameter 1.9 nm and a minimum length

estimate of 700 nm – see Fig. 4.4) is $2.5\times10^4$ W/mK. This is an unrealistically high value, a factor of 4 greater than the room temperature thermal conductivity of diamond, and a factor of 10 greater than the thermal conductivity reported by Kim et al in [Kim'01]. Bearing in mind that this is only a lower bound for the conductivity, given that the nanotube is not a solid rod, the only explanation for such high thermal conductivity is thus ballistic transport.

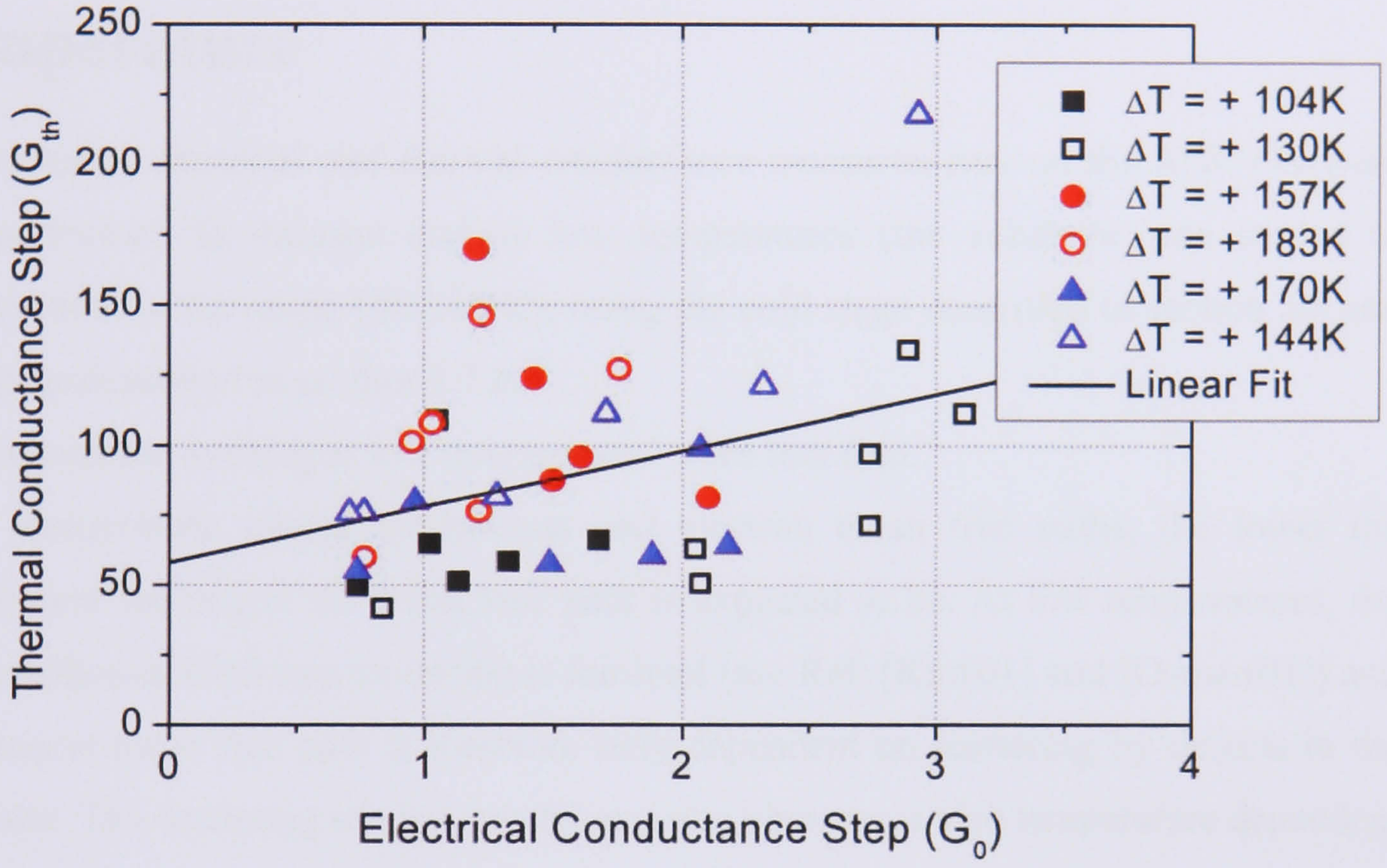



**Figure 4.17**: Plot of the thermal versus its corresponding electrical conductance step. These measurements were taken using HOPG as substrate (kept at room temperature), in vacuum (pressures in the range $5.4–3.9 \times 10^{-5}$ mbar), with a voltage bias ($V_i$) between the nanotube and the substrate equal to 0.5V and the series resistance $R_S$ equal to 10 kΩ. The temperature difference across the MWNT bundle is shown in the legend. The data from 6 different sets of measurements (taken with the same MWNT bundle) is fitted by a straight line with slope $20G_{th}/G_0$.

The observation of regions of diffusive electron transport and their difference from regions of ballistic electron transport was used, in Section 4.2, as an argument to confirm ballistic electron transport in the nanotubes at room temperature. A similar argument can also be used for phonon transport.

In some instances, the measured $G_{th}/G_0$ correlation was greatly reduced from the value shown in Fig. 4.16 and attributed to diffusive phonon transport. One such example is shown in Fig. 4.17, where the linear fit to the data has slope of $20G_{th}/G_0$ (this data is also shown in Fig. 4.18 in Section 4.4 where the reason why the fitted line does not pass through the origin is explained). This low value implies that most phonon modes are reflected along the nanotube. The thermal conductivity of the nanotube in this set of data, is $1.69\times10^3$ W/mK (assuming the nanotube to be a solid rod of diameter 1.9 nm

and to be 700 nm long as done for the data shown in Fig. 4.16*) which is of the same order of magnitude as the thermal conductivity measured by Kim et al in [Kim'01].
The clear difference between the data sets shown in Figures 4.16 and 4.17 is thus a further piece of evidence that two different types of phonon transport were observed in the nanotubes: ballistic (Fig. 4.16) and diffusive (Fig.4.17).

## 4.4 Measurements on MWNTs at Low Temperature

Simultaneous electrical and thermal conductance measurements on the MWNTs were also performed in vacuum and at low temperatures (the substrate was cooled to temperatures in the range 160-180 K), using the cold stage described in section 3.6 and the set-up described in section 3.7.2.
The reasons for working at low temperatures were two-fold.
First: temperature affects the phonon and electron mean free paths, the lower the temperature the longer the mean free path is expected to be. At low temperatures, the phonon-phonon Umklapp scattering is minimal (see Ref. [Kim'01] and [Osman'01]) and the phonon mean free path is therefore only dependent on scattering by defects in the nanotube. The scattering of electrons by acoustic phonons is also temperature dependent and the higher the temperature the higher the scattering rate (see Ref. [Kajiura'05] and [Park'04]), reducing the temperature of the nanotube would thus increase the phonon-electron scattering length thus enabling ballistic transport over longer (defect-free) portions of the nanotube (scattering would be ultimately limited by impurities in the nanotubes).
Second, temperature also determines the number of active optical phonon modes. At low enough temperatures all the optical phonon modes 'freeze' out and only the acoustic phonon modes contribute to heat transport. The temperature necessary to reach this limit is of the order of a few Kelvins, depending on the nanotube diameter, and it is thus beyond the cooling capability of the cold stage used in this work, however, a partial reduction in the number of optical modes was expected.
The correlation between the electrical and the thermal conductance of the nanotubes (expressed in units of $G_0$ and $G_{th}$ respectively) was measured both at room temperature and at lower temperatures: this was done by plotting the height of thermal conductance

---

* The assumption that the same set of dimensions can be used in both cases is reasonable in the light of what observed in Fig. 4.4: i.e. that nanotube dispersions from different fibres gave very similar diameter nanotube distribution.

steps versus the height of their corresponding electrical conductance steps as the nanotube fibre was lowered onto a substrate. As discussed in Section 4.3, from the slope of the curve thus obtained it is possible to extract information about the type of phonon transport occurring in the nanotube and the number of phonon modes transported in each tube.

In Fig. 4.18 are shown two sets of thermal conductance vs. electrical conductance data: one taken at room temperature and one at low temperatures. Both sets of data were

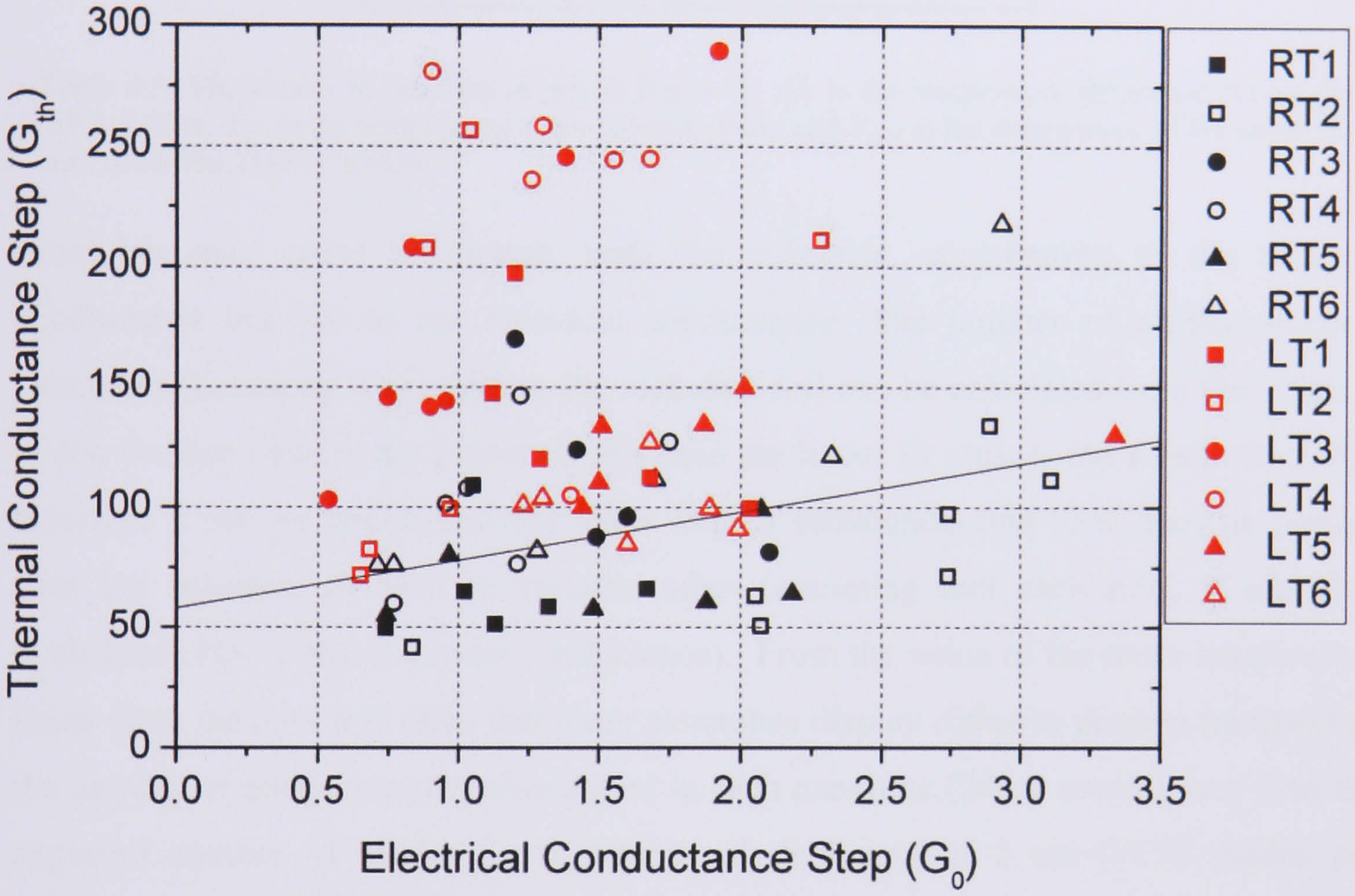



**Figure 4.18**: Thermal conductance step and corresponding electrical conductance step data taken at room temperature (RT) and low temperature (LT) as the nanotube fibre was lowered onto an HOPG substrate. The data was taken with the same nanotube fibre. Details of the temperature difference across the nanotube fibre for each measurement are to be found in Table 4.5.

acquired with the same nanotube fibre, and in both cases the substrate was HOPG. The AC voltage bias applied across the nanotube fibre was 0.5 V for both data sets. The temperature difference across the nanotube fibre for each set of measurements and the value of $T_{cold}$ and $T_{hot}$ are shown in Table 4.5.

The black line in Fig. 4.18 is the linear fit to the data taken at room temperature. It has $G_{th}/G_0$ slope equal to 20 and crosses the y-axis at a value of $58G_{th}$. The reason why the linear fit does not pass through the origin is due to the fact that some semiconducting

| Data | $T_{hot}$ (K) | $T_{cold}$ (K) | $\Delta T$ (K) |
|---|---|---|---|
| **LT1** | 333.5 | 165.4 | 168.1 |
| **LT2** | 333.5 | 166.9 | 166.6 |
| **LT3** | 360.0 | 167.6 | 192.4 |
| **LT4** | 373.0 | 167.8 | 205.2 |
| **LT5** | 333.5 | 166.0 | 167.5 |
| **LT6** | 333.5 | 166.6 | 166.9 |
| **RT1** | 400.0 | 296 | 104.0 |
| **RT2** | 426.4 | 296 | 130.4 |
| **RT3** | 453.0 | 296 | 157.0 |
| **RT4** | 479.0 | 296 | 183.0 |
| **RT5** | 466.0 | 296 | 170.0 |
| **RT6** | 439.6 | 296 | 143.6 |

**Table 4.5**: The details of the data shown in Fig. 4.18. $\Delta T$ is the temperature difference across the MWNT fibre, $T_{hot}$ is the temperature at the thermal probe and $T_{cold}$ is the temperature of the substrate unto which the fibre is lowered.

nanotubes also come in contact with the substrate, contributing to the thermal conductance but not to the electrical conductance. The number of semiconducting nanotubes (assuming it is constant for each data set) can be calculated from the value at which the line crosses the x-axis; in this case the linear fit crosses the x-axis at $-2.9G_0$ therefore it can be concluded that there were 3 semiconducting nanotubes in contact with the substrate as well as metallic tubes (assuming that each tube, if metallic, contributes $1G_0$ to the electrical conductance). From the value of the room temperature linear fit to the data it is clear that these nanotubes display *diffusive* phonon transport as the number of phonon modes transmitted in each nanotube (20) is much lower than the expected number of modes for nanotubes of diameters of 2 nm (>150 modes per nanotube, see Section 4.3). The diffusive phonon transport in the nanotubes is probably due to scattering at the tubes' defects sites.

At low temperatures the thermal conductance step size, for a given electrical conductance step is, in general much larger than at room temperature indicating that the maximum number of phonon modes transmitted along the tubes increases. This is consistent with an increase of the phonon scattering length due to the fact that Umklapp phonon scattering is reduced at lower temperature. The data taken at low temperatures is however, very scattered and this is due to the fact that the electrical conductance signal was very unstable. This was attributed to the presence of a residual insulating ice layer on the surface of the substrate due to the moisture in the vacuum chamber; the ice layer could not be completely removed even by heating the substrate above $0^{o}C$ during the cooling of the low-temperature stage.

The measurements at room and low temperature were repeated, using the same nanotube fibre and set-up, after having increased the bias across the nanotube fibre from 0.5V to 4V (thus increasing the current flow through the fibre from ~5μA to ~40μA). This was done in order to improve the electrical conductance signal when acquiring measurements at low temperature. The increased current flowing through the nanotubes was expected to overcome the problem of the residual insulating ice-layer because of the localised current-induced heating and the higher probability of electrons to tunnel through the thin ice barrier. Indeed the electrical conductance traces taken at high currents were more stable than those taken with low currents under the same conditions as shown in Fig. 4.19.

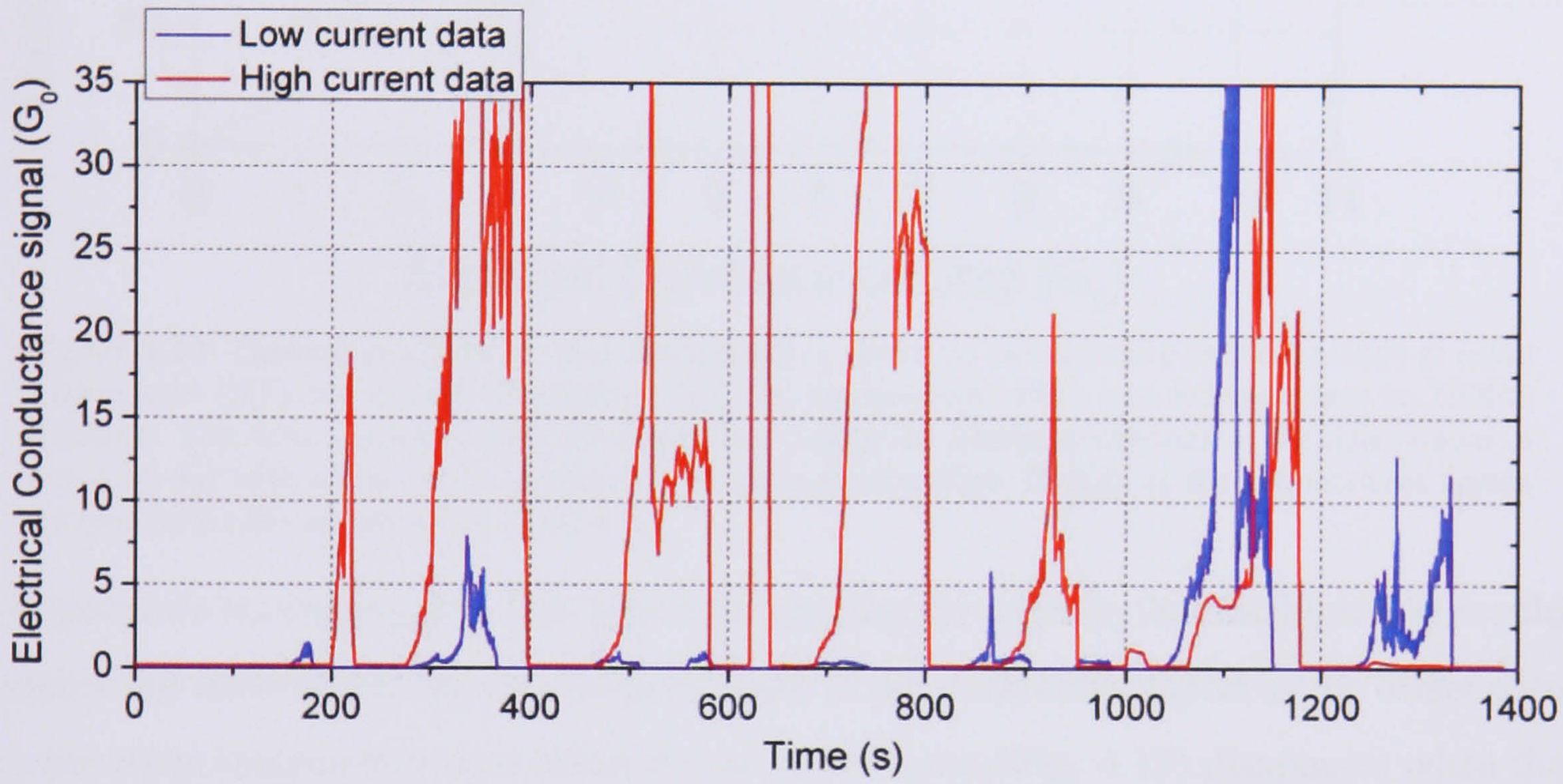



**Figure 4.19**: The electrical conductance signal as the nanotube fibre was repeatedly lowered onto an HOPG substrate at low temperature (T ~164K). The blue trace was taken with a bias of 0.5V across the nanotube fibre corresponding to approximately 5μA of current flowing across the fibre. The red trace was taken with the same conditions and set-up but with a bias of 4V, corresponding to a current of approximately 40μA. The poor signal at low bias is caused by a residual insulating ice layer due to moisture present on the HOPG at room temperature. The high bias allows current to flow through it thus enabling to measure the full signal from the nanotube fibre.

The high current data taken at room temperature and at low temperature is shown in Fig. 4.20 where the thermal conductance steps are plotted versus their corresponding electrical conductance steps. Details of the temperatures across the nanotube fibre for each data set shown in Fig. 4.20 are reported in Table 4.6.

The increased bias across the nanotubes was also expected to cause most of the small band-gap semiconducting tubes to contribute to the electrical conductance as it enabled electrons to tunnel across the gap. The lines shown in Fig. 4.20 are the linear fits to the data at room temperature (black) and at low temperature (red) with the constraint that they pass through the origin. The slope of the linear fit for the room temperature data is $22.3 G_{th}/G_0$ which is in good agreement with the slope derived from the low bias room

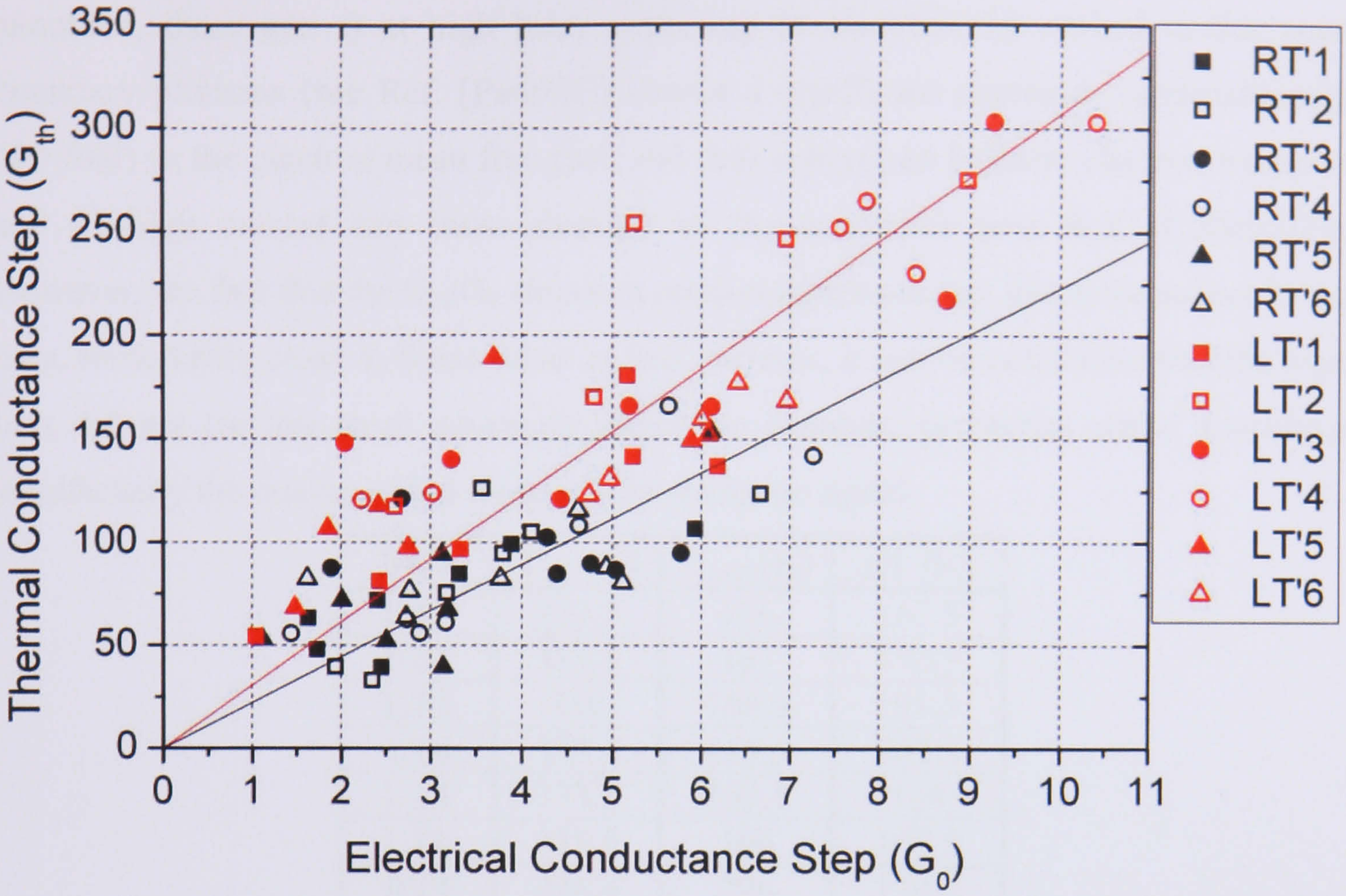



**Figure 4.20**: Thermal conductance and corresponding electrical conductance step data taken at room temperature (RT) and at low temperature (LT) as the nanotube fibre was lowered onto an HOPG substrate. The data was taken with the same fibre and under similar conditions to the data shown in Fig. 4.18 but with a bias of 4V applied across the nanotube fibre. Details of the temperatures across the nanotube fibre are shown in Table 4.6.

temperature measurements. This thus confirms the expectation that the high bias would enable the semiconducting tube to participate in the electron transport as the offset seen in the room temperature data taken at low currents (see Fig. 4.18) disappears when the same measurements are repeated at high currents.

The data at low temperature is fitted by a line with slope $30.7G_{th}/G_0$. The increase in the slope from the room temperature data confirms the fact that more phonon modes are transmitted through the tubes at low temperatures in line with the expected reduction in phonon Umklapp scattering. The phonon transport though remains diffusive as the number of phonon modes transmitted by each tube is still well below that expected for tubes of ~2nm diameter.

Finally, in the low temperature data set it is apparent that there are more data points occurring at high electrical conductance step values ($>7G_0$) this is due to the fact that the total z-movement of the fibre at low temperature is greater than at room temperature due to the upward expansion of the copper cylinder in the cold stage (see Section 3.7.2). This thus causes a greater number of nanotubes to come into contact with the substrate and generates high electrical and thermal conductance data points.

There are however, two potential problems arising from the use of a high bias across the nanotube, these are: i) at high bias, scattering of electrons by optical and/or zone boundary phonons (see Ref. [Park'04]) causes a significant decrease (approximately 100 fold) in the electron mean free path and thus suppresses ballistic electron transport and ii) high current can cause damage to the nanotubes (see Ref. [Collins'02]). However, the fact that the $G_{th}/G_0$ slopes at room temperature are, given the scatter in the data, remarkably close to those taken at low currents, it can be concluded that the high bias did not (in this case) adversely affect the nanotube properties while improving significantly the quality of the electrical conductance signal.

| Data | $T_{hot}$ (K) | $T_{cold}$ (K) | $\Delta T$ (K) |
|---|---|---|---|
| **LT1** | 333.5 | 166 | 167.5 |
| **LT2** | 333.5 | 163 | 170.5 |
| **LT3** | 360 | 168.5 | 191.5 |
| **LT4** | 373.3 | 165.5 | 207.8 |
| **LT5** | 333.5 | 165.5 | 168 |
| **LT6** | 333.5 | 166 | 167.5 |
| **RT1** | 426.4 | 296 | 130.4 |
| **RT2** | 399.8 | 296 | 103.8 |
| **RT3** | 452.9 | 296 | 157.0 |
| **RT4** | 479.4 | 296 | 183.4 |
| **RT5** | 466.2 | 296 | 170.2 |
| **RT6** | 439.6 | 296 | 143.6 |

**Table 4.6**: The details of the data shown in Fig. 4.20. $\Delta T$ is the temperature difference across the MWNT fibre, $T_{hot}$ is the temperature at the thermal probe and $T_{cold}$ is the temperature of the substrate unto which the fibre is lowered.

Data was also acquired on a gold foil substrate, both at room and low temperature and at high and low bias, with the same nanotube fibre used for the measurements on HOPG. The thermal conductance steps versus their corresponding electrical conductance steps for the data on gold, taken at low and high temperature with low bias (0.5V) are shown in Fig. 4.21; the details of the temperatures of the thermal probe and of the substrate for each data set are shown in Table 4.7.

The linear fit to the data at room temperature (the fit was constrained so that it went through the origin) has a $G_{th}/G_0$ slope of 108. Thus, assuming all the nanotubes contributed $1G_0$ to the electrical conductance, this means that there were 108 phonon modes transmitted in each nanotube. While this value is lower than the number of modes expected if the phonon transport was ballistic (>150), it is of the same order of magnitude and thus transport in the nanotube can be regarded as quasi-ballistic. The thermal conductivity of the nanotube, derived from these data is, assuming the nanotube to be a cylindrical rod of diameter 1.9nm and length 700 nm (the nanotube average sizes

as estimated in Section 4.1.1), 8860 W/mK. This value is of the same order of magnitude as that predicted by Berber et al (see Ref. [Berber'00]) and more than twice the thermal conductivity of nearly isotopically pure diamond which is 3320 W/mK at room temperature (see Reference 16 in [Berber'00]). This value confirms the expectation that nanotubes free of defects are extremely good thermal conductors.

| Data | $T_{hot}$ (K) | $T_{cold}$ (K) | $\Delta T$ (K) |
|---|---|---|---|
| **Au LT1** | 349.7 | 168.2 | 181.5 |
| **Au LT2** | 316.6 | 165.1 | 151.5 |
| **Au LT3** | 333.2 | 164.5 | 168.7 |
| **Au LT4** | 382.9 | 165.7 | 217.2 |
| **Au LT5** | 346.4 | 163.7 | 182.8 |
| **Au RT1** | 382.9 | 296 | 86.9 |
| **Au RT2** | 396.2 | 296 | 100.2 |
| **Au RT3** | 416.1 | 296 | 120.1 |
| **Au RT4** | 436.0 | 296 | 140.0 |
| **Au RT5** | 449.3 | 296 | 153.3 |

**Table 4.7**: The details of the temperature difference $\Delta T$ across the nanotube fibre for the data shown in Fig. 4.21.

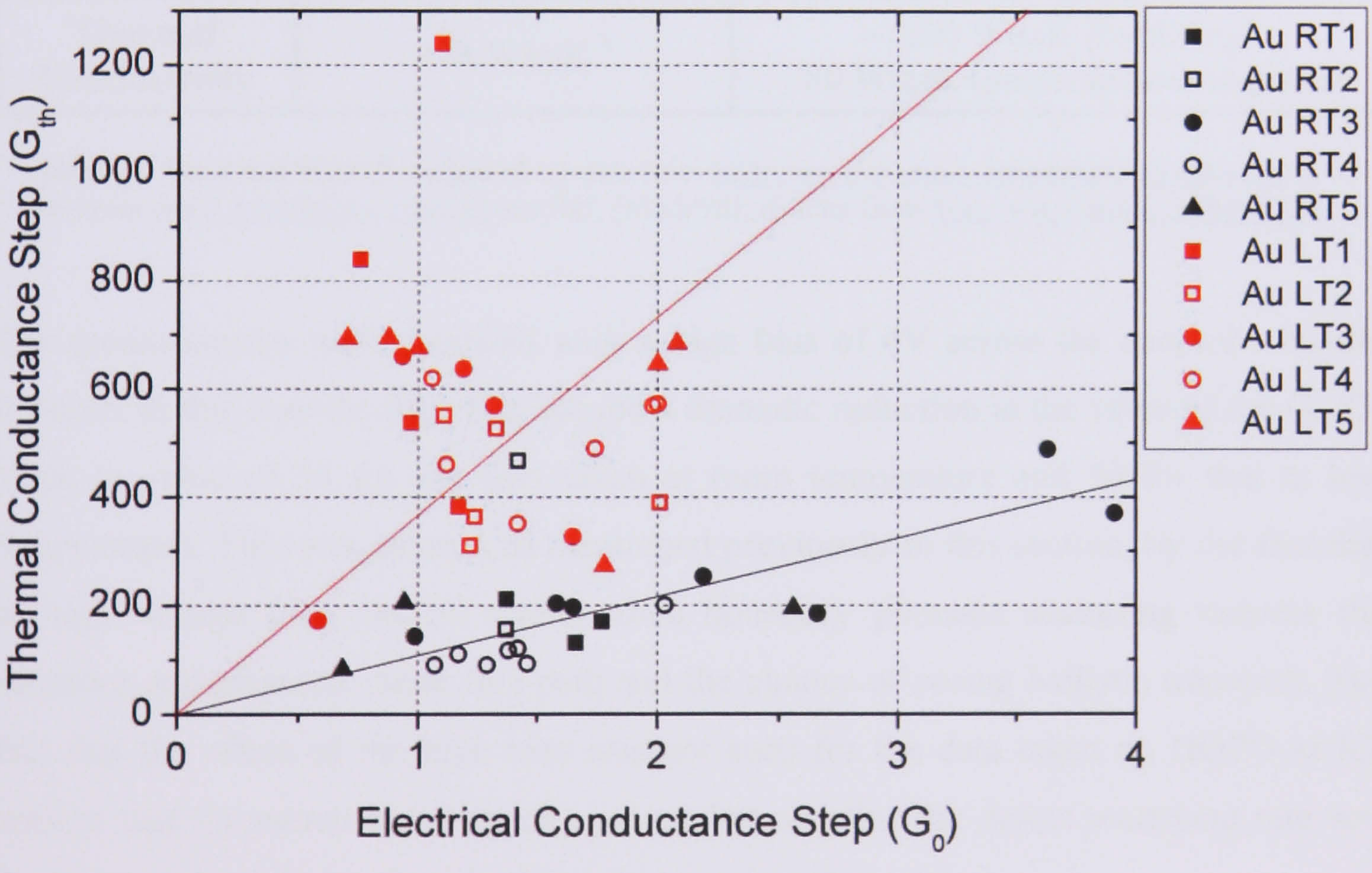



**Figure 4.21**: Electrical conductance and corresponding thermal conductance step data taken at RT and at LT as the nanotube fibre was lowered into a gold foil substrate. The data was taken with the same fibre and same set-up as that shown in Fig. 4.18, just using a different substrate. Details of the temperatures across the nanotube fibre are to be found in Table 4.7.

The data points taken at low temperatures are more scattered than those at room temperature; the cause for this scatter was most probably the presence of a residual insulating ice-layer on the gold surface, which affected the electrical conductance measurements. It is clear however, that the thermal conductance steps at low

temperatures are much higher than those at room temperature for a given electrical conductance step. Just as in the discussion of the data on HOPG, this increase in the thermal conductance steps size is to be attributed to the fact that Umklapp phonon scattering is reduced at lower temperature, thus increasing the phonon mean free path in the nanotube. If a line is fitted to the low temperature data (with the added constraint of passing through the origin) its slope is $366G_{th}/G_0$. This value is to be taken as an estimate because of the large scatter in the data, however, it implies that >300 phonon modes are transported in each nanotube, which is a signature for ballistic phonon transport (see Section 4.3.3). Therefore, lowering the data acquisition temperature caused a transition from quasi-ballistic to ballistic phonon transport in the nanotube by reducing the phonon scattering rate.

| Physical | Gold (Au) | HOPG |
|---|---|---|
| **Fermi Energy** | 5.5 eV [a] | 5.0 eV [c] |
| **Work function** | 4.7 eV [a] | 4.81 eV [c] |
| **Electrical Resistivity** | $2.2 \times 10^{-6}$ Ωcm (at RT) [b] | $\sim 4 \times 10^{-5}$ Ωcm (in plane) [d]<br>~0.2 Ωcm (perpendicular to the plane) |
| **Thermal Conductivity** | 318 W/mK [b] | ~1800 W/mK (in plane) [d]<br>~ 80 W/mK (perpendicular to plane) |

**Table 4.8**: Gold and HOPG compared. a) data from http://www.du.edu/~jcalvert/phys/copper.htm; b) data from www.goodfellow.com; c) see Ref. [Márk'98]; d) data from http://www.tectra.de/hopg.htm.

The measurements were repeated with a high bias of 4V across the nanotube bundle however in this case the high bias caused a dramatic reduction in the value of the $G_{th}/G_0$ slope (a value of 34 for the data taken at room temperature and 56 for that at low temperature). This was caused, as mentioned previously in this section, by the fact that at high voltage bias, optical and/or zone boundary phonons scattering reduces the electrons and phonons mean free path and the chance of seeing ballistic transport. The fact that the effect of the high bias was not seen for the data taken on HOPG at RT implies that the nanotubes were of poor quality and that the defect scattering rate was the limiting factor in the length of the phonon mean free path.

What remains to be discussed is why ballistic phonon transport was observed on gold and not on HOPG. In Table 4.8 are shown some of the relevant physical properties of gold and of HOPG. The work function and Fermi energy of the two materials are very similar; gold is a better electrical conductor than HOPG, which is a better thermal conductor if in-plane thermal conductivity is considered. HOPG was the substrate of preference in this work as it was expected that, being of the same material as the carbon

nanotubes, it would cause the least reflection at the nanotube-substrate contact. This was confirmed from the fact that ballistic phonon transport was observed at room

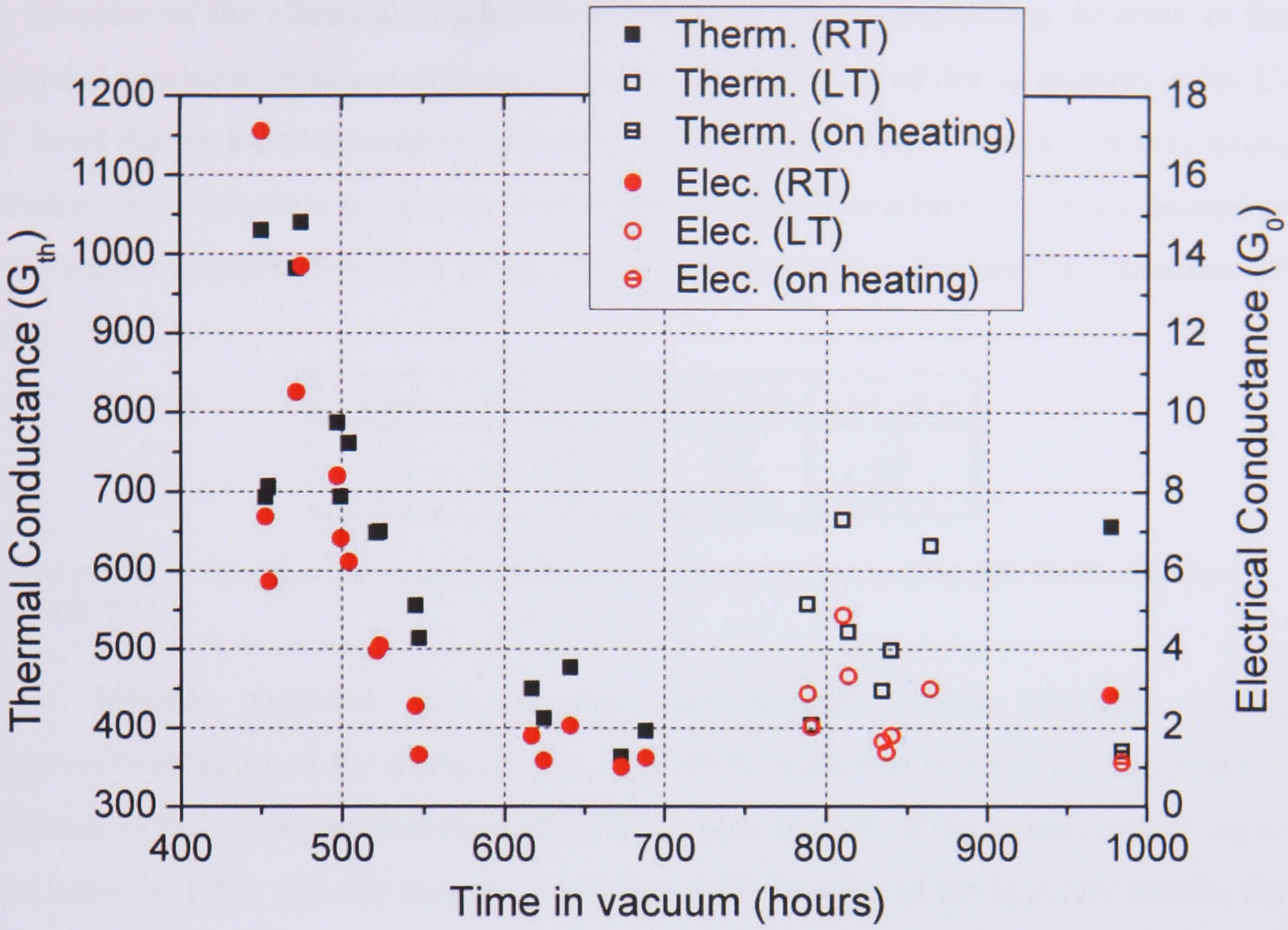



**Figure 4.22**: Maximum electrical and thermal conductance values after prolonged time in vacuum. The data was acquired at room temperature (RT) and low temperatures (LT) and at room temperature after heating for 5.5 hours at 85°C. The details of the temperature differences across the nanotube fibre for each data set are to be found in Table 4.9.

temperature on an HOPG substrate as reported in Section 4.3.3 (with a different nanotube fibre). Therefore the most likely cause of the differences between the two substrates is that two different nanotubes, both protruding from the same nanotube fibre were measured on the two substrates, one displaying ballistic transport and one diffusive phonon transport.

Measurements of the thermal and electrical conductance of nanotubes were performed also on a different nanotube bundle after this had spent more than 30 days in high vacuum (pressures $<1\times10^{-5}$ mbar) and had been repeatedly heated to 55°C. During the prolonged time in vacuum the highest* electrical and thermal conductance values recorded during approach/withdraw of the nanotube from an HOPG substrate were monitored and observed to monotonically decrease as a function of time spent in the vacuum chamber (see Fig. 4.22). This was interpreted as due to the gradual desorption of oxygen from the nanotubes in the fibre: since oxygen dopes the semiconducting

* The highest electrical and thermal conductance values in a lowering-withdrawing cycle occur when the bulk of the fibre comes into contact with the substrate.

nanotubes and makes them metallic (see Section 2.1.1), the removal of oxygen from the tubes would cause an increase in the number of semiconducting nanotubes thus causing a decrease in the electrical conductance observed. The corresponding decrease in the thermal conductance is less obvious, but could be explained as due to changes in the C-C bond due to the physisorption of oxygen on the tubes which would therefore cause changes in the number of phonon modes and the thermal conductance of the nanotubes (for a more detailed discussion of the effect of oxygen on the nanotubes see Sections 4.5 and 4.6).

| Data | $T_{hot}$ (K) | $T_{cold}$ (K) | $\Delta T$ (K) |
|---|---|---|---|
| **RT** | 351 | 296 | 55 |
| **LT** | 290 | 162±1 | 128±1 |

**Table 4.9**: The details of the temperature difference $\Delta T$ across the nanotube fibre for the data shown in Fig. 4.22.

The highest electrical and thermal conductance values recorded during approach/withdraw of the nanotube from the HOPG substrate taken at low temperature (details of the temperatures across the MWNT fibre in each of the measurements are to be found in Table 4.9) are also shown in Fig. 4.22. In spite of the apparent scatter, the low temperature data is a factor of 7-20% higher than the data at room temperature (the low temperature data values were scaled down to take into account the higher forces applied on the nanotube fibre due to the heating of the sample stage). This increase in the electrical and thermal conductance values was attributed to oxygen doping of the nanotubes during the measurements at low temperature. Oxygen is desorbed from the nanotubes when these are heated in high vacuum, during the measurements at low temperature the nanotubes were brought into contact with a substrate at temperatures between 160 and 170K thus allowing the residual oxygen present in the vacuum chamber (pure or in the water moisture) to condense on the nanotubes. A confirmation that the tubes were oxygen doped comes also from the data collected *after* the low temperature measurements. The first set of data acquired at room temperature *after* the low temperature measurements, occurs at values 10-25% higher than the room temperature data collected *before* those measurements. Furthermore, heating the nanotube fibre at 85°C for 5.5 hours caused both the electrical and thermal conductance data points to dramatically decrease to values within 1-2% from those acquired *before* the low temperature measurements. This rapid change upon heating thus confirms that the cause for the higher electrical and thermal conductance values measured at low temperatures was indeed oxygen doping of the tubes.

In conclusion, ballistic phonon transport was observed at low temperatures on nanotubes that showed quasi-ballistic phonon transport at room temperature thus confirming the expectation that lowering the nanotube temperature would increase the phonon mean free path by decreasing the phonon-phonon scattering rate. Nanotubes that showed clear diffusive phonon transport at room temperature though, remained diffusive even at low temperatures, because the defect scattering rate intrinsic of the nanotube was the main factor in the determination of the phonon mean free path.

Working at low temperatures was also found to have an undesirable effect on the nanotubes: the residual oxygen in the vacuum chamber condensed on the nanotubes on cooling, causing at least a partial doping of the nanotube fibre. Working at lower pressures (in the Ultra-High Vacuum regime) would be necessary to avoid oxygen contamination of the nanotubes at low temperatures.

The lowest temperatures to which the substrates could be cooled were in the range 160-170K thus not low enough to freeze out all the optical phonon modes of the nanotubes, and there was no evidence for even a partial reduction of the number of phonon modes in the nanotube on cooling. Therefore the cold stage was found to be inadequate for the study of the thermal conductance quantisation in nanotubes, a new set-up would be necessary to reach the low temperatures (and pressures – to avoid oxygen contamination) required for this work; this will be discussed further in Section 5.

## 4.5 Oxygen Doping Effects on Electron Transport in MWNTs

In order to investigate the effect of air exposure on the electronic properties of the MWNTs, nanotube electrical conductance traces were taken at room temperature and pressure (air) and at room temperature in high vacuum (pressures from $3.5\times10^{-4}$mbar to $1.7\times10^{-5}$mbar) using the set-up described in Section 3.3. In all traces the voltage bias applied between the nanotube and the substrate ($V_i$) was 9mV and the gain (G) in the Stanford voltage preamplifier was 1,000; all the traces taken in vacuum used a series resistance $R_S$ equal to 1.2 kΩ, while for the traces taken in air $R_S$ ranged between 0.7 to 1.2kΩ. The two sets of data points were collected in two histograms (using just the data from conductance traces taken while approaching the substrate – in both cases HOPG) with bin size $0.02G_0$.

Peaks in the histograms correspond to plateaus in the electrical conductance curves. In an ideal case, for a ballistic conductor, peaks in the histograms will be expected at

integer values of $G_0$ (see histograms in Ref. [Frank'98]), one example is given in Fig 4.23 where the red conductance curve shown in Fig 4.11 (which had clear plateaus at 2 and $5G_0$) is reproduced with its corresponding histogram next to it (the histogram bin size is also $0.02G_0$).

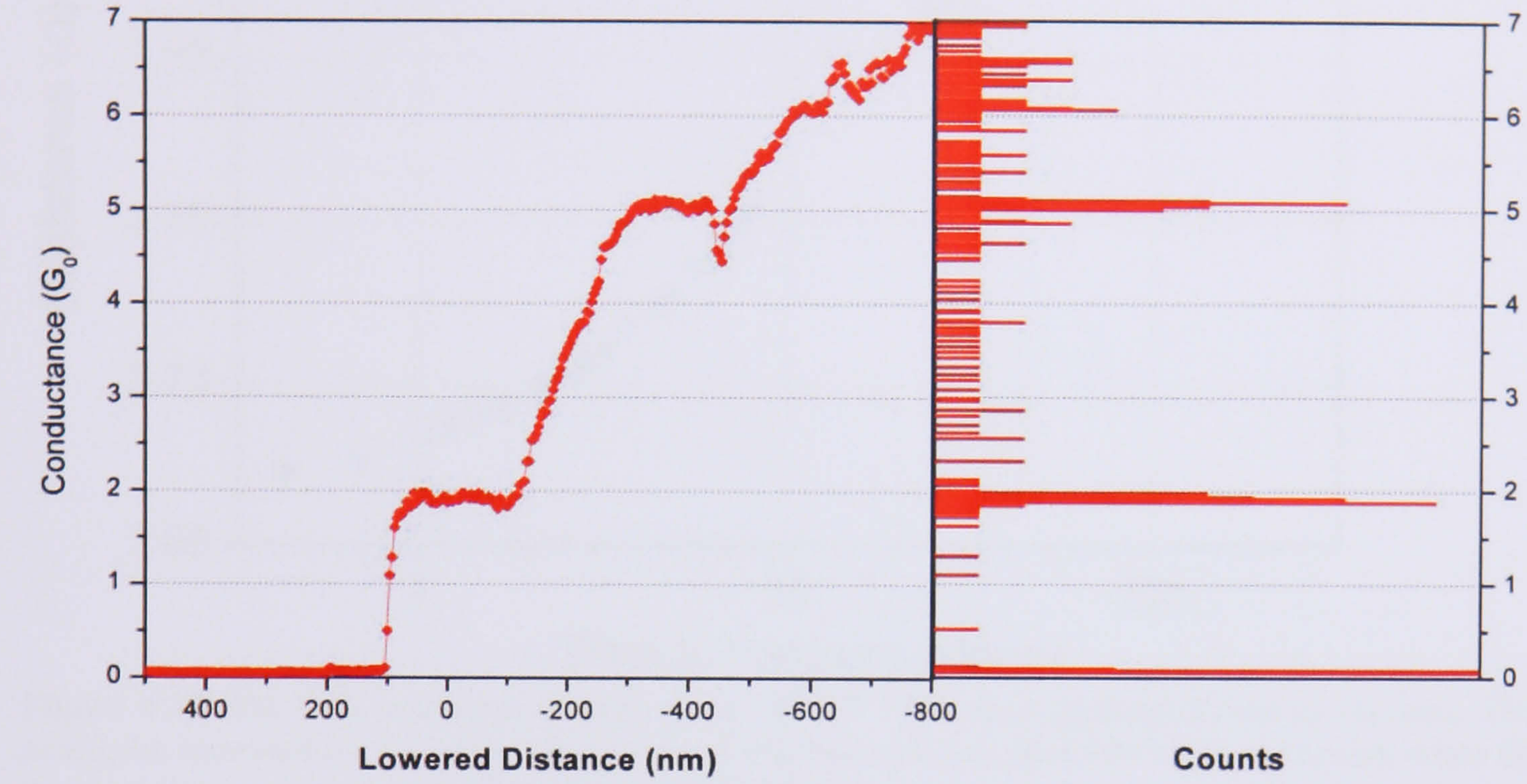



**Figure 4.23**: Electrical conductance curve (b) from Fig. 4.11 (left) and its corresponding histogram (right). The histogram has bin size $0.02G_0$. The two plateaus visible in the electrical conductance curve correspond to peaks in the histogram chart.

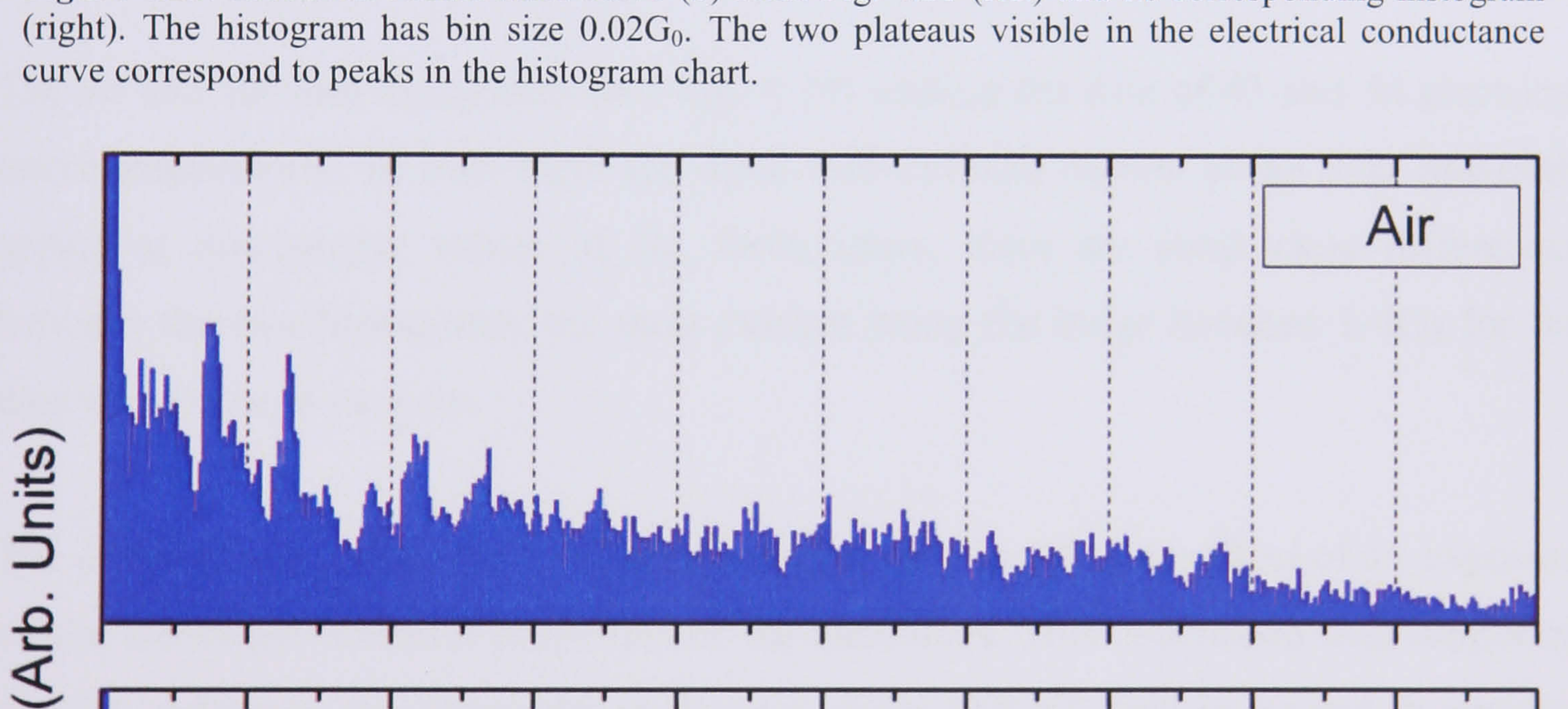



**Figure 4.24**: Histograms of the electrical conductance traces taken as the nanotube approached an HOPG surface in air (top) and in high vacuum (bottom). The bin size is $0.02G_0$ in both cases.

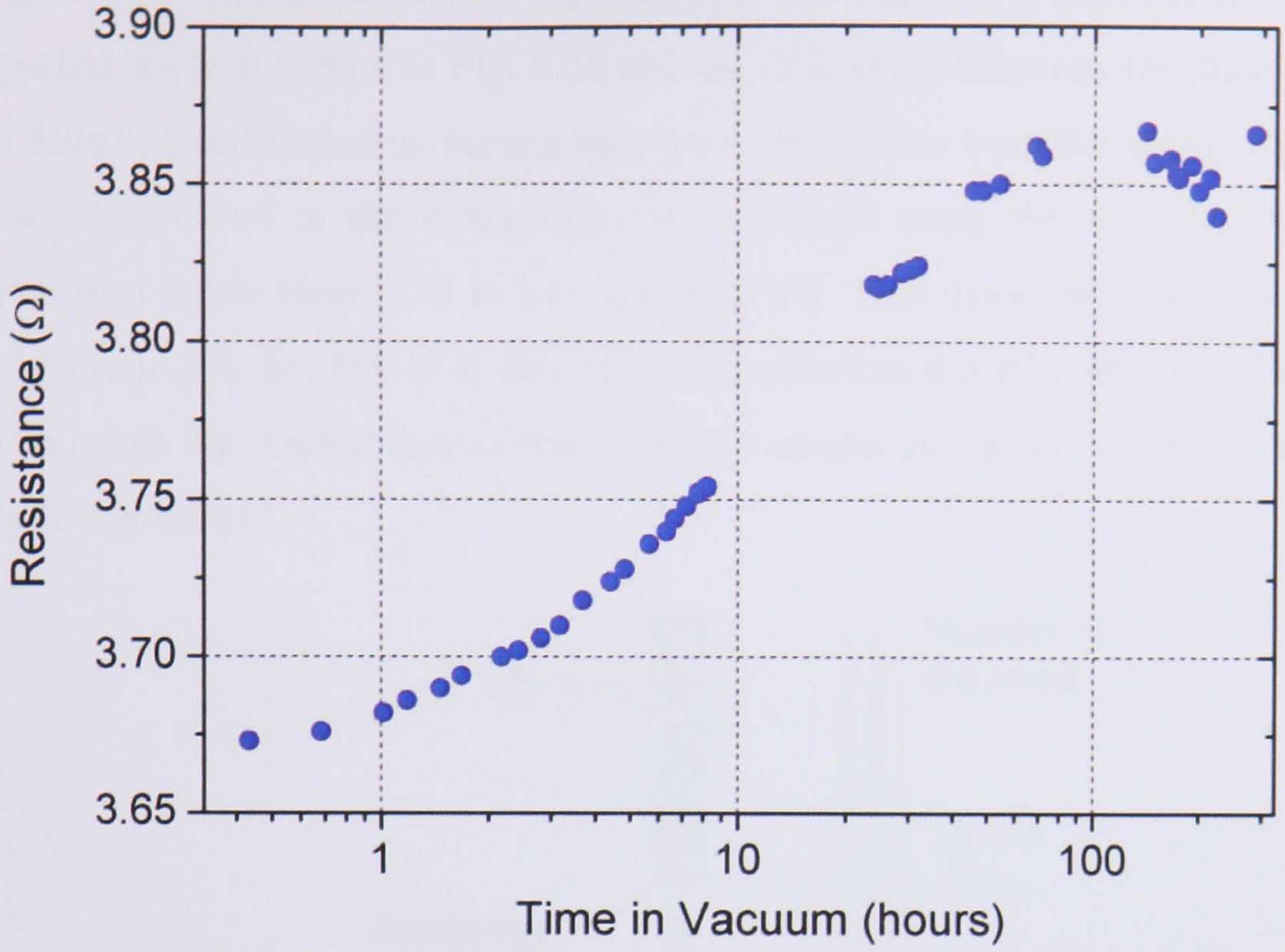



**Figure 4.25**: The bulk resistance change of an MWNT fibre upon prolonged time in vacuum. The resistance increases by 5% of its initial value, it reaches a plateau after 100 hours in vacuum when all the air molecules are desorbed from the nanotube fibre.

The air and vacuum histograms (see Fig. 4.24) contain the data of 43 and 44 electrical traces respectively. In both there are some well defined, narrow peaks that, however, appear at non-integer values of $G_0$, furthermore, there are some clear differences between the two histograms, the most evident being the bulge between 1-4$G_0$ for the data taken in high vacuum.

The differences between the two histograms were attributed to the effect of air exposure on the electronic transport properties of the nanotubes. This conclusion was supported by bulk resistance measurements made on a single MWNT fibre in air and in vacuum (using the set-up described in Section 3.2). The change in resistance of the nanotube fibre after a prolonged time in vacuum is shown in Fig. 4.25. The resistance change was a 5% increase from the value in air, and occurred gradually over a period of over 100 hours in vacuum. After 100 hours the resistance stops increasing, due to the fact that all the air molecules have been desorbed from the nanotube.

Collins et al in Ref. [Collins'00] measured a 10-15% resistance change in mats of single-walled nanotubes when these were cycled between air and vacuum at room temperature. By repeating the experiment independently with the different major gas constituents of air they determined that the changes in resistance were due only to the

oxygen present in the air and no other gas. The oxygen sensitivity of carbon nanotubes is now well documented in the literature (see Section 2.1.1), therefore in this work too, the changes in R shown in Fig. 4.25 and the differences between the histograms of Fig. 18 have been attributed to oxygen adsorption/desorption from the nanotubes.

The data plotted in the histograms was analysed using the semi-classical approach developed by de Heer et al in Ref. [de Heer'97]. This model was described in Section 2.2.2 (page 29): de Heer at al derived a semi-classical formula, shown in equation (2.5), to calculate the conductance of more ballistic conductors in series connected by electron scattering centres.

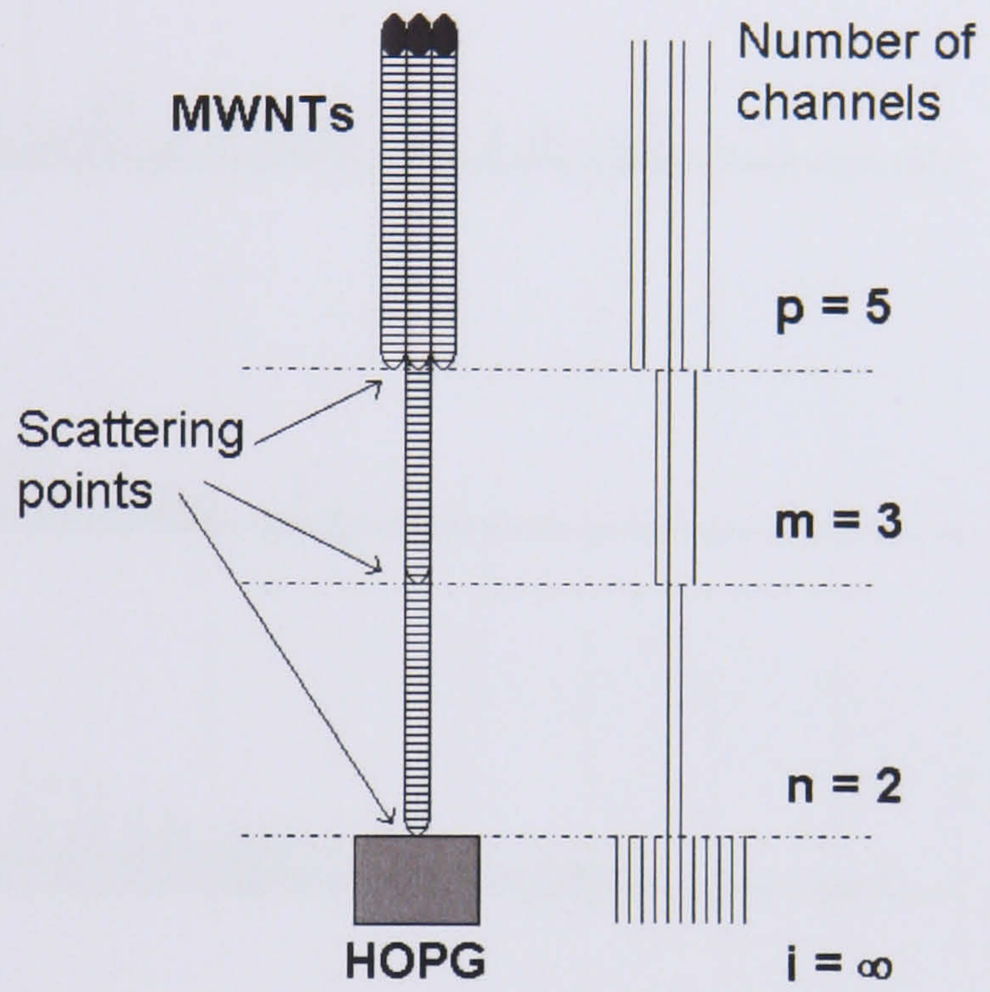



**Figure 4.26**: Schematic diagram of a MWNT bundle coming into contact with the HOPG. Defects in the nanotubes or in the connections between nanotubes in the bundle can act as electron scattering centre. Each scatter-free section has a number of conducting channels as shown on the right. The HOPG has an infinite number of channels.

In this work defects in the MWNTs and/or in the connecting regions between two MWNTs in a bundle could act as electron scattering centres. In Fig. 4.26 is shown, on the left, a schematic diagram representing one or more MWNTs (with defects acting as scattering centres) coming in contact with the graphite substrate and, on the right, the corresponding structure in terms of the number of conducting channels involved.

Using MathCAD (see Appendix C for the MathCAD programme) and equation (2.5) a mathematical model was written to calculate the value of the step increases in the total conductance $G_{tot}$ when one or more MWNTs protruding from the bulk of the MWNT fibre come into contact with the graphite substrate one after the other.

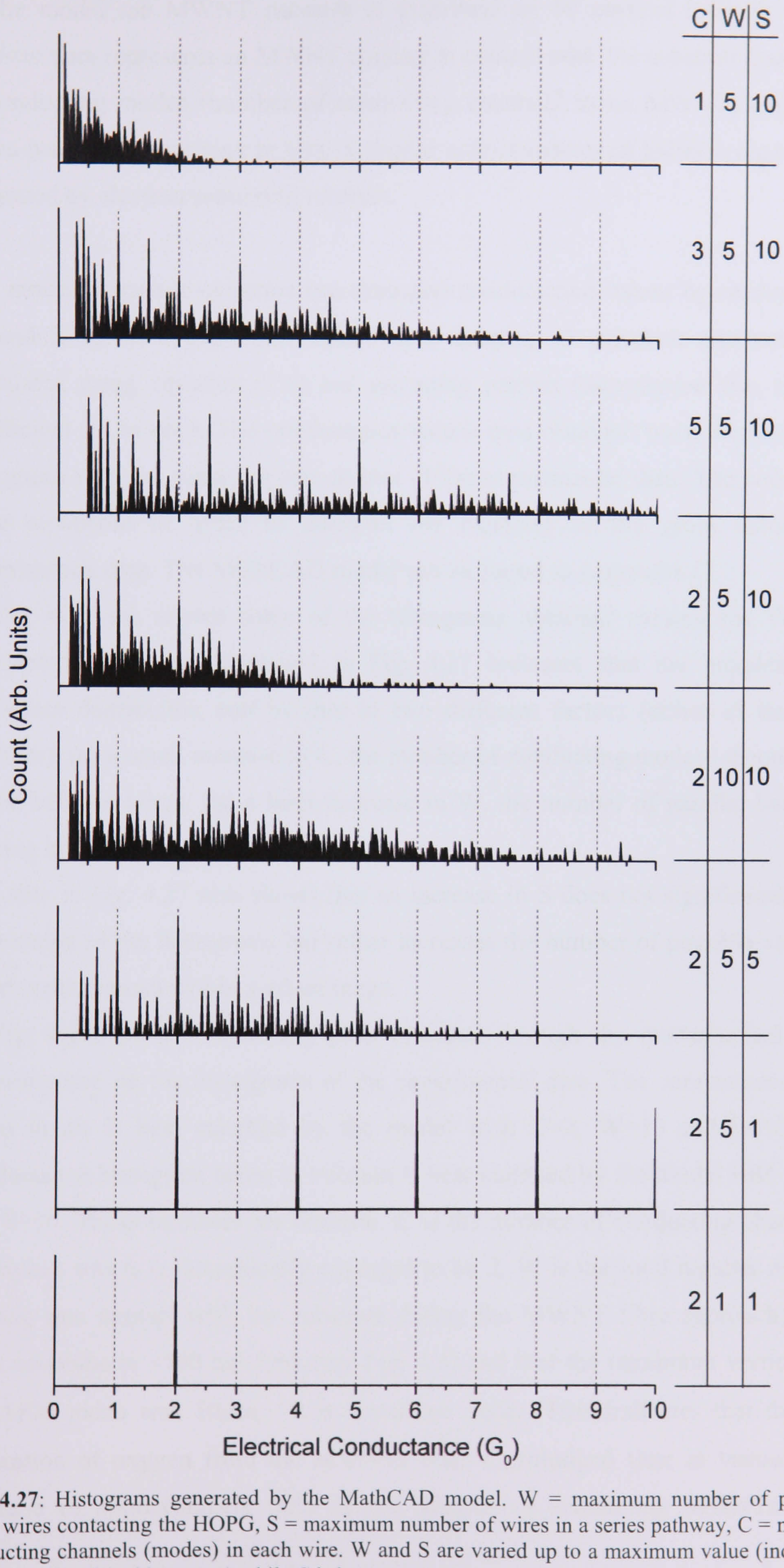



**Figure 4.27**: Histograms generated by the MathCAD model. W = maximum number of parallel ballistic wires contacting the HOPG, S = maximum number of wires in a series pathway, C = number of conducting channels (modes) in each wire. W and S are varied up to a maximum value (indicated on the right side of the histogram) while C is kept constant.

In the model the MWNT network is described by W parallel ballistic wires (each ballistic wire represents an MWNT coming in contact with the substrate); each wire has C conducting modes (number of conducting channels in an MWNT) and it forms a series pathway comprising in total S similar wires (number of ballistic regions in series separated by electron scattering centres).

The model was set to generate one thousand conductance values by randomly varying W and S up to a maximum value while keeping C constant; conductances were calculated using equation (2.5) and assuming perfect transmission (i.e. transmission coefficient set to one). The conductance values thus obtained were then collected in a histogram with the same bin size as that of the experimental data. The two histograms were compared in order to interpret the meaning of the gross features of the experimental data. The MathCAD model can be found in Appendix C.

In Fig. 4.27 are shown some of the histograms obtained varying the W, S and C parameters. The data displayed in Fig. 4.27 indicates that the broadening of the histogram distribution can be due to two different factors (either of them or both together): (a) a small increase in C, the number of conducting modes (channels) in each of the ballistic wires; (b) a large increase in W, the number of parallel ballistic wires coming in contact with the HOPG.

The data in Fig. 4.27 also shows that an increase in S does not significantly affect the broadening of the histograms but rather increases the number of possible values of $G_{tot}$ (total conductance) within a given range.

In Fig. 4.28, the best matching plots obtained through the mathematical model are superimposed on the histograms of the experimental data. The conductance histogram taken in air is best matched by the model with C=2, W=10 and S=10 while the conductance histogram taken in vacuum is best matched by the model with C=2, W=5, and S=10. These numbers are realistic: C is the number of conducting channels in the nanotubes which is theoretically expected to be 2. W is the total number of nanotubes coming into contact with the substrate during the MWNT fibre approach; given that each nanotube is ~700 nm long (see Fig. 4.4) and that the maximum vertical travel of the AFM piezo was 10μm, 10 is a realistic value. This indicates that the (partial*) desorption of oxygen from the MWNTs after a prolonged time in vacuum causes a decrease of approximately 50% in the number of conducting MWNTs coming in

---

* In order to fully desorb the oxygen from the nanotubes it is necessary for them to be heated in vacuum (see Section 4.6).

contact with the substrate one after the other. This could be caused by a decrease in the number of conducting MWNTs within an MWNT fibre. This conclusion is supported by what was observed by Collins et al in Ref. [Collins'00]: semiconducting nanotubes with a small band gap can become metallic upon oxygen exposure. Therefore, desorbing the oxygen from the nanotubes will decrease the number of conducting tubes in the fibre, as the changes in the electrical conductance histograms seems to suggest.

It is also possible, however, that the changes between the two histograms are due to changes in the number of conducting channels within the nanotubes (C). Support for this conclusion comes from the work of Sanvito et al (see Ref. [Sanvito'00]) where changes in the position of the Fermi level in a coupled multi-wall nanotube system cause an increase in the number of conducting modes of the tubes. Therefore, the adsorption of oxygen on the MWNT fibre could indeed change the number of conducting layers in an MWNT by shifting the position of the Fermi level in the tubes (evidence that oxygen adsorption p-dopes nanotubes and affects the position of the Fermi level is well documented, see Ref. [Dag'03] and [Zhao'02]). The histogram of the electrical conductance traces taken in air could thus be modelled with the histogram

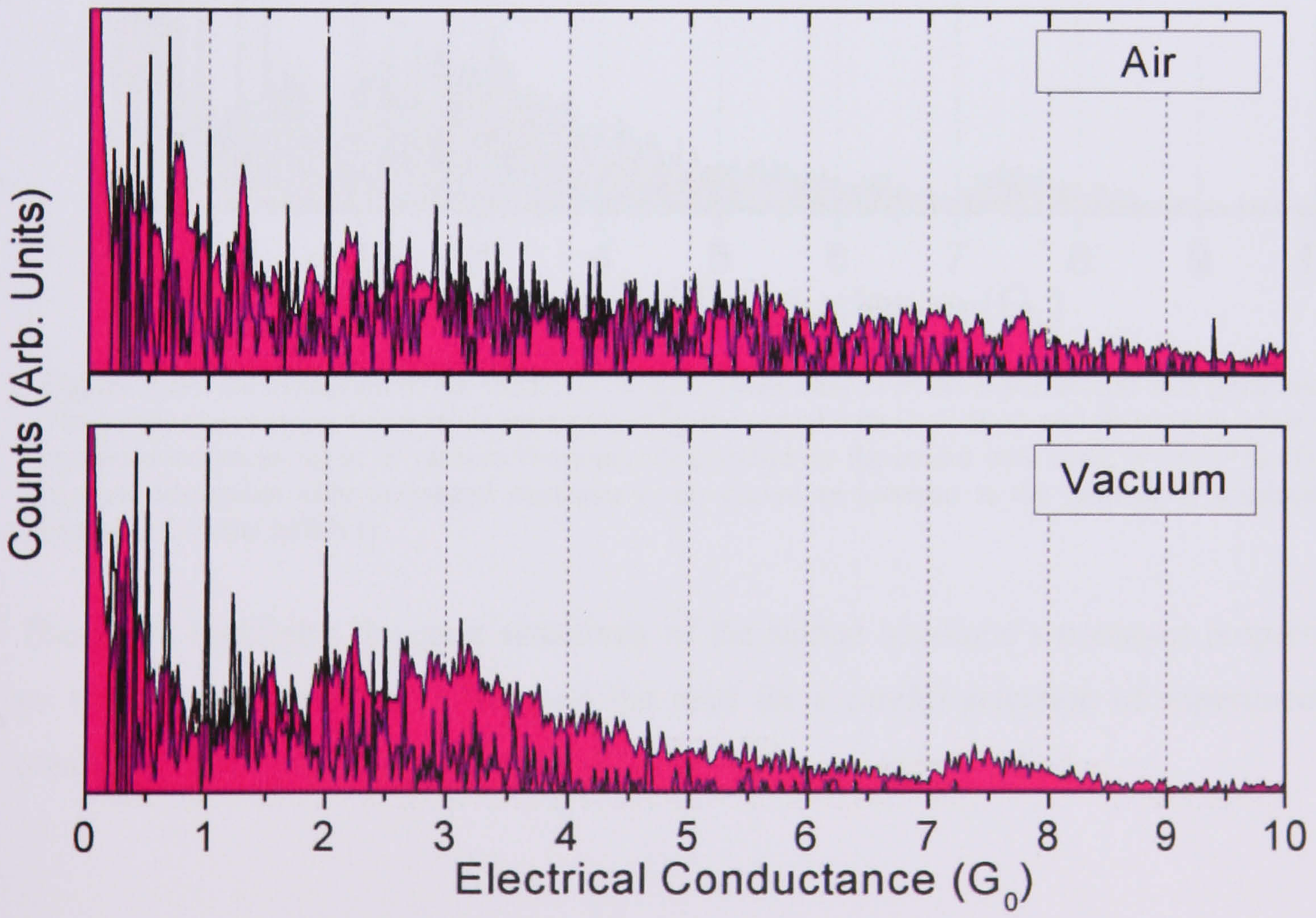



**Figure 4.28**: the histogram of the MathCAD model (black line) that best matches the experimental data (pink area). The conductance traces taken in air are best matched by the model with C=2, W=10 and S=10 (top) while the conductance traces taken in vacuum (bottom) are best matched by the model with C=2, W=5, S=10. Thus oxygen adsorption after prolonged exposure to air causes a large increase in the number of ballistic wires W (i.e. the number of conducting MWNTs in the fibre).

produced setting C=3, W=5 and S=10 and that in vacuum by setting C=2, W=5, and S=10 (see Fig. 4.29). The effect of oxygen on the nanotubes would have caused then a decrease in the number of conducting channels in the nanotube from 3 to 2.

Given the uncertainty in the measurements it is impossible to choose the more likely of the two scenarios, even though the first gives a better fit of the data in air; however both of these scenarios fit the data and are consistent with what has been reported in the literature.

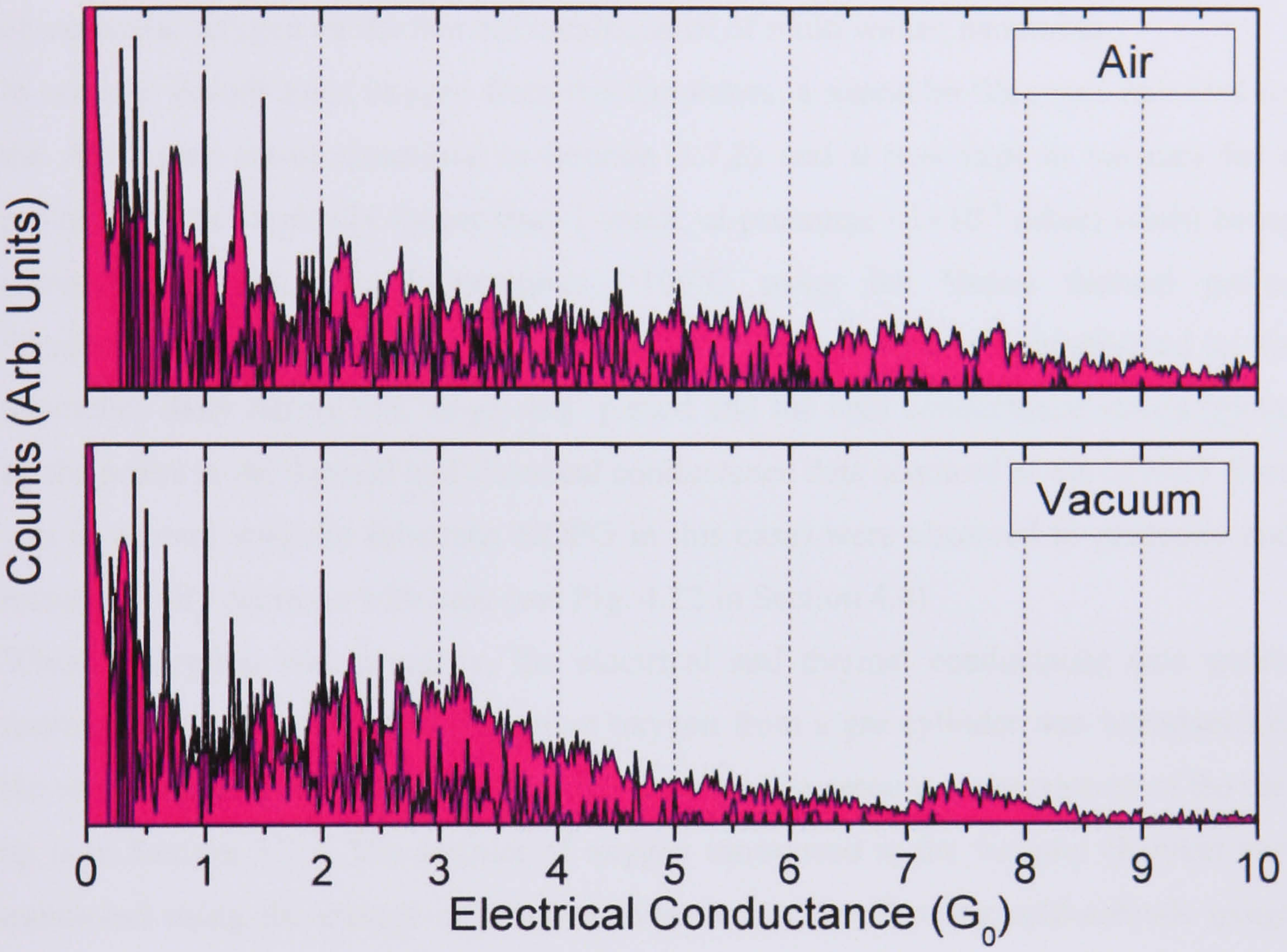



**Figure 4.29**: the histogram of the MathCAD model (black line) over the experimental data (pink area). The conductance traces taken in air are matched by the model with C=3, W=5 and S=10 (top) while the conductance traces taken in vacuum (bottom) are matched by the model with C=2, W=5, S=10. Thus oxygen adsorption after prolonged exposure to air causes an increase in the number of conducting channels C in the MWNTs.

This work highlights the great sensitivity of the carbon nanotube's transport properties on the environmental conditions and the need for a careful selection of experimental conditions if the intrinsic properties of the nanotubes are to be studied.

## 4.6 Comparison of the Oxygen Effects on Electrical and Thermal Transport in MWNTs

Whilst the effect of oxygen and other gases on the carbon nanotubes electrical properties has been the subject of intense investigations, there is no report of studies on the effect of the gas exposure history on the nanotube's thermal properties.

The aim of this work was therefore to perform a preliminary investigation of the effect of molecular oxygen on the thermal conductance of multi walled nanotubes.

In order to desorb most oxygen from the nanotubes, a nanotube fibre was mounted on the AFM (see set-up described in Section 3.7.2) and it was kept in vacuum for a prolonged time (typically longer than 1 week, at pressures $<1\times10^{-5}$ mbar) whilst being continuously heated to temperatures $>100^{o}$C using the Veeco thermal probe. Simultaneous thermal and electrical conductance measurements were performed on the nanotubes daily during this 'degassing' period and the bulk conductance values (given by the peaks in the thermal and electrical conductance data acquired as the MWNT fibre was in contact with the substrate, HOPG in this case) were observed to gradually and monotonically decrease with time (see Fig. 4.22 in Section 4.4).

When desorption was complete, the electrical and thermal conductance data points reached a plateau, and at this point pure oxygen from a gas cylinder was introduced in the vacuum chamber using a needle valve to control its amount, a description of the set-up is in Section 3.7.3. The amount of oxygen introduced in the vacuum chamber was monitored using the change in pressure indicated by the Penning cold-cathode gauge fitted in one of the feedthroughs of the chamber (see Section 3.2). In order not to compromise the quality of the thermal conductance measurements the pressure in the vacuum chamber was always kept below $3\times10^{-4}$ mbar. When oxygen was introduced, the heating of the nanotube fibre with the Veeco thermal probe was stopped, to allow oxygen to adsorb onto the nanotubes.

Thermal and electrical conductance measurements were taken on the nanotubes with oxygen being added to the vacuum chamber. Measurements were taken every 2-3 hours and oxygen was fed in the vacuum chamber for a period of typically 6-7 hours. Then the flow of oxygen was stopped and the nanotube was heated again, typically overnight in order for the oxygen to be desorbed.

Measurements were taken for different amounts of oxygen and with different nanotube fibres.

In Fig. 4.30 is shown a series of oxygen additions to the vacuum chamber and the changes they caused on the electrical and thermal conductance values of the nanotubes.

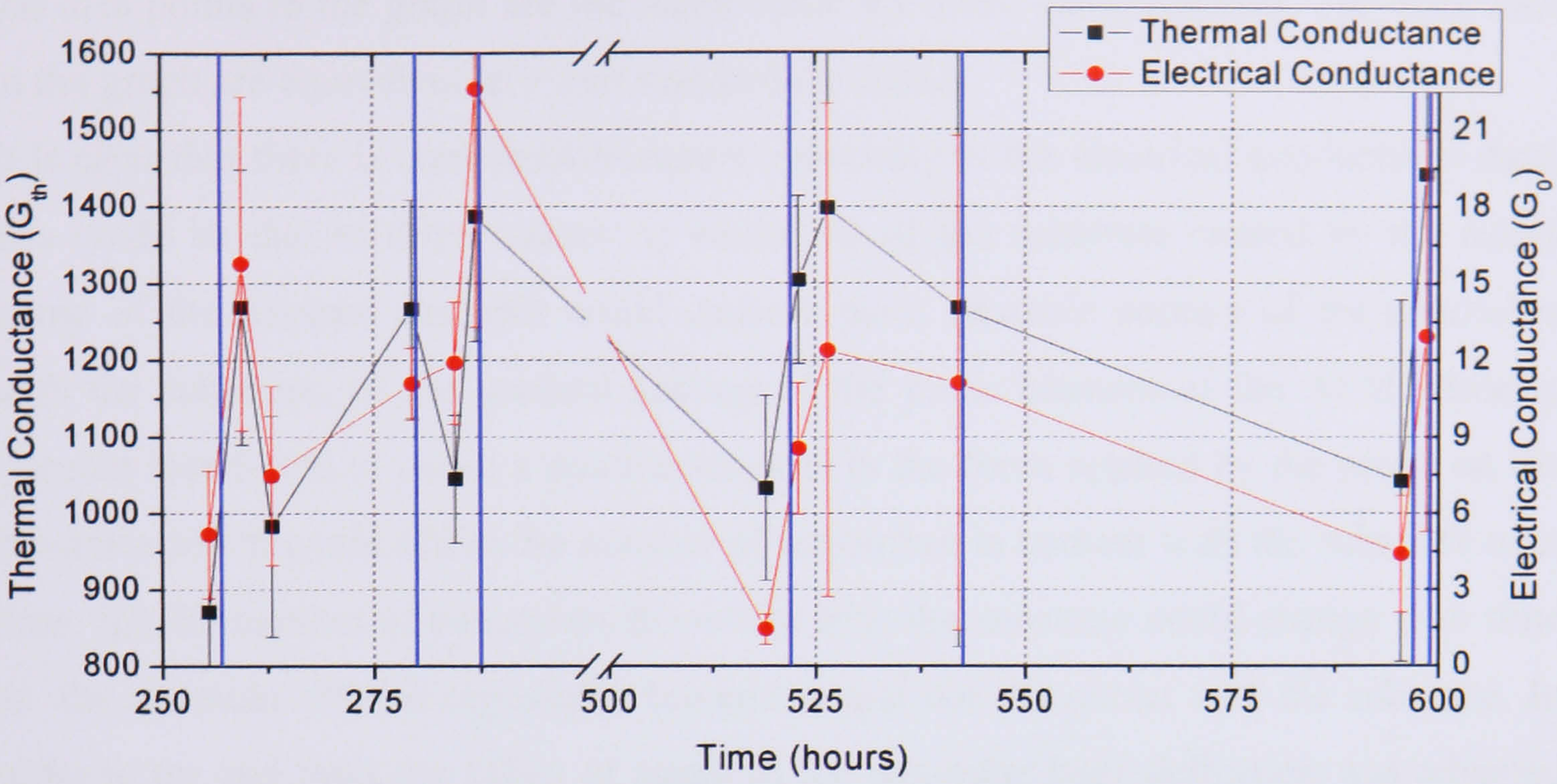



**Figure 4.30**: The changes in the electrical and thermal conductance when oxygen is added to the nanotube. The vertical blue lines indicate the introduction/switching off of the oxygen. The oxygen pressure are respectively: 1st line) Oxygen in at $5\times10^{-5}$mbar; 2nd line) Oxygen in at $6.8\times10^{-5}$mbar; 3rd line) Oxygen off; 4th line) Oxygen in at $6.4\times10^{-6}$mbar; 5th line) Oxygen off; 6th line) Oxygen in at $8.1\times10^{-6}$mbar; 7th line) Oxygen off. The temperature gradient applied across the nanotube fibre was 55K, the substrate being kept at room temperature. The voltage bias across the nanotube fibre was 10mV.

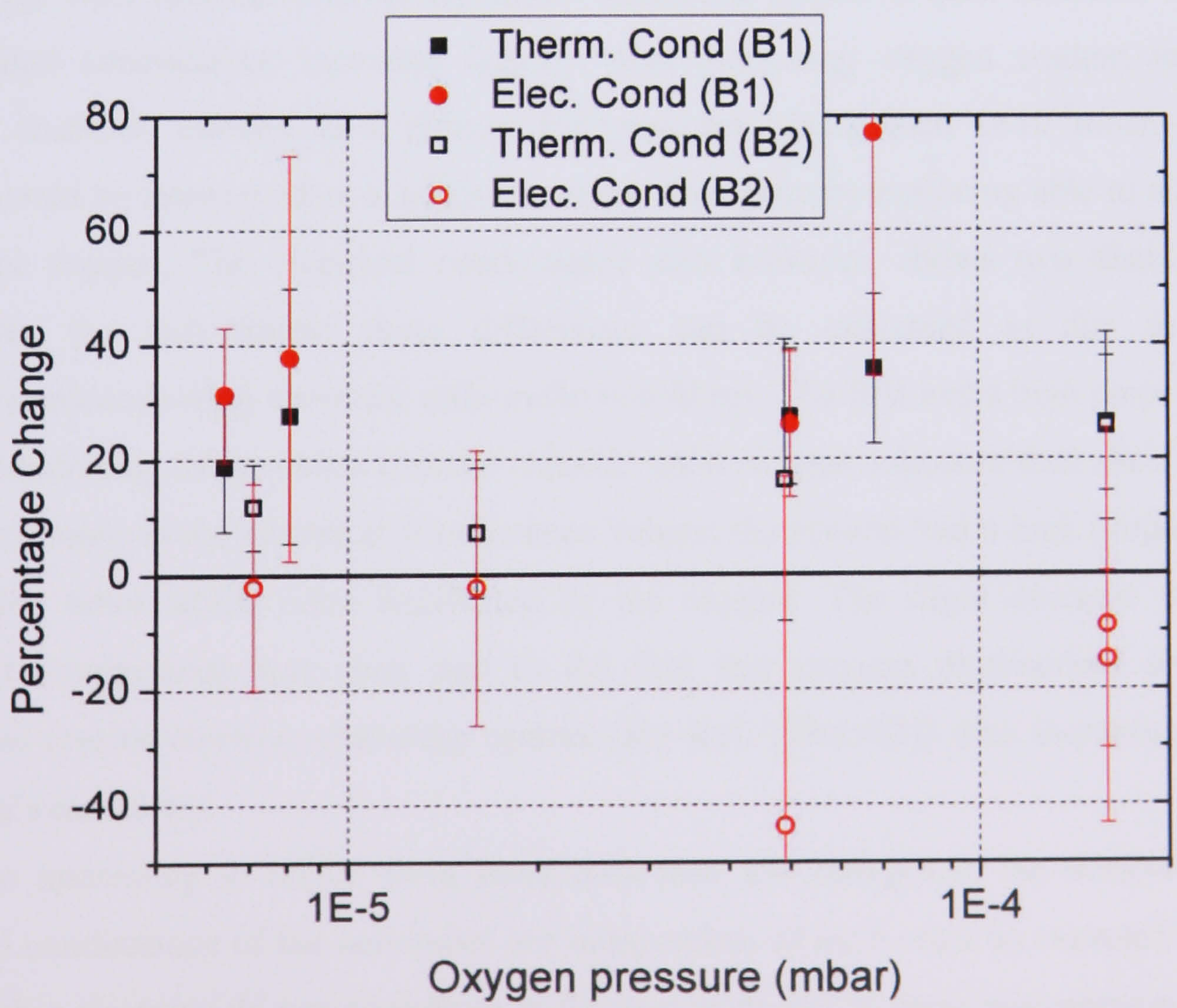



**Figure 4.31**: Percentage changes in the electrical and the thermal conductance values as oxygen is introduced in the vacuum chamber in different amounts (pressures). The data was collected with two different nanotube fibres (B1 and B2). The data shown in Fig. 4.29 corresponds to that taken with sample B1. The same force and voltage bias were applied across the fibres, but the temperature difference across B2 was 118K, while that across B1 was 55K.

The conductances were measured when the nanotube was in contact with the HOPG substrate (with the force applied by the nanotube onto the substrate kept constant) and the data points in the graph are the mean value for these measurements. The error bars in the graph are equivalent to ± one standard deviation.

It is clear that there is considerable scatter especially in the electrical conductance data, this could be due to three causes: i) vibrations of the substrate caused by the rotary pump of the vacuum chamber could cause a poor, unstable contact of the nanotubes with the substrate; ii) the gradual heating of the piezo element of the AFM while in vacuum was found to cause a continuous drift in the force applied by the probe on the substrate which could affect the number of nanotubes in contact with the substrate over time; iii) the number of nanotubes in contact with the substrate could change over time as the nanotube fibre is repeatedly brought in and out of contact with the substrate. In order to try and limit the effect of cause ii) the nanotube laser deflection was adjusted manually every ~10 minutes in vacuum to compensate for the AFM piezo drift.

The percentage changes in the electrical and thermal conductance as a function of the oxygen pressure for the data shown in Fig. 4.30 and for another data set acquired with a different nanotube fibre are shown in Fig. 4.31 (including error bars). In spite of the rather large error bars the data clearly shows distinctive trends: in both nanotube fibres the thermal conductance increases linearly with increasing oxygen content in the vacuum chamber, coming to a plateau for pressures higher than $1\times10^{-4}$mbar. This plateau could be interpreted as a saturation point, the nanotube not being able to adsorb any more oxygen. The electrical conductance data however, shows two distinctive trends for the two fibres: these differences can be explained as due to the metallic/semiconducting nanotube ratio in the two fibres. The first had a high proportion of semiconducting tubes which became metallic upon oxygen exposure thus showing a marked increase in the electrical conductance values; the second had a high proportion of metallic tubes which were unaffected by the oxygen. The slight decrease in the electrical conductance was then due to the fact that oxygen physisorbed on the nanotubes creates electron scattering centres (see Ref. [Zhao'02]) thus increasing the nanotube's resistivity.

It is also interesting to notice from these data how the changes in the thermal and electrical conductance of the nanotubes are independent of each other as expected from the fact that electrons do not contribute to the heat transport at these temperatures (see the calculation of the nanotube's Lorentz number in Section 4.3).

All the electrical and the thermal conductance data points acquired in the presence of oxygen (at different pressures) and when oxygen was degassed from the nanotubes were

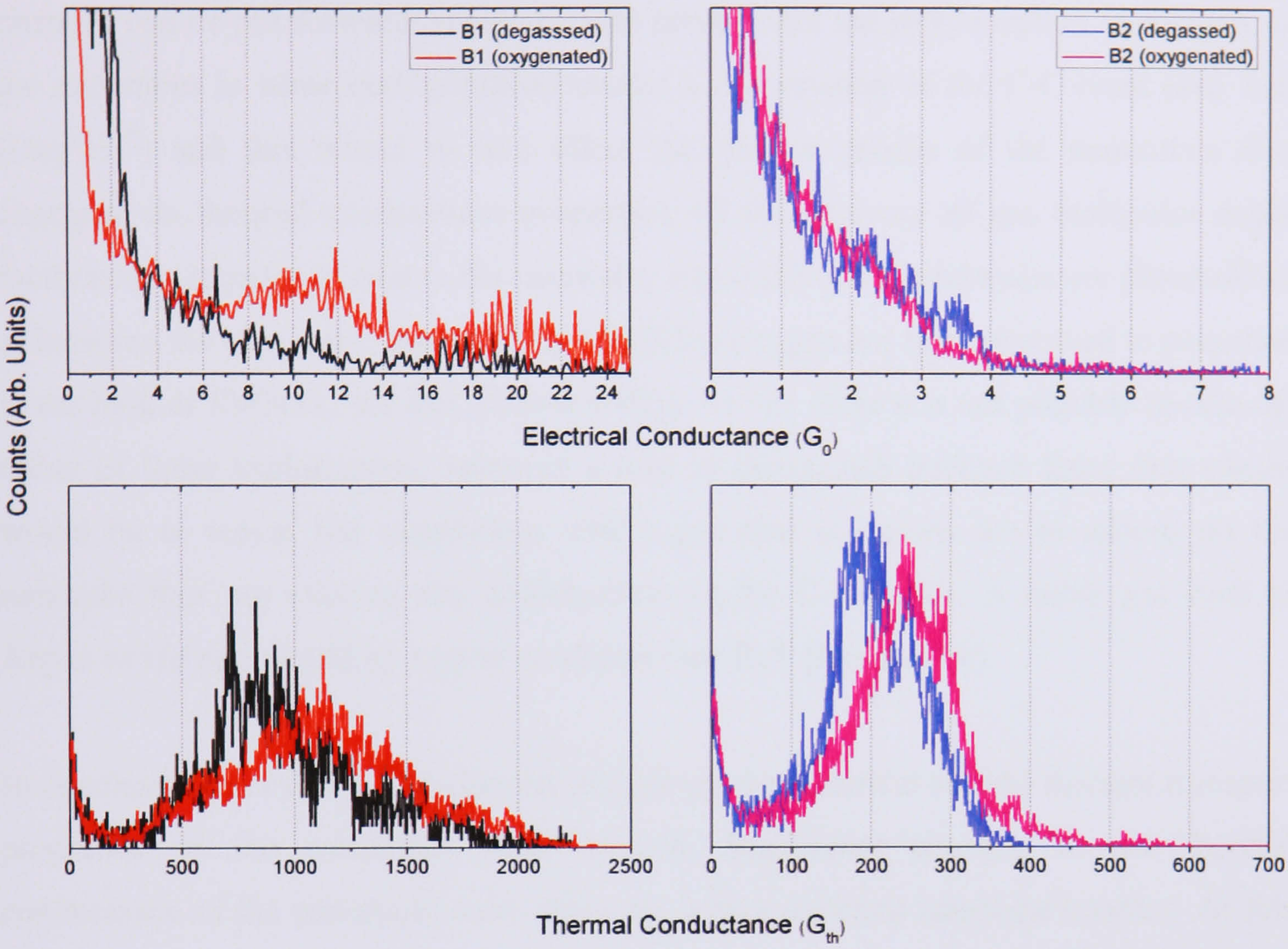



**Figure 4.32**: Histograms of the electrical and thermal conductance data acquired with two different fibres (B1 and B2) with oxygen desorbed and adsorbed on the nanotubes. The histograms have different bin sizes, these are: $0.1G_0$ and $3G_{th}$ for B1, $0.02G_0$ and $1G_{th}$ for B2.

plotted in two separate histograms for each of the two fibres. These are shown in Fig. 4.32.

The histograms include data from individual nanotubes coming into contact with the HOPG substrate and confirm what had been observed in the changes of the bulk electrical and thermal conductance plotted in Fig. 4.31. The histogram of the electrical conductance data shows how oxygen affects the properties of the first fibre (B1) by shifting the electrical measurements to higher $G_0$ values, as the semiconducting tubes that are predominant in the fibre become metallic under the effect of oxygen. On the other hand the histograms of the electrical conductance on the second fibre (B2) show how oxygen hardly affects the electrical properties of the nanotubes and confirm that this fibre must have had a predominance of metallic tubes.

The thermal conductance data for both fibres shows a clear shift to higher values when oxygen is adsorbed onto the tubes. The shift is ~$300G_{th}$ for B1 and ~$70G_{th}$ for B2 which corresponds in both cases to ~20% of the bulk value of the thermal conductance.

While the changes in the electrical conductance upon oxygen adsorption can be explained from the literature (see Section 2.1.1), there is no such information available to explain the changes in the thermal conductance. Two possible causes for these changes can be put forward: i) calculations predict that the physisorption of oxygen on the nanotubes in some configurations causes a deformation of the C-C bond (see Ref. [Dag'03]*) and this would in turn affect the phonon modes of the nanotubes thus changing its thermal conductance properties; ii) the presence of gas molecules could facilitate the transfer of heat in the nanotube, especially if the molecules are physisorbed in between the concentric layers of the MWNTs (oxygen has been observed to penetrate in the bulk of SWNTs, see Ref. [Ulbricht'02]). At this stage it is not possible to rule out either of these explanations, however a way to distinguish between these two causes would be to repeat the experiment with a gas that is known not to adsorb on the nanotube thus not causing any deformations in the C-C bonds. A noble gas such as Argon or Helium would be a good candidate (see Ref. [Collins'00]).

In conclusion the effects of molecular oxygen on the electrical and the thermal transport properties of the nanotubes were studied. Significant changes in the thermal conductance of the nanotubes were observed in two different nanotube bundles. At this stage it is not yet possible to determine the cause for these changes but two likely factors: the C-C bond deformation as a consequence of gas physisorption and the physisorption of gas molecules between the concentric carbon layers of the tubes have been considered. There is no significant amount of information on the effect of gases on the thermal conductance of the nanotubes in the literature and thus further work in this area is important to understand the causes for the changes observed here.

---

* Larger deformations in the C-C bond are predicted in the case of oxygen chemisorption on the nanotubes, however most oxygen adsorption experiments report that oxygen is just physisorbed on the nanotubes, without the formation of C-O bonds (see Section 2.1.1).

# Chapter 5 Conclusions and Further Work

The aim of this work was to study the transport properties of individual carbon nanotubes. The nanotubes under study were those that protruded from the bulk of an arc-grown MWNT fibre mounted on a commercially available Veeco AFM thermal probe.

The nanotubes were brought – in a controlled way (using the piezo element of the AFM) – in and out of contact with a conducting substrate (HOPG and/or gold) and the current and heat flow through the nanotubes were simultaneously monitored as the tubes were progressively lowered/withdrawn from the substrate together with the force applied onto the nanotubes. On several occasions both the electrical and thermal conductance of the tubes were observed to form flat plateaus during this lowering/withdrawing cycle. A physical model to study the nanotubes deformation was developed, this showed that the transport length of the tubes changed as they were lowered onto/withdrawn from a substrate. This therefore implied that the observed conductance plateaus were evidence of length independent, i.e. ballistic, electron *and* phonon transport in MWNTs. Ballistic electron transport in MWNTs at RT had already been reported in the scientific literature; however the observation of ballistic phonon transport (which had been expected in carbon nanotubes but never observed) was a first. The simultaneous measurement of the electrical and thermal flow in the nanotubes allowed the study of the ratio of the thermal and electrical conductance in the nanotubes. This was used to calculate the number of phonon modes transported in the tubes and to estimate the tube's thermal conductivity; in some tubes this was found to have an unrealistically high value thus providing further evidence for ballistic phonon transport.

The effect of exposure to molecular oxygen on the transport properties of MWNTs was also investigated. The electrical conductance of the nanotubes was measured in air and in high vacuum and compared: using a statistical analysis programme it was found that the number of metallic nanotubes contributing to the electrical conductance increased in air due to oxygen doping as expected from the literature. The effect of oxygen on both electrical *and* thermal conductance was studied by adding small amounts of pure oxygen to the vacuum chamber housing the AFM while keeping the total pressure below $10^{-4}$mbar in order to minimise heat losses through the air. The thermal

conductance of the tubes was always observed to increase in the presence of oxygen, independently of the changes in the electrical conductance (which depended on the metallic-semiconducting nanotube ratio of the MWNT fibre under study). This was attributed to two possible factors: an increase in the number of phonon modes supported by the tubes, or an increase in heat transport across the shells of the MWNT.

The results regarding the observation of ballistic phonon transport in MWNTs were published in the summer of 2005 (see [Brown'05]), since then there has been another experimental report of ballistic phonon transport in nanotubes (see [Chiu'05] - published in November 2005) describing investigations on the thermal properties of individual MWNTs performed by using the phenomenon of electrical breakdown*. This is significant since it supports the conclusions made here. These two publications seem also to have spurred a renewed interest in the topic of thermal transport in carbon nanotubes as confirmed by a recent theoretical paper (see [Wang'06] - March 2006) that cites both this work and that of Chiu et al and seeks to develop a theory to cover both the diffusive and ballistic phonon transport behaviour observed in carbon nanotubes.

While a lot was achieved in the course of this work the experimental set-up used has made it hard to determine exactly how many and what kind of nanotubes protruded most from the MWNT fibre at any one time. In order to progress with the study of the electrical and thermal properties of individual nanotubes, a better-defined system with only few or, ideally, one nanotube is needed. The nanotube/s could be either attached to an AFM probe or suspended across a trench using a 'bridge' technique (something similar to that employed by Kim et al [Kim'01]). One problem arising from this set-up is however, the probe-nanotube or nanotube-trench contact resistance. This would not only affect the electron transport along the nanotube but also its phonon transport. This area is of key importance if nanotubes are to be integrated in macroscopic circuits and has therefore been the subject of much study; there are now several reports of near-ohmic low-resistance contacts made onto carbon nanotubes, one example is the report of ballistic electron transport in nanotubes with palladium contact electrodes [Mann'03].
The development of a better-defined nanotube system is being pursued along two separate lines of work: one aims to have a small nanotube bundle attached onto the tip of the Veeco thermal probe, the second aims to place a nanotube across a bridge made of platinum whose arms could act as heat sources and as thermometers.

---

* Electrical breakdown indicates the progressive breaking of individual carbon shells in an MWNT when a high current is applied along its axis.

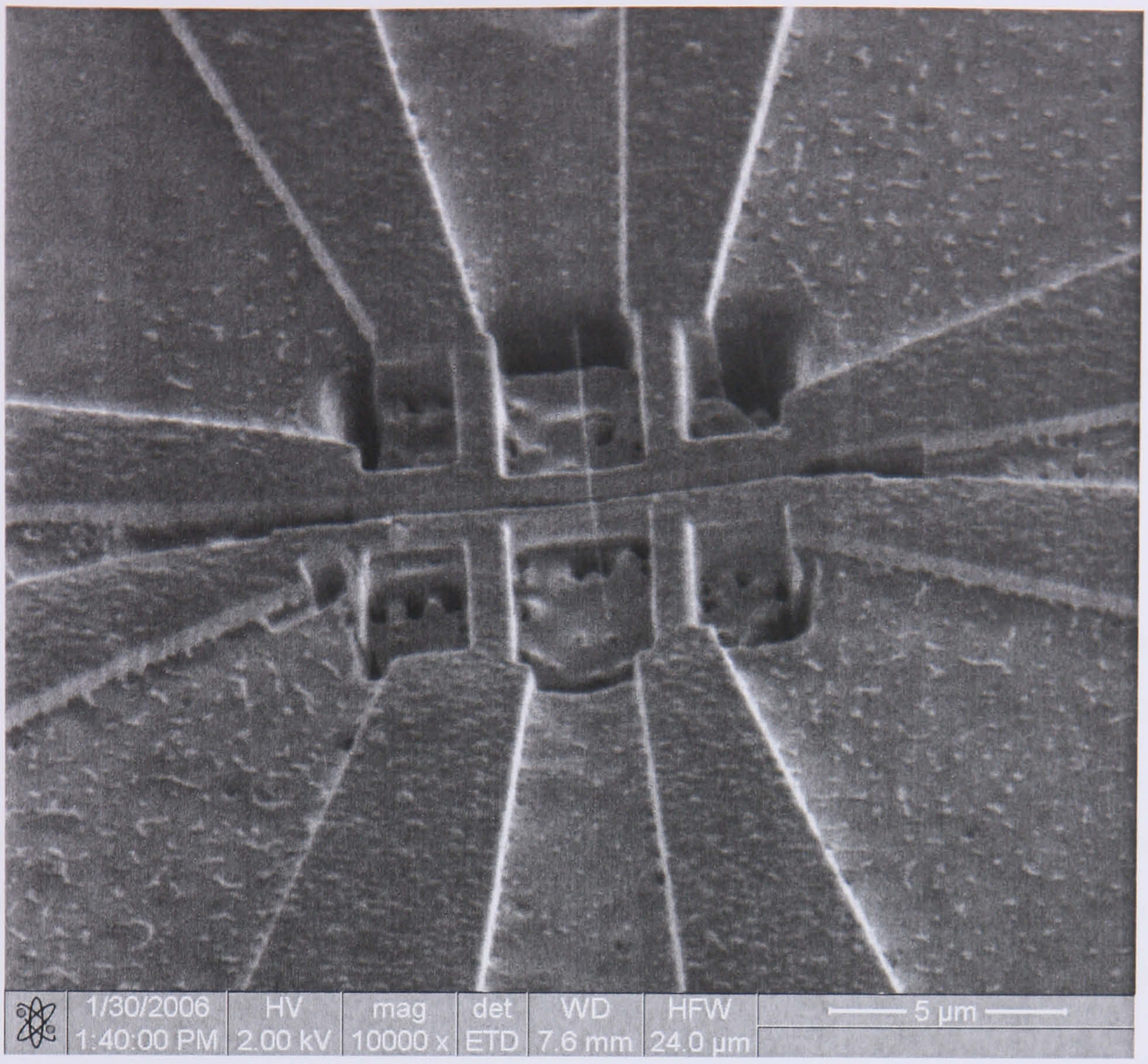



**Figure 5.1**: an SEM picture of a prototype bridge structure built on a thin film of platinum on mylar by Dr David Cox at the University of Surrey. An MWNT attached across the narrow part of the bridge is visible. One of the bridge arms would be used as a heat source and both arms would act as thermometers to determine the temperature difference across the nanotube.

The first line of work has the goal to develop an AFM thermal probe with a nanotube attached in order to exploit the very high thermal conductivity of the nanotube for study of thermal transport at the nanoscale. Applications of such thermal probes would be sought especially in the field of biology; the AFM-CNT thermal probe could be used to scan biological samples (with a temperature gradient set between the tip and the sample) and simultaneously acquire information on their topography and thermal properties. This would allow for example a correlation to be made between a given structure and its physical properties at the cellular/sub-cellular level thus enabling the study of thermal dissipation and energy transfer in individual cells (see Appendix D for more details of the DTI funded project of which this work is a part). The nanotubes will be attached to the Veeco thermal probes using the facilities and the technique developed at the University of Surrey (see Ref. [Cox'05]). Evidence that nanotubes do enhance the performance of AFM thermal probes comes from a nano-indentation report by IBM (see Ref. [Lantz'03]) where the addition of a nanotube to a silicon tip increased the tip-to-polymer heat transfer for a given load.

The second line of work involves the design of a nano-bridge made of platinum, the nanotube would be suspended across the bridge: one arm of the bridge would be heated

using Joule heating and both arms of the bridge would be used as resistive temperature sensors to determine the temperature difference across the nanotube. An SEM picture of one prototype bridge with a nanotube fixed across it is shown in Fig. 5.1. The advantage of this structure is that it could be fitted in a cryostat and cooled to liquid Helium temperatures (4.2K) in order to monitor how the heat flow in the nanotube changes and whether it does level off to $4G_{th}$ as predicted by theory [Yamamoto'04]. This bridge structure is being developed through a collaboration with the University of Surrey.

This work has also highlighted the shortcomings of the Veeco thermal probe, especially when operating in air. Therefore other supplies of AFM thermal probes have been investigated. Some nanomachined thermal AFM probes were acquired from the group of John Weaver at Glasgow University and preliminary tests of their performance in vacuum have been made. These probes are the size of conventional AFM probes and are therefore better suited for studies of thermal transport at the nanoscale as reported in Ref. [Hammiche'00].

The study of the effect of oxygen on the thermal properties of the nanotubes is also to be continued. At the time of writing tests on the effect of helium on the nanotubes are being performed in order to understand the specific cause for the changes in the thermal properties of the nanotubes when exposed to molecular oxygen.

Finally, because the DTI funded project of which this work is a part (see Appendix D) has interest in the future use of carbon nanotubes as interconnects, further work will also include measurements of the current carrying capabilities of the tubes in air and in vacuum. Preliminary results not reported here have shown that the tubes can support current densities greater than $10^{13}A/m^2$ before shell breakdown occurs (these values are of the same order of magnitude as those reported by Yao et al in [Yao'00] and confirm the high quality and ballistic properties of the tubes used in this work). Investigations of the breakdown behaviour and mechanism will also be pursued.

# Conclusion

This work confirms that the interest of the scientific community in the physical properties of carbon nanotubes is not unjustified. It also supports the fact that nanotubes are the material of choice for the study of transport at the nanoscale. Evidence of ballistic electron transport at room temperature was shown in this work and evidence for ballistic phonon transport at room temperature was also reported for the first time and discussed. In some samples ballistic phonon transport was only observable at temperatures of 160K and in others the phonon transport remained diffusive, even at cryogenic temperatures. This suggests that only defect-free, crystalline tubes are expected to display ballistic transport properties, thus making the nanotube quality a factor of key importance in the selection of the nanotube source to be used in any experimental work.

The effect of molecular oxygen on the electron and phonon transport was studied and observed to cause significant changes. The number of semiconducting nanotubes in a bundle was observed to decrease two-fold upon oxygen adsorption and the number of phonon modes in the nanotubes was observed to increase by 30% upon the introduction of oxygen. This study therefore confirms that nanotubes are extremely sensitive to their gas exposure history. This on one hand implies that nanotubes are good candidates for use in gas-sensing devices, but on the other highlights the fact that careful environment control is necessary for the study of the intrinsic properties of the nanotubes and not those caused by gas adsorption-induced effects.

Ultimately this work has shown that nanotubes can display ballistic phonon transport thus leading to an extremely high thermal conductivity. It has therefore laid the foundation for further investigations on individual nanotubes: these investigations will aim to incorporate nanotubes in AFM nano-thermal sensors and to study evidence of thermal conductance quantisation in nanotubes at temperatures below 10K.

# References


[Ashcroft'76] N. W. Ashcroft and N. D. Mermin, *Solid State Physics*: Saunders College Publishing, 1976.

[Bachtold'99] A. Bachtold, C. Strunk, J.-P. Salvetat, J.-M. Bonard, L. Forró, T. Nussbaumer, and C. Schönenberger, "Aharonov-Bohm oscillations in carbon nanotubes," *Nature*, vol. 397, pp. 673-675, 1999.

[Berber'00] S. Berber, Y.-K. Kwon, and D. Tománek, "Unusually High Thermal Conductivity of Carbon Nanotubes," *Physical Review Letters*, vol. 84, pp. 4613-4616, 2000.

[Berger'02] C. Berger, Y. Yi, Z.L.Wang, and W. A. de Heer, "Multiwalled carbon nanotubes are ballistic conductors at room temperature," *Applied Physics A*, vol. 74, pp. 363-365, 2002.

[Binnig'86] G. Binnig, C. F. Quate, and C. Gerber, "Atomic Force Microscope," *Physical Review Letters*, vol. 56, pp. 930-933, 1986.

[Binnig'93] G. Binnig and H. Rohrer, "Scanning Tunneling Microscopy – From Birth to Adolescence," in *Nobel Lectures, Physics 1981-1990.* Singapore: World Scientific Publishing Co., 1993, pp. 389-409.

[Bourlon'04] B. Bourlon, C. Miko, L. Forro´, D. C. Glattli, and A. Bachtold, "Determination of the Intershell Conductance in Multiwalled Carbon Nanotubes," *Physical Review Letters*, vol. 93, pp. 176806, 2004.

[Brown'05] E. Brown, L. Hao, J. C. Gallop, and J. C. Macfarlane, "Ballistic thermal and electrical conductance measurements on individual multiwall carbon nanotubes," *Applied Physics Letters*, vol. 87, pp. 023107, 2005.

[Chan'03] S.-P. Chan, G. Chen, X. G. Gong, and Z.-F. Liu, "Oxidation of Carbon Nanotubes by Singlet $O_2$," *Physical Review Letters*, vol. 90, pp. 086403, 2003.

[Chiu'05] H.-Y. Chiu, V.V. Deshpande, H.W. Ch. Postma, C. N. Lau, C. Miko´, L. Forro´, and M. Bockrath, " Ballistic Phonon Thermal Transport in Multiwalled Carbon Nanotubes," *Physical Review Letters*, vol. 95, pp. 226101, 2005.

[Choi'05] T. Y. Choi, D. Poulikakos, J. Tharian, and U. Sennhauser, "Measurement of thermal conductivity of individual multiwalled carbon nanotubes by the 3-ω method," *Applied Physics Letters*, vol. 87, pp. 013108, 2005.

[Chopra'03] S. Chopra, K. McGuire, N. Gothard, A. M. Rao, and A. Pham, "Selective gas detection using a carbon nanotube sensor," *Applied Physics Letters*, vol. 83, pp. 2280-2282, 2003.

[Collins'02] P. G. Collins and P. Avouris, "Multishell conduction in multiwalled carbon nanotubes," *Applied Physics A*, vol. 74, pp. 329-332, 2002.

[Collins'00] P. G. Collins, K. Bradley, M. Ishigami, and A. Zettl, "Extreme Oxygen Sensitivity of Electronic Properties of Carbon Nanotubes," *Science*, vol. 287, pp. 1801-1804, 2000.

[Cox'05] D. C. Cox, R. D. Forrest, P. R. Smith, V. Stolojan, and S. R. P. Silva, "Study of the current stressing in nanomanipulated three-dimensional carbon nanotube structures," *Applied Physics Letters*, vol. 87, pp. 033102, 2005.

[Dag'03] S. Dag, O. Gülseren, T. Yildirim, and S. Ciraci, "Oxygenation of carbon nanotubes: Atomic structure, energetics, and electronic structure," *Physical Review B*, vol. 67, pp. 165424, 2003.

[Datta'97] S. Datta, *Electronic Transport in Mesoscopic Systems*. Cambridge: Cambridge University Press, 1997.

[de Heer'97] W. A. de Heer and D. Ugarte, "Fractional Quantized Conductance in Ballistic Metal Nanowires and Carbon Nanotube Networks," in *Nanowires*: Kluwer Academic Publishers, 1997, pp. 227-236.

[de Podesta'96] M. de Podesta, *Understanding the Properties of Matter*: Taylor & Francis, 1996.

[Delaney'99a] P. Delaney, H. J. Choi, J. Ihm, S. G. Louie, and M. L. Cohen, "Broken symmetry and pseudogaps in ropes of carbon nanotubes," *Physical Review B*, vol. 60, pp. 7899-7904, 1999a.

[Delaney'99b] P. Delaney, M. Di Ventra, and S. T. Pantelides, "Quantized conductance of multiwalled carbon nanotubes," *Applied Physics Letters*, vol. 75, pp. 3787-3789, 1999b.

[Demczyk'02] B. G. Demczyk, Y. M. Wang, J. Cumings, M. Hetman, W. Han, A. Zettl, and R. O. Ritchie, "Direct mechanical measurement of the tensile strength and elastic modulus of multiwalled carbon nanotubes," *Materials Science and Engineering A*, vol. 334, pp. 173-178, 2002.

[Dresselhaus'01] M. S. Dresselhaus, G. Dresselhaus, P. Avouris (Eds.), *Carbon Nanotubes Synthesis, Structure, Properties and Applications*. Heidelberg: Springer, 2001.

[Ebbesen'94] T. W. Ebbesen, "Carbon Nanotubes," *Annual Review of Materials Science*, vol. 24, pp. 235-264, 1994.

[Falvo'97] M. R. Falvo, G. J. Clary, R. M. Taylor, II, V. Chi, F. P. Brooks, Jr., S. Washburn, and R. Superfine, "Bending and buckling of carbon nanotubes under large strain," *Nature*, vol. 389, pp. 582-584, 1997.

[Falvo'00] M. R. Falvo, J. Steele, R. M. Taylor, II, and R. Superfine, "Gearlike rolling motion mediated by commensurate contact: Carbon nanotubes on HOPG," *Physical Review B*, vol. 62, pp. R10665-R10667, 2000.

[Fisher'99] T. E. Fisher, A. F. Oberhauser, M. Carrion-Vazquez, P. E. Marszalek, and J. M. Fernandez, "The study of protein mechanics with the atomic force microscope," *Trends in Biochemical Sciences*, vol. 24, pp. 379-384, 1999.

[Frank'98] S. Frank, P. Poncharal, Z. L. Wang, and W. A. de Heer, "Carbon Nanotube Quantum Resistors," *Science*, vol. 280, pp. 1744-1746, 1998.

[Fujii'05] M. Fujii, X. Zhang, H. Xie, H. Ago, K. Takahashi, T. Ikuta, H. Abe, and T. Shimizu, "Measuring the Thermal Conductivity of a Single Carbon Nanotube," *Physical Review Letters*, vol. 95, pp. 065502, 2005.

[Giannozzi'03] P. Giannozzi, R. Car, and G. Scoles, "Oxygen adsorption on graphite and nanotubes," *Journal of Chemical Physics*, vol. 118, pp. 1003-1006, 2003.

[Gomès'99] S. Gomès, N. Trannoy, and P. Grossel, "DC thermal microscopy: study of the thermal exchange between a probe and a sample," *Measurement Science and Technology*, vol. 10, pp. 805-811, 1999.

[Hammiche'00] A. Hammiche, L. Bozec, M. Conroy, H. M. Pollock, G. Mills, J. M. R. Weaver, D. M. Price, M. Reading, D. J. Hourston, and M. Song, "Highly localized thermal, mechanical, and spectroscopic characterization of polymers using miniaturized thermal probes," *Journal of Vacuum Science and Technology B*, vol. 18, pp. 1322-1332, 2000.

[Harris'99] P. J. F. Harris, *Carbon Nanotubes and Related Structures*: Cambridge University Press, 1999.

[Hone'00] J. Hone, B. Batlogg, Z. Benes, A. T. Johnson, and J. E. Fischer, "Quantized Phonon Spectrum of Single-Wall Carbon Nanotubes," *Science*, vol. 289, pp. 1730-1733, 2000.

[Hone'02] J. Hone, M. C. Llaguno, M. J. Biercuk, A. T. Johnson, B. Batlogg, Z. Benes, and J. E. Fischer, "Thermal properties of carbon nanotubes and nanotube-based materials," *Applied Physics A*, vol. 74, pp. 339-343, 2002.

[Hone'99] J. Hone, M. Whitney, C. Piskoti, and A. Zettl, "Thermal conductivity of single-walled carbon nanotubes," *Physical Review B*, vol. 59, pp. R2514-R2516, 1999.

[Huang'05] J. Y. Huang, S. Chen, S. H. Jo, Z. Wang, D. X. Han, G. Chen, M. S. Dresselhaus, and Z. F. Ren, "Atomic-Scale Imaging of Wall-by-Wall Breakdown and Concurrent Transport Measurements in Multiwall Carbon Nanotubes," *Physical Review Letters*, vol. 94, pp. 236802, 2005.

[Iijima'91] S. Iijima, "Helical microtubules of graphitic carbon," *Nature*, vol. 354, pp. 56-58, 1991.

[Jhi'00] S.-H. Jhi, S. G. Louie, and M. L. Cohen, "Electronic Properties of Oxidized Carbon Nanotubes," *Physical Review Letters*, vol. 85. pp. 1710-1713, 2000.

[Kajiura'05] H. Kajiura, A. Nandyala, U. C. Coskun, A. Bezryadin, M. Shiraishi, and M. Ata, "Electronic mean free path in as-produced and purified single-wall carbon nanotubes," *Applied Physics Letters*, vol. 86, pp. 122106, 2005.

[Kim'01] P. Kim, L. Shi, A. Majumdar, and P. L. McEuen, "Thermal Transport Measurements of Individual Multiwalled Nanotubes," *Physical Review Letters*, vol. 87, pp. 215502, 2001.

[Kong'00] J. Kong, N. R. Franklin, C. Zhou, M. G. Chapline, S. Peng, K. Cho, and H. Dai, "Nanotube Molecular Wires as Chemical Sensors," *Science*, vol. 287, pp. 622-625, 2000.

[Kong'01] J. Kong, E. Yenilmez, T. W. Tombler, W. Kim, H. Dai, R. B. Laughlin, L. Liu, C. S. Jayanthi, and S. Y. Wu, "Quantum Interference and Ballistic Transmission in Nanotube ElectronWaveguides," *Physical Review Letters*, vol. 87, pp. 106801, 2001.

[Kroto'85] H. W. Kroto, J. R. Heath, S. C. O'Brien, R. F. Curl, and R. E. Smalley, "$C_{60}$: Buckminsterfullerene," *Nature*, vol. 318, pp. 162-163, 1985.

[Lambin'00] P. Lambin, V. Meunier, and A. Rubio, "Electronic structure of polychiral carbon nanotubes," *Physical Review B*, vol. 62, pp. 5129-5135, 2000.

[Lantz'03] M. A. Lantz, B. Gotsmann, U. T. Dürig, P. Vettiger, Y. Nakayama, T. Shimizu, and H. Tokumoto, "Carbon nanotube tips for thermomechanical data storage," *Applied Physics Letters*, vol. 83, pp. 1266-1268, 2003.

[Lefèvre'02] S. Lefèvre, S. Volz, and J.-B. Saulnier, "Calibration of scanning thermal microscopes for conductivity measurements " presented at 12th International heat transfer conference, Grenoble, 2002.

[Liu'98] J. Liu, A. G. Rinzler, H. Dai, J. H. Hafner, R. K. Bradley, P. J. Boul, A. Lu, T. Iverson, K. Shelimov, C. B. Huffman, F. Rodriguez-Macias, Y.-S. Shon, T. R. Lee, D. T. Colbert, and R. E. Smalley, "Fullerene Pipes," *Science*, vol. 280, pp. 1253-1256, 1998.

[Llaguno'01] M. C. Llaguno, J. Hone, A. T. Johnson, and J. E. Fischer, "Thermal conductivity of single wall carbon nanotubes: Diameter and annealing dependence," *AIP Conference Proceedings* vol. 591, pp. 384-387, 2001.

[Majumdar'99] A. Majumdar, "Scanning Thermal Microscopy," *Annual Review of Materials Science*, vol. 29, pp. 505-585, 1999.

[Mann'03] D. Mann, A. Javey, J. Kong, Q. Wang, and H. Dai, "Ballistic Transport in Metallic Nanotubes with Reliable Pd Ohmic Contacts," *Nano Letters*, vol. 3, pp. 1541-1544, 2003.

[Márk'98] G. I. Márk, L. P. Biró, and J. Gyulai, "Simulation of STM images of three-dimensional surfaces and comparison with experimental data: Carbon nanotubes," *Physical Review B*, vol. 58, pp. 12645-12648, 1998.

[McEuen'02] P. L. McEuen, M. S. Fuhrer, and H. Park, "Single-Walled Carbon Nanotube Electronics," *IEEE Transactions on Nanotechnology*, vol. 1, pp. 78-85, 2002.

[Modi'03] A. Modi, N. Koratkar, E. Lass, B. Wei, and P. M. Ajayan, "Miniaturized gas ionization sensors using carbon nanotubes," *Nature*, vol. 424, pp. 171-174, 2003.

[Osman'01] M. A. Osman and D. Srivastava, "Temperature dependence of the thermal conductivity of single-wall carbon nanotubes," *Nanotechnology*, vol. 12, pp. 21-24, 2001.

[Park'04] J.-Y. Park, S. Rosenblatt, Y. Yaish, V. Sazonova, H. Üstünel, S. Braig, T. A. Arias, P. W. Brouwer, and P. L. McEuen, "Electron-Phonon Scattering in Metallic Single-Walled Carbon Nanotubes," *Nano Letters*, vol. 4, pp. 517-520, 2004.

[Pendry'83] J. B. Pendry, "Quantum limits to the flow of information and entropy," *Journal of Physics A: Mathematical and General*, vol. 16, pp. 2161-2171, 1983.

[Poncharal'02] P. Poncharal, C. Berger, Y. Yi, Z. L. Wang, and W. A. de Heer, "Room Temperature Ballistic Conduction in Carbon Nanotubes," *Journal of Physical Chemistry B*, vol. 106, pp. 12104-12118, 2002.

[Poncharal'99] P. Poncharal, S. Frank, Z.L.Wang, and W. A. de Heer, "Conductance quantization in multiwalled carbon nanotubes," *The European Physical Journal D*, vol. 9, pp. 77-79, 1999.

[Qi'03] P. Qi, O. Vermesh, M. Grecu, A. Javey, Q. Wang, H. Dai, S. Peng, and K. J. Cho, "Toward Large Arrays of Multiplex Functionalized Carbon Nanotube Sensors for Highly Sensitive and Selective Molecular Detection," *Nano Letters*, vol. 3, pp. 347-351, 2003.

[Qin'00] L.-C. Qin, X. Zhao, K. Hirahara, Y. Miyamoto, Y. Ando, and S. Iijima, "The smallest carbon nanotube," *Nature*, vol. 408, pp. 50, 2000.

[Rego'98] L. G. C. Rego and G. Kirczenow, "Quantized Thermal Conductance of Dielectric Quantum Wires," *Physical Review Letters*, vol. 81, pp. 232-235, 1998.

[Saito'98a] R. Saito, G. Dresselhaus, and M. S. Dresselhaus, *Physical Properties of Carbon Nanotubes*. London: Imperial College Press, 1998a.

[Saito'98b] R. Saito, T. Takeya, T. Kimura, G. Dresselhaus, and M. S. Dresselhaus, "Raman intensity of single-wall carbon nanotubes," *Physical Review B*, vol. 57, pp. 4145-4153, 1998b.

[Salvetat'99] J.-P. Salvetat, G. A. D. Briggs, J.-M. Bonard, R. R. Bacsa, A. J. Kulik, T. Stöckli, N. A. Burnham, and L. Forró, "Elastic and Shear Moduli of Single-Walled Carbon Nanotube Ropes," *Physical Review Letters*, vol. 82, pp. 944-947, 1999.

[Sanvito'00] S. Sanvito, Y.-K. Kwon, D. Tománek, and C. J. Lambert, "Fractional Quantum Conductance in Carbon Nanotubes," *Physical Review Letters*, vol. 84, pp. 1974-1977, 2000.

[Schwab'00] K. Schwab, E. A. Henriksen, J. M. Worlock, and M. L. Roukes, "Measurement of the quantum of thermal conductance," *Nature*, vol. 404, pp. 974-977, 2000.

[Sumanasekera'00] G. U. Sumanasekera, C. K. W. Adu, S. Fang, and P. C. Eklund, "Effects of Gas Adsorption and Collisions on Electrical Transport in Single-Walled Carbon Nanotubes," *Physical Review Letters*, vol. 85, pp. 1096-1099, 2000.

[Sumanasekera'02] G. U. Sumanasekera, B. K. Pradhan, H. E. Romero, K. W. Adu, and P. C. Eklund, "Giant Thermopower Effects from Molecular Physisorption on Carbon Nanotubes," *Physical Review Letters*, vol. 89, pp. 166801, 2002.

[Tekleab'01] D. Tekleab, D. L. Carroll, G. G. Samsonidze, and B. I. Yakobson, "Strain-induced electronic property heterogeneity of a carbon nanotube," *Physical Review B*, vol. 64, pp. 035419, 2001.

[Tian'94] W. Tian and S. Datta, "Aharonov-Bohm-type effect in graphene tubules: A Landauer approach," *Physical Review B*, vol. 49, pp. 5097-5100, 1994.

[Tománek'87] D. Tománek, S. G. Louie, H. J. Mamin, and D. W. Abraham, "Theory and observation of highly asymmetric atomic structure in scanning-tunneling-microscopy images of graphite," *Physical Review B*, vol. 35, pp. 7790-7793, 1987.

[Tombler'00] T. W. Tombler, C. Zhou, L. Alexseyev, J. Kong, H. Dai, L. Liu, C. S. Jayanthi, M. Tang, and S.-Y. Wu, "Reversible electromechanical characteristics of carbon nanotubes under local-probe manipulation," *Nature*, vol. 405, pp. 769-772, 2000.

[Ulbricht'02] H. Ulbricht, G. Moos, and T. Hertel, "Physisorption of molecular oxygen on single-wall carbon nanotube bundles and graphite," *Physical Review B*, vol. 66, pp. 075404, 2002.

[Urbina'03] A. Urbina, I. Echeverría, A. Pérez-Garrido, A. Díaz-Sánchez, and J. Abellán, "Quantum Conductance Steps in Solutions of Multiwalled Carbon Nanotubes," *Physical Review Letters*, vol. 90, pp. 106603, 2003.

[Valentini'03] L. Valentini, I. Armentano, J. M. Kenny, C. Cantalini, L. Lozzi, and S. Santucci, "Sensors for sub-ppm $NO_2$ gas detection based on carbon nanotube thin films," *Applied Physics Letters*, vol. 82, pp. 961-963, 2003.

[van Wees'88] B. J. van Wees, H. van Houten, C. W. J. Beenakker, J. G. Williamson, L. P. Kouwenhoven, D. van der Marel, and C. T. Foxon, "Quantized Conductance of Point Contacts in a Two-Dimensional Electron Gas," *Physical Review Letters*, vol. 60, pp. 848-850, 1988.

[Wang'06] J. Wang and J.-S. Wang, "Carbon nanotube thermal transport: Ballistic to diffusive," *Applied Physics Letters*, vol. 88, pp. 111909, 2006.

[Waters'05] J. F. Waters, P. R. Guduru, M. Jouzi, J. M. Xu, T. Hanlon, and S. Suresh, "Shell buckling of individual multiwalled carbon nanotubes using nanoindentation," *Applied Physics Letters*, vol. 87, pp. 103109, 2005.

[Wharam'88] D. A. Wharam, T. J. Thornton, R. Newbury, M. Pepper, H. Ahmed, J. E. F. Frost, D. G. Hasko, D. C. Peacock, D. A. Ritchie, and G. A. C. Jones, "One-dimensional transport and the quantisation of the ballistic resistance," *Journal of Physics C: Solid State Physics*, vol. 21, pp. L209-L214, 1988.

[Wong'97] E. W. Wong, P. E. Sheehan, and C. M. Lieber, "Nanobeam Mechanics: Elasticity, Strength, and Toughness of Nanorods and Nanotubes," *Science*, vol. 277, pp. 1971-1975, 1997.

[Xiao'04] Y. Xiao, X. H. Yan, J. X. Cao, J. W. Ding, Y. L. Mao, and J. Xiang, "Specific heat and quantized thermal conductance of single-walled boron nitride nanotubes," *Physical Review B*, vol. 69, pp. 205415, 2004.

[Yakobson'97] B. I. Yakobson and R. E. Smalley, "Fullerene Nanotubes: $C_{1,000,000}$ and Beyond," *American Scientist*, vol. 85, pp. 324-337, 1997.

[Yamamoto'04] T. Yamamoto, S. Watanabe, and K. Watanabe, "Universal Features of Quantized Thermal Conductance of Carbon Nanotubes," *Physical Review Letters*, vol. 92, pp. 075502, 2004.

[Yao'00] Z. Yao, C. L. Kane, and C. Dekker, "High-Field Electrical Transport in Single-Wall Carbon Nanotubes," *Physical Review Letters*, vol. 84, pp. 2941-2944, 2000.

[Yu'00] M.-F.Yu, O. Lourie, M. J. Dyer, K. Moloni, T. F. Kelly, and R. S. Ruoff, " Strength and Breaking Mechanism of Multiwalled Carbon Nanotubes Under Tensile Load," *Science*, vol. 287, pp. 637-640, 2000.

[Zhang'03] X. Zhang, W. Zhang, L. Liu, and Z. X. Shen, "Surface-enhanced Raman of Z-vibration mode in single-walled and multi-walled carbon nanotube," *Chemical Physics Letters*, vol. 372, pp. 497-502, 2003.

[Zhao'02] J. Zhao, A. Buldum, J. Han, and J. P. Lu, "Gas molecule adsorption in carbon nanotubes and nanotube bundles," *Nanotechnology*, vol. 13, pp. 195-200, 2002.

# Appendices

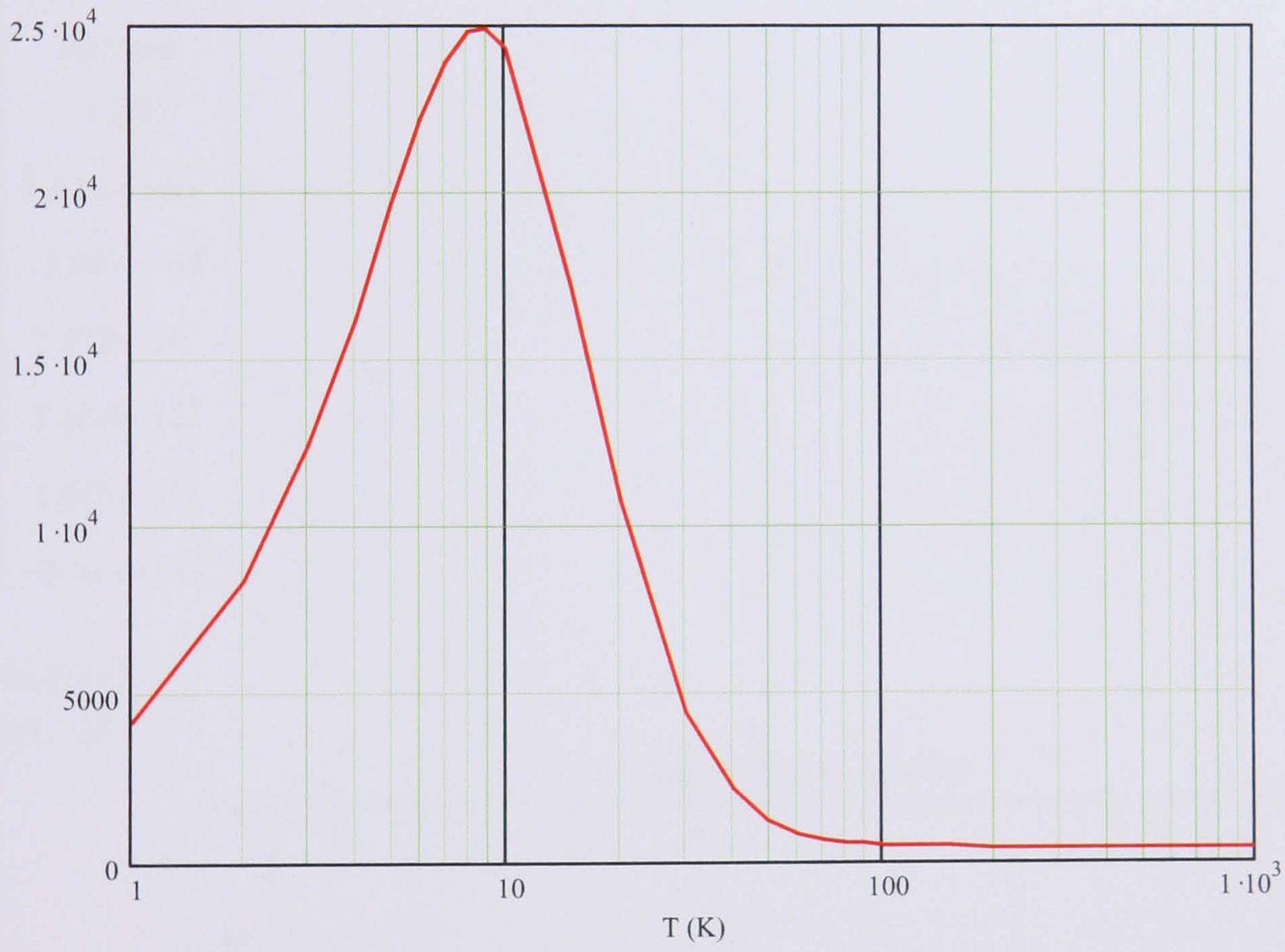
## A - MathCAD programme to model the cooling of the AFM cold stage

---

First it is necessary to find a function to model the behaviour of the conductivity k of copper between 70K and 300K.
Data taken from www.efunda.com.

:= N := 0.. 29

P:\..\Cu conductivity.txt




The model is then fitted with a polynomial curve in the temperature range of interest:

$vxl_N := Cu\_cond_{29-N,0}$

$vyl_N := Cu\_cond_{29-N,1}$

N1 := 0.. 9

$vx_{N1} := vxl_{13-N1}$

$vy_{N1} := vyl_{13-N1}$

$$vx = \begin{array}{|c|r|}\hline & 0 \\ \hline 0 & 70 \\ \hline 1 & 80 \\ \hline 2 & 90 \\ \hline 3 & 100 \\ \hline 4 & 150 \\ \hline 5 & 200 \\ \hline 6 & 250 \\ \hline 7 & 300 \\ \hline 8 & 350 \\ \hline 9 & 400 \\ \hline \end{array} \qquad vy = \begin{array}{|c|r|}\hline & 0 \\ \hline 0 & 647 \\ \hline 1 & 557 \\ \hline 2 & 508 \\ \hline 3 & 482 \\ \hline 4 & 429 \\ \hline 5 & 413 \\ \hline 6 & 406 \\ \hline 7 & 401 \\ \hline 8 & 396 \\ \hline 9 & 393 \\ \hline \end{array}$$

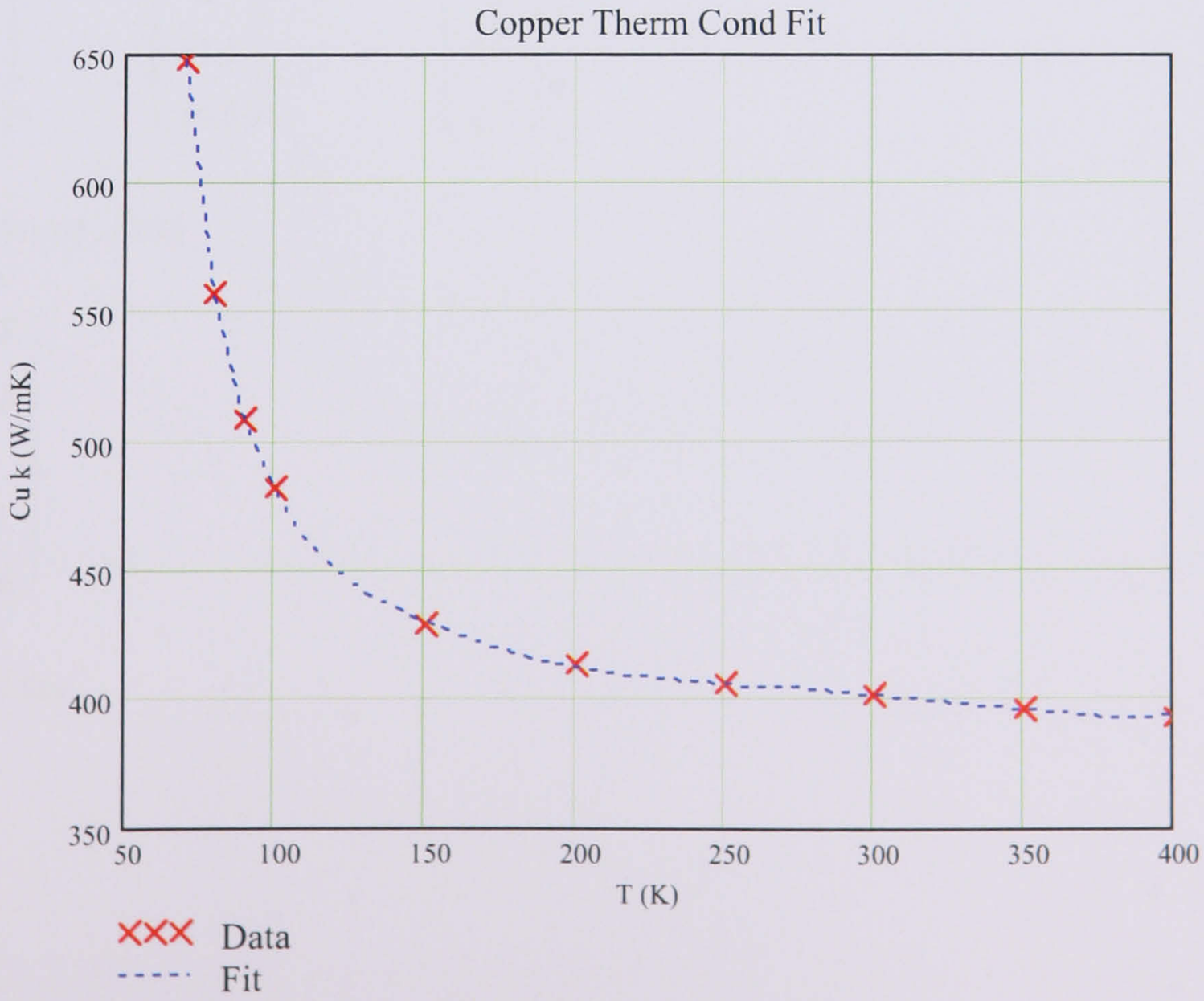
$$F(x) := \begin{pmatrix} 1 \\ x \\ x^2 \\ x^3 \\ x^{\frac{1}{2}} \\ x^{-1} \\ x^{-2} \\ x^{\frac{1}{3}} \\ x^{\frac{1}{4}} \end{pmatrix}$$

$S := linfit(vx, vy, F)$

$$S = \begin{pmatrix} -1.585 \times 10^{5} \\ 687.288 \\ -0.285 \\ 1.212 \times 10^{-4} \\ -5.981 \times 10^{4} \\ 7.272 \times 10^{5} \\ 7.404 \times 10^{4} \\ 1.855 \times 10^{5} \\ -5.611 \times 10^{4} \end{pmatrix}$$

$G(t) := F(t) \cdot S$

$r := 0, 1 .. 33$

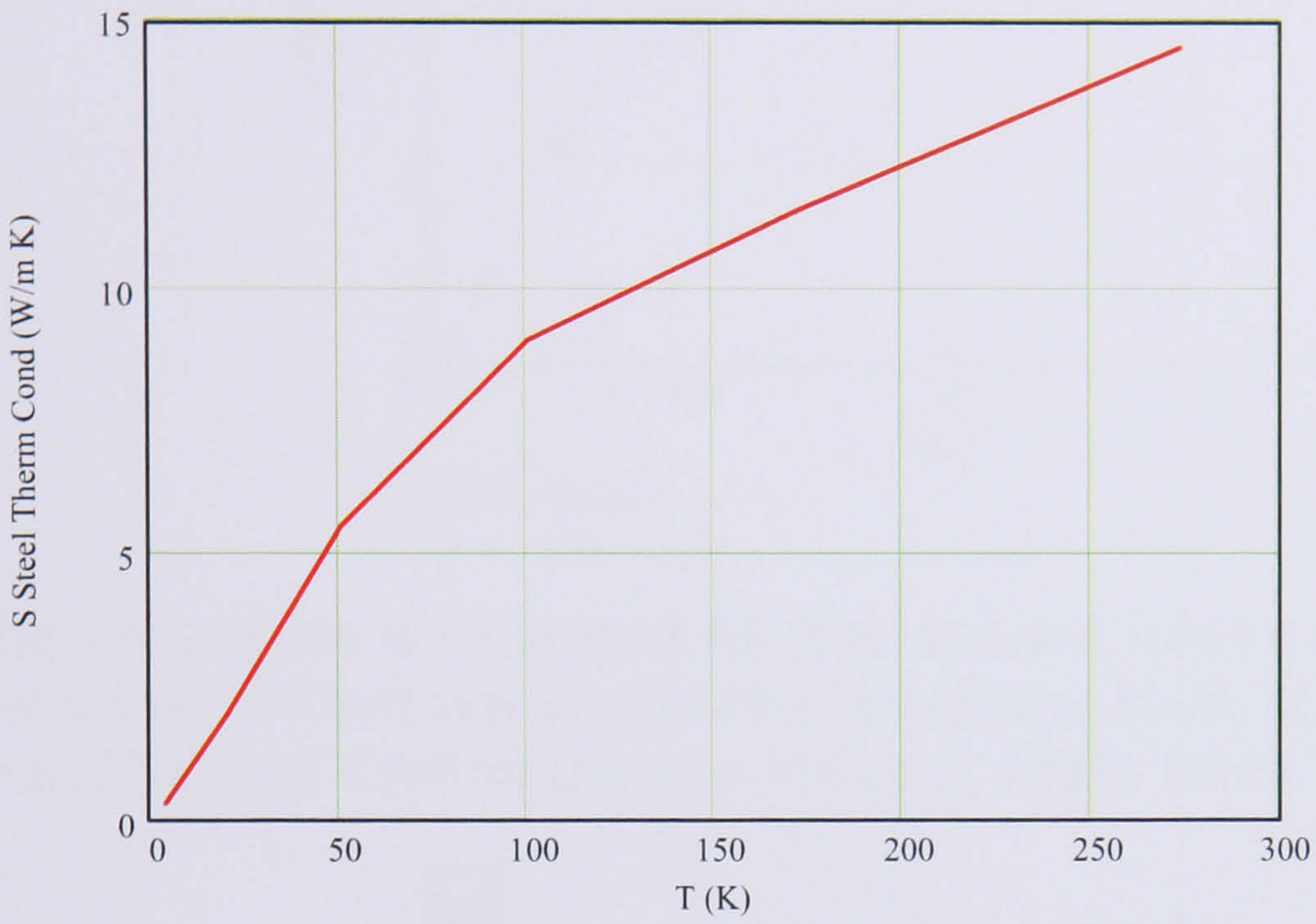


Then the same is done for the thermal conductivity of stainless steel. Data is taken from Kaye and Laby online: www.kayelaby.npl.co.uk.

:=

P:\..\s-steel conductivity.txt

SS := 0.. 5




The stainless steel data if fitter with a polynomial curve.

$ssx_{5-SS} := ssteel\_cond_{SS,0}$

$ssy_{5-SS} := ssteel\_cond_{SS,1}$

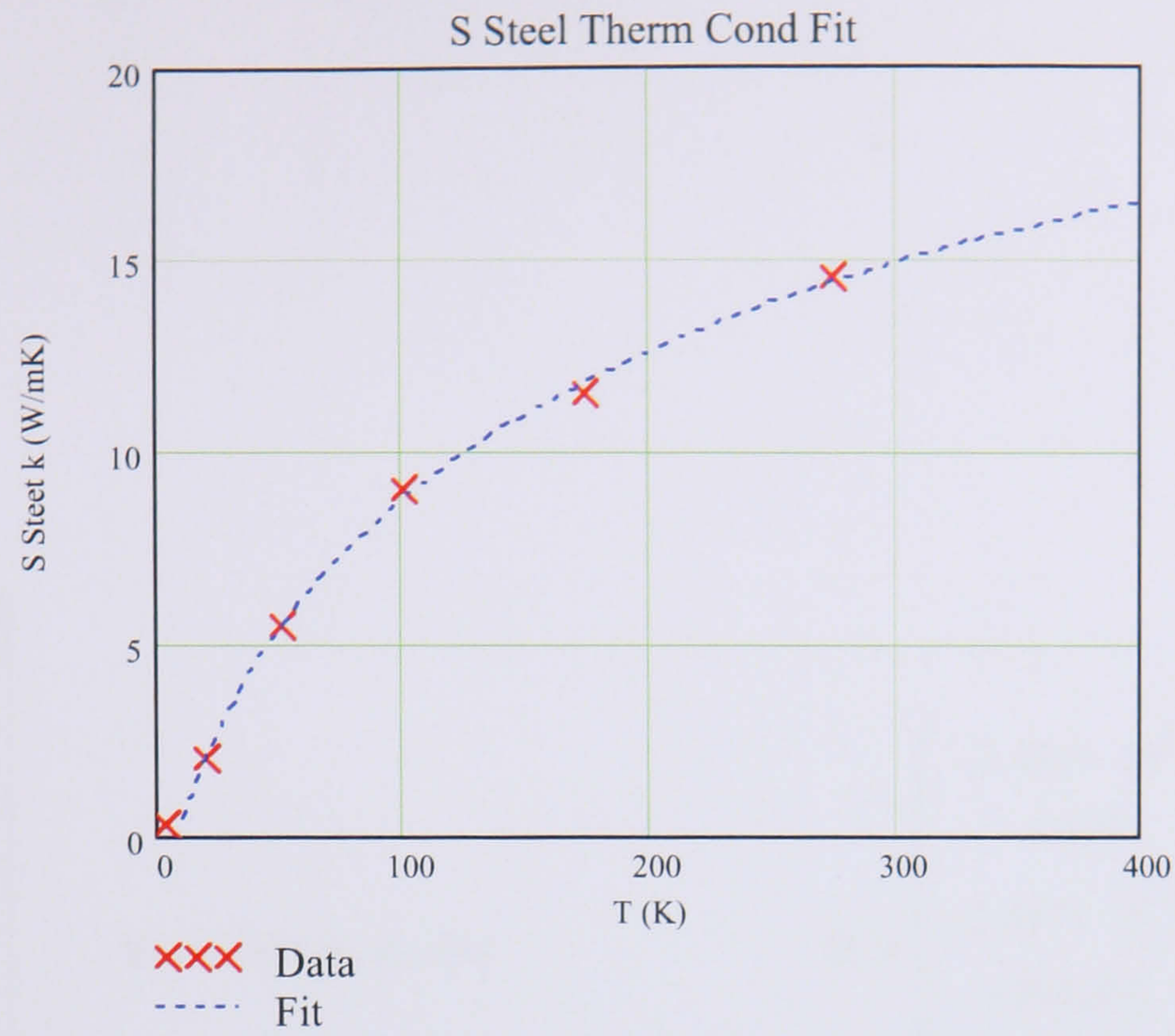
$$ssx = \begin{pmatrix} 4 \\ 20 \\ 50 \\ 100 \\ 173 \\ 273.2 \end{pmatrix} \quad ssy = \begin{pmatrix} 0.3 \\ 2 \\ 5.5 \\ 9 \\ 11.5 \\ 14.5 \end{pmatrix} \quad Fss(x) := \begin{pmatrix} 1 \\ x \\ 0 \\ x^{\frac{1}{3}} \\ x^{-1} \end{pmatrix}$$

Sss := linfit(ssx, ssy, Fss)

$$Sss = \begin{pmatrix} -10.18 \\ -0.014 \\ 0 \\ 4.348 \\ 14.496 \end{pmatrix}$$

S(s) := Fss(s)·Sss

$sr := 0, 10 .. 400$

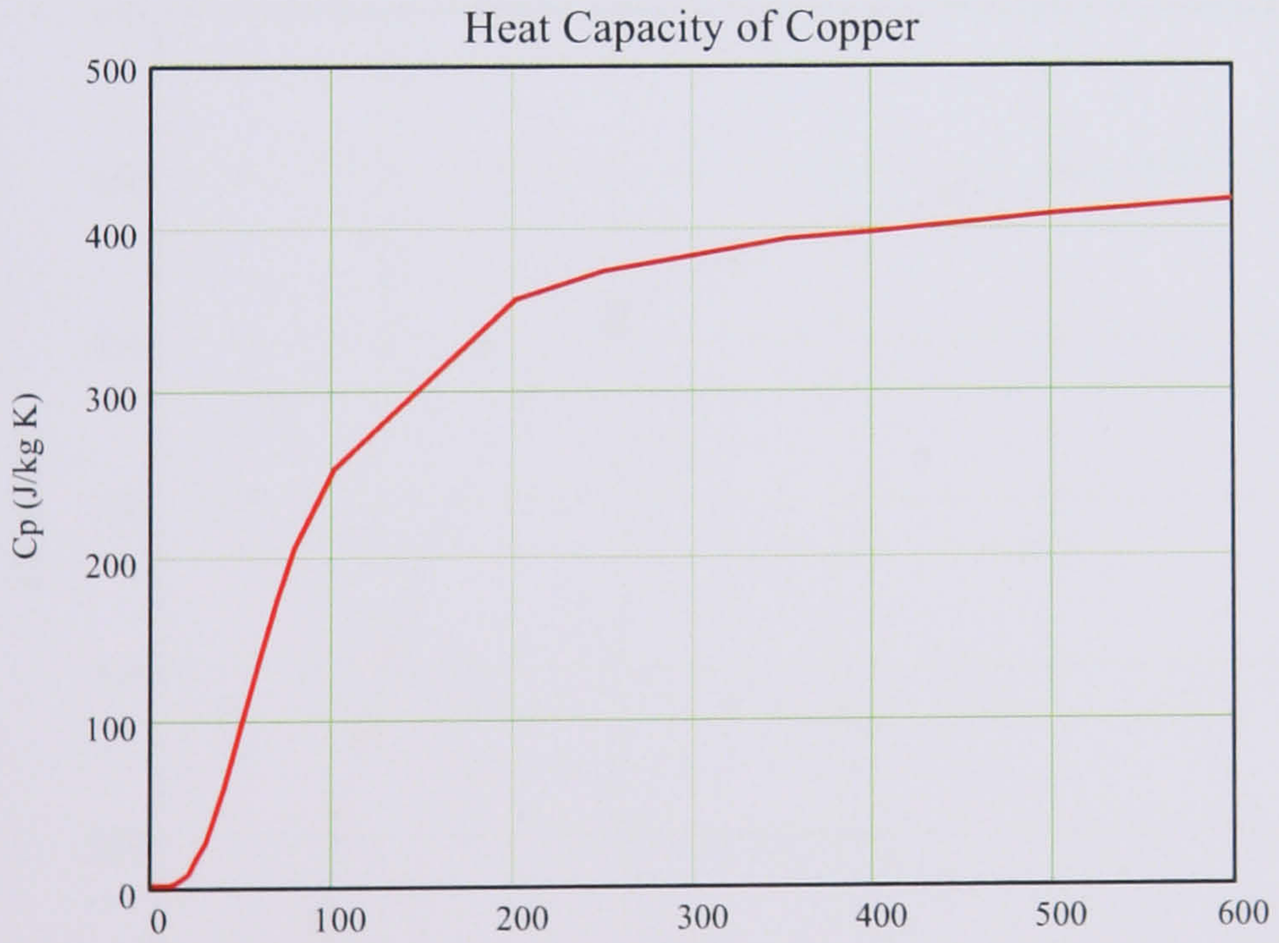



The procedure is repeated for the specific heat capacity Cp of copper. Data taken from www.efunda.com (from 200K upwards) and from the 'Handbook of Chemistry and Physics' -data from 100 K downwards.

:=

P:\..\Cu heat capacity.txt

$P := 0 .. 23$




The polynomial fit procedure is repeated for the specific heat capacity data.

$P1 := 0 .. 9$

$cx_{9-P1} := Cu\_Cp_{23-P1,0}$

$cy_{9-P1} := Cu\_Cp_{23-P1,1}$

$$Fc(x) := \begin{pmatrix} 1 \\ x \\ x^3 \\ \frac{1}{x^2} \\ \frac{1}{x^3} \\ 0 \end{pmatrix}$$

$cy =$

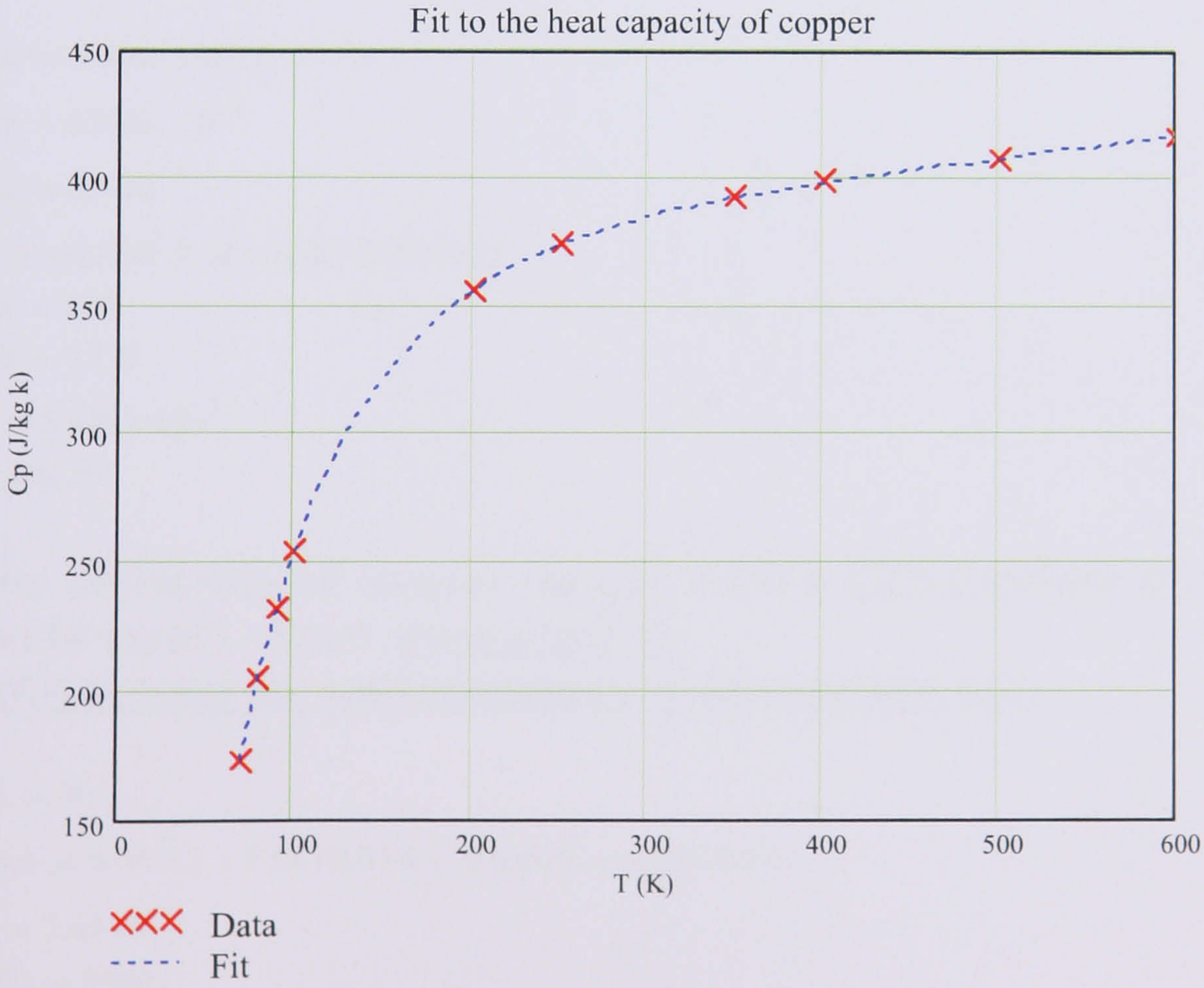
| | 0 |
|---|---|
| 0 | 173 |
| 1 | 205 |
| 2 | 232 |
| 3 | 254 |
| 4 | 356 |
| 5 | 374 |
| 6 | 392.6 |
| 7 | 398.6 |
| 8 | 407.7 |
| 9 | 416.7 |

$Sc := linfit(cx, cy, Fc)$

$$Sc = \begin{pmatrix} -2.469 \times 10^{3} \\ 4.049 \\ -2.417 \times 10^{-7} \\ -585.805 \\ 1.762 \times 10^{3} \\ 0 \end{pmatrix}$$

$C(c) := Fc(c) \cdot Sc$

$r1 := 0, 10.. 530$




Now that the variation of the K and Cp of copper with T can be modelled, the simple lump capacitance method can be applied to the cold stage to see how the temperature of the Cu block changes in time, assuming that the Cu block is all at a uniform temperature T

and considering the 4 braids as one larger braid. It is also assumed that the cold finger is at a constant temperature of 78K.

The equation (to be solved numerically) is:
Q in - Q out = DQst
$[A_{tot}es(T_{sur}^4-T^4)+k_S(T)A_S(T_{sur}-T)/L_S] - k(T)A_2(T-T_1)/L = rVC_p(T)dT/dt$

where :
Atot = surface area of Cu block
Tsur = room temp
e = emissivity of Cu
k(T) = thermal conductivity of Cu (T dependent)
s = Stefan Boltzmann constant
A2 = contact area of copper braid to Cu block
T1 = temperature of cold finger
L = length of copper braid
r = density of Cu
V = volume of Cu block
$k_S(T)$ = thermal cond of s steel (T dep)
$A_S$ = contact area of s steel to Cu block
$L_S$ = length of s steel studding
Cp(T) = specific heat capacity of Cu (T dependent)

$As := 0.01 \cdot \pi \cdot 0.007 \cdot 2$

$As = 4.398 \times 10^{-4}$

$A2 := 2.5 \cdot 10^{-4}$

$V := \pi \cdot 0.006^2 \cdot 0.12 + 0.067 \cdot 0.067 \cdot 0.01$

$Ls := 0.05$

$Lb := 0.125$

$V = 5.846 \times 10^{-5}$

$\varepsilon := 0.75$

The emissivity of copper ranges from 0.023 (polished) to 0.78 (thick oxide layer). From www.electro-optical.com/bb_rad/emissivity/matlemisivty.htm

$T1 := 90$

$Atot := 0.067^2 \cdot 2 + 0.067 \cdot 0.01 \cdot 4 + \pi \cdot 0.006^2 + \pi \cdot 0.012 \cdot 0.12$

$\sigma := 5.67 \cdot 10^{-8}$

$\rho Cu := 8960$

$Atot = 0.016$

$Tsur := 300$

$k(T) := G(T)$

$Cp(T) := C(T)$

$ks(T) := S(T)$

The interactions start at the time when the cold finger reaches the min temp (~90K) as before then the cold finger is also gradually cooling from RT down. The starting temperature of the interaction is that of the copper base at the time the cold finger has reached its base temperature. If the fit is good and the implications are that all the parameters are realistic!

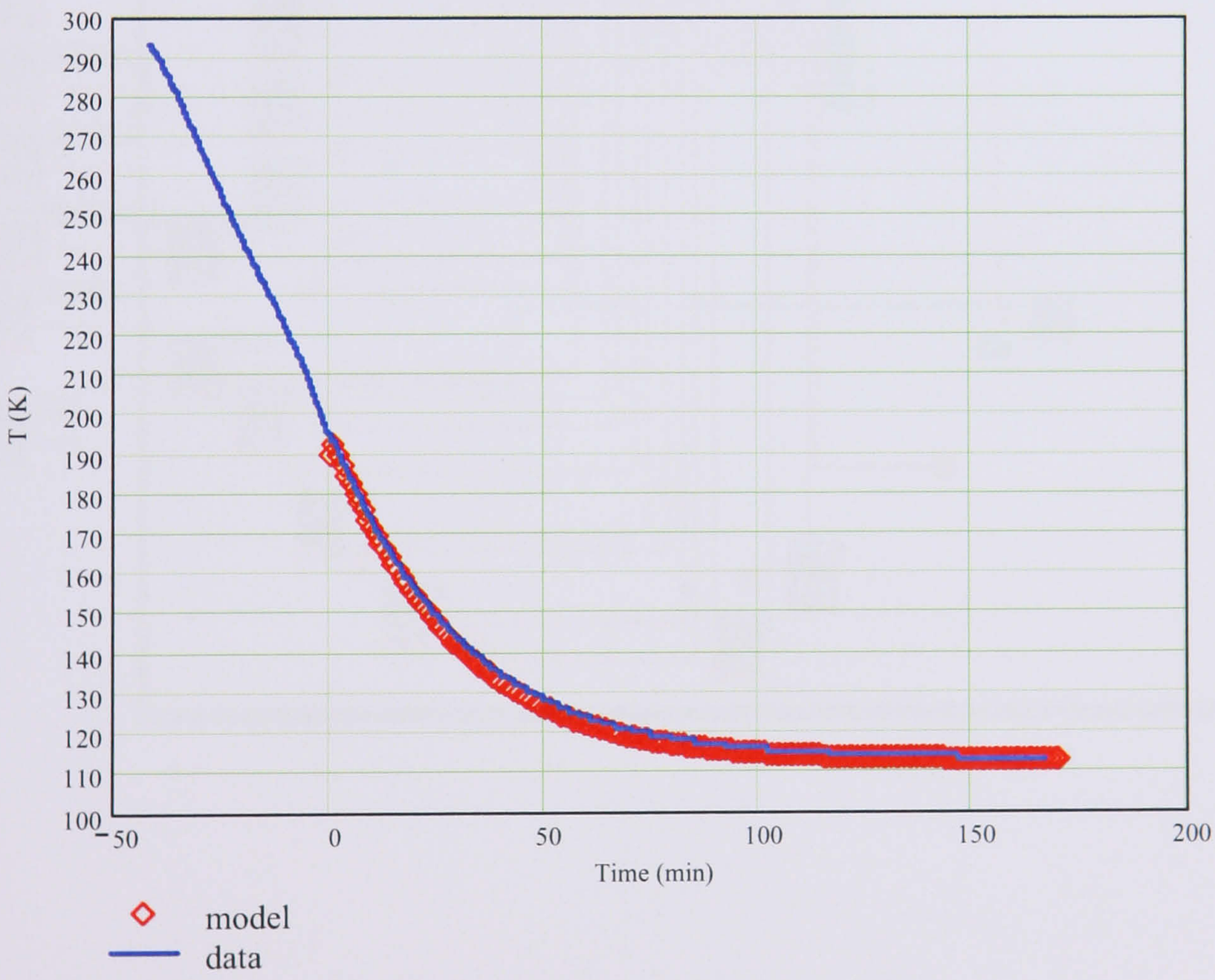
$$\text{theory}(h) := \left| \begin{array}{l} H \leftarrow 195 \\ \text{for } i \in 1..h \\ \quad H \leftarrow \dfrac{\left[ Atot \cdot \varepsilon \cdot \sigma \cdot \left( Tsur^4 - H^4 \right) + ks(H) \cdot \dfrac{As \cdot (Tsur - H)}{Ls} - k(H) \cdot \dfrac{A2 \cdot (H - T1)}{Lb} \right] \cdot 7}{\rho Cu \cdot V \cdot Cp(H)} + H \end{array} \right.$$

$:=$ 💾

P:\..\TEMP210604.txt

n21 := 0.. 2510

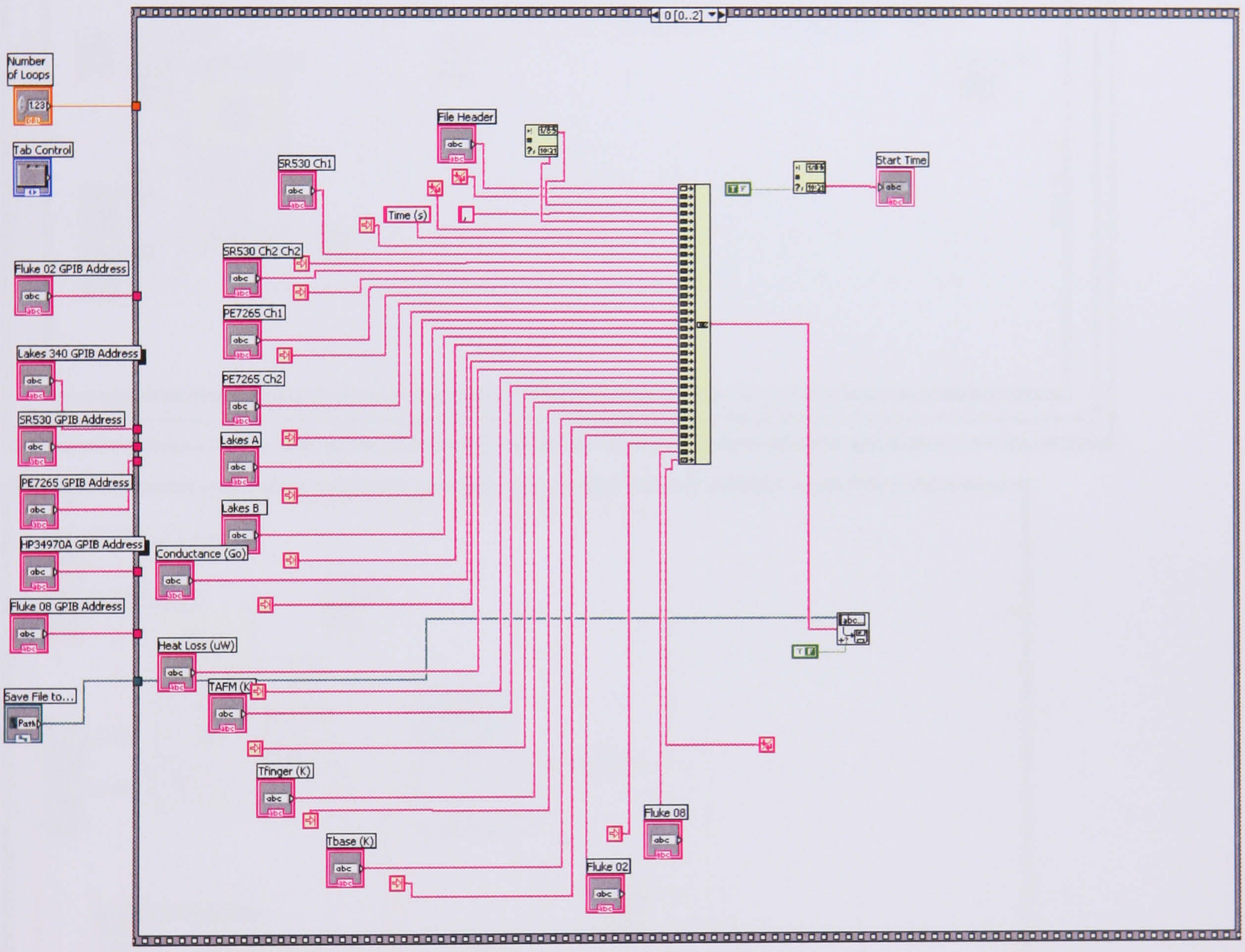
h := 0.. 170

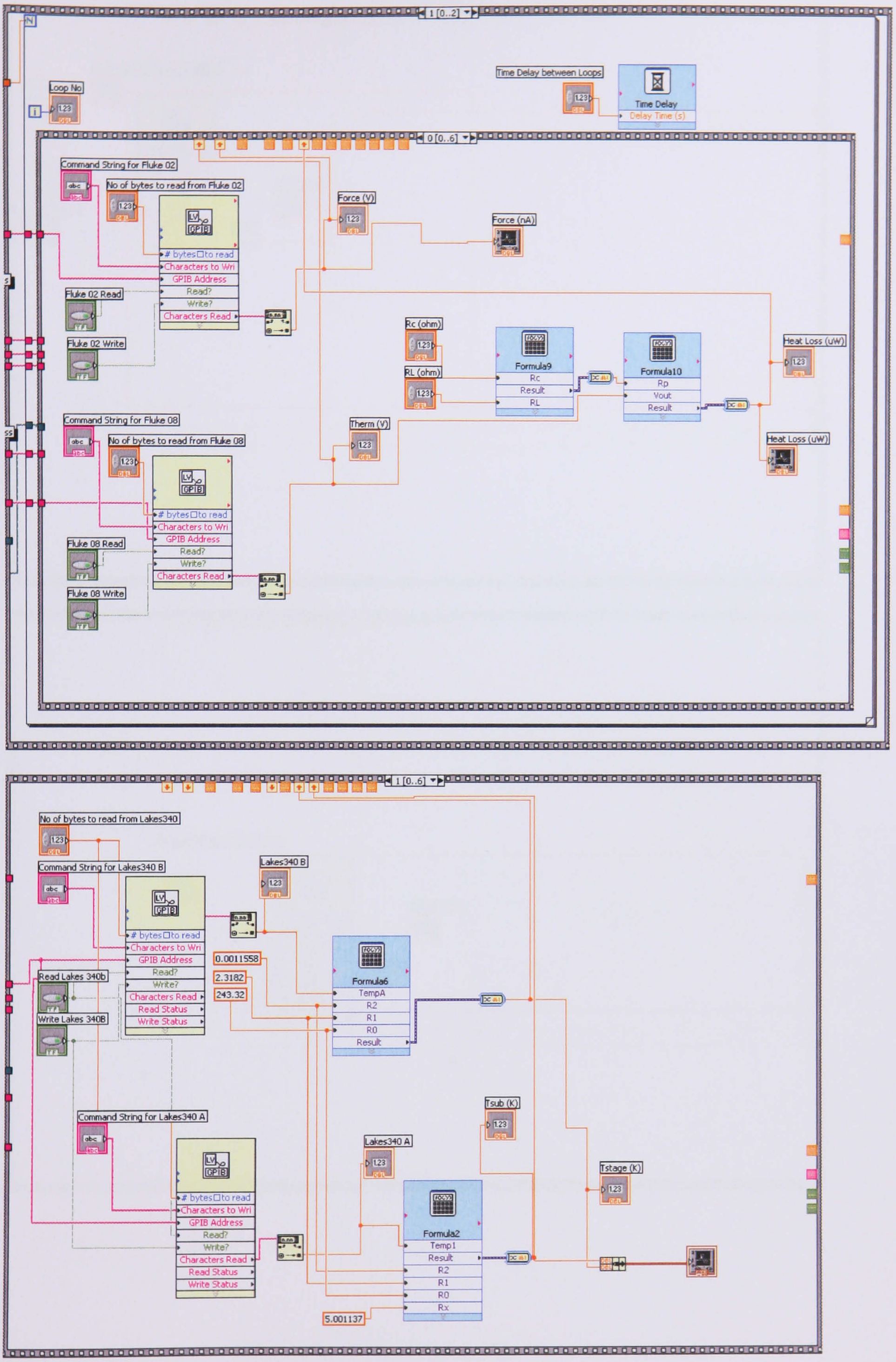


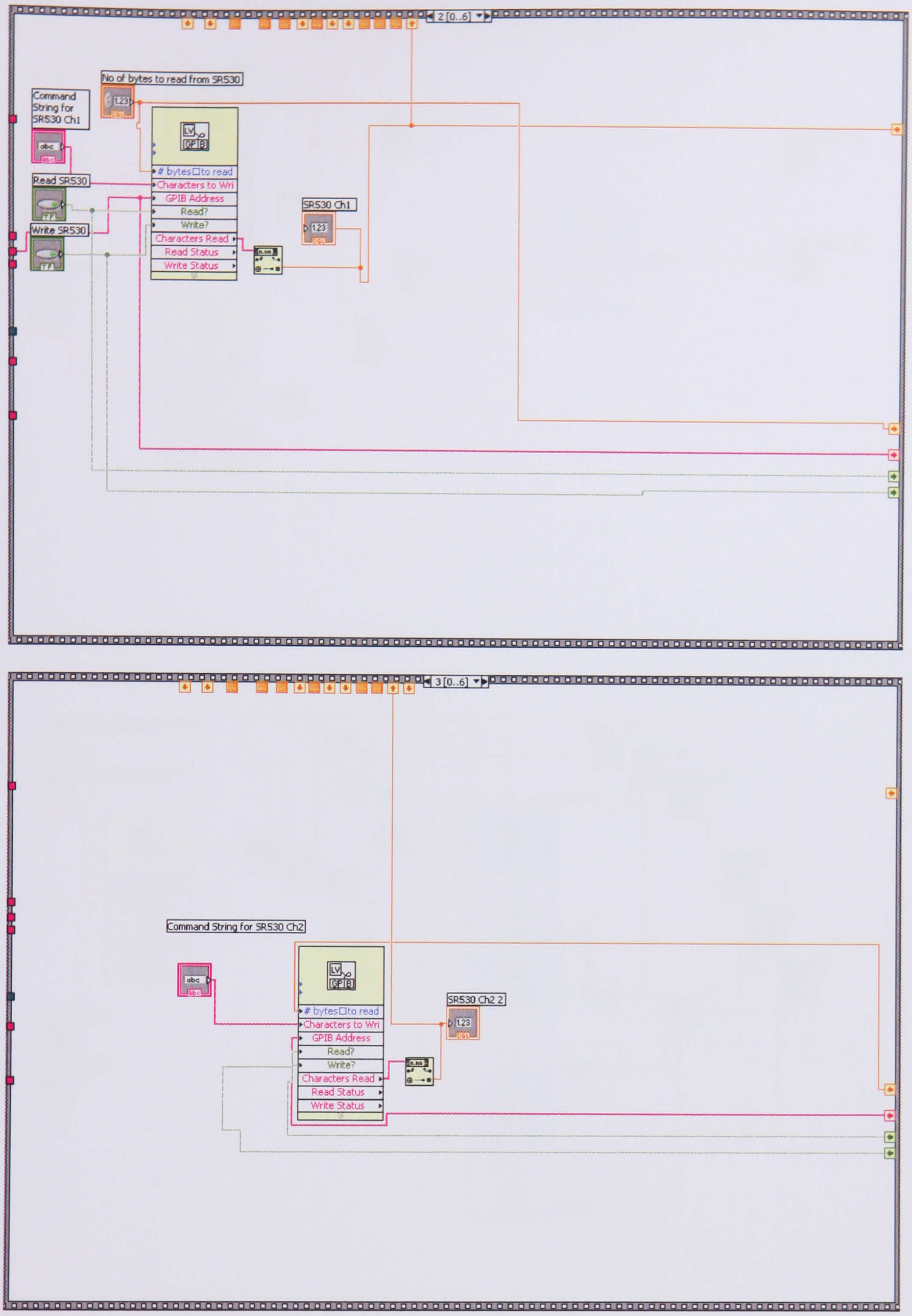
# B - Labview 7.0 programme for simultaneous thermal conductance, electrical conductance and cantilever deflection acquisition

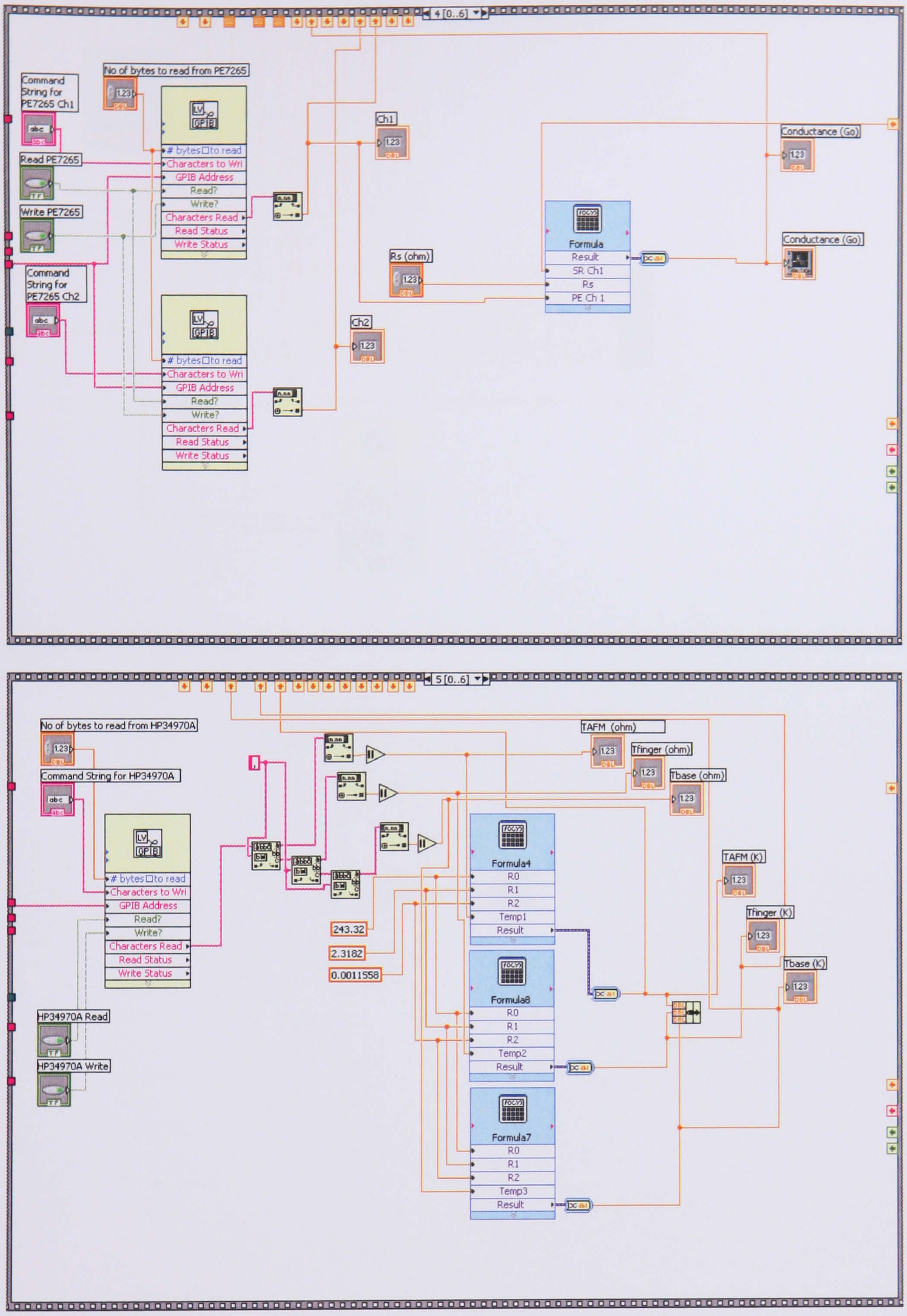
What follows is a copy of the block diagram of the programme including details of the formulas used.

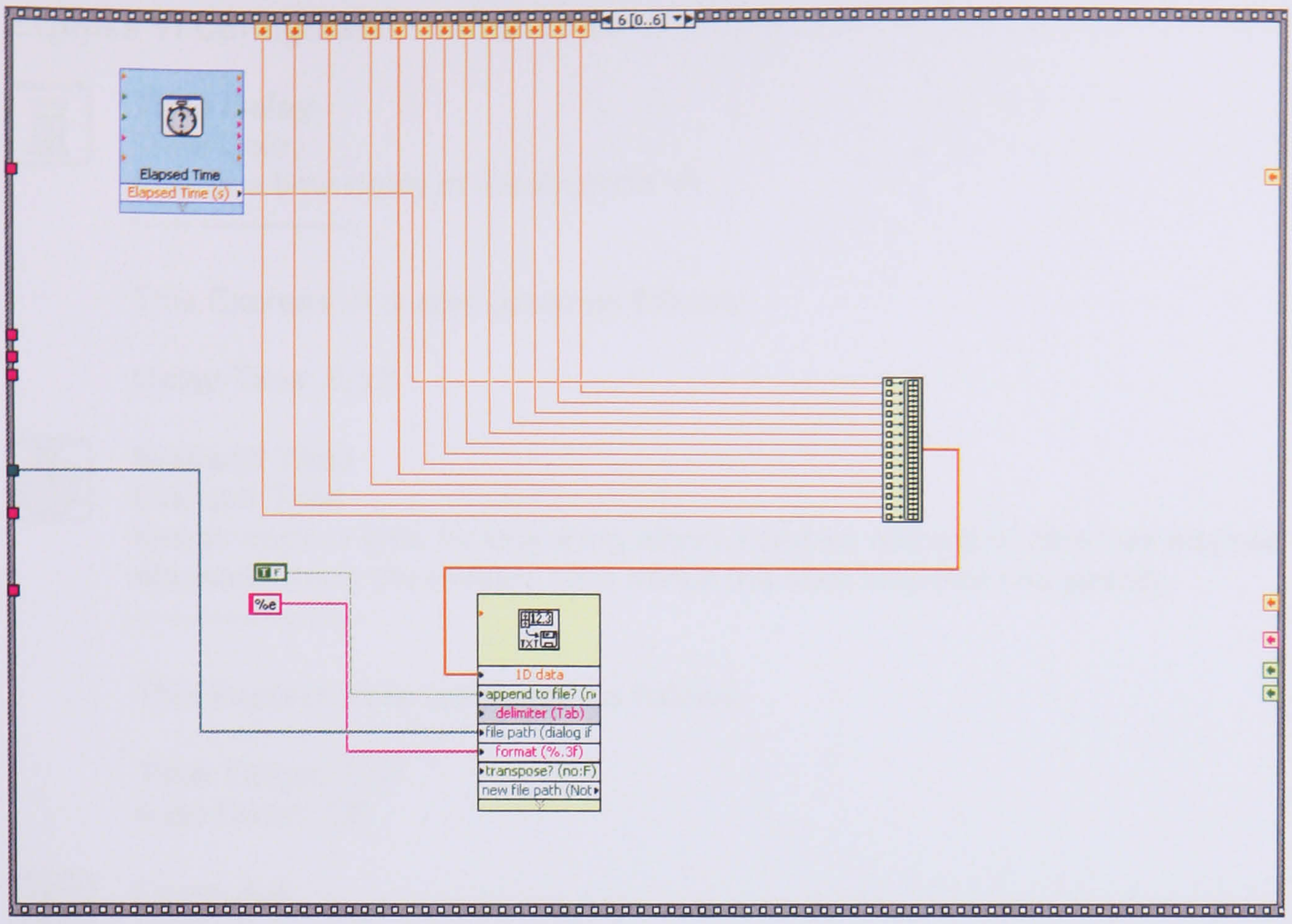
---

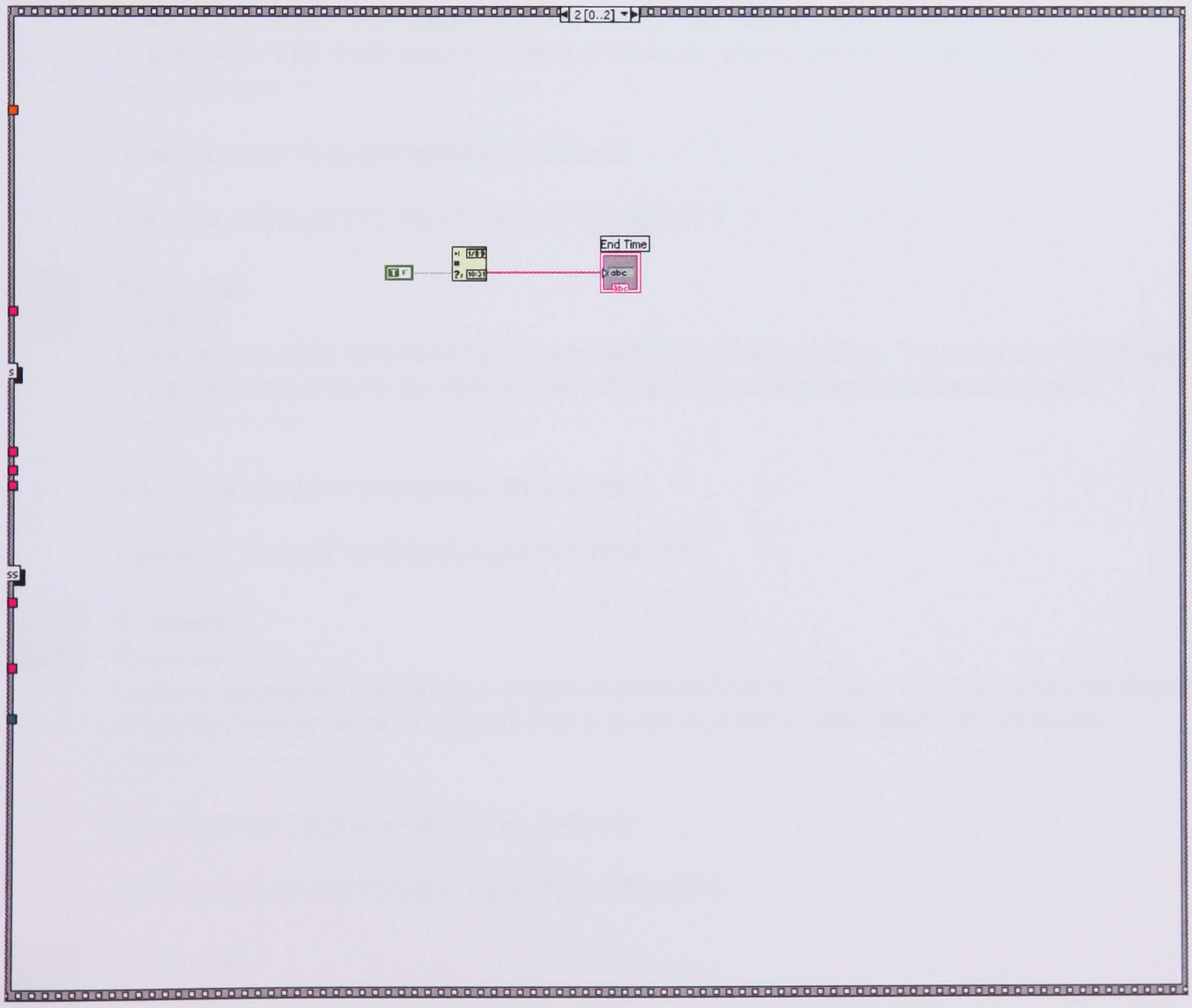



1 [0..2]
Loop No
i
Time Delay between Loops
Time Delay
Delay Time (s)
0 [0..6]
Command String for Fluke 02
No of bytes to read from Fluke 02
Force (V)
Force (nA)
LV GPIB
# bytes to read
Characters to Wri
GPIB Address
Read?
Write?
Characters Read
Fluke 02 Read
Fluke 02 Write
Rc (ohm)
RL (ohm)
Formula9
Rc
Result
RL
Formula10
Rp
Vout
Result
Heat Loss (uW)
Therm (V)
Command String for Fluke 08
No of bytes to read from Fluke 08
Fluke 08 Read
Fluke 08 Write
1 [0..6]
No of bytes to read from Lakes340
Command String for Lakes340 B
Lakes340 B
Read Lakes 340b
Write Lakes 340B
Characters Read
Read Status
Write Status
0.0011558
2.3182
243.32
Formula6
TempA
R2
R1
R0
Result
Command String for Lakes340 A
Lakes340 A
Tsub (K)
Tstage (K)
Formula2
Temp1
Result
R2
R1
R0
Rx
5.001137


2 [0..6]
No of bytes to read from SR530
Command String for SR530 Ch1
Read SR530
Write SR530
# bytes to read
Characters to Wri
GPIB Address
Read?
Write?
Characters Read
Read Status
Write Status
SR530 Ch1
3 [0..6]
Command String for SR530 Ch2
# bytes to read
Characters to Wri
GPIB Address
Read?
Write?
Characters Read
Read Status
Write Status
SR530 Ch2 2


4 [0..6]
Command String for PE7265 Ch1
No of bytes to read from PE7265
Read PE7265
Write PE7265
Command String for PE7265 Ch2
# bytes to read
Characters to Wri
GPIB Address
Read?
Write?
Characters Read
Read Status
Write Status
Ch1
Ch2
Rs (ohm)
Formula
Result
SR Ch1
Rs
PE Ch 1
Conductance (Go)
Conductance (Go)
5 [0..6]
No of bytes to read from HP34970A
Command String for HP34970A
HP34970A Read
HP34970A Write
243.32
2.3182
0.0011558
Formula4
Formula8
Formula7
R0
R1
R2
Temp1
Temp2
Temp3
TAFM (ohm)
Tfinger (ohm)
Tbase (ohm)
TAFM (K)
Tfinger (K)
Tbase (K)


6 [0..6]
Elapsed Time
Elapsed Time (s)
%e
1D data
append to file? (n
delimiter (Tab)
file path (dialog if
format (%.3f)
transpose? (no:F)
new file path (Not


2 [0..2]
End Time
abc
S
SS

## Express VI Configuration Information



**Time Delay**
Time Delay
Inserts a time delay in the Express VI.
---

This Express VI is configured as follows:

Delay Time: 0.5 s



**Elapsed Time**
Elapsed Time
Keeps track of time by indicating when a certain amount of time has elapsed. The elapsed time is the present time minus the start time that you specify.
---

This Express VI is configured as follows:

Time Target: 12 s
Auto Reset: Off



**Formula4**
Formula
Uses a calculator interface to create mathematical formulas. You can use this Express VI to perform most math functions that a basic scientific calculator can compute.
---

This Express VI is configured as follows:

Formula: (Temp1)**2*R2+(Temp1)*R1-R0+273



**Formula6**
Formula
Uses a calculator interface to create mathematical formulas. You can use this Express VI to perform most math functions that a basic scientific calculator can compute.
---

This Express VI is configured as follows:

Formula: TempA**2*R2+TempA*R1-R0+273



**Formula7**
Formula
Uses a calculator interface to create mathematical formulas. You can use this Express VI to perform most math functions that a basic scientific calculator can compute.
---

This Express VI is configured as follows:

Formula: (Temp3)**2*R2+(Temp3)*R1-R0+273



**Formula8**
Formula
Uses a calculator interface to create mathematical formulas. You can use this Express VI to perform most math functions that a basic scientific calculator can compute.
---

This Express VI is configured as follows:

Formula: (Temp2)**2*R2+(Temp2)*R1-R0+273

**Formula9**
Formula
Uses a calculator interface to create mathematical formulas. You can use this Express VI to perform most math functions that a basic scientific calculator can compute.
---

This Express VI is configured as follows:

Formula: (Rc-RL)/5

**Formula10**
Formula
Uses a calculator interface to create mathematical formulas. You can use this Express VI to perform most math functions that a basic scientific calculator can compute.
---

This Express VI is configured as follows:

Formula: Vout**2*Rp/(Rp+20)**2*10**6

**Formula2**
Formula
Uses a calculator interface to create mathematical formulas. You can use this Express VI to perform most math functions that a basic scientific calculator can compute.
---

This Express VI is configured as follows:

Formula: (Temp1/Rx)**2*R2+(Temp1/Rx)*R1-R0+273

**Formula**
Formula
Uses a calculator interface to create mathematical formulas. You can use this Express VI to perform most math functions that a basic scientific calculator can compute.
---

This Express VI is configured as follows:

Formula: 1/(abs(PE Ch 1)/abs(SR Ch1)*Rs)*12900

# C - MathCAD model of the electrical conductance histograms

Setting the 'rounding off' function:

$$\text{mantissa}(x) := x - \text{floor}(x)$$

$$\text{roff}(x) := \text{if}(\text{mantissa}(x) < .5, \text{floor}(x), \text{ceil}(x))$$

Choosing the parameters for the MWNT fibre: W=no of ballistic paths contacting the HOPG (i.e. no of nanotubes contacting the HOPG), S=max. no of ballistic wires in series, T=max. no of parallel ballistic wires in the series, C=number of conducting channels per wire.

$$s := 10$$

$$c := 2$$

$$w := 5$$

$$t := 1$$

n is the number of conductance values generated:

$$n := 0 .. 999$$

Produce n random entries with min 1 and max t.

$$W_{0,n} := \text{roff}(\text{rnd}(w) + 0.501)$$

W =

| | 0 | 1 | 2 | 3 | 4 | 5 | 6 | 7 | 8 | 9 |
|---|---|---|---|---|---|---|---|---|---|---|
| 0 | 1 | 1 | 3 | 2 | 5 | 1 | 4 | 2 | 1 | 1 |

Each wire is taken individually:

$$p := 0 .. w$$

$$\text{Range}_{p,n} := \text{if}(W_{0,n} - p < 1, 0, 1)$$

Range =

| | 0 | 1 | 2 | 3 | 4 | 5 | 6 | 7 | 8 | 9 |
|---|---|---|---|---|---|---|---|---|---|---|
| 0 | 1 | 1 | 1 | 1 | 1 | 1 | 1 | 1 | 1 | 1 |
| 1 | 0 | 0 | 1 | 1 | 1 | 0 | 1 | 1 | 0 | 0 |
| 2 | 0 | 0 | 1 | 0 | 1 | 0 | 1 | 0 | 0 | 0 |
| 3 | 0 | 0 | 0 | 0 | 1 | 0 | 1 | 0 | 0 | 0 |
| 4 | 0 | 0 | 0 | 0 | 1 | 0 | 0 | 0 | 0 | 0 |
| 5 | 0 | 0 | 0 | 0 | 0 | 0 | 0 | 0 | 0 | 0 |

Each ballistic wire is a current pathway made by up to s similar wires in series:

$$S_{p,n} := \text{if}(\text{Range}_{p,n} < 1, 0, \text{roff}(\text{rnd}(s) + 0.501))$$

$S =$

| | 0 | 1 | 2 | 3 | 4 | 5 | 6 | 7 | 8 | 9 |
|---|---|---|---|---|---|---|---|---|---|---|
| 0 | 1 | 2 | 8 | 1 | 10 | 8 | 7 | 7 | 1 | 9 |
| 1 | 0 | 0 | 6 | 2 | 4 | 0 | 2 | 9 | 0 | 0 |
| 2 | 0 | 0 | 3 | 0 | 1 | 0 | 6 | 0 | 0 | 0 |
| 3 | 0 | 0 | 0 | 0 | 5 | 0 | 10 | 0 | 0 | 0 |
| 4 | 0 | 0 | 0 | 0 | 8 | 0 | 0 | 0 | 0 | 0 |
| 5 | 0 | 0 | 0 | 0 | 0 | 0 | 0 | 0 | 0 | 0 |

Using equation $G=(1/ct+1/ct'+1/ct''...)^{-1}$ we calculate the conductance contribution from each series:

$$G1_{p,n} := \text{if}\left[S_{p,n} = 1, \left(\frac{1}{c\cdot\text{roff}(\text{rnd}(t) + 0.501)}\right)^{-1}, 0\right]$$

$$G2_{p,n} := \text{if}\left[S_{p,n} = 2, \left(\frac{1}{c\cdot\text{roff}(\text{rnd}(t) + 0.501)} + \frac{1}{c\cdot\text{roff}(\text{rnd}(t) + 0.501)}\right)^{-1}, 0\right]$$

$$G3_{p,n} := \text{if}\left[S_{p,n} = 3, \left(\frac{1}{c\cdot\text{roff}(\text{rnd}(t) + 0.501)} + \frac{1}{c\cdot\text{roff}(\text{rnd}(t) + 0.501)} + \frac{1}{c\cdot\text{roff}(\text{rnd}(t) + 0.501)}\right)^{-1}, 0\right]$$

$$G4_{p,n} := \text{if}\left[S_{p,n} = 4, \left(\frac{1}{c\cdot\text{roff}(\text{rnd}(t) + 0.501)} \ldots + \frac{1}{c\cdot\text{roff}(\text{rnd}(t) + 0.501)} + \frac{1}{c\cdot\text{roff}(\text{rnd}(t) + 0.501)} + \frac{1}{c\cdot\text{roff}(\text{rnd}(t) + 0.501)}\right)^{-1}, 0\right]$$

$$G5_{p,n} := \text{if}\left[S_{p,n} = 5, \left(\frac{1}{c\cdot\text{roff}(\text{rnd}(t) + 0.501)} + \frac{1}{c\cdot\text{roff}(\text{rnd}(t) + 0.501)} \ldots + \frac{1}{c\cdot\text{roff}(\text{rnd}(t) + 0.501)} + \frac{1}{c\cdot\text{roff}(\text{rnd}(t) + 0.501)} + \frac{1}{c\cdot\text{roff}(\text{rnd}(t) + 0.501)}\right)^{-1}, 0\right]$$

$$G6_{p,n} := \text{if}\left[S_{p,n} = 6, \left(\frac{1}{c\cdot\text{roff}(\text{rnd}(t) + 0.501)} + \frac{1}{c\cdot\text{roff}(\text{rnd}(t) + 0.501)} + \frac{1}{c\cdot\text{roff}(\text{rnd}(t) + 0.501)} \ldots + \frac{1}{c\cdot\text{roff}(\text{rnd}(t) + 0.501)} + \frac{1}{c\cdot\text{roff}(\text{rnd}(t) + 0.501)} + \frac{1}{c\cdot\text{roff}(\text{rnd}(t) + 0.501)}\right)^{-1}, 0\right]$$

$$G7_{p,n} := \text{if}\left[S_{p,n} = 7, \left(\frac{1}{c\cdot\text{roff}(\text{rnd}(t) + 0.501)} \ldots + \frac{1}{c\cdot\text{roff}(\text{rnd}(t) + 0.501)} + \frac{1}{c\cdot\text{roff}(\text{rnd}(t) + 0.501)} + \frac{1}{c\cdot\text{roff}(\text{rnd}(t) + 0.501)} \ldots + \frac{1}{c\cdot\text{roff}(\text{rnd}(t) + 0.501)} + \frac{1}{c\cdot\text{roff}(\text{rnd}(t) + 0.501)} + \frac{1}{c\cdot\text{roff}(\text{rnd}(t) + 0.501)}\right)^{-1}, 0\right]$$

$$G8_{p,n} := \text{if}\left[S_{p,n} = 8, \left(\frac{1}{c\cdot\text{roff}(\text{rnd}(t) + 0.501)} + \frac{1}{c\cdot\text{roff}(\text{rnd}(t) + 0.501)} \ldots + \frac{1}{c\cdot\text{roff}(\text{rnd}(t) + 0.501)} + \frac{1}{c\cdot\text{roff}(\text{rnd}(t) + 0.501)} + \frac{1}{c\cdot\text{roff}(\text{rnd}(t) + 0.501)} \ldots + \frac{1}{c\cdot\text{roff}(\text{rnd}(t) + 0.501)} + \frac{1}{c\cdot\text{roff}(\text{rnd}(t) + 0.501)} + \frac{1}{c\cdot\text{roff}(\text{rnd}(t) + 0.501)}\right)^{-1}, 0\right]$$

$$G9_{p,n} := \text{if}\left[S_{p,n} = 9, \left(\frac{1}{c\cdot\text{roff}(\text{rnd}(t) + 0.501)} + \frac{1}{c\cdot\text{roff}(\text{rnd}(t) + 0.501)} + \frac{1}{c\cdot\text{roff}(\text{rnd}(t) + 0.501)} \ldots + \frac{1}{c\cdot\text{roff}(\text{rnd}(t) + 0.501)} + \frac{1}{c\cdot\text{roff}(\text{rnd}(t) + 0.501)} + \frac{1}{c\cdot\text{roff}(\text{rnd}(t) + 0.501)} \ldots + \frac{1}{c\cdot\text{roff}(\text{rnd}(t) + 0.501)} + \frac{1}{c\cdot\text{roff}(\text{rnd}(t) + 0.501)} + \frac{1}{c\cdot\text{roff}(\text{rnd}(t) + 0.501)}\right)\right]$$

$$G10_{p,n} := \text{if}\left[S_{p,n} = 10, \left(\frac{1}{c\cdot roff(rnd(t)+0.501)} \ldots + \frac{1}{c\cdot roff(rnd(t)+0.501)} + \frac{1}{c\cdot roff(rnd(t)+0.501)} + \frac{1}{c\cdot roff(rnd(t)+0.501)} \ldots + \frac{1}{c\cdot roff(rnd(t)+0.501)} + \frac{1}{c\cdot roff(rnd(t)+0.501)} + \frac{1}{c\cdot roff(rnd(t)+0.501)} \ldots + \frac{1}{c\cdot roff(rnd(t)+0.501)} + \frac{1}{c\cdot roff(rnd(t)+0.501)} + \frac{1}{c\cdot roff(rnd(t)+0.501)}\right)^{-1}, 0\right]$$

$$G_{p,n} := G1_{p,n} + G2_{p,n} + G3_{p,n} + G4_{p,n} + G5_{p,n} + G6_{p,n} + G7_{p,n} + G8_{p,n} + G9_{p,n} + G10_{p,n}$$

$G =$

| | 0 | 1 | 2 | 3 | 4 | 5 | 6 | 7 | 8 | 9 |
|---|---|---|---|---|---|---|---|---|---|---|
| 0 | 2 | 1 | 0.25 | 2 | 0.2 | 0.25 | 0.286 | 0.286 | 2 | 0.222 |
| 1 | 0 | 0 | 0.333 | 1 | 0.5 | 0 | 1 | 0.222 | 0 | 0 |
| 2 | 0 | 0 | 0.667 | 0 | 2 | 0 | 0.333 | 0 | 0 | 0 |
| 3 | 0 | 0 | 0 | 0 | 0.4 | 0 | 0.2 | 0 | 0 | 0 |
| 4 | 0 | 0 | 0 | 0 | 0.25 | 0 | 0 | 0 | 0 | 0 |
| 5 | 0 | 0 | 0 | 0 | 0 | 0 | 0 | 0 | 0 | 0 |

The sum of the series conductances is the conductance through an individual MWNT:

$$Gsum_{0,n} := \sum G^{\langle n \rangle}$$

$Gsum =$

| | 0 | 1 | 2 | 3 | 4 | 5 | 6 | 7 | 8 | 9 |
|---|---|---|---|---|---|---|---|---|---|---|
| 0 | 2 | 1 | 1.25 | 3 | 3.35 | 0.25 | 1.819 | 0.508 | 2 | 0.222 |

The conductance values are plotted in a histogram with the same bin size as the experimental data:

$i := 1 .. 510$

$int_i := i \cdot 0.02$

$Counts := hist(int, Gsum)$

and are compared with the histograms of the experimental data:

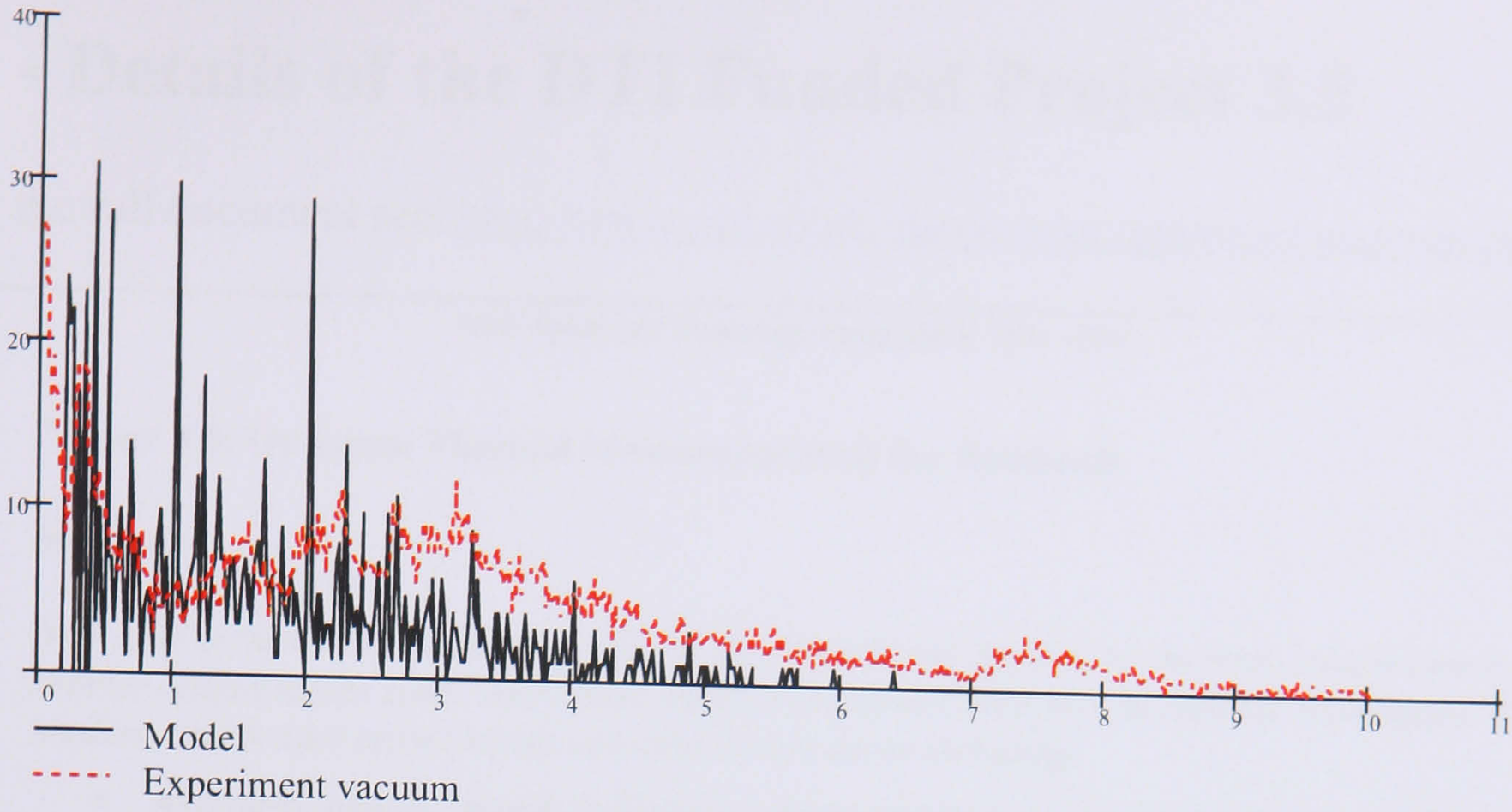
:= 💾

P:\..\in air experimental hist.txt

:= 💾

P:\..\in vacuum experimental hist.txt

The two sets of data are plotted on the same graph:


40
30
20
10
0
1
2
3
4
5
6
7
8
9
10
11
Model
Experiment vacuum

# D - Details of the DTI Funded Project 3.5

For the full document see: http://www.npl.co.uk/quantum/programme/quantum.pdf.

NMS Quantum Metrology Programme 2004 –2007

**Project 3.5: Quantum Thermal Measurements at the Nanoscale**

**Summary**


*New and advanced technologies will be developed and applied to thermal measurement at shorter length scales (μm - nm) where there is an almost total lack of reliable techniques. The medium and longer term outputs are expected in areas including:*

- ***microelectronics:*** *trends to higher-density circuits causes heat dissipation problems*
- ***cellular and sub-cellular metabolic studies****: thermal dissipation and energy transfer at the cell or sub-cell level needs to be understood*
- ***improved medical science and food processing technology****: e.g. improved microsurgical techniques e.g. diathermy, understanding thermal issues in food processing*

*The nanoscale thermal conductance scanning probe measurement capability we are developing will open up routes to improved heat characterisation and management across nanotechnology. This project combines an original NPL approach for a measurement of a fundamental constant together with the development of new, widely applicable nanoscale thermal measurement techniques. Thus a precision determination of the Boltzmann constant, $k_B$, may require several programme cycles to complete, but the short to medium term output of this project will be wide ranging nanoscale thermal measurement capabilities for NPL.*

*The 'test-bed' for our thermal nanoscale measurements is the carbon nanotube. Unique properties of carbon nanotubes offer a wealth of applications in nanoelectronic devices, electromechanical oscillators, chemical probes and biosensors, field emission displays, etc. Carbon based materials display the highest measured thermal conductivity of any known material and carbon nanotubes as one-dimensional structures are predicted to have enormously high thermal conductivity[1]. Unlike electrical and mechanical properties which have been studied at a single nanotube level, the thermal properties of carbon nanotubes have not been measured at a mesoscopic scale or for a Single Wall NanoTube (SWNT). The latter possess nearly perfect crystal symmetry and are typically 1nm and upwards in diameter. Also carbon nanotubes may prove to be ideal materials for the study of low dimensional phonon physics and for thermal management from the macro- to the nano-scale. SWNT properties such as exceptional stiffness and ballistic electrical and (predicted) thermal conductance may also allow the tubes to act as novel thermometers which possess, on account of their ultra small size, very low heat capacity and thus high sensitivity. Our work in the present project has begun to explore the temperature variation of Youngs modulus, with a view to using temperature-dependent mechanical resonance as a means for measuring tube temperature sensitively. This will be extended in the next stage of the project. Our nanoscale thermal measurements, based around the unique properties of SWNTs, provide a means for integrating a number of research areas within one project. Thus a temperature sensing SWNT, attached to a scanned probe microscope will be used in future to investigate temperature gradients or heat production in nanoscale electronic circuits or even within single living cells. SWNTs will also act as phonon waveguides and as a result of their small size we predict that quantised thermal conductance can be observed at temperatures as high as 100-200 K.*

*In the longer term an experimental confirmation of quantised thermal conductance will enable progress to be made towards a novel route towards the determination of $k_B$. The present definition of the kelvin may be regarded as a quasi-artefact definition since it is based on the choice of water and its unique phase diagram and is hence arbitrary. An alternative*

*definition in terms of a fixed value for $k_B$ would bring to temperature measurement some of the benefits which accrued to length measurement with the redefinition of the velocity of light.*

**Deliverables**

**3.5.1** Development of low thermal conductance scanning probe integrated into a cryogenic atomic force microscope (AFM) operating at 77 K and above. This will require an extremely sensitive thermometer which will be based on microwave resonance interrogation of a small single crystal disc with strongly temperature-dependent permittivity. The device will be demonstrated to work with biological samples.

**3.5.2** A report on measurements of the thermal conductivity of carbon nanotubes under a variety of conditions of temperature, termination and surface contact, including any observed quantisation effects. The effects of oxygen doping and other chemical adsorption on carbon nanotube thermal conductance will be investigated.

**Background**

In 1998 Rego and Kirczenow[2] using the Landauer formulation of transport theory predicted that for dielectric quantum wires *thermal conductance* is quantised at low temperatures, in a ballistic phonon regime. The fundamental quantum of thermal conductance ($G_{th}$) is

$$G_{th} = \frac{\pi^2 k_B^2 T}{3h} \qquad (1)$$

where $k_B$ is Boltzmann constant, $h$ is Plank's constant and $T$ is the temperature. It is equal to $9.456 \times 10^{-13}$ W/K$^2$ × T. In 2000, a group at Caltech[3] provided experimental evidence for these calculations and effectively confirmed the quantisation of thermal conductance using a suspended insulating nanostructure at very low temperatures. Such measurements were extremely demanding as, in order to observe $G_{th}$ it is necessary not only to have a 1D phonon waveguide (where phonons propagate ballistically) but also to have optimal coupling between the phonons modes of the waveguide and the thermal reservoir. Furthermore, they required extremely low temperatures as well as a way to measure the temperature of the system with minimal power dissipation. Recently J. Hone et al at Caltech and Berkeley[4] have begun to explore the thermal properties of carbon nanotubes by measuring the specific heat and thermal conductivity of bulk SWNTs samples. They concluded that nanotubes could be the ideal material for the study of low dimensional phonon physics. Thermal measurements on individual nanotubes (especially on single wall nanotubes) still present great challenges. To date only Kim et al. have performed studies of individual Multi-Wall NanoTubes (MWNTs)[5]. In MWNTs however, due to their larger tube radius, the onset of 1D phonon quantisation is expected to occur only at temperatures below 1K. We suggest that, in their case, 1D phonon quantisation was probably suppressed due to the long length of the MWNT compared with the mean free path for phonons.

Our work to date, on single MWNTs at room temperature has confirmed the very high thermal conductivity of carbon nanotubes and we will extend our investigations to the thermal conductivity of single SWNTs at reduced temperatures during the remainder of this project. We are thus internationally competitive with two or three other groups at leading US labs. This project, being rather innovative, must be regarded as internationally leading, though the work at Caltech, which is not primarily driven by metrology has progressed some way towards demonstrating the correctness of equation (1)[3].

**Rationale**

This project aims to provide underpinning of several NMS Unit Programmes, most obviously the Thermal Programme but also several others (Biometrology, Electrical, VAM & Materials) through development of novel quantum thermal transport measurement at the micro to nanoscale. In the longer term this project addresses a crucial tenet of the QMP, the precise determination of a fundamental constant, $k_B$, which would allow a redefinition of the kelvin.

Our approach addresses the following highly relevant issues:

- Development of thermal conductivity measurement methods on a very small scale where there is already a demonstrated demand
- Application of these techniques to a range of cross-Programme metrology problems
- The provision of a quantum scale of thermal conductance
- Realisation of a fundamental constant capable of redefining the kelvin.

The project is exploiting novel temperature sensors to investigate nanoscale structures in a geometry which may have wide-ranging potential across measurement areas including low frequency and microwave electrical measurements. In addition the work will have relevance to the nanoscale research work being undertaken within CETM, where the properties of nansocale electrical circuits may be profoundly influenced by issues of thermal management in nanocircuits. Also, the Metrology for Biotechnology Programme may find important applications of this work, relating to fundamental studies of thermal dissipation and transfer at the cell or sub-cell level.

**Scope**

We plan to explore nanoscale thermal measurement methods in parallel with a developing long-term capability to measure the quantum of thermal conductance and a possible high accuracy determination of the kelvin. Thus the project will provide short, medium and long-term outputs of relevance to the Quantum Programme.

The longer term aim of this project is to analyse routes towards more precise determinations of $k_B$, including novel methods based on ballistic phonon transport and spectroscopy in the quantum limit. In working towards this, radically new experimental techniques are proposed which may have a strong input into the present problem of making accurate spatially resolved measurements of thermal conductivity on a length scale between 10 nm and 100 μm.

Recent work on quantised electrical conductance in reduced dimension electrical conductors has provided promising metrological outputs including a possible future quantum standard of diagonal electrical conductance. But it has only been realised very recently that at cryogenic temperatures, for sub micron-sized single crystal samples, *thermal* conductance can also become quantised. The essential requirement here is that the linear dimension of the thermal conductor must be less than the dominant phonon wavelength in the structure. Theoretically the thermal conductance of an insulating perfect crystal under this restriction is given by equation (1) and $G_{th}$ corresponds to the maximum value of energy that can be transported by a single phonon mode. Preliminary work on 1D thermal conductance structures has been undertaken, especially by a group at Caltech who have concentrated on suspended Si mesoscale structures, and indications of the onset of quantised thermal conductance at modest low temperatures (~0.5 K) have been observed.

In this project we are pursuing a quite different experimental approach to this problem. Single walled carbon nanotubes possess nearly perfect crystal symmetry and are typically 1 nm and upwards in diameter. Carbon nanotubes also have an extremely high thermal conductivity. Simulations by Tomanek[1] have predicted that carbon nanotube could have an enormously high thermal conductivity of about 6600 W/mK for an isolated (10,10) nanotube at room temperature (higher than diamond and graphite). These large thermal conductivity values are principally due to the large phonon mean free path in the tubes (calculated to be 0.5-1.5 μm at 30 K[6]). However the interactions between nanotubes in a bundle or a mat could dramatically reduce these theoretical values and indeed experimental measurements of the thermal conductivity (carried on mats of entangled single-walled nanotubes) have shown much lower values, of the order of 200 W/ m K at room temperature[4].

We have shown in the present programme that such structures provide an excellent starting point for nanoscale thermal measurements, on account of their extremely high thermal conductivity. As one of the first steps in this programme we have looked at the electrical conductance of carbon nanotubes mounted in an AFM structure and have observed clearly quantised electrical conductance at room temperature[7, 8]. Nanotubes are expected to behave as 1D phonon waveguides at low temperatures, and, given their small dimensions and high phonon velocities, we have proposed that they represent the ideal test bed for the observation of the quantum of thermal conductance. A very interesting feature of these results is that the interfaces between nanotube and electrodes have high transparency although a number of experts had predicted low transparency. Our preliminary findings are that the same result seems to apply also to thermal transport.

When Schwab et al. detected first signs of $G_{th}$ in 2000[3], they used a suspended silicon-nitride device with four waveguides whose narrowest width was 200 nm. Given that the phonon speed in silicon nitride is 6 km/s the onset of the 1D quantisation regime was, in their case, 0.8 K. This because the cross-over temperature for the depopulation of all the optical phonon modes is given by: $T_{CO} \sim \pi\hbar v/k_B w$, where $\hbar$ is Plank's constant over $2\pi$, $v$ is the phonon speed, $w$ is the width of the waveguide and $k_B$ is Boltzmann's constant. But for a typical single wall nanotube, $w$ is about 2.0 nm or less and the phonon speed in the different acoustic modes goes from 9 to 24 km/s (9 km/s is the lowest limit); with these values $T_{CO}$ is about 108 K (this is to be considered a lower limit) to 288 K. Detecting thermal conductance quantisation should then be easier with a nanotube, provided its phonon modes are suitably coupled to the thermal reservoir (i.e. there is no reflection at the contacts).

In order to pursue such measurements we will design and further develop our home built cryogenic AFM. This will involve investigation and optimisation of temperature control and stability, and vibration issues. The low temperature AFM operating initially from 77 K up to higher temperature should allow us to observe thermal conductance quantisation in single wall carbon nanotubes. To measure quantised thermal conductance an extremely sensitive thermometer is required. We have already demonstrated that microwave resonance interrogation of a small single crystal discwith strongly temperature-dependent permittivity allows non-contacting ultra-high resolution thermometry. In this project we aim to maximise the sensitivity of this thermometer and integrate it with our low temperature AFM to improve the nanotube thermal conductance determinations.

Gas adsorption in carbon nanotubes and nanotube bundles is an important issue for both fundamental research and technical applications of nanotubes. Recently the modification of the electronic properties of carbon nanotubes by the adsorption of foreign atoms or molecules has been actively studied[9, 10]. It is important to understand the effect on the carbon nanotubes thermal properties by introducing a chemical doping profile or local defects, elastic radial or

other types of deformation, and also by the adsorption of foreign atoms. We will investigate the oxygen doping and other chemical adsorption effects on the carbon nanotube thermal conductance.

Another important development of this study may allow the investigation and implementation of the use of nanotubes as a new temperature/thermal-conductivity sensing technique at the micron/nano-scale. Carbon nanotubes attached (or grown) on AFM tips have already proved to be extremely useful in enhancing the scanning capabilities of the AFM. In the current project, arising from investigations begun under SR project 9SRP4070 we are researching thermal properties such as the temperature dependence of Youngs modulus. This may allow the use of such tips for thermal measurements with ultralow heat capacity sensors and high sensitivity to temperature changes while able to scan across samples since it is attached to an AFM. Application areas include microelectronics where the trend towards small high-density circuits is causing heat dissipation difficulties; medical science, for development and validation of new microsurgical techniques; cellular metabolic studies, and for improved food processing technology. This project therefore has great scientific potential as, by devising a way to measure the thermal conductivity of an individual carbon nanotube, we can not only further increase the understanding of the transport properties of these nanostructures but also test the equation predicting thermal quantised conductance. In the short to medium term this will enable the development of scanned probe methods for measuring thermal properties at the micron/nano level.

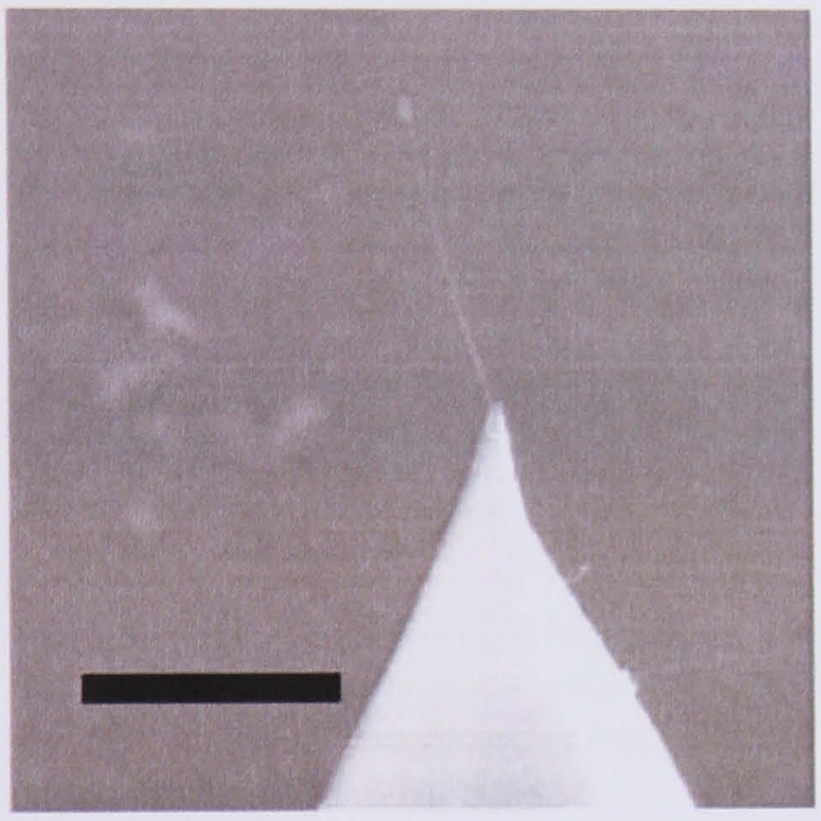
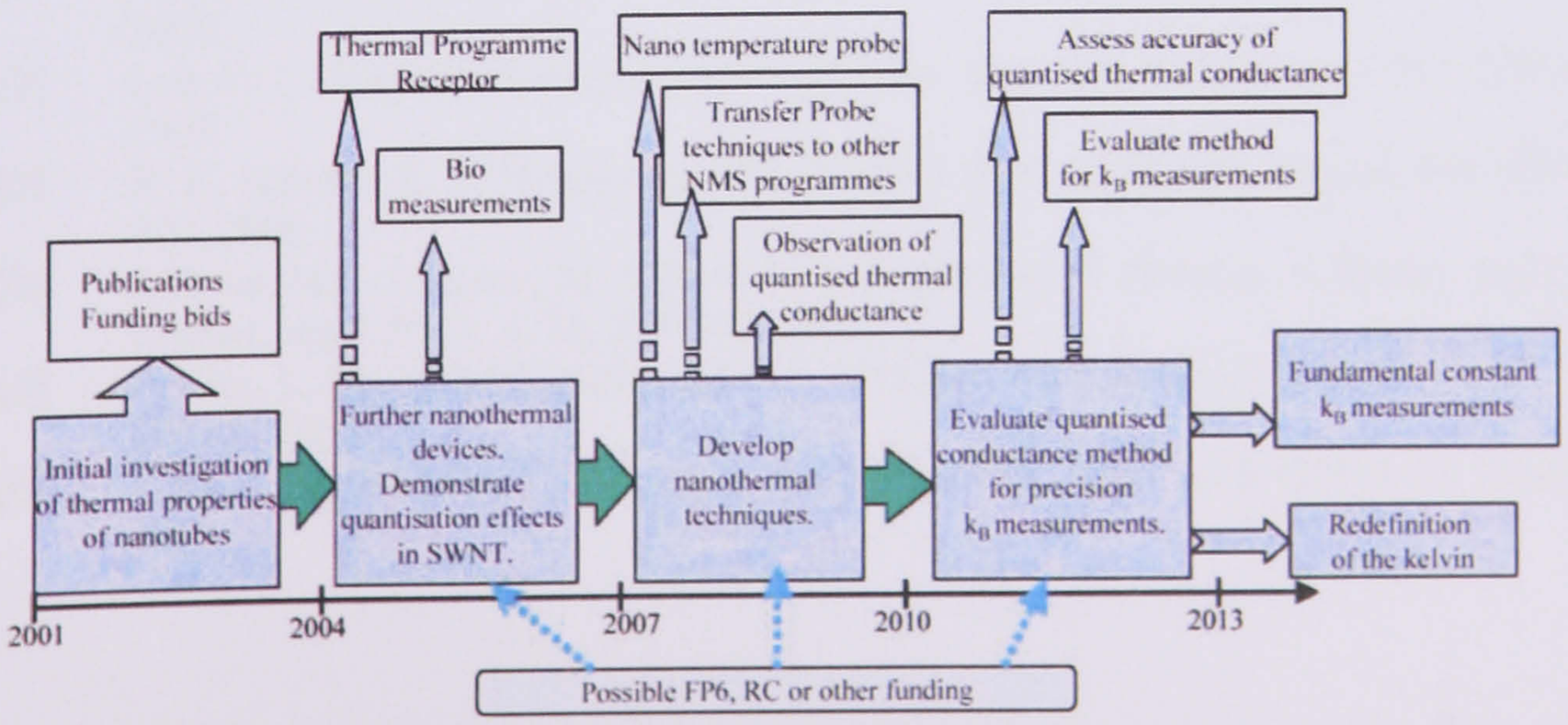


*Fig.1 SEM image of Carbon nanotubes grown on AFM tip (bar is one micron).*

**Time line and progression strategy**

This project represents the second phase of a strategic plan to underpin a base unit of the SI, namely the kelvin. It is assumed that a number (minimum of three, maximum of five) of three year cycles would be required to complete a measurement at the level of precision required to replace the current definition of the kelvin, but in the intermediate period a number of important nanoscale thermal measurement breakthroughs will have been demonstrated and a number of important research papers in this area will have been published.




88

**Consequences of success**

This project, being rather innovative, must be regarded as internationally leading, though the work at Caltech, which is not primarily driven to metrology has progressed some way towards demonstrating the correctness of quantised thermal conductance as given in eq.(1). Work in the current Quantum Programme on the limitations of commercial scanned thermal probes has attracted considerable attention at conferences and workshops and will be written up shortly for publication[8, 11].

**Exploitation route**

Since this project is continuing the development of new science and technology in the precision metrology area it will underpin a wide range of NMS Programmes in future. Specific Programmes to benefit in the medium term would include Thermal (quantised thermal conductance), Electrical (analysis of heat dissipation in microelectronics), VAM and Biotechnology (micro-scale dissipative processes in chemistry and biology), as well as other materials metrology applications (materials analysis by thermal scanning at the nanoscale).

**Other sources or potential sources of financial support**

This project will benefit from continued input from a CASE student who is growing nanotubes directly on AFM cantilevers and will attempt to control their orientation. Our involvement in the present project has enabled us to join a FP6 STREP bid for funding in the area of electromechanical nanoscale oscillators. The collaborations noted below will also contribute support in kind through SWNT samples etc.

**Collaborations**

Collaboration with other groups is already strong. Prof. Andrew Briggs' group in Oxford are supplying us with various single wall carbon nanotube samples. We also have a CASE student with Dr Baxendale at QMUL. A potential collaboration could also arise with Glasgow University where Dr John Weaver is developing a novel design for a new AFM thermal probe. Contacts have been made with a major thermal studies laboratory in Lyons and collaboration with this group is being pursued. Within NPL we will work closely with John Redgrove and Marc Broussely (CBTLM) to identify Thermal Programme and industrial need for future measurement capability.

**References** (NPL presentations & publications in bold)

[1] S. Berber, Y.K. Kwon and D. Tomanek, *Phys. Rev. Let.* 84, no. 20, p.46134616, May, 2000.

[2] Luis G. C. Rego and George Kirczenow; *Phys. Rev. Lett.* Vol. 81, no. 1 232- 235 July 1998.

[3] W K. Schwab, E. A. Henriksen, J. M. Worlock & M. L. Roukes, *Nature* 404, 974 – 977, 2000.

[4] J. Hone, M.C. Llaguno, M. J. Biercuk, A.T. Johnson, B. Batlogg , Z. Benes and J.E. Fischer, *Appl. Phys. A*, 74, 339-343, 2002.

[5] P. Kim, L. Shi, A. Majumdar, and P. L. McEuen, *Phys. Rev. Lett.* Vol. 87, no. 21, 205502 2001.

[6] J. Hone, M. Whitney, C. Piskoti, A. Zettl: *Phys. Rev. B* 59, no. 4, R2514-59, January 1999.

**[7] E. Brown, M. Baxendale and J. Gallop, "Oxygen doping of carbon nanotubes: fractional quantised conductance studies", poster presentation at International Conference on Nano Structures (Frascati) Sept. 2002.**

**[8] E. Brown and J. Gallop, "Study on Probe-Sample heat exchange in an AFM in air and in vacuum", poster presentation at Oxford Workshop on Scanned Probe Microscopy, 2003.**

[9] Collins P. G., Bradley K., Ishigami M and Zettl A, *Science* vol 287, 1801-1804, March 2000.

[10] Dag S., Gulseren O., Yidirim T. and Ciraci S, *Phys. Rev. B* 67, 165424-1-10, 2003.

**[11] E. Brown, M, Baxendale and J. Gallop, submitted to Phys. Rev. B., 2003.**